

**Harmonisation of the  
GOME, SCIAMACHY, and GOME-2 total ozone  
data records for a better understanding of  
long-term trends and their causes**

Dissertation  
zur Erlangung des Grades  
Dr. rer. nat.  
der Universität Bremen

vorgelegt von

M.Sc. Env. Phys.  
**Wissam Chehade**

Institut für Umweltphysik IUP  
FB 1, Physik und Elektrotechnik  
Universität Bremen



**1. Gutachter** : Prof. Dr. John P. Burrows  
**2. Gutachter** : Prof. Dr. Otto Schrems

**Weitere Prüfer** : Dr. Helmut Fischer  
: PD Dr. Volker Perlick

**Eingereicht am** : 14.02.2014  
**Tag des Promotionskolloquiums** : 19.06.2014

# Abstract

This thesis addresses the issue of the accurate measurements of ozone distributions in the atmosphere obtained from different satellite borne atmospheric chemistry spectrometers which represent a major need and pre-requisite for determining whether the atmospheric burden of ozone depleting substances (ODS) are reduced in accordance to the Montreal Protocol, and valuable for long-term trend analysis to detect a subsequent ozone recovery. A consolidated and homogeneous long term dataset requires a careful analysis of the relevant parameters used in the retrievals, one important parameter is the absorption cross section.

This work presents the procedures followed to correct the ozone cross section data of SCIAMACHY and GOME-2 spectrometers starting from original raw data (optical density spectra). Using the available versions of SCIAMACHY and GOME-2 FM cross sections in the retrieval of total ozone from each satellite leads to an overestimation in the total ozone by 3–5% and 8–9% compared to collocated GOME data, respectively. The quality of the revised temperature-dependent ozone absorption cross sections is investigated over GOME-2 and SCIAMACHY's entire spectral range. The revised data agree well within 3% with other published ozone cross sections and preserve the correct temperature dependence in the Hartley, Huggins, Chappuis and Wulf bands as displayed by the literature data. SCIAMACHY's total ozone columns retrieved using the revised cross section data are shown to be within 1% compared to the ozone amounts retrieved routinely from SCIAMACHY, which uses Bogumil et al. (2003) data but adjusted with a scaling factor of 5.3% and a wavelength shift of 0.08 nm. The total ozone column retrieved from the GOME-2/MetOp-A satellite using the new cross section data is within 1% compared to the ozone amounts retrieved from the standard retrieval performed for GOME-2.

The study also presents a long term statistical trend analysis of total ozone datasets obtained from various satellites. A multi-variate linear regression was applied to annual mean zonal mean data using various natural and anthropogenic explanatory variables that represent dynamical and chemical processes which modify global ozone distributions in a changing climate. The study investigated the magnitude and zonal distribution of the different atmospheric chemical and dynamical factors contributing to long-term total ozone changes. The regression model included the Equivalent Effective Stratospheric Chlorine (EESC), the 11 year solar cycle, the Quasi-Biennial Oscillation (QBO), stratospheric aerosol loading describing the effects from major volcanic eruptions, the El Niño/ Southern Oscillation (ENSO), the Arctic and Antarctic Oscillation, and accumulated eddy heat flux (EHF), the latter representing changes due to the Brewer Dobson circulation. The total ozone column dataset used here comprises the SBUV/TOMS/OMI merged data (1979 – 2012) MOD V8.0. The analysis explained most of the ozone variability. The results show that QBO dominates the ozone variability in the tropics ( $\pm 7$  DU) while at higher latitudes, the dynamical indices, AO/AAO and eddy heat flux, have substantial influence on total ozone variations by up to  $\pm 10$  DU. ENSO signal are more evident in the Northern Hemisphere. EESC is found to be a main contributor to the long-term ozone decline and the trend changes after the end of 1990s. A positive significant trend in total ozone columns is found after 1997 (between 1 and  $8.2 \text{ DU decade}^{-1}$ ) which points at the slowing of ozone decline and the onset of ozone recovery. The EESC based trends are compared with the trends obtained from the statistical piecewise linear trend (PWLT or hockey stick) model to examine the differences between both approaches. The results do indicate that the positive PWLT turnaround trends are larger than indicated by the EESC trends, however, they agree within 2-sigma, thus demonstrating the success of the Montreal Protocol phasing out of the ozone depleting substances (ODS). A sensitivity study is carried out by comparing the regression results, using different satellite merged datasets as well as the ground based measurements (1979 – 2012) in the regression analysis in order to investigate the uncertainty in the long-term trends due to different ozone datasets and data versions. All the datasets show almost identical pre-turnaround trends before 1979 for both EESC and PWLT approaches while the positive trends after 1997 are greatly influenced by the short-term variability. In spite of that, all datasets agree within 2-sigma fit parameters.

# Publications and Contributions

## Publications

- Chehade, W., Burrows, J. P., and Weber, M., *Total ozone trends and variability during 1979 – 2012 from merged datasets of various satellites*, *Atmospheric Chemistry and Physics Discussions*, 13, 2013, 11, 30407 – 30452, <http://www.atmos-chem-phys-discuss.net/13/30407/2013,10.5194/acpd-13-30407-2013>.
- Chehade, W., Gür, B., Spietz, P., Gorshchev, V., Serdyuchenko, A., Burrows, J. P., and Weber, M., *Temperature dependent ozone absorption cross section spectra measured with the GOME-2 FM3 spectrometer and first application in satellite retrievals*, *Atmos. Meas. Tech.*, 6, 7, 1623–1632, doi:10.5194/amt-6-1623-2013, <http://www.atmos-meas-tech.net/6/1623/2013/>, 2013.
- Chehade, W., Gorshchev, V., Serdyuchenko, A., Burrows, J. P. and Weber, M., *Revised temperature dependent ozone absorption cross section spectra (Bogumil et al.) measured with the SCIAMACHY satellite spectrometer*, *Atmos. Meas. Tech.*, 6, 11, 3055–3065, <http://www.atmos-meas-tech.net/6/3055/2013/>, doi:10.5194/amt-6-3055-2013, 2013.
- Gorshchev, V., Serdyuchenko, A., Weber, M., Chehade, W., and Burrows, J. P., *High spectral resolution ozone absorption cross-sections around 293 K Part 1: Measurements, data analysis and comparison with previous measurements around 293 K*, *Atmos. Meas. Tech. Discuss.*, 6, 6567-6611, doi:10.5194/amtd-6-6567-2013, 2013.
- Serdyuchenko, A., Gorshchev, V., Weber, M., Chehade, W., and Burrows, J. P., *High spectral resolution ozone absorption cross-sections – Part 2: Temperature dependence*, *Atmos. Meas. Tech. Discuss.*, 6, 6613-6643, doi:10.5194/amtd-6-6613-2013, 2013.

Weber, M., Chehade, W., Fioletov, V. E., Frith, S. M., Long, C. S., Steinbrecht, W. and Wild, J. D., [*Global Climate*] *Stratospheric Ozone [in State of the Climate in 2012]*, Bull. Amer. Meteor. Soc., 94, S36-S37, 2013.

Weber, M., Chehade, W., Spietz, P., *Impact of ozone cross-section choice on WFDOAS total ozone retrieval applied to GOME, SCIAMACHY, and GOME-2 (1995-present)*, Contribution to ACSO. (IGACO Activity: Absorption Cross-Sections for Ozone), Version 2.0, [http://www.iup.uni-bremen.de/UVSAT\\_material/technotes/weber\\_acso\\_201101.pdf](http://www.iup.uni-bremen.de/UVSAT_material/technotes/weber_acso_201101.pdf) (last access: May 2011), Universität Bremen, Bremen, Bremen, 2011.

Weber, M., Chehade, W., Gorshelev, V., Serdyuchenko, A., Spietz, P., *Impact of ozone cross-section choice on WFDOAS total ozone retrieval applied to GOME, SCIAMACHY, and GOME-2 (1995-present)*, Technical Note Issue 2 with updates from November 2013, a contribution to ACSO, 2013.

WMO–UNEP Ozone Assessment, 2014: CHAPTER 2, *Update on Global Ozone: Past, Present and Future*, Lead Authors: Pawson, S. and Steinbrecht, W., Authors: Charlton-Perez, A.J., Fujiwara, M., Karpechko, A.Yu., Petropavlovskikh, I., Urban, J. and Weber, M., Contributors: Aquila, V., Cionni, I., Chehade, W., Coldewey-Egbers, M., Delcloo, A., Fioletov, V.E., Fleming, E., Frith, S.H., Gillet, N.P., Loyola, D., McLinden, C.A., Revell, L.E., Sakazaki, T., Sevoir, W., van der A, R.J., and Wild, J.

## **Selected Conferences or Workshops Contributions**

Chehade, W., Burrows, J.P., and Weber, M., *What can we learn from the GOME2 CATGAS Campaign: Potential error sources*, 1 April 2009, Bremen, Germany.

Chehade, W., Burrows, J.P., and Weber, M., *Temperature Dependent O<sub>3</sub> Absorption Cross Section Spectra (235–795 nm) Obtained with GOME-2: Re-analysis*, 15 January 2010, Bremen, Germany.

Gorshelev, V., Serdyuchenko, A., Weber, M., Chehade, W., and Burrows, J. P., *Harmonization of GOME, SCIAMACHY and GOME-2 ozone absorption cross-sections*, DPG Frühjahrstagung 8–12 March 2010, Hannover, Germany.

Chehade, W., Gorshelev, V., Serdyuchenko, A., Burrows, J. P., and Weber, M., *TEMPERATURE DEPENDENT O<sub>3</sub> ABSORPTION CROSS SECTIONS FOR GOME, SCIAMACHY AND GOME-2: I. Re-analysis*

*of Flight Model Data and Retrieval Tests, 38th COSPAR Scientific Assembly, 18–25 July 2010, Bremen, Germany.*

Gorshchev, V., Serdyuchenko, A., Weber, M., Chehade, W., and Burrows, J. P., *TEMPERATURE DEPENDENT O<sub>3</sub> ABSORPTION CROSS SECTIONS FOR GOME, SCIAMACHY AND GOME-2: II. NEW LABORATORY MEASUREMENTS*, 38th COSPAR Scientific Assembly, 18–25 July 2010, Bremen, Germany.

Chehade, W., Weber, M., and Burrows, J. P., *Temperature dependent O<sub>3</sub> absorption cross sections for GOME, SCIAMACHY and GOME-2: Re-analysis of Flight Model Data and Retrieval Tests*, European Geosciences Union General Assembly 03–08 April 2011, Vienna, Austria.

Serdyuchenko, A., Gorshchev, V., Chehade, W., Weber, M., and Burrows, J. P., *Harmonisation of GOME, SCIAMACHY and GOME-2 cross-sections*, European Geosciences Union General Assembly 03–08 April 2011, Vienna, Austria.

Chehade, W., Weber, M., and Burrows, J. P., *Long term ozone trend analysis for the years 1979 – 2011 from merged data sets of various satellites*, European Geosciences Union General Assembly 22–27 April 2012, Vienna, Austria.

Chehade, W., Gorshchev, V., Serdyuchenko, A., Burrows, J. P., and Weber, M., *Harmonisation of GOME, SCIAMACHY, GOME-2 Ozone and Nitrogen Dioxide Cross-sections HARMONICSi Re-analysis of SCIAMACHY and GOME-2 ozone flight model data and retrieval tests: Final Results I. Ozone II. Nitrogen Dioxide*, May 8, 2012, ESA ESRI, Frascati, Italy.

Chehade, W., Weber, M., and Burrows, J. P., *Long term total ozone trend analysis of the years 1979–2011 from merged data sets of various satellites*, June 19, 2012, Advances in Atmospheric Science and Applications ATMOS 2012, Bruges, Belgium.

Chehade, W., Weber, M., and Burrows, J. P., *Long term ozone trend analysis for the years 1979 – 2011 from merged data sets of various satellites*, TOSCA - Towards a more complete assessment of the impact of solar variability on the Earth's climate, 10–15 March 2013, Thessaloniki, Greece.

Chehade, W., Weber, M., and Burrows, J. P., *Long term ozone trend analysis for the years 1979 – 2011 from merged data sets of various satellites*, European Geosciences Union General Assembly 07–12 April 2013, Vienna, Austria.

Chehade, W., Weber, M., Burrows, J. P., Frith, S.M. and Fioletov, V., *Long*

*term total ozone trend analysis of the years 1979 – 2011 from merged data sets of various satellites, DFG Research Unit, SHARP Annual Meeting, 26–28 June 2013, Berlin, Germany.*

Weber, M., Chehade, W., and Burrows, J. P., *The impact of the Brewer-Dobson circulation on total ozone trends, SHARP II Kickoff Meeting, 2–4 July 2012, Wessling, Germany.*

Weber, M., Chehade, W., Dikty, S., Burrows, J. P. and Frith, S.M., *Total ozone trends and variability during 1979 – 2011 from merged data sets of various satellites – onset of ozone recovery, Quadrennial Ozone Symposium, 27–31 August 2012, Toronto, Canada.*

# Contents

<b>Contents</b>	<b>1</b>
<b>1 Motivation and Objective</b>	<b>7</b>
1.1 Motivation . . . . .	7
1.2 Thesis Structure . . . . .	10
<b>2 Ozone in the Atmosphere</b>	<b>13</b>
2.1 The Atmosphere: Composition and Structure . . . . .	14
2.2 Ozone Chemistry . . . . .	18
2.2.1 Stratospheric Ozone Chemistry . . . . .	19
2.2.2 Catalytic Ozone Destruction Cycles (Gas Phase) . .	20
2.2.3 Ozone Hole . . . . .	26
2.2.4 Tropospheric Ozone Chemistry . . . . .	30
2.3 Ozone Transport . . . . .	31
2.4 Ozone Measurements . . . . .	33
<b>3 Spectroscopic Aspects of Ozone Molecule</b>	<b>37</b>
3.1 Ozone Spectroscopy and Cross Section . . . . .	38
<b>4 Harmonisation of SCIAMACHY and GOME-2 Ozone Cross Sections</b>	<b>47</b>
4.1 Introduction . . . . .	47
4.2 The Spectrometers . . . . .	53
4.2.1 SCIAMACHY Spectrometer . . . . .	53
4.2.2 GOME-2 Spectrometer . . . . .	54
4.3 Measurement Settings and Procedures . . . . .	55
4.4 Re-analysis of SCIAMACHY FM and GOME-2 FM3 Ozone Cross Sections . . . . .	57
4.4.1 Data Reduction . . . . .	57
4.4.2 Manual concatenation . . . . .	58
4.4.3 Absolute Scaling . . . . .	64

4.5	Evaluation of the Re-analysis . . . . .	66
<b>5</b>	<b>Validation of the Revised Cross Section Spectra and Application in Satellite Retrievals</b>	<b>73</b>
5.1	Absorption Cross Sections . . . . .	74
5.2	Comparisons with Literature Data . . . . .	80
5.2.1	Comparisons at Hg Lamp and He-Ne Laser Lines at Room Temperature . . . . .	81
5.2.2	Integrated Cross Sections at Different Temperatures	83
5.2.3	Temperature Parametrizations and Smoothness Comparisons . . . . .	85
5.3	Comparisons in DOAS Retrieval Window . . . . .	88
5.4	Retrieval Tests Using the Revised Ozone Cross Section Data	95
<b>6</b>	<b>Total Ozone Trends and Variability during 1979 – 2012 from Merged Datasets of Various Satellites</b>	<b>105</b>
6.1	Main Contributors to Ozone Variability . . . . .	107
6.1.1	Brewer-Dobson Circulation . . . . .	107
6.1.2	Quasi-biennial Oscillation . . . . .	110
6.1.3	El Niño-Southern Oscillation . . . . .	111
6.1.4	Chlorine and Bromine containing ODS . . . . .	112
6.1.5	Solar Cycle . . . . .	113
6.1.6	Aerosols . . . . .	114
6.2	Satellite Total Ozone Time Series . . . . .	114
6.3	Multivariate Linear Regression . . . . .	115
6.4	Results . . . . .	117
6.4.1	Contribution of Proxies to Ozone Variability . . . . .	120
6.5	ODS Related Trends in Ozone Total Column . . . . .	123
6.6	Sensitivity of the Trends Acquired from Different Satellite Ozone Data Records . . . . .	125
6.6.1	Quality of Satellite Ozone Data Records . . . . .	125
6.6.2	EESC/Linear Trends for all Data Records . . . . .	128
<b>7</b>	<b>Summary and Perspectives</b>	<b>131</b>
7.1	Summary . . . . .	131
7.2	Perspectives . . . . .	135
<b>A</b>	<b>Total Ozone Trends (EESC)</b>	
	<b>TOMS/SBUV/OMI MOD V8.0 (1979 – 2012)</b>	<b>139</b>
<b>B</b>	<b>Total Ozone Trends</b>	
	<b>F10.7 cm vs. MgII Index</b>	<b>147</b>
<b>C</b>	<b>Total Ozone Trends (PWLT)</b>	
	<b>TOMS/SBUV/OMI MOD V8.0 (1979 – 2012)</b>	<b>149</b>

<b>List of Figures</b>	<b>157</b>
<b>List of Tables</b>	<b>161</b>
<b>References</b>	<b>163</b>
<b>Acknowledgements</b>	<b>185</b>



# Part I

## Introduction



# Motivation and Objective

## 1.1 Motivation

The atmosphere plays an essential role in supporting life on our planet by providing oxygen (O<sub>2</sub>) required for respiration and carbon dioxide (CO<sub>2</sub>) used by plants and bacteria for photosynthesis. It protects from the harmful short-wavelength solar radiations and regulates the energy budget as well as water cycle. This is mainly done through the photochemical interactions between the atmospheric molecules and radiations. The atmosphere is greatly influenced by the huge impact of anthropogenic activities that increased its chemical complexity and resulted in some of the major political and environmental issues namely: severe ozone depletion, acid rain, smog and green house effect.

The discovery of the massive Antarctic ozone hole in 1985 by Farman et al. [1985] and the decline in the global ozone abundances between the eighties and the nineties, lead to an increased interest in the scientific community as well as the general public in the evolution of Earth's ozone layer. Ozone filters the solar ultra-violet radiations (UV) in the UVB and UVC ranges ( $\lambda \leq 320$  nm) which damage macromolecules like proteins and nuclear acids that may cause human skin cancer, and cause eye cataract and suppression of immune system (World Meteorological Organization, [WMO, 1995]). Furthermore, climate is affected by varia-

tions in ozone amounts, depletion in the stratospheric ozone yields limited negative radiative forcing (cooling) while a positive radiative forcing accompanies an increase in tropospheric ozone as it is a green house gas (Intergovernmental Panel on Climate Change [IPCC, 1995]). Enhanced UVB radiations in the troposphere quicken some photolysis rates [Tang et al., 1998] which consequently influence tropospheric ozone formation rates and the oxidation capacity of the troposphere (depending on nitrogen oxides concentrations) that determines the removal rate of many greenhouse gases which in turn impacts climate change.

The large ozone depletion was mainly due to the impact of the uncontrolled anthropogenic emissions of chlorofluorocarbons (CFCs), nitrogen oxides and other ozone-depleting substances (ODS) containing chlorine and bromine. The Montreal Protocol (1987) and its Amendments and Adjustments have successfully controlled the global emissions of the ozone-depleting substances and as a consequence, the turnaround in the stratospheric ozone and an increase in global abundances is expected to take place.

The identification of a statistically significant trend in ozone abundances (measured as total column) after the global phase-out of many ODS in the stratosphere requires the proper accounting of all the different factors and processes contributing to the long-term evolution of ozone and its variability, which induce considerable uncertainty in trend determination. Ozone levels exhibit natural variability in space and time and are influenced by atmospheric transport (dynamics), variations in the incoming solar radiation, aerosols, and other natural compounds. The influence of the chemical and dynamical contributors should be separated and quantified. A multiple linear regression including independent explanatory variables which represent atmospheric variability, have been used to quantitatively analyze and assess the observed total ozone variations due to different natural and anthropogenic influences and the attributions to long-term total ozone trends.

As a response to the decrease of ODS, ozone decline decreased and ozone amounts stabilized from 1997 onwards, a statistically significant increase in ozone levels is identified and reported in the previous ozone assessments (eg. [WMO, 2007, 2011] and references therein). An update of the assessment of the global ozone trends and its statistical significance is required.

To address this issue, accurate and global ozone measurements spanning over several decades are essential, the measurements are required to be consistent such that no trends arises from instrumental performance or operation. Global ozone distributions in Earth's atmosphere are best monitored by employing satellite-based remote sensing methods. This

method employs measurements of electromagnetic radiations in which the trace gas amounts are acquired from these measurements by including a quantitative description of the interactions between the trace gases and radiations in the retrieval. As the lifetime of satellites is limited, global and long-term total ozone (or any trace gas) measurements is acquired by merging several datasets acquired from various satellite borne atmospheric chemistry sensors. In order to achieve homogeneous and consolidated ozone datasets, an accurate absorption cross section of ozone at representative temperatures relevant to stratospheric ozone are required. Using the instrument's own reference data (absorption cross section measured with the satellite spectrometer prior to its launch) in the trace gas retrieval might reduce the fit residuals and obviates the exact knowledge of the instrumental slit function or spectral resolution.

The Global Ozone Monitoring Experiment (GOME) aboard the European Remote Sensing (ERS-2) satellite since 1995 and the SCanning Imaging Absorption spectroMeter for Atmospheric CHartographY (SCIAMACHY) on the ENVironmental SATellite (ENVISAT) since 2002, are atmospheric chemistry spectrometers operated by the European Space Agency (ESA) and provided eight (1995 – 2003) and ten (2002 – 2012) years of global ozone data, respectively. In addition, the EUropean organisation for the exploitation of METeorological SATellites (EUMETSAT) currently operates GOME-2 instrument launched in 2006 aboard the Meteorological Operational satellite programme (MetOp-A) and MetOp-B GOME-2 spectrometer launched in 2012, GOME-2 series (MetOp programme) is based upon the heritage of GOME and SCIAMACHY and will continue with the launch of MetOp-C (expected in 2017). The European instruments have very similar observation principles and differ slightly in spectral resolution, this allows the development of a long-term homogeneous ozone dataset in nadir observation mode. Laboratory absorption measurement of temperature dependent absorption cross sections under controlled in-flight conditions representative for atmospheric state, were performed using the GOME, SCIAMACHY and GOME-2 satellite instruments as laboratory spectrometers during the general instrument calibration period [Burrows et al., 1998, 1999a; Bogumil et al., 2003; Gür et al., 2005; Gür, 2006]. The pre-flight absorption measurements were relative cross sections scaled to absolute values using literature data.

Eskes et al. [2005] reported a systematic differences of about 3–5% in the total ozone columns retrieved in the 325 – 335 nm spectral range (Huggins band) using SCIAMACHY ozone cross sections when compared to collocated GOME data. GOME was very stable over the operational period (1995 – 2012), GOME cross sections were used in the retrieval. GOME total ozone data agree very well with ground observations [Weber et al., 2005; Balis et al., 2007]. SCIAMACHY retrieved ozone us-

ing GOME absorption cross section data [Burrows et al., 1999a] smoothed to SCIAMACHY's spectral resolution shows a relative differences of 1% with collocated GOME data. Moreover, GOME-2 total O<sub>3</sub> column retrieved in the same spectral window and using GOME-2 cross sections resulted in an overestimation of 8% [Weber et al., 2011]. This indicates that the approaches used to determine the absolute absorption cross sections were not consistent for the three instruments, a re-analysis of the absorption measurements of SCIAMACHY and GOME-2 is required to correct the overestimation in the retrieved ozone from both instruments.

## 1.2 Thesis Structure

The thesis is divided into three parts as follows:

The first part presents a brief introduction of the atmosphere, ozone chemistry as well as the ozone molecule and comprises Chapters 2 and 3. Chapter 2 presents an overview of the vertical structure of the atmosphere and the atmospheric composition, the general features of ozone chemistry of formation and destruction including catalytic cycles, atmospheric dynamics as well as the ozone measurement techniques to follow the discussions presented in this work.

A short description of the ozone molecule and the importance of accurate knowledge of absorption features of the ozone molecule are outlined in Chapter 3.

The harmonization of SCIAMACHY and GOME-2 absorption ozone cross sections are described in the second part which constitutes the fourth and fifth chapters.

Chapter 4 explains the procedures of harmonisation of cross sections, the re-analysis was carried out by re-evaluating the available cross section data that included calculating relative cross section (optical density) spectra, producing one consistent relative cross section spectrum by concatenation and the method used in converting to absolute absorption cross sections. An evaluation of the re-analysis of the absorption measurements of both satellites is also included.

The verification of the re-analyzed satellite cross sections is further extended in Chapter 5, comparisons were performed over the entire spectral range of both spectrometers with an emphasis on the total ozone retrieval spectral window in the Huggins band. Finally, the cross section spectra were included in DOAS test retrievals on real satellite data.

The merged datasets from GOME, SCIAMACHY and COME-2 satellite instruments together with other consolidated long-term ozone records from 1979 till 2012 are used to diagnose the trends in total ozone columns, the results are summarized in Chapter 6, the third part. A regression model using various natural and anthropogenic explanatory variables is developed and applied to the different satellite data to investigate the uncertainty in the long-term trends due to the use of different datasets. Furthermore, the response of ozone at different latitudes with respect to several explanatory variables are also investigated.

Finally, Chapter 7 concludes and summarizes the main findings from this thesis.

The ultimate aim of this work is to derive a consolidated and consistent set of absorption cross sections for GOME, SCIAMACHY, and GOME-2 series that will allow the derivation of a harmonised long-term dataset and the use of the different ozone records in the assessment of ozone trends



# Chapter 2

## Ozone in the Atmosphere

Ozone is one of the most important atmospheric trace gas that plays a major role in the chemistry and dynamics of the atmosphere [Holloway and Wayne, 2010; WMO, 2011]. It protects life by shielding the damaging ultra violet radiation in the stratosphere, and acts as a pollutant due to its high oxidation potential that may cause respiratory problems and destroys plant tissues in the troposphere. It plays a significant role in the radiative budget, absorbing UV-visible solar radiation in the stratosphere and infrared radiations emitted by Earth in the troposphere. Global ozone measurements show large spatial and temporal variability, this variability is controlled by various atmospheric processes. This chapter presents a brief introduction of the chemical and dynamical processes that affect ozone. The chapter is divided into four sections: Section 2.1 presents the general characteristics of the atmosphere and explains the vertical structure of the atmosphere (layers), the atmospheric composition and the temperature distribution. A detailed overview of ozone chemistry is introduced in Section 2.2. The relevant mechanisms governing ozone production and natural destruction (Chapman cycles) in the stratosphere are described as well as the important catalytic ozone destruction cycles and the chemical and dynamical processes associated with the rapid destruction of ozone in the poles (ozone hole), tropospheric ozone is also discussed. The atmospheric dynamics relevant for the distribution of stratospheric ozone is briefly described in Section 2.3. The last section presents the different techniques and instruments for measuring ozone.

## 2.1 The Atmosphere: Composition and Structure

The atmosphere is the thin layer of gaseous mixture enveloping the planet Earth. Earth's atmosphere is characterized by its unique composition as well as pressure and temperature. It supports life on Earth by regulating the incoming solar radiation and outgoing terrestrial radiation (radiative equilibrium) as well as the water cycle. The atmosphere has no definite boundary with the outer space and extends to 600 – 1000 km above the surface. Most of the atmosphere is near the surface (99% below 100 km) since the density and pressure decrease with altitude. The main constituents of the atmosphere are listed in Table 2.1, the contents are also given as mixing ratios by volume (volume fraction is identical to mole fraction). Nitrogen, oxygen and argon are the major constituents and account for about 99.9% of the total atmosphere, they exist in very stable and constant concentrations and are well mixed in the atmosphere. The remaining 0.1% consists of the trace gases because they exist in small quantities, among them: water vapour, carbon dioxide, ozone, methane, hydrogen, various oxides of nitrogen, neon, krypton and helium. The small and variable concentrations of the trace gases play a major role regarding the chemistry and the radiative equilibrium of the atmosphere and are essential to life on Earth. The interactions between radiation (solar and terrestrial) with the atmosphere's composition determine the vertical temperature structure of the atmosphere.

The atmosphere is generally divided vertically into four distinct layers based on the characteristic temperature profile or the rate of change of temperature with elevation in the atmosphere (lapse rate,  $dT/dz$ ). Figure 2.1 sketches the vertical temperature structure through the atmosphere and shows the different layers: the troposphere, the stratosphere, the mesosphere and the thermosphere. The layers also differ in the chemistry, composition (trace gases), density and air motion (dynamics). The transition regions between the layers are characterized with zero vertical temperature gradient and are defined as pauses: the tropopause, stratopause and mesopause, respectively.

**Troposphere** The lowest layer of the atmosphere where life exists and all weather phenomena take place. It is the densest layer containing 90% of the total mass of the atmosphere. It extends from Earth's surface up to the tropopause and the height depends on the latitude and season ranging from 6 – 8 km near the poles to 14 – 16 km in the tropics. This layer is

*Table 2.1: The major and minor constituents of the atmosphere.*

Constituent	Molecular Weight [g/mole]	Content (fraction of molecules)
Nitrogen (N <sub>2</sub> )	28.016	0.7808
Oxygen (O <sub>2</sub> )	32.00	0.2095
Argon (Ar)	39.94	0.0093
Water vapour (H <sub>2</sub> O)	18.02	0 – 0.04
Carbon dioxide (CO <sub>2</sub> )	44.01	395 ppm
Helium (He)	4.00	5 ppm
Neon (Ne)	20.18	18 ppm
Krypton (Kr)	83.7	1 ppm
Ozone (O <sub>3</sub> )	48.00	0 – 12 ppm
Methane (CH <sub>4</sub> )	16.05	1.79 ppm
Hydrogen (H <sub>2</sub> )	2.02	0.5 ppm
Nitrous oxide (N <sub>2</sub> O)	44.016	0.325 ppm
Nitrogen dioxide (NO <sub>2</sub> )	46.01	0.02 ppm

characterized by a negative temperature gradient as the temperature decreases with height (6.5 K/km) till the tropopause where the temperature gradient suddenly changes. Earth's surface is warmed by the absorption of the short wavelength solar radiation (ultraviolet UV-A, and visible) transmitted through the atmosphere. The surface emits long wavelength radiations (infrared, IR) which are trapped in the spectral windows of the absorption bands of certain trace gases (green house gases e.g. H<sub>2</sub>O, CO<sub>2</sub>, O<sub>3</sub> and CH<sub>4</sub>) and warms the overlying atmosphere, such phenomenon is called the greenhouse effect. The green house gases re-emit this energy in all directions. The part emitted upward gradually cools down as the air density decreases. Such temperature structure is unstable, the warm air rises up, expands (cools) and mixes with the surrounding cold air (convection). This leads to a rapid vertical mixing (hence the name troposphere; tropos is Greek and means mixing or turning) in which the trace gases can be transported quickly to upper layers (tropospheric dynamics). The tropopause lies directly above the troposphere and is the first minima in the temperature structure (isothermal layer, temperature does not change with height). It is about 9 km transition layer and acts as a cold trap that reduces the exchange between the troposphere and stratosphere.

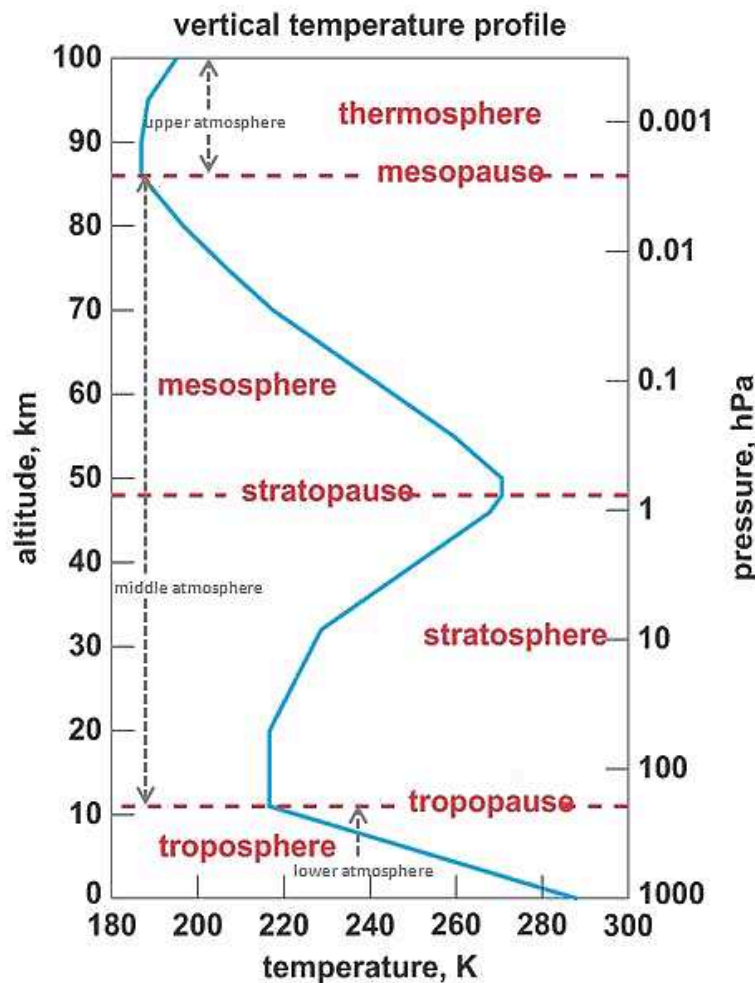


*Figure 2.1: Schematic sketch of the vertical thermal structure of the atmospheric temperature (solid turquoise curve) and layers.*

**Stratosphere** This layer extends up to 50 km, it is less dense and dry. It contains approximately 90% of atmospheric ozone as well as other trace gases like  $\text{CO}_2$ ,  $\text{H}_2\text{O}$  and  $\text{NO}_2$ , 99% percent of air is located in the troposphere and stratosphere. The temperature increases with increasing altitude (positive temperature gradient), this inversion is due to the absorption of the high energetic short wavelength solar radiation (UV-B and UV-C) by the ozone layer and then re-emission of thermal long wavelength radiation in all directions that heats the stratosphere. Ozone in the upper region of the stratosphere absorbs most of the UV radiation where maximum heating, associated with maximum temperature, occurs. This leaves less UV radiations penetrating down to heat the lower region and therefore temperature increases with altitude. Such temperature structure results in a vertical stratification of the air masses making the layer dynamically stable and inhibits vertical mixing (stratus is Latin for lay-

ered), the dynamics is driven by radiative processes. For this reason, the trace gases endure longer times (order of years) in the stratosphere. Stratopause, the upper limit of the stratosphere, is the second isothermal transition layer (about 5 km) of maximum temperature separating the stratosphere from the mesosphere.

**Mesosphere** The mesosphere (mesos, Greek for middle) starts directly above the stratopause and extends to an altitude range between 50 and 90 km. It acts as shield protecting the Earth from the meteorites by slowing them down and eventually melting or vaporizing. It is much less dense than the previous two layers. Due to the direct heating from the high energetic solar radiations, the species contained there are found in an excited state. This layer is characterized by a decrease of temperature with altitude; this is due to less solar heating (low O<sub>3</sub> concentration) and more radiative cooling by CO<sub>2</sub>. As a consequence, the mesosphere is dynamically instable and is characterized by rapid vertical mixing. The mesopause layer is the upper boundary region of the mesosphere and located at altitudes between 88 and 100 km (season and latitude dependent). It is the second minima in the temperature structure with the coldest place on Earth with temperatures reaching 120 – 130 K in the high latitude mesosphere in summer. The regions of the stratosphere and the mesosphere are called the middle atmosphere.

**Thermosphere** The next layer above the mesopause where auroras occur and many satellites orbit the Earth, it reaches altitudes between 600 and 1000 km. The air here has an extremely low density and poorly mixed, the gas molecules are so distant from each other that a molecule transverses around 1 km before colliding with another one. This layer is characterized by a positive lapse rate. Below 200 – 300 km altitude, the temperature rises sharply then remains fairly constant with increasing altitude. The temperature inversion is a result of the absorption of the high energetic short wavelength solar radiations by oxygen and nitrogen molecules that break the strong bonds and consequently atoms are dominant. The temperature is strongly influenced by solar activity, the highest temperature (around 2000 K) in the atmosphere is found in the upper thermosphere when the Sun is active. Thermopause marks the boundary of the thermosphere, its height varies according to the absorbed heat.

The outer most layer is the exosphere where the atmosphere turns into the outer space. This region starts at 600 – 1000 km above Earth's surface and contains light molecules moving fast enough (almost no collision) to reach the escape velocity and overcome the gravitational field

to escape into outer space. The atmosphere is also divided into the homosphere and heterosphere according to how the atmospheric constituents are mixed throughout the atmosphere. Homosphere is the region from the troposphere till the mesosphere where the different constituents are well mixed in the air. The region above is termed as the heterosphere, air here is poorly mixed and molecules are distant from each other and travel with large mean free paths, diffusion drives the vertical mixing.

The atmosphere also contains clouds as well as suspended solid or liquid particulates called aerosols. They greatly influence the global energy budget of Earth by scattering, absorption and transmission. Aerosols can be of natural source like dust, sea salt, water droplets and volcanic emissions or anthropogenic as products of combustion. Both clouds and aerosols play a role in the chemistry of the atmosphere in creating or destroying some species including ozone.

## 2.2 Ozone Chemistry

Ozone ( $O_3$ ) plays a vital role in the atmospheric chemistry despite of its relatively small concentration. The total concentrations of ozone in a column extending vertically from Earth's surface to the top of the atmosphere are measured in Dobson units<sup>1</sup> while the vertical distribution (profile) is measured in mixing ratio<sup>2</sup> (fraction composition) or number density. Ozone columns and profiles depend on the balance between production, destruction and transport. Global measurements of the last three decades demonstrated a strong depletion of the ozone layer over the poles and mid-latitudes. The decline is mostly attributed to the complex chemistry of the trace gases that initiate catalytic ozone destruction. The ozone changes are also influenced by the broad meridional circulation.

---

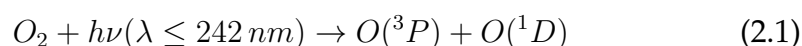
<sup>1</sup>Dobson unit (DU) is a measure of the abundance of atmospheric ozone, 1 DU is the thickness that ozone would occupy if brought down to the surface (height integrated) of standard temperature and pressure (273 K, 1 atm) in the unit of hundredths of millimetre.

<sup>2</sup>Mixing ratio is a dimensionless ratio of trace gas number density ( $cm^{-3}$ ) and total number density ( $cm^{-3}$ ), common units: e.g. (ppb) ( $10^{-9}$ ) parts per billion.

### 2.2.1 Stratospheric Ozone Chemistry

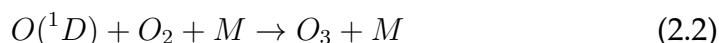
The basic principles governing the formation and natural destruction of stratospheric ozone were formulated first by Sydney Chapman [Chapman, 1930]. The mechanism, termed oxygen only and dominated by photochemical reactions, states that  $O_3$  is maintained in a steady state concentration and described in the following:

Oxygen radical (very reactive) is produced at around 100 km through the photolysis of oxygen molecules by the short wavelength radiations in the Schumann-Runge band (175 – 200 nm) and in the Herzberg continuum.



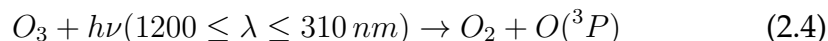
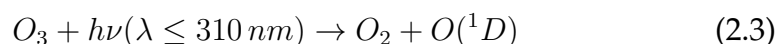
where  $h\nu$  denotes the ultraviolet photon and  $O(^3P)$  is the ground state of atomic oxygen while  $O(^1D)$  is in metastable state.

The oxygen atom ( $O(^1D)$ ) quickly reacts with an oxygen molecule to generate ozone:



where M is a third molecule (mainly  $O_2$  or  $N_2$ ) which is collided with and capable of absorbing the excess energy liberated in the exothermic chemical reaction, i.e., required for energy and momentum conversation.

Ozone strongly absorbs solar radiations with wavelengths less than 310 nm, the molecule formed in (reaction 2.2) can be destroyed in the stratosphere through photolysis to form back  $O_2$  and atomic oxygen:



The electronically excited oxygen atom  $O(^1D)$  that is highly reactive, quickly dissipates its internal energy and convert to  $O(^3P)$  by collisional deactivation with a third molecule. Reactions 2.4 and 2.5 are not regarded as ozone destruction mechanisms due to the short lifetime of the oxygen

atom in which it quickly interacts with an oxygen molecule to form ozone (as in reaction 2.2). In this process, the solar radiations are converted to thermal energy (the energy is transferred to the third body,  $M$ ) and heats the stratosphere and maintains the positive temperature gradient with altitude.

Chapman also proposed a mechanism of ozone loss (or odd-oxygen  $O$  and  $O_3$ ) to balance the production through the reaction of  $O_3$  molecule with oxygen radical:

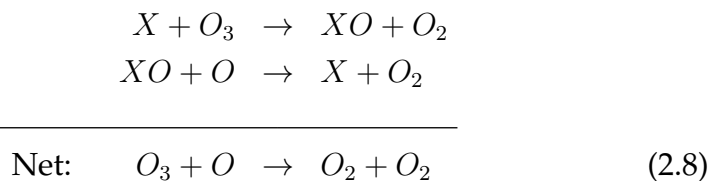


Chapman cycle explains the formation of the ozone layer. At high altitudes, less  $O_2$  is found to produce oxygen through radical photolysis (reaction 2.2). On the other hand, at low altitudes less solar intensity can penetrate and reach the region of high  $O_2$  concentration. In the middle (25 – 30 Km), maximum oxygen atom production occurs which leads to high ozone concentrations, the maxima has a seasonal and latitude dependence as shown in Fig 2.2.

### 2.2.2 Catalytic Ozone Destruction Cycles (Gas Phase)

Chapman's photochemical theory could not correctly predict the ozone equilibrium concentrations, the reaction scheme overestimates the observed ozone by a factor of 2. Reaction 2.6 is very slow to destroy the produced ozone. It was later reported that the natural destruction of stratospheric ozone was not solely by atomic oxygen but rather through pure gas phase chemistry.

The odd oxygen is removed from the Chapman cycle by several trace constituents involving in catalytic processes. The general form of the catalytic destruction is as follows:



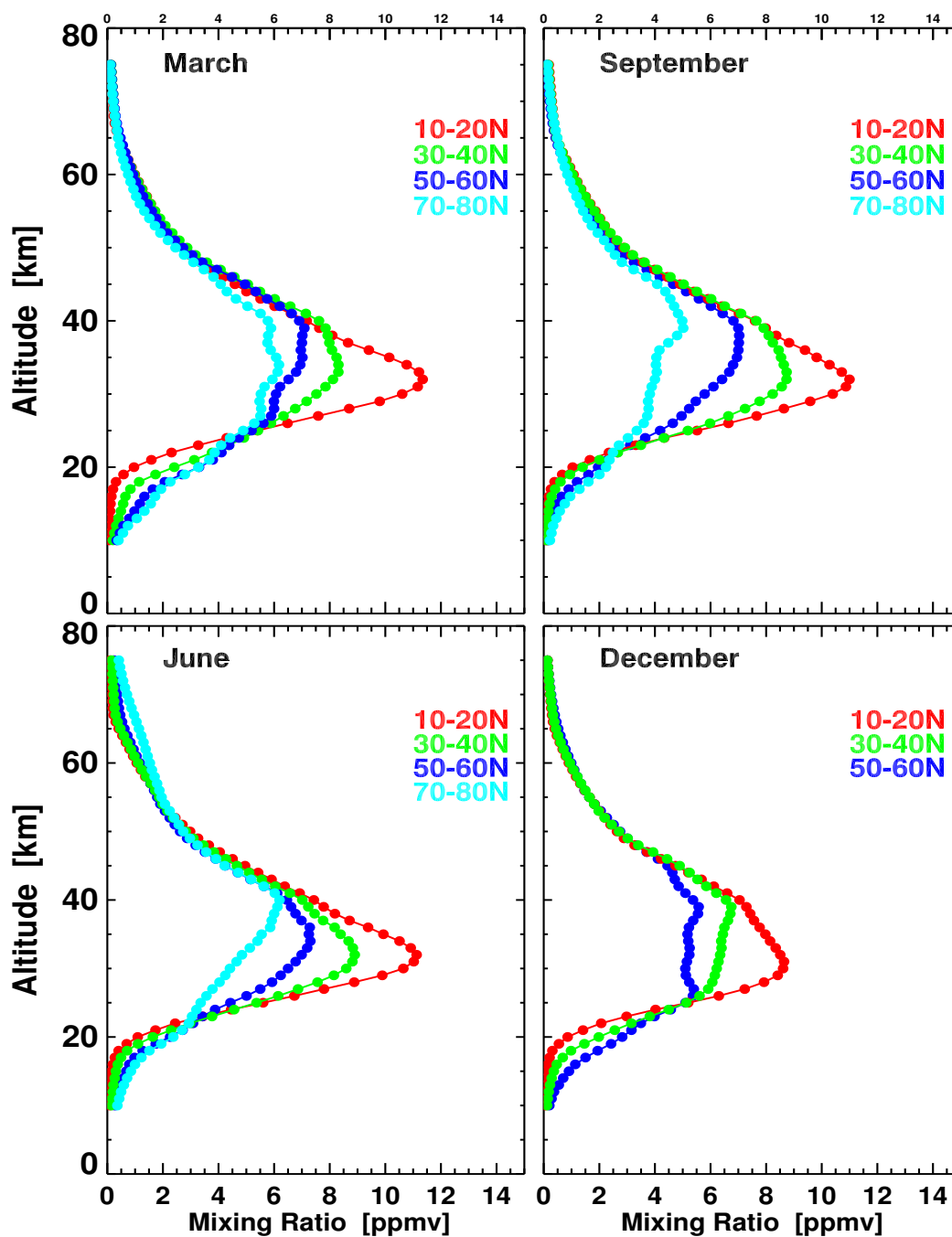
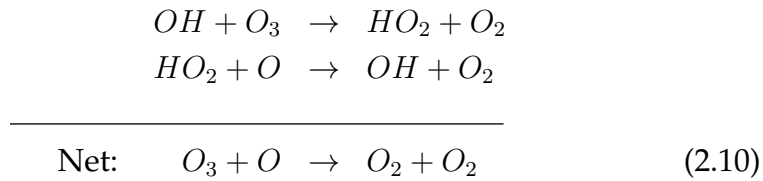
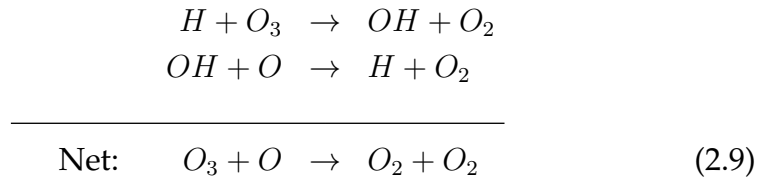


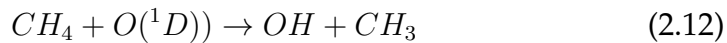
*Figure 2.2: SCIAMACHY's ozone profiles measured at different latitude bands in the Northern Hemisphere (10–20°N in red, 30–40°N in green, 50–60°N in blue and 70–80°N in turquoise) and different months (March, June, September and December). No measurements were recorded in the polar region during December due to the lack of sunlight (polar night).*

X represents several species in the atmosphere, among them H, OH, NO, Cl and Br. These species belong to the HO<sub>x</sub>, NO<sub>x</sub>, ClO<sub>x</sub>, BrO<sub>x</sub><sup>4</sup> families, respectively. X is formed back in the second reaction, so that its participation in odd-oxygen removal would not change its abundance.

Bates and Nicolet [1950] first suggested that stratospheric ozone is catalytically destroyed by HO<sub>x</sub> according to the cycles:



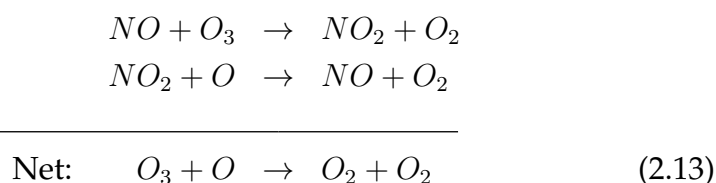
These cycles contribute largely above 40 Km (blue curve in Fig. 2.3). The HO<sub>x</sub> source in the stratosphere is the oxidation of methane and water vapour or photolysis of water, both transported from the troposphere.



Crutzen [1970] proposed the odd nitrogen oxides NO<sub>x</sub> cycle which is dominant in the stratosphere under 35 Km (green curve in Fig. 2.3):

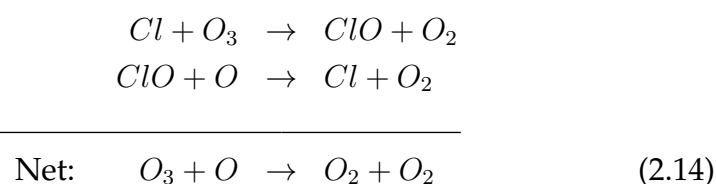
---

<sup>4</sup>HO<sub>x</sub> = H + OH + HO<sub>2</sub>  
 NO<sub>x</sub> = NO + NO<sub>2</sub>  
 ClO<sub>x</sub> = Cl + ClO + OCIO + HOCl + BrCl  
 BrO<sub>x</sub> = Br + BrO + HOBr + BrCl



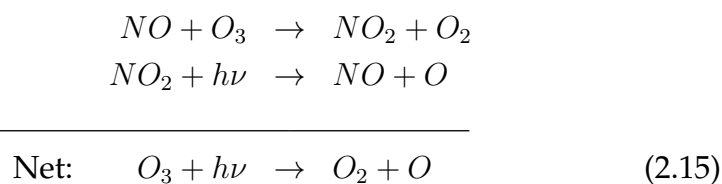
The  $NO_x$  molecules originate mostly from  $NO_2$  (microbiological) transported from the troposphere, and to less extent from aircrafts and ionization reactions.

Halogens (Cl, Br) also participate in ozone destruction cycle [Stolarski and Cicerone, 1974], the halogens are dominated by chlorine [Solomon, 1999].



This cycle is important at around 45 Km (red curve in Fig. 2.3). The main source of  $ClO_x$  in stratosphere is the photo-dissociation of the anthropogenic chlorofluorocarbons (CFC) and hydrocarbons [Molina and Rowland, 1974] transported from the troposphere. Methyl chloride ( $CH_3Cl$ ), a natural precursor of  $ClO_x$ , is emitted from volcanoes and oceans.

The set of catalytic cycles described previously follows the general scheme  $X \rightarrow XO \rightarrow X$  and limited in which both  $O_3$  and  $O$  (odd-oxygen) are destroyed. Some catalytic cycles destroy  $O_3$  without odd-oxygen removal where  $X$  and  $XO$  are inter converted:



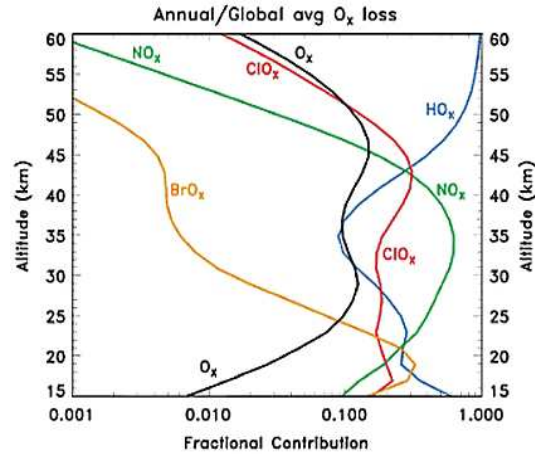
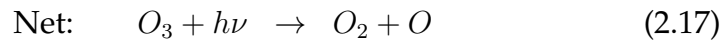
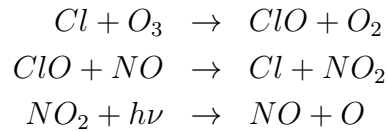
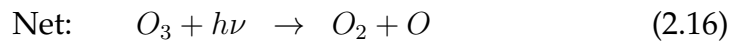
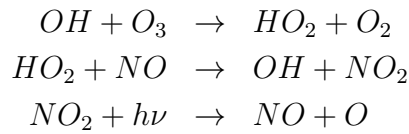


**Figure 2.3:** Fraction of the odd-oxygen ( $O_x$ , black curve) loss rate due to the catalytic destruction of  $HO_x$  (blue),  $NO_x$  (green),  $ClO_x$  (red) and  $BrO_x$  (orange) families adapted from Holloway and Wayne [2010].

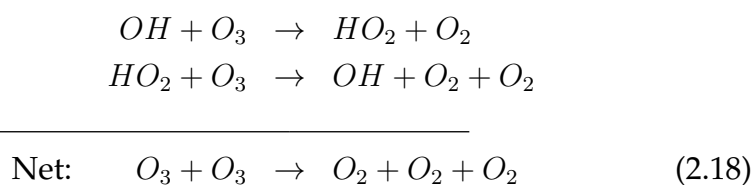
Such cycle is called null cycle with  $O_3$  photolysis is the overall effect.

The members of the different families can react with each other:



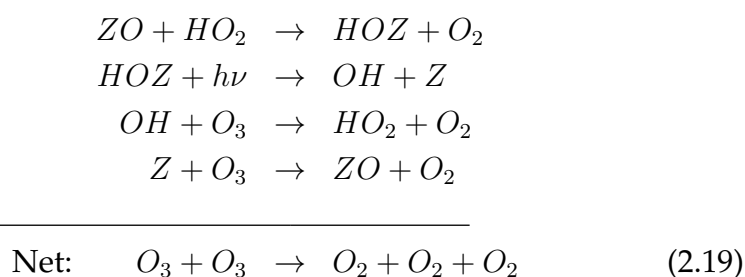
the photolysis of  $NO_2$  completed the null cycle in each case.

In the lower stratosphere (30 Km), different cycles destroy ozone without utilizing atomic oxygen and involve  $HO_x$ :



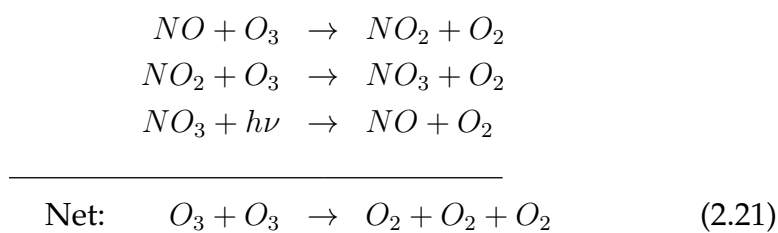
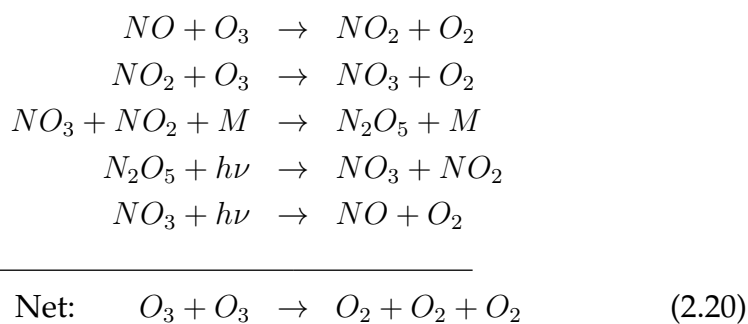
Two ozone molecules are converted to three oxygen molecules.

At lower altitudes (20 Km),  $HO_x$  cycle interacts with halogens:

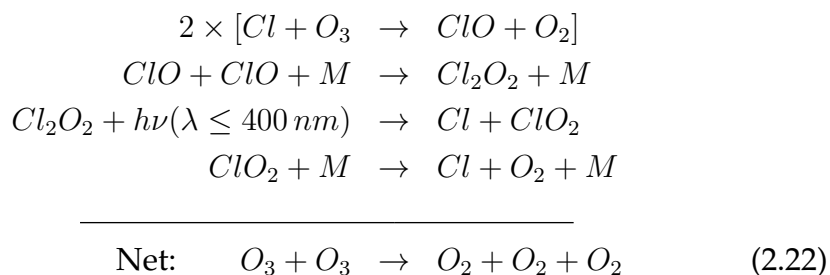


where Z is Cl or Br.

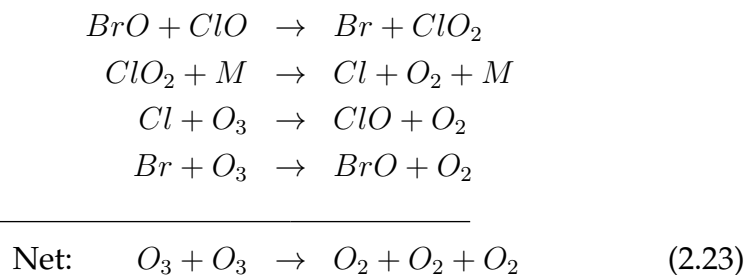
The complicated structure of the  $NO_x$  cycles is also noted:



Catalytic cycles involving chlorine strongly deplete the ozone layer in the lower polar stratosphere. The first cycle, involving the formation of ClO-dimer, was proposed by Molina and Molina [1987]



The second cycle [Wofsy et al., 1975; Yung et al., 1980; McElroy et al., 1986] showed that cycles involving Br and Cl contribute to the O<sub>3</sub> loss:



### 2.2.3 Ozone Hole

An intense depletion in the ozone layer was first reported over the Antarctic at the British Antarctic Survey station at Halley 76° S during spring [Farman et al., 1985]. The study showed a recurring springtime Antarctic ozone loss since the mid-seventies, October ozone levels registered losses of about 35% compared to the sixties average. Datasets from the Total Ozone Mapping Spectrometer (TOMS) on-board Nimbus-7 satellite confirmed the drop in ozone [Stolarski et al., 1986] as well as measurements by other Antarctic stations [Komhyr et al., 1986; Mount et al., 1987; Farmer et al., 1987]. This regular seasonal phenomena taking place in the high latitudes during spring was called ozone hole<sup>3</sup>.

The depletion was first attributed to the NO<sub>x</sub> and ClO<sub>x</sub> gas phase catalytic cycles (reactions 2.13 and 2.14), but the atomic oxygen utilized

<sup>3</sup>The ozone hole is defined as the area wherein the total ozone is less than 220 DU.

in these cycles is less available in the lower polar stratosphere (where depletion occurs) due to large solar zenith angle, this limits the photo-dissociation of  $O_2$ . The loss is due to an interaction of polar stratospheric dynamic and particular meteorological conditions with chemical processes involving heterogeneous reaction occurring on the surface of polar stratospheric clouds (PSCs).

During the polar night and the absence of heating due to solar UV and emission of thermal radiations (radiative cooling), air cools down due to the very cold temperatures. The cold polar masses are surrounded by warmer air at the lower latitudes, this creates a large temperature and pressure gradients which in turn results in a strong downward winds from the mid-latitude stratosphere into the low pressure poles. The descending winds are then deflected by the Coriolis force leading to a eastward flowing jet (westerly circulation) of the air masses around the polar terminator. The rotating core of very cold air forms the polar vortex (polar night jet) which very efficiently isolates the stratospheric polar air masses from the lower latitude stratospheric air for quite long time (till the onset of spring). The polar vortex is more pronounced in the Antarctic than in the Arctic due to the topography and greater land sea temperature contrast in the northern hemisphere which induces more frequent and intense planetary wave activity.

Inside the extremely cold and dry conditions of the polar vortex, little amounts of water vapour condense and lead to the formation of Polar Stratospheric Clouds (PSCs) in the lower stratosphere; aerosols (mainly sulphates) provide the required cloud condensation nuclei. The PSCs are typically formed at altitudes between 15 – 25 km and divided into two classes [McCormick et al., 1982]:

**Type I** PSC particles are small (about 1 micron in diameter). The frost point<sup>5</sup> for Type I PSCs is 195 K and their sedimentation rate is on the order of 10 meters per day. Type I is further subdivided into:

**Type Ia** is composed of almost pure nitric acid trihydrate ( $HNO_3 \cdot 3H_2O$ ) NAT [Crutzen and Arnold, 1986].

**Type Ib** is formed at temperatures of about 191 K and composed of a liquid ternary solution of nitric acid ( $HNO_3$ ), sulphuric acid ( $H_2SO_4$ ), and water vapor ( $H_2O$ ).

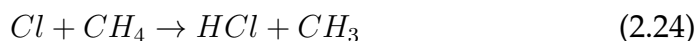
---

<sup>5</sup>The temperature at which PSCs form

**Type II** are frozen water ice large particles (about 10 micron in diameter) form at temperatures below 188 K, sediment rather rapidly at about 1.5 kilometres per day.

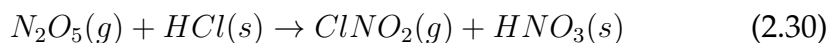
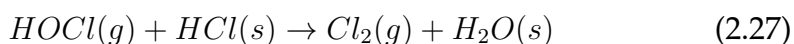
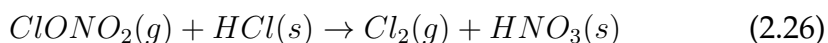
Type II PSCs are formed frequently inside Antarctic polar due to the extremely low temperatures.

PSCs are fundamental to ozone hole as the surfaces of cloud particles provide a platform for heterogeneous chemistry which allows the release of the catalytically active species or their precursors from the non reactive reservoir compounds (non-ozone gases). The chlorine species are mainly found in the reservoir molecules of hydrogen chloride (HCl) and chlorine nitrate (ClONO<sub>2</sub>) and formed in a complex way as follows:



### Chlorine and nitrogen activation/deactivation

The principal heterogeneous reactions are:



Photochemically active molecular chlorine (Cl<sub>2</sub>), hypochlorous acid (HOCl) and nitryl chloride (ClNO<sub>2</sub>) are released as gases. The heterogeneous reactions remove gaseous nitrogen (dinitrogen pentoxide N<sub>2</sub>O<sub>5</sub> and ClONO<sub>2</sub>) to produce nitric acid (HNO<sub>3</sub>) which is absorbed by the

PSCs as a reservoir species for nitrogen. This process of storing nitrogen is known as denoxification. As a result no reactive nitrogen is available to restrain the chlorine ozone catalytic destruction which might otherwise react with ClO to the reservoir form ClONO<sub>2</sub> through reaction 2.25.

In the early spring, the chlorine (and bromine) containing gas are subsequently photolyzed by near UV and visible light to yield ClO<sub>x</sub> radicals and initiate the catalytic ozone depletion cycle through the cycles. Cycle 2.22 (ClO-dimer) is the largest contributor to ozone destruction and responsible for 75% of the ozone removal in the ozone hole, 20% are attributed to cycle 2.23 (Cl-Br) [Solomon, 1999]. Anderson et al. [1989] indicates that the ClO-O cycle 2.14 accounts for only 3% of the observed ozone loss.

The PSCs undergo sedimentation to lower altitudes and the nitric acid and water are transported out of the vortex leading to the de-nitrification and dehydration<sup>6</sup> of the polar stratosphere.

The photolysis of HNO<sub>3</sub> results in the releasing of reactive NO<sub>2</sub>, which in turn reacts with ClO to reform the reservoir ClONO<sub>2</sub> species through reaction 2.25. The vortex eventually breaks down in the spring due to increasing temperatures and the catalytic depletion stops. This allows the regeneration of the ozone layer that is enhanced by a flow of air from the mid latitudes rich in ozone and contains nitrogen oxide compounds that creates halogen reservoirs.

In Arctic stratosphere, the ozone depletion mechanisms are the same but less pronounced. The vortex is less stable which results in less formation of PSCs as it is warmer, as a consequence weaker ozone loss occur compared to that in the Antarctic. Therefore the halogen activation, de-nitrification and dehydration in the stratosphere are less intense.

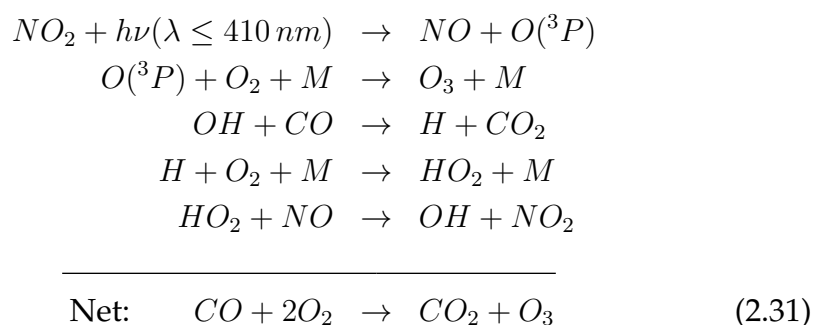
In mid-latitude, ozone destruction by heterogeneous chemistry also occurs on the surface of sulphate aerosols [Fahey et al., 1993] where denoxification and chlorine deactivation happen. The depletion is considerably smaller compared to that in the poles, but significant ozone loss were observed after major volcanic eruptions [Hofmann and Solomon, 1989; WMO, 1995, 1999, 2003, 2007, 2011].

---

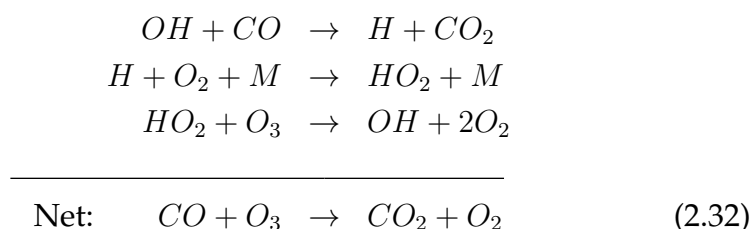
<sup>6</sup>De-nitrification: the removal of the reactive nitrogen.  
Dehydration: the removal of water vapour.

## 2.2.4 Tropospheric Ozone Chemistry

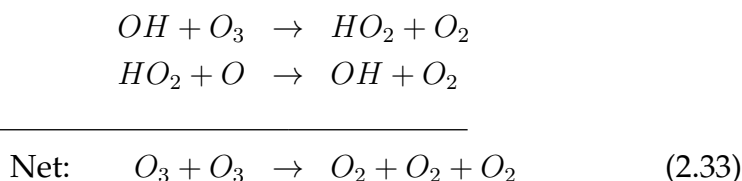
The tropospheric ozone formation is a complex process; it involves reactions of large number of precursors. Tropospheric ozone is a photochemical pollutant and formed during daylight time, but is destroyed throughout the day and night. Therefore, ozone concentrations depends upon both the time of day and the location, high concentrations are found in urban regions on hot and sunny days. As mentioned before, ozone results from the reaction between atomic and molecular oxygen (reaction 2.2), but the mechanism differs from the Chapman cycle in the stratosphere, UV-C radiation cannot reach the lower layer of the atmosphere to photodissociate molecular oxygen (reaction 2.1). Photolysis of  $\text{NO}_2$  is the primary source of atomic oxygen and the dominant way to form ozone in the troposphere.



The nitrogen cycle is limited by the slow photolysis reaction, reaction 2 is comparatively fast. It depends on the amount of  $\text{NO}_x$  to produce or destroy  $\text{O}_3$  [Crutzen, 1973, 1974], with low  $\text{NO}_x$ , the ozone loss is through the following:

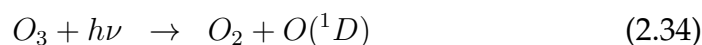


or



$HO_x$  and  $NO_x$  catalyse ozone production and destruction in the troposphere and stratosphere, respectively.

Ozone is also a powerful oxidizing agent and its photolysis is the dominant source of OH radical in the troposphere.



Another source of tropospheric  $O_3$  is the stratosphere-troposphere exchange (SET). Thin stratified air (about 1 km) from the lowermost stratosphere enters the troposphere at mid-latitudes parallel to the tropospheric jet stream and mixes up with the turbulent tropospheric air. The SET process accounts for about 40% of tropospheric ozone [Holloway and Wayne, 2010].

## 2.3 Ozone Transport

Ozone is abundantly produced in the tropical stratosphere where the Sun provides maximum UV radiations to initiate the photolysis of oxygen molecules and Chapman cycle. Highest ozone columns are observed in the mid and high latitudes rather than its photochemical production region. This discrepancy between the photochemical theory and observations in the distribution of ozone can be explained as a poleward transport of ozone rich air from the tropics into the higher latitudes. The poleward drift is part of a broad hemispheric meridional circulation in the middle and lower stratosphere in which the poleward branch is balanced by an upward motion in the tropics and a descending motion in both the

stratospheric extra-tropics and polar latitudes. A Schematic sketch of the meridional circulation is shown in Fig. 2.4

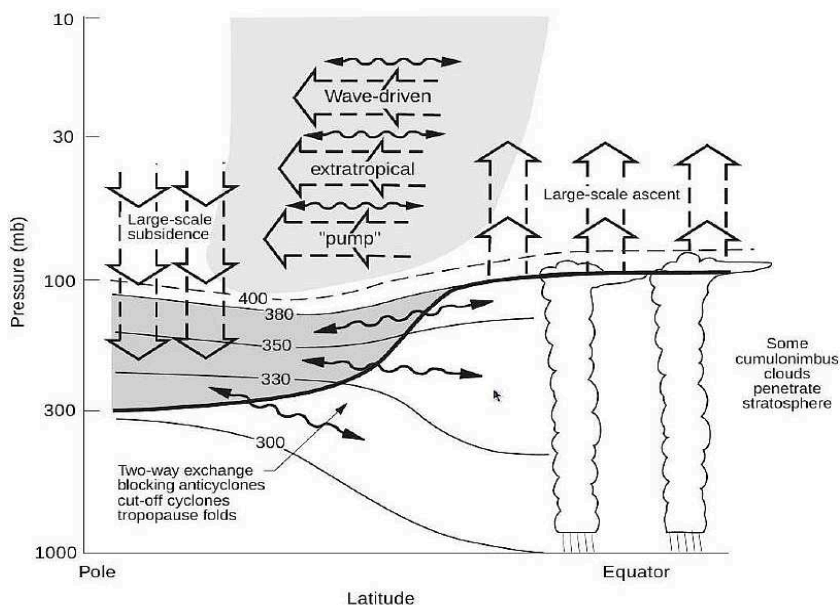


**Figure 2.4:** Schematic sketch of the general broad hemispheric meridional circulation in the stratosphere adapted from Holton et al. [1995]. Tropospheric air masses enter the stratosphere via the tropical tropopause, from where they are distributed via different pathways in the stratosphere.

The slow meridional circulation is also known as the Brewer-Dobson circulation BDC [Brewer, 1949; Dobson, 1956]. The main features of the transport of air masses in stratosphere were postulated by Brewer and Dobson to explain the observed low water vapour mixing ratios in the stratosphere and the observed high ozone concentration in the polar lower stratosphere, respectively. The circulation is intense in the winter season and stronger in the Northern Hemisphere due to larger scale topographical features and more land-ocean contrasts compared to the Southern Hemisphere. The circulation is driven by the planetary scale atmospheric waves (Rossby and gravity waves) which are generated in troposphere and propagated upwards [Haynes et al., 1991; Rosenlof and Holton, 1993; Newman et al., 2001; Plumb, 2002] where they break and dissipate due to wave breaking processes. The mechanisms driving the BDC are explained in Section 6.1.1.

## 2.4 Ozone Measurements

The abundance of ozone in the atmosphere is measured since the 1920s by a variety of techniques employing ground based spectrometers and instruments or spectrometers carried aloft on balloons, aircraft, rockets, and satellites (see Fig. 2.5). The measurements extend from the atmosphere above the ground station to daily global coverage and profiles. Long-term and global ozone datasets are considered as an essential tool to monitor the changes in the ozone layer and to study its inter-annual and decadal variability to determine the long-term global trends. Ozone observations are also required to validate various climate models that are used to predict future evolution of the atmospheric trace gases [Eyring et al., 2005]. Ozone is basically measured by two principal kinds of measurement techniques: in-situ and remote sensing, both techniques employ ozone's chemical and optical characteristics.

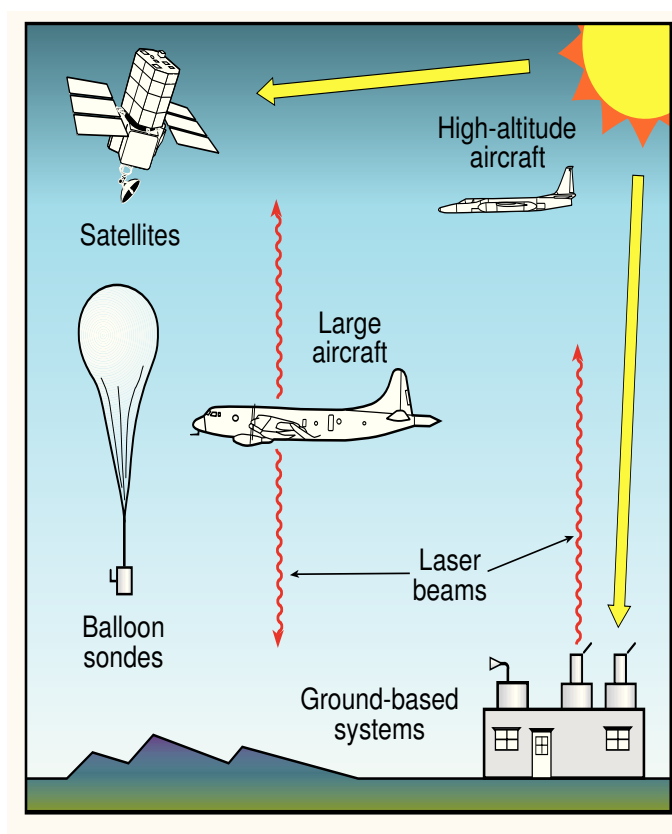


*Figure 2.5: Illustration of the ozone measurements performed locally or remotely from ground, on board aircraft/high-altitude balloons and satellites [WMO, 2007].*

**In-situ** measurement is a direct method of determining atmospheric ozone concentrations which involves collecting air samples in an instrument carried by balloons, aircraft or rockets. The ozone amounts are then measured using its characteristic wavelength dependence of absorption of light especially in the UV spectral region or by an electrical current produced in an ozone chemical reaction. Ozonesondes, launched on small balloons, use an Electrochemical Concentration Cells (ECC) to measure the current produced from the second method. Balloon measurements can also perform absorption spectroscopy by carrying devices like ozone photometers which conduct absorption measurements at 253.7 nm (Hg line) or laser in-situ sensors that record the laser light absorption reflected back to the sensor from a mirror placed under the balloon. Balloon measurements provide profile of the stratospheric ozone layer up to 40 km and several days of continuous coverage. Both optical or chemical ozone detecting methods are routinely performed on board research aircraft (sometimes commercial aircraft) to measure ozone distributions in the troposphere and lower stratosphere as well as chemicals related to its production and destruction. High-altitude research aircraft (U2 airplane) can reach the ozone layer at most locations over the globe. Ozone profiles up to 75 km are measured by rockets equipped with devices performing absorption spectroscopy.

In-situ measurements are the most accurate and detailed methods of measuring atmospheric ozone. However, the measurements are performed over localized regions and cannot provide a global picture of ozone distribution and have to cover a wide range of concentrations, temperatures and pressures in the atmosphere as well as coping with large number of species present in any air sample.

**Remote sensing** is the science of quantification or acquisition of information about an object, area, or phenomenon through the analysis of data acquired by an instrument at large distances from the object, area, or phenomenon under investigation without any physical contact [Lillesand and Kiefer, 1987]. This method is an indirect measurement applied on locations that are not accessible (atmosphere, ice, ocean). Ozone is remotely detected using its unique absorption of UV, visible or infrared radiation. The remote sensing technique is classified into active or passive depending on the source of radiation that is used for detection, e.g. the Sun and lasers.

Light Detection and Ranging (LIDAR) on board aircrafts or at ground sites, is an ozone measurement technique that operates in the optical range of 100 – 1000 nm. It emits simultaneously two laser pulses into the atmosphere at specific wavelengths characterized by different absorption

cross sections (strong and weak absorption). For ozone, the UV region (200 – 400 nm) spectral range is chosen and the choice of wavelength pairs depends on the altitude range of the measurement. A telescope collects the backscattered radiations that are transmitted to the detector (photomultiplier tube). By comparing the intensity of light scattered at each wavelength, a profile of ozone is measured from 10 km to 50 km along the laser light path.

A network of ground-based spectrometers measure total ozone amounts and the altitude distribution based on the absorption of light that reaches Earth's surface. Dobson ozone spectrometers measure atmospheric ozone column using differences in ozone absorption spectroscopy at wavelength pairs (strong and weak) in the UV spectral region. The vertical distribution is also measured from Dobson measurements using Umkehr method, the reflected UV intensities rather than direct light are measured during the sunset and the distribution is derived from the change in the ratio of two UV frequencies with time. Dobson measurements are the most precise and the only long term source of ozone data, characterised by high accuracy and good long term stability, and are often used to calibrate data obtained from satellites. On the other hand, Dobson method is strongly affected by the interference of aerosols and pollutants (SO<sub>2</sub>) in the atmosphere and provides measurements only over the stations. In many stations, Dobson spectrophotometers are succeeded with the fully automated improved Brewer spectrometers which have the same measurement principle for consistency.

Other instruments use ozone absorption in the UV and visible spectral region over many wavelengths for measurements (e.g. Differential Optical Absorption Spectroscopy (DOAS, 330 – 350 nm) and Systeme d'Analyse par Observation Zenitale (SAOZ, 450 – 570 nm) spectrometers)

Satellites measure ozone columns and profiles over nearly the entire globe on a daily basis, the measurement principles are similar to Dobson instrument but over wide wavelength windows and are satellite based. Satellite spectrometers measure the absorption of UV light by the atmosphere or the absorption of sunlight scattered from the surface of Earth. Other spectrometers measure ozone using its absorption of infrared or visible radiation or its emission of microwave or infrared radiations.



# Chapter 3

## Spectroscopic Aspects of Ozone Molecule

The presence of ozone in Earth's atmosphere is fundamental to atmospheric chemistry. The interaction of the solar radiations with ozone molecule (photolysis) initiates the chemical reactions in the troposphere, stratosphere and mesosphere. In the troposphere, ozone photolysis leads to the formation of OH radicals (reactions 2.34 and 2.35), the most important radical in the troposphere that initiates the oxidation of a wide variety of atmospheric trace constituents. Ozone photolysis in the stratosphere filters the biologically harmful ultraviolet radiations (UVB and UVC between 230 and 290 nm) from the incoming solar radiations, this is vital to human well-being. The photochemistry of ozone molecule is complex and is controlled by the structure, spectroscopy and excited states of the molecule, different photo-products of O and O<sub>2</sub> are released due to the weak bonds of ozone molecule.

Global distribution of ozone amounts in Earth's atmosphere can be determined by remote sensing methods in different spectral regions, mostly in the UV, visible, and thermal IR from ground-based and satellite based instruments. This requires an accurate quantitative information describing the interactions between electromagnetic radiation and the ozone molecule; i.e. temperature dependent absorption cross section spectra and line parameters in the different spectral regions at appropri-

ate physical conditions representing the true state of the atmosphere (e.g. pressure, temperature, mixing ratio), to be used in the retrievals.

This chapter presents a short description of the ozone molecule and outlines the importance of accurate knowledge of absorption features of the ozone molecules in the UV, visible and NIR ranges.

### 3.1 Ozone Spectroscopy and Cross Section

Ozone is a form of oxygen ( $O_3$ , trioxygen). In the ground state, the oxygen atoms are covalently bonded and arranged in the form of triangular shape with an apical angle of  $116.8^\circ$  and a bond length of  $1.278 \text{ \AA}$  (Fig. 3.1). The central oxygen atom forms a covalent bond with each terminal atom leaving an unpaired electron on each atom. The two unpaired electrons are weakly coupled into a singlet or triplet state and occupy  $\pi$  orbitals. The central oxygen atom is positively charged and the terminal oxygen atoms each carry partial negative charge.

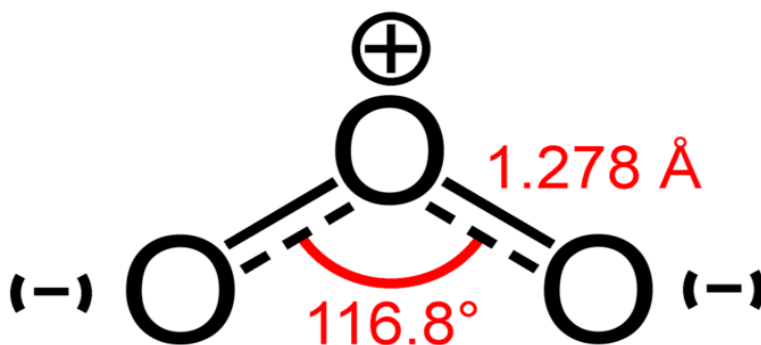


**Figure 3.1:** The ozone molecule [[http://www.globalwarmingart.com/wiki/File:Ozone\\_Molecule\\_Formula\\_png](http://www.globalwarmingart.com/wiki/File:Ozone_Molecule_Formula_png)].

Ozone is assigned to a hybrid (average) resonance<sup>2</sup> structure (Fig. 3.2). The molecule changes between the two forms as the single and double bonds exchange their places which changes the polarity of the molecule along with it, neither form accurately represents the structure and bonding in the  $O_3$  molecule. Spectroscopic studies indicate that both O-O

<sup>2</sup>The existence of a molecule in many structures due to delocalization of electrons.

bonds (single and double) are equal in length and strength and intermediate between characteristic single and double bond.

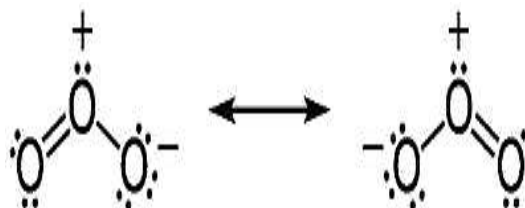


**Figure 3.2:** Resonance structures of ozone molecule in its ground state [<http://en.wikipedia.org/wiki/File:Ozone-resonance-Lewis-2D.png>].

The ground state of the ozone molecule has a  $C_{2v}$  equilibrium structure similar to water molecule (Fig. 3.3).

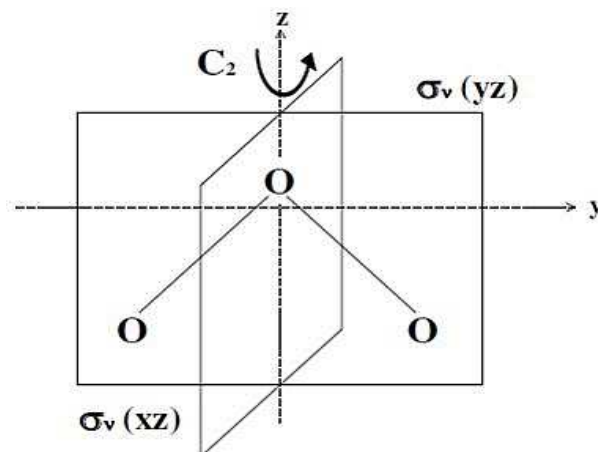
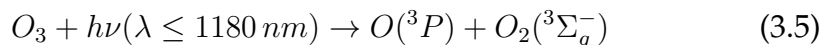
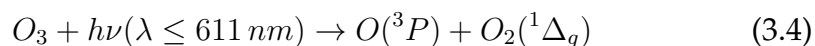
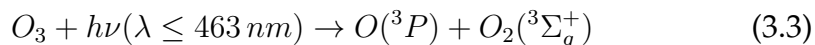


**Figure 3.3:** Symmetry elements of ozone molecule in the  $C_{2v}$  point group of the ground state.

The principal ozone forming reaction in the atmosphere is the three body recombination of atomic and molecular oxygen (eq. 2.2), therefore ozone in its ground state is approximated as a compound of  $O-O_2$ . The weak bonding between the singly occupied  $\pi$  orbitals on the terminal oxygen atoms makes ozone an instable molecule and a stronger oxidization agent than the oxygen molecule. The complex photolysis of ozone leads to a transition from the ground state to some higher excited states or to the dissociation of the molecule depending on the wavelength of the photons, different excited states  $O$  and  $O_2$  are produced:



where the wavelengths in parentheses indicate the thermochemical thresholds for the photo-products.

These reactions correspond to transitions between the ground vibrational, ground electronic and an electronically excited state; i.e ozone's near infrared, visible and ultraviolet spectra in which four distinct band systems are recognized namely the Hartley, Huggins, Chappuis and Wulf bands. The lowest electronic excited states of ozone molecule corresponding to these band systems are displayed in Fig. 3.4.

### Hartley and Huggins bands

The broad continuum of the strongest Hartley absorption band of  $O_3$  in the UV region is assigned to an electronic transition from the ground  $X^1A_1$  state to the upper electronic state  $1^1B_2$  state in the  $C_{2v}$  point group of the ground state followed by fast photo dissociation. The characteristic band shape arises from a symmetric stretching progression. The small diffused structures superimposed on the continuum correspond to transitions between the (0, 0, 0) vibrational level of  $X^1A_1$  and vibrational states in the  $1^1B_2$  upper electronic state [Joens, 1994a].

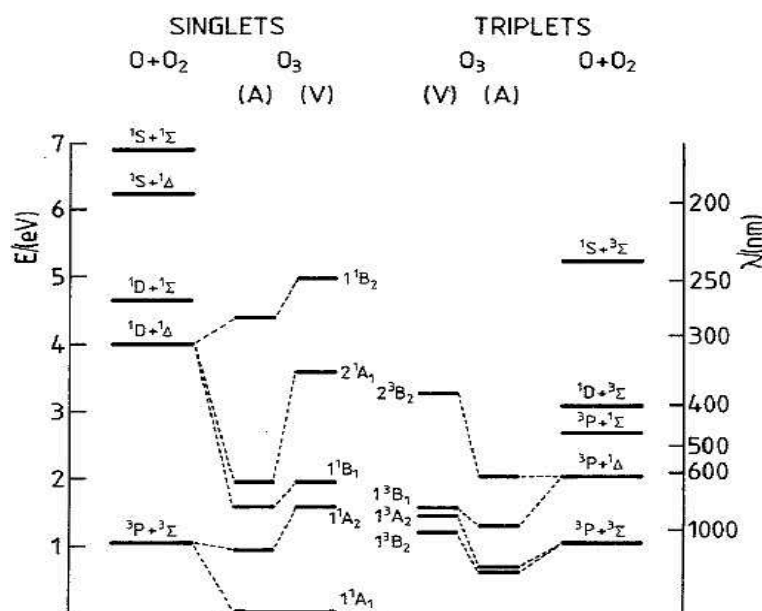


**Figure 3.4:** The lowest lying electronic states at the ground state  $C_{2v}$  geometry of the ozone molecule with the states of  $O_2$  and  $O$  [Mason and Pathak, 1997].

The Huggins absorption band is located at the red tail of the strong Hartley band, the cross section is exceedingly small and characterized by a series of diffused vibrational structures superimposed on the continuum of the UV range that decrease by about four orders of magnitude within the band range. The assignment of the Huggins band has been a subject of disagreements and inconsistencies; it is due to the transitions to the upper electronic state of either the second or the third singlet; i.e.,  $2^1A_1$  or  $1^1B_2$ .

Banichevich et al. [1993] assigned the Huggins absorption to the electronic transition to the excited  $2^1A_1$  state. Although this transition is orbitally forbidden [Hay and Dunning, 1977; Thunemann et al., 1978; Banichevich et al., 1990, 1993; Banichevich and Peyerimhoff, 1993], the  $2^1A_1$  surface showed a minimum below the minimum of the  $1^1B_2$  state allowing a coupling process with the  $1^1B_2$  state in  $C_s$  symmetry<sup>3</sup>. This interpretation was confirmed by Joens [1994b] as well as O’Keeffe et al. [2001].

On the other hand, the theoretical analysis published in Qu et al. [2004a,b] reconfirmed the initial assignment of the Huggins to the same transition state as the Hartley band [Katayama, 1979, 1986; Sinha et al.,

<sup>3</sup>The ozone molecule is distorted with one bond length being substantially longer than the other one.

1986; Le Quèrè and Leforestier, 1992; Yamashita et al., 1992] in which the Huggins band is due to the excitation to the potential wells of the  $1^1B_2$  state in which the structures are due to excitation of the vibrational states in the two wells with  $C_s$  symmetry as illustrated in Fig. 3.5.

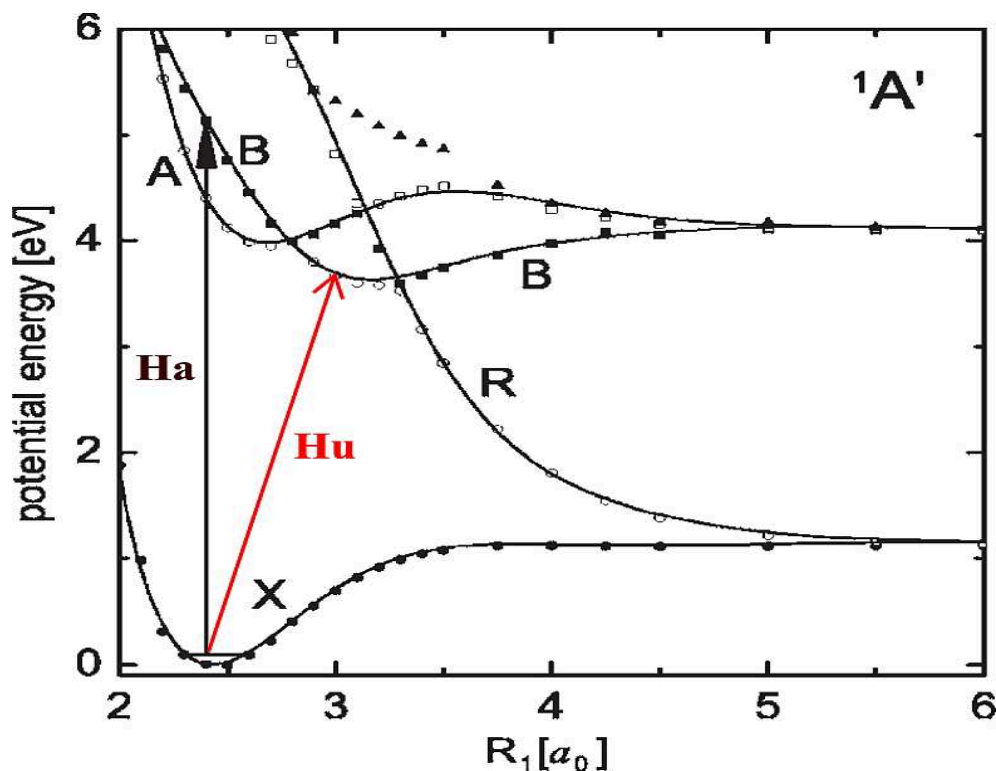


Figure 3.5: Potential energy surfaces of the lowest  $2^1A_1$  or  $1^1B_2$  states as a function of the dissociation coordinate (O-O bond distance) [Qu et al., 2004a].

### Chappuis and Wulf bands

The contributions of the visible and near-IR absorptions to ozone spectrum are weak compared to the ultraviolet region in the Hartley band, but remain significant in the atmospheric window. The Chappuis and Wulf bands correspond to excitations to the lowest states of ozone.

The Chappuis band is more than  $10^3$  times weaker than the Hartley band and centred in the red region. The Chappuis band corresponds to absorption from the  $X^1A_1$  ground state to the  $1^1A_2$  and  $1^1B_1$  state in  $C_{2v}$  symmetry. The band is composed of an irregular series of vibrational bands superposed on a continuum absorption feature in the blue wing

between 400 and 550 nm corresponding to an absorption to the  $1^1B_1$  state. The  $1^1A_2 \leftarrow X^1A_1$  transition is only vibronically allowed via the anti-symmetric stretch [Steinfeld et al., 1987] and contributes to the underlying featureless absorption in the red wing of the Chappuis system.

The Wulf band consists of weak absorptions in the visible (overlap with the Chappuis band) and near infrared region which are five orders of magnitude below those near the peak of the Hartley band. The Wulf system is due to the  $1^3A_2 \leftarrow X^1A_1$  and  $1^3B_1 \leftarrow X^1A_1$  transitions just above the dissociation limit of the ground state of the  $O_3$  molecules.

Figure 3.6 shows SCIAMACHY's ozone temperature dependent cross section spectra displaying the Hartley, Huggins, Chappuis and Wulf bands [Bogumil et al., 2003].

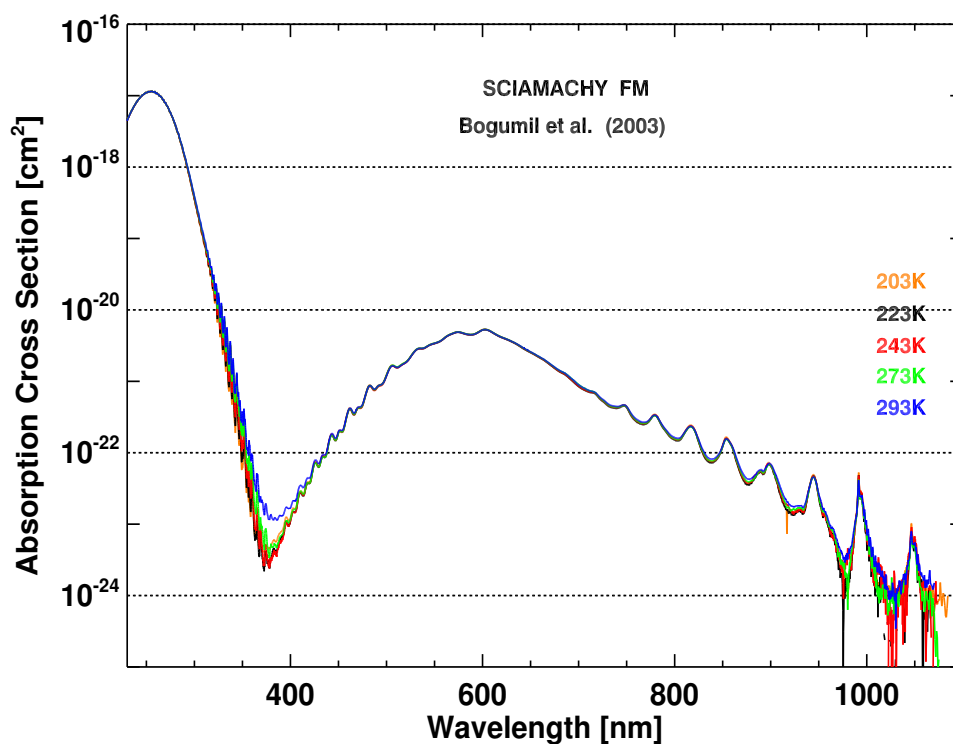


**Figure 3.6:** Temperature dependent ozone absorption cross section spectra [Bogumil et al., 2003] measured with the SCIAMACHY spectrometer (230 – 1070 nm) covering the Hartley, Huggins, Chappuis and the Wulf bands at 203 K, 223 K, 243 K, 273 K, and 293 K.

The accuracy of the cross sections as well as the correct temperature dependence are essential for ozone retrieval and the temperature variation of the absorption spectra in the different bands are key param-

ters in the ozone retrieval from satellite observations [Weber et al., 2005]. The changes in the population distribution in the ground electronic state (rotational vibrational levels) are responsible for the temperature dependence of the ozone absorption cross section spectra.

## Part II

# Ozone Cross Sections



# Harmonisation of SCIAMACHY and GOME-2 Ozone Cross Sections

## 4.1 Introduction

The satellite borne atmospheric chemistry sensors present a powerful tool to monitor changes in the global atmospheric trace gas concentrations as well as other parameters describing clouds, aerosols and surface properties. Global and long term measurements of atmospheric minor constituents are key factors to improve our understanding of the phys-

---

<sup>1</sup>Part of this chapter is published in:

Cehade, W., Gür, B., Spietz, P., Gorshelev, V., Serdyuchenko, A., Burrows, J. P., and Weber, M., Temperature dependent ozone absorption cross section spectra measured with the GOME-2 FM3 spectrometer and first application in satellite retrievals, *Atmos. Meas. Tech.*, 6, 7, 1623–1632, doi:10.5194/amt-6-1623-2013, <http://www.atmos-meas-tech.net/6/1623/2013/>, 2013.

Cehade, W., Gorshelev, V. Serdyuchenko, A. Burrows, J. P. and Weber, M., Revised temperature dependent ozone absorption cross section spectra (Bogumil et al.) measured with the SCIAMACHY satellite spectrometer, *Atmos. Meas. Tech.*, 6, 11, 3055–3065, doi:10.5194/amt-6-3055-2013, <http://www.atmos-meas-tech.net/6/3055/2013/>, 2013.

ical and chemical processes that determine the behaviour of the atmosphere in a changing climate. Long term datasets of total ozone column amounts (and trace gases relevant to ozone chemistry) and vertical distributions are required to verify that the reduction in ozone depleting substances according to the Montreal Protocol (1987) and its subsequent amendments and its later adjustments, resulted in the onset of recovery [WMO, 2011].

SCIAMACHY [Burrows et al., 1995; Bovensmann et al., 1999], launched in 2002 aboard ESA's ENVISAT, provided ten years (2003 – 2012) of ozone data (operations ceased after losing communication with ENVISAT). This data together with that retrieved from GOME (1995 – 2005) aboard the ERS-2 satellite since 1995 [Burrows et al., 1999b] and GOME-2 (2007 – present) launched in 2006 aboard EUMETSAT's MetOp-A satellite [Callies et al., 2000; Munro et al., 2006.] and two additional GOME-2 spectrometers commissioned as part of the MetOp programme (MetOp B and C, MetOp-B GOME-2 spectrometer launched in 2012), will enable a homogeneous dataset in nadir observations since all instruments have very similar observation principles and differ slightly in spectral resolution. The consistency among the total column trace gas data from multiple space-borne instruments requires cautious investigation of the relevant parameters that present a significant source of error in the data processing, among them is the absorption cross section.

Accurate and high quality ozone absorption cross sections are essential input reference data in the retrieval of column densities and vertical distributions of atmospheric ozone and other trace gases from various platforms. They are also required to maintain consistency between the instruments, an instrumental drift of less than 1% per decade is needed to identify changes in the long-term trends as a response to the Montreal protocol.

For this purpose, laboratory measurements of the temperature dependent ozone absorption cross section spectra under representative in-flight controlled conditions were performed with the SCIAMACHY [Bogumil et al., 2003] and the GOME-2 [Gür et al., 2005; Gür, 2006] spectrometers at representative temperatures covering the atmospheric temperature gradient and relevant to ozone measurements (203 K, 223 K, 243 K, 273 K, and 293 K). The absorption measurements were carried out before setting the satellites in orbit and were conducted with a mobile spectroscopy setup CATGAS (Calibration Apparatus for Trace Gas Absorption Spectroscopy) built by IUP/IFE at the University of Bremen to carry out ab-

sorption measurements with GOME spectrometer [Burrows et al., 1998, 1999a]. The flight model (FM) measurements are motivated by the fact that the fit residuals of the trace gas retrieved are reduced when the satellite characteristic reference data are used. There is also no need to know the exact instrument slit function (ILS) when using the FM cross sections in the retrieval. The ozone absorption cross section measurements with GOME, SCIAMACHY, and GOME-2 cover the entire Hartley-Huggins (UV) and Chappuis band (visible), in case of SCIAMACHY the measurements include the near IR Wolf bands. The FM absorption measurements were relative cross section since the ozone amounts could not precisely measured during the campaigns. Several absorption measurements (at each temperature) with different ozone concentrations and path lengths were performed to cover the large dynamical range of the spectrometers. The spectra were concatenated together to form one consistent relative cross section spectrum in arbitrary units. The relative spectrum was then scaled to absolute absorption cross section values at a set of wavelengths or wavelength ranges.

The use of SCIAMACHY ozone FM cross sections in the SCIAMACHY total ozone retrieval in the 325 – 335 nm spectral range (Huggins band) resulted in systematic differences of about 3-5% when compared to collocated GOME data [Eskes et al., 2005], while the GOME-2 total O<sub>3</sub> retrieval in the same spectral window and using GOME-2 FM3 resulted in an overestimation of 8% [Weber et al., 2011]. The GOME total ozone data retrieved using the GOME FM cross sections [Burrows et al., 1999a] agree very well with ground observations [Weber et al., 2005; Balis et al., 2007]. This indicates that the approaches used to determine the absolute absorption cross sections were not consistent for the two instruments. The harmonisation of cross sections from multiple atmospheric sensors is essential for developing a homogeneous and consolidated data record needed for international ozone assessments.

Figure 4.1 displays Bogumil et al. [2003] ozone absorption cross section in total ozone retrieval window from Nadir observation in the Huggins band at 225 K together with high spectral resolution literature data [Bass and Paur, 1985; Paur and Bass, 1985; Brion et al., 1993, 1998; Malicet et al., 1995; Daumont et al., 1992] convolved with the appropriate SCIAMACHY slit function. It can be clearly seen that the absorption structures of Bogumil et al. [2003] data are smaller, this discrepancy appears as an overestimation in the retrieved total ozone columns.

Moreover, the variation of the temperature dependent ozone spectra

in the Chappuis and Wulf bands shown in Fig. 4.2, needed for ozone profiles retrieval from SCIAMACHY limb and occultation measurements, are not consistent with Burkholder and Talukdar [1994], Brion et al. [1998] and El Helou et al. [2005] data. For this reason, the ozone FM spectra need to be corrected in order to be use in the retrieval of atmospheric trace gases.

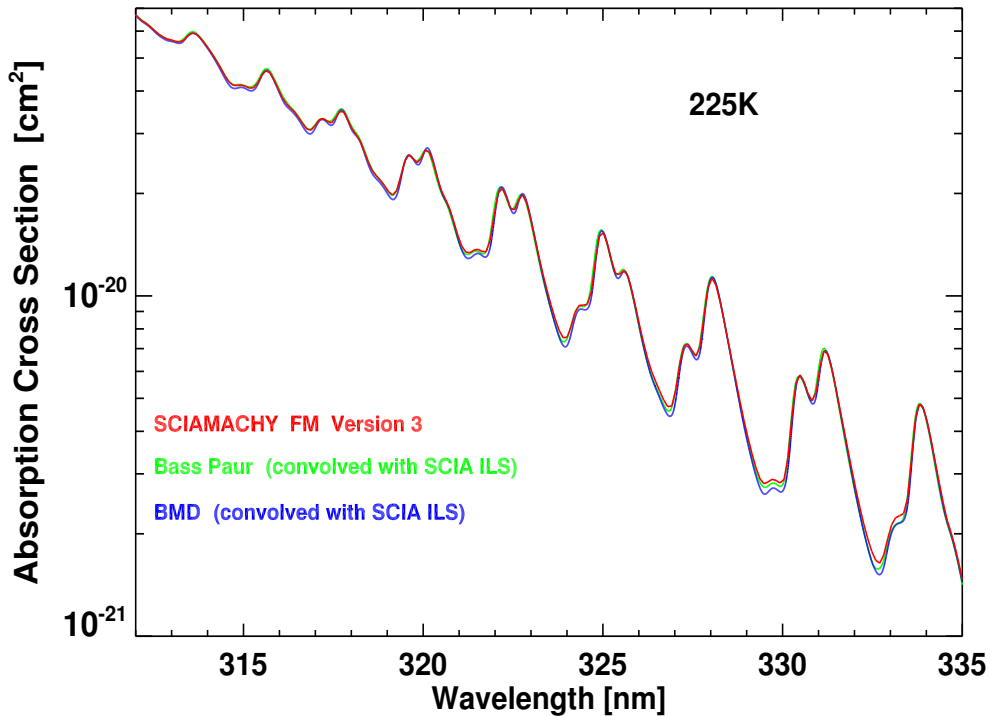


*Figure 4.1: Comparison between Bogumil et al. [2003] version 3 in red, Bass Paur (BP) [Bass and Paur, 1985; Paur and Bass, 1985] in green and BMD data [Brion et al., 1993, 1998; Malicet et al., 1995; Daumont et al., 1992] in blue in the Huggins band. The amplitudes of the absorption structures of the Bogumil et al. [2003] data at the absorption minima are smaller compared to Bass Paur and BMD.*

On the other hand, the absolute absorption cross section values of [Gür et al., 2005; Gür, 2006] version 3 data in the Huggins band show some discrepancies compared to the high resolution data smoothed to GOME-2 spectral resolution as shown in Fig. 4.3, this discrepancy also appears as an overestimation in the retrieved total ozone columns. Similarly, the temperature dependence of the data in the Chappuis band (Fig. 4.4) is also not consistent with literature data.

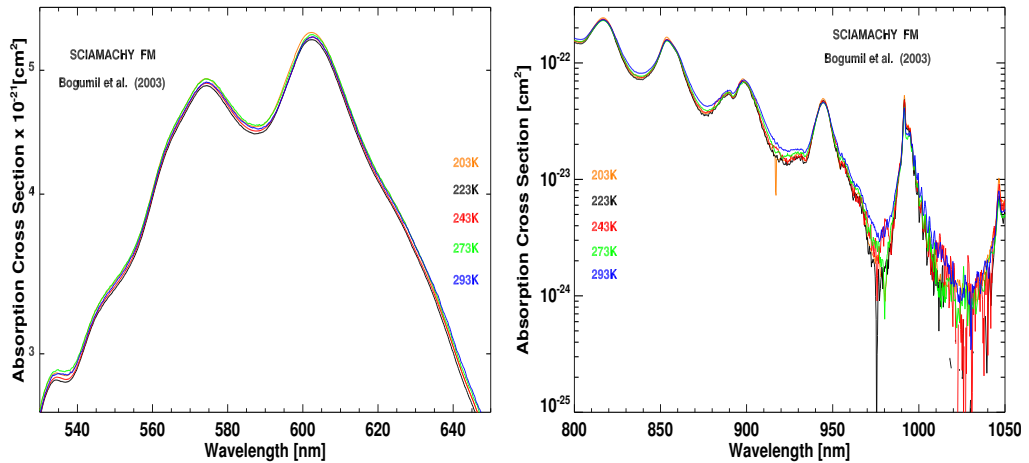


**Figure 4.2:** Temperature variation of Bogumil et al. [2003] version 3 data in the Chappuis and Wulf bands. The temperature dependence in both bands is not consistent with literature data.

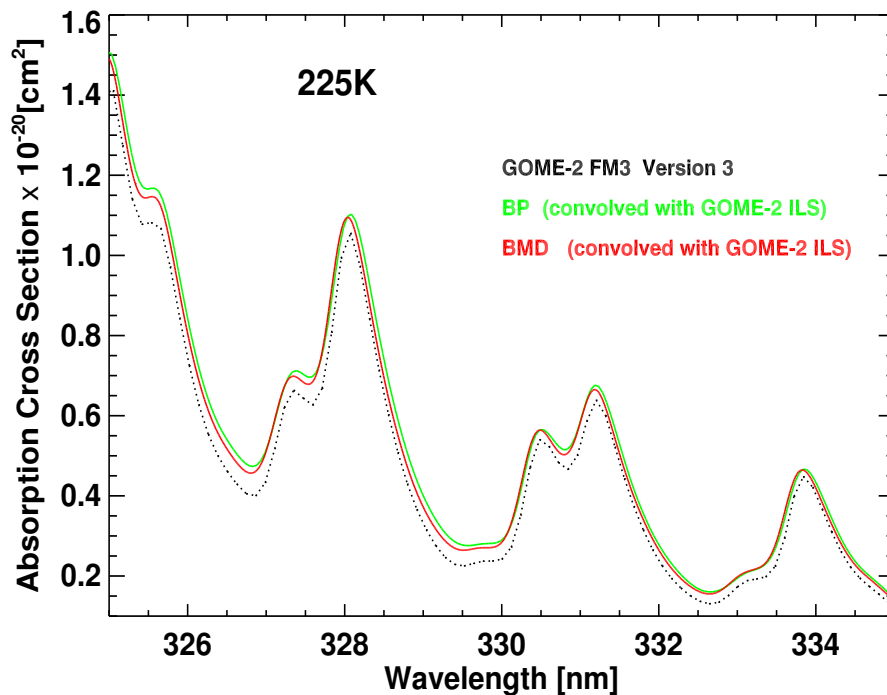


**Figure 4.3:** Comparison between the GOME-2 FM3 version 3 data (black dotted spectrum) and the literature data convolved with GOME-2 slit function in the Huggins band (DOAS region) at 225 K. The amplitudes of the version 3 data from Gür et al. [2005] and Gür [2006] are smaller compared to the literature.

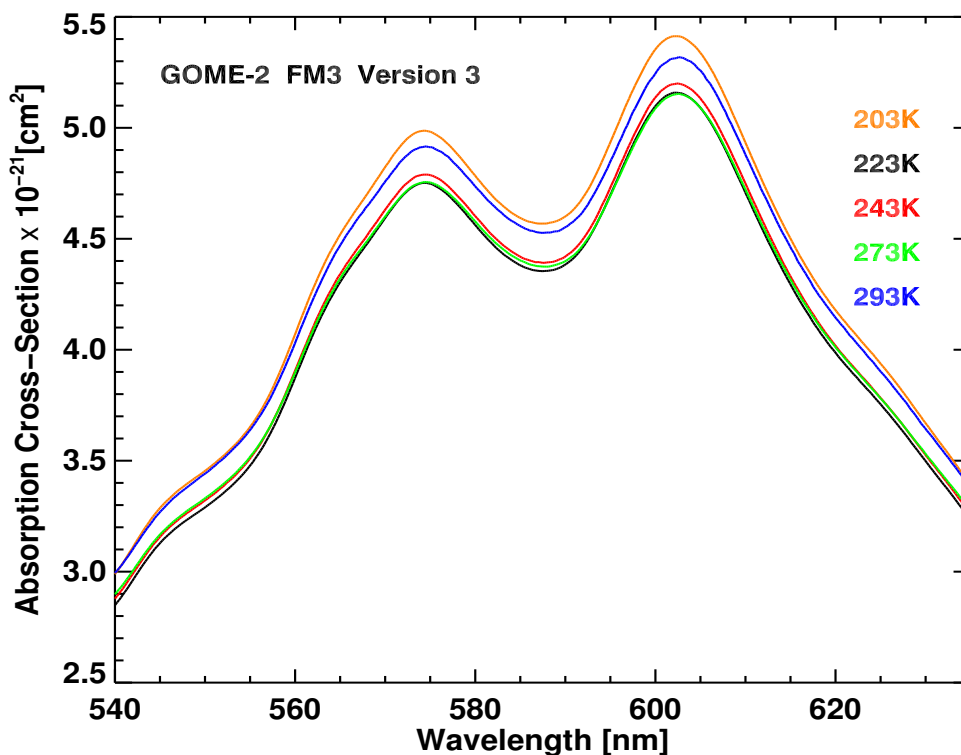


*Figure 4.4: Temperature variation of Gür et al. [2005] and Gür [2006] version 3 data in the Chappuis. The temperature dependence is not consistent with literature data.*

A re-analysis of the FM data is, however, needed to improve upon the overestimation in total  $O_3$  retrieved using the SCIAMACHY FM and GOME-2 FM3 reference spectra, respectively. There are two potential error sources in generating the ozone cross section spectra from the FM campaigns (first analysis) that need particular attention: the concatenation of relative measurements and scaling of relative spectra to absolute absorption cross sections. The reanalysis requires the full understanding of the experimental setup and the absorption measurements conducted and the procedures carried out for converting them into ozone absorption cross section spectra. The procedures followed to correct the ozone cross sections are generally similar to that used to determine the absolute cross section in Bogumil et al. [2003], Gür et al. [2005] and Gür [2006]. The first step was to analyse and carry out the same steps to produce absolute absorption cross sections from original raw spectra as a starting point and to try to identify potential problems that may require modifications from the prior analysis.

The aim of this chapter is to give a general overview on how the re-analysis was performed. The raw absorption cross section spectra mea-

sured during the FM campaigns (GOME-2 and SCIAMACHY) were considered as the starting point for modifications/corrections to be applied. The next section briefly describes SCIAMACHY and GOME-2 spectrometer followed by the settings used in the cross section measurement campaigns. Section 4 explains the procedures of re-analysing the data that includes calculating relative cross section (optical density) spectra, concatenating the different relative spectra together to form one consistent relative cross section spectrum and the method used to convert to absolute absorption cross sections. The last section presents an evaluation of the re-analysis and shows the modification obtained for both FM measurements.

## 4.2 The Spectrometers

### 4.2.1 SCIAMACHY Spectrometer

The Scanning Imaging Absorption spectroMeter for Atmospheric CHartography (SCIAMACHY) spectrometer [Burrows et al., 1995; Bovensmann et al., 1999] is a moderate resolution of 0.2 – 1.5 nm FWHM (Full Width of Half Maximum of the instrumental line shape, see Table 4.1) passive remote sensing instrument launched in 2002 aboard ESA's ENVISAT. It is an eight channel double spectrometer grating that collects at the top of the atmosphere the up-welling backscattered and cloud or surface reflected solar fluxes in the ultra-violet (UV), visible and near-infrared (NIR) spectral regions (230 – 2380 nm).

The spectrometer is highly stable and can measure very small absorptions due to its high dynamic range. Light with wavelengths below 1000 nm is detected by 1024 pixel cooled silicon diode arrays detectors while in the near infrared wavelength region InGaAs arrays are used. For each channel, the pixel exposure times (PET) are independently chosen. Spectral and radiometric calibration and instrument monitoring is performed during flight through a CrPt/Ne-hollow cathode emission lamp and a broad-band white light source.

SCIAMACHY has two scanning mirrors that perform alternative nadir and limb observation modes as well as lunar and solar occultations [Bovensmann et al., 1999; Gottwald and Bovensmann, 2011]. Total column amounts

**Table 4.1:** Spectral ranges and resolutions of each channel of the SCIAMACHY spectrometer.

Channels	Spectral Range	Spectral Resolution
1	240 – 314 nm	0.24 nm
2	309 – 405 nm	0.26 nm
3	394 – 620 nm	0.44 nm
4	640 – 805 nm	0.48 nm
5	785 – 1050 nm	0.54 nm
6	1000 – 1750 nm	1.48 nm
7	1940 – 2040 nm	0.22 nm
8	2265 – 2380 nm	0.28 nm

and vertical distributions of atmospheric trace gases relevant to ozone chemistry and global warming are inferred from SCIAMACHY's data. In addition to other geophysical parameters including mesopause temperature, cloud coverage and top height, aerosols, Mg II index (solar activity) and polar stratospheric clouds are retrieved [Gottwald and Bovensmann, 2011].

A more detailed description of the characteristics of SCIAMACHY instrument and the fundamentals of its measurement protocol is given in [Gottwald and Bovensmann, 2011].

## 4.2.2 GOME-2 Spectrometer

The Global Ozone Monitoring Experiment (GOME-2), launched in October 2006 aboard MetOp-A, is a passive atmospheric sounding that measures the back scattered and reflected solar irradiance at the top of the atmosphere and earth-shine radiance in the nadir observation mode in the UV and visible spectral range and decomposes it into its spectral components [Callies et al., 2000; Munro et al., 2006.]. Total column densities of O<sub>3</sub>, NO<sub>2</sub> and other trace gases and the vertical profile of O<sub>3</sub> are determined from the measured data using their characteristic absorption structures [Orphal et al., 2002]. Several geophysical quantities can also be inferred from GOME-2 data such as cloud parameters, surface reflectivity, and aerosol optical parameters [Munro et al., 2006.].

The GOME-2 instrument (successor of GOME) is a four-channel grating spectrometer measuring continuously in the 230 – 790 nm at a spectral resolution of 0.24 to 0.53 nm. The spectral ranges and resolutions of each channel of the GOME-2 spectrometer are listed in Table 4.2. A double spectrometer design with a pre-disperser prism and a holographic grating are used to collect the light in four cooled silicon diode array detectors (channels) each of 1024 pixels with a spectral sampling of 0.1 – 0.2 nm per pixel. The pixel exposure time is chosen independently for each channel. The GOME-2 spectrometer shows high stability and has a large dynamic range that can easily measure very small absorption from 0.001 to 2 in units of Optical Density (OD). An on-board calibration unit is included for spectral and radiometric calibration and instrument monitoring during flight. This unit contains a well isolated spectral line source (hollow cathode lamp filled with a mixture of neon and argon) and a quartz tungsten halogen lamp (White Light Source, WLS) for a broad band continuum. A detailed descriptions on the GOME-2 instrument can be found in Callies et al. [2000].

*Table 4.2: Spectral ranges and resolutions of each channel of the GOME-2 spectrometer.*

Channels	Spectral Range	Spectral Resolution
1	240 – 315 nm	0.24 – 0.29 nm
2	311 – 403 nm	0.26 – 0.28 nm
3	401 – 600 nm	0.44 – 0.53 nm
4	590 – 790 nm	0.44 – 0.53 nm

### 4.3 Measurement Settings and Procedures

The ozone absorption cross section measurements were performed in special facilities: SCIAMACHY at Fokker Space (Schiphol, The Netherlands) [TPD, 1999], and GOME-2 at TPD/TNO in Delft (The Netherlands) [TPD, 2005a]. Both spectrometers were maintained at in-flight conditions in a stabilized cryo-vacuum tank and calibrated.

The FM campaigns were conducted using the Calibration Apparatus

for Trace Gas Absorption Spectroscopy (CATGAS) setup connected to the FM spectrometers during each instrument calibration phase prior to the launch. The instrument was built by IUP/IFE at the University of Bremen and has been used in previous campaigns [Burrows et al., 1998, 1999a]. The light from a stabilized high pressure Xenon lamp (Hamamatsu) traversed the absorption cell by a White type multi-path optics [White, 1942] and directed to the spectrometers via optical fibers. The measurements performed used a continuous flow of oxygen-ozone mixture. The gas was passed from an oxygen bottle (5.0 purity) and separated into a gas exchange unit (oxygen-ozone mixing unit) and an ozoniser where ozone was produced by an electrical discharge in pure O<sub>2</sub>. From the ozoniser, the ozone was fed to the exchange unit. The oxygen-ozone mixture branch was connected to the absorption cell. Afterwards, the gas mixture was evacuated and ozone was destroyed by a hot platinum wire. The optical path length was varied between 2.4 to 33.6 m. Different combinations of O<sub>3</sub> concentrations and optical path-length (mixtures) were used to cover the range of seven orders of magnitudes over which the absorption spectrum varies.

For GOME-2, modifications were made to the setup of previous FM campaigns to improve the stability of measurements. The pressure was controlled continuously by a pressure regulator to ensure pressure stability (better than 1%) and continuous flow was used in all measurements by using the gas exchange unit. This helped avoiding any deformation in the vessel, optical windows or the mirrors arising from variations in the gas flow pressure. Moreover, the broad-band light source was monitored during the absorption measurements by integrating a flip mirror into the optical system to correct for an effective light source drift. The modifications significantly improved baseline (background intensity without absorption) stability in the absorption measurements.

The detector pixel exposure times were optimized for each measurement such that the obtained intensity was within the linear range of the detector. The thermal stability during measurements was within  $\pm 0.5$  K and the accuracy of the absolute temperature values was  $\pm 0.5$  K at 293 K and  $\pm 4$  K at 203 K for GOME-2 and  $\pm 1$  K between the two temperatures for SCIAMACHY.

The measurements were conducted for each gas mixture and temperature (with constant pressure and continuous flow of oxygen) using the following sequence:

1. measurement of a reference spectrum without any ozone in the CATGAS vessel,  $I_{ref}(\lambda, t_1)$
2. measurement of an absorption spectrum with ozone in the vessel,  $I_{abs}(\lambda, t_2)$
3. measurement of a second reference spectrum without ozone in the CATGAS vessel,  $I_{ref}(\lambda, t_3)$

The dark current spectrum of the detector was measured at an arbitrary time by blocking the optical path to the spectrometers. This spectrum was normalized to unit exposure time and could then be scaled to the exposure time selected for each measurement.

The wavelength calibration and instrument slit function (line shape) were determined independently during the on-ground characterization and calibration campaigns [TPD, 1999, 2005b].

Detailed descriptions of the experimental setup and measurement procedures of the FM campaigns are presented in Bogumil et al. [2003], Gür et al. [2005] and Gür [2006].

## 4.4 Re-analysis of SCIAMACHY FM and GOME-2 FM3 Ozone Cross Sections

### 4.4.1 Data Reduction

Measurements of the cross section spectra are based on absorption spectroscopy, in which the intensity  $I(\lambda)$  of the light at wavelength  $\lambda$  transmitted through an absorbing medium of number density ( $n$ , molecule/cm<sup>3</sup>) inside a gas cell, is a function of temperature  $T$ , pressure  $P$ , the length of the cell ( $l$ , cm), the absorption cross section of the absorbing medium ( $\sigma$ , cm<sup>2</sup>/molecule) and the initial light intensity  $I_0(\lambda)$  according to the Beer-Lambert law:

$$I = I_0 e^{-\sigma \cdot n \cdot l} \quad (4.1)$$

In order to obtain accurate absorption cross section measurements, precisely known number densities of the absorber volume through which the light beam traversed, are required. The concentrations and optical path lengths of the absorbing gas ( $n \cdot l$ ) in Eq. 4.1 were not measured as ozone was contained in an oxygen mixture under continuous flow conditions. The optical density ( $OD$ ), the ratio of light intensities with and without the gas absorber ( $OD = \ln(I_0/I)$ ) was, therefore, scaled to absolute cross section by referencing them to published literature data.

All recorded spectra were corrected for dark signal by subtracting the dark current spectrum from the measured intensities. The baseline stability (a measure for lamp drift<sup>2</sup>) which is defined as the optical density calculated from the reference intensities before and after the absorption measurements, was found to be smaller than 1%.

The reference intensity corresponding to the measured absorption spectrum at time  $t_2$  is obtained by linear interpolation of the reference intensities before and after the absorption measurement as follows:

$$I_0(\lambda, t_2) = \frac{t_3 - t_2}{t_3 - t_1} \cdot I_0(\lambda, t_1) + \frac{t_2 - t_1}{t_3 - t_1} \cdot I_0(\lambda, t_3) \quad (4.2)$$

The optical densities were derived for all absorption measurements at the five different temperatures.

#### 4.4.2 Manual concatenation

SCIAMACHY and GOME-2 full spectral range of absorption cross section varies over seven orders of magnitudes. In order to cover this large dynamical range a set of absorption measurements with different experimental conditions (certain combinations of cell length and flow condi-

---

<sup>2</sup>Any drift in the light source output between reference and absorption measurements appears as an additional broad-band absorber in the cross section spectra.

tion) called "mixtures" were carried out to cover the entire UV, visible and NIR (SCIAMACHY ) spectral regions. Each absorption measurement is representative for a given O<sub>3</sub> concentration and optical path length and targets a specific region of the spectrum.

A single continuous absorption cross section in arbitrary optical density units covering the entire ozone wavelength range of each spectrometer was obtained by gluing the useful parts of each absorption measurement.

### SCIAMACHY

Three measurement campaigns were performed with the SCIAMACHY spectrometer: "PI-Period" (October 1998), "Delta-PI-Period" (January 1999) and "Delta2-PI-Period" (January 2000). The latter two campaigns were conducted after the reconstruction and readjustment of channels 7 and 8 and the modifications introduced to reduce stray light in channel 1, respectively. Two independent optical density (OD) spectra are calculated for ozone from the absorption measurements for each temperature:

1. Delta2-PI-Period data (channel 1, 230 – 310 nm)
2. PI-Period data (channel 2 – 6, 310 – 1070 nm)

The OD spectra calculated for each temperature from different campaigns cannot be scaled to each other to produce a single spectrum. They need to be scaled to absolute absorption cross section independently.

Three versions of SCIAMACHY ozone absorption cross section data were produced, the last version contains corrections for the memory effect and baseline in channel 1. Therefore, a re-analysis of at least the PI-Period data is required.

The absorption measurements performed during the PI-period campaign used four different gas mixtures (trace gas concentrations) and partial pressures targeting different wavelength ranges of the SCIAMACHY spectral regions. The ozone optical density spectra calculated for the channels 2 – 6 comprises of 4 partial spectra. Figure 4.5 shows the com-

plete ozone OD spectra at 293K in the Huggins band (channel 2). For each spectrum, the limited regions above the detection limit and below saturation are useful for concatenation.

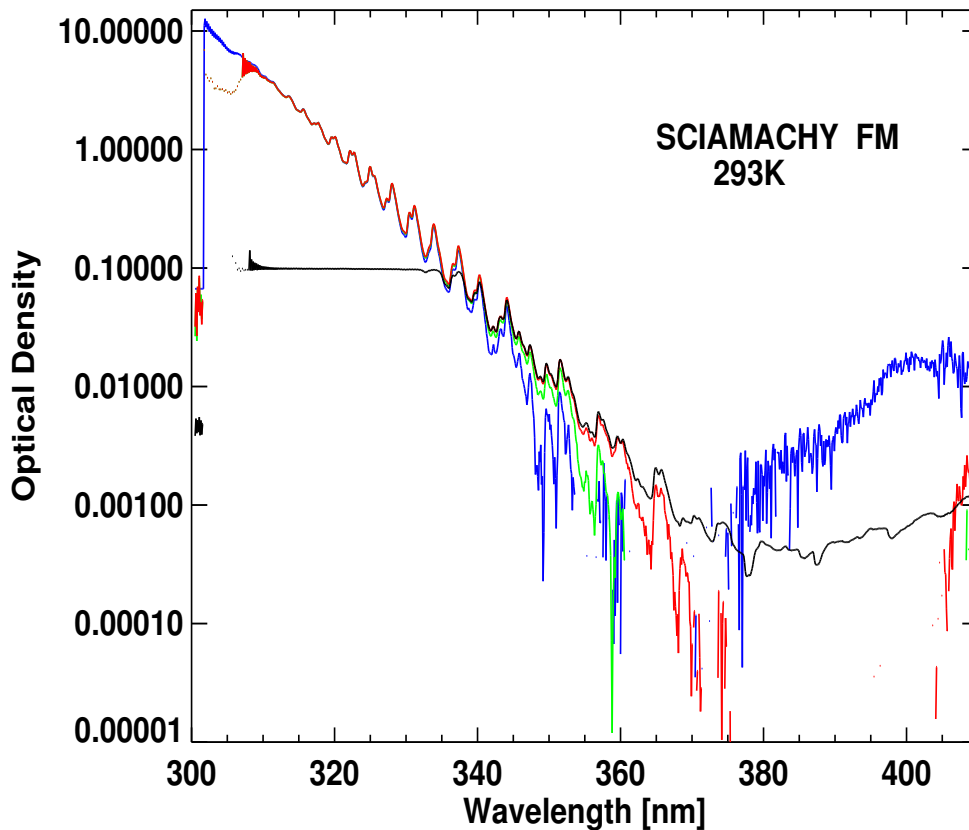


*Figure 4.5: SCIAMACHY's spectra of optical density obtained from the four absorption measurements "mixtures" in the Huggins band (channel 2) at 293 K, using different ozone concentrations and optical lengths. Only the limited regions of each spectrum above the detection limit and below saturation are useful for concatenation.*

A single continuous absorption cross section in arbitrary optical density units covering the entire SCIAMACHY's ozone wavelength range is obtained by gluing the useful parts of each absorption measurement, an example of concatenating the useful parts in the Huggins band is shown in Fig. 4.6 where the useful parts (indicated in respective colors as in Fig. 4.5) are glued together. This process is performed for each temperature profile.

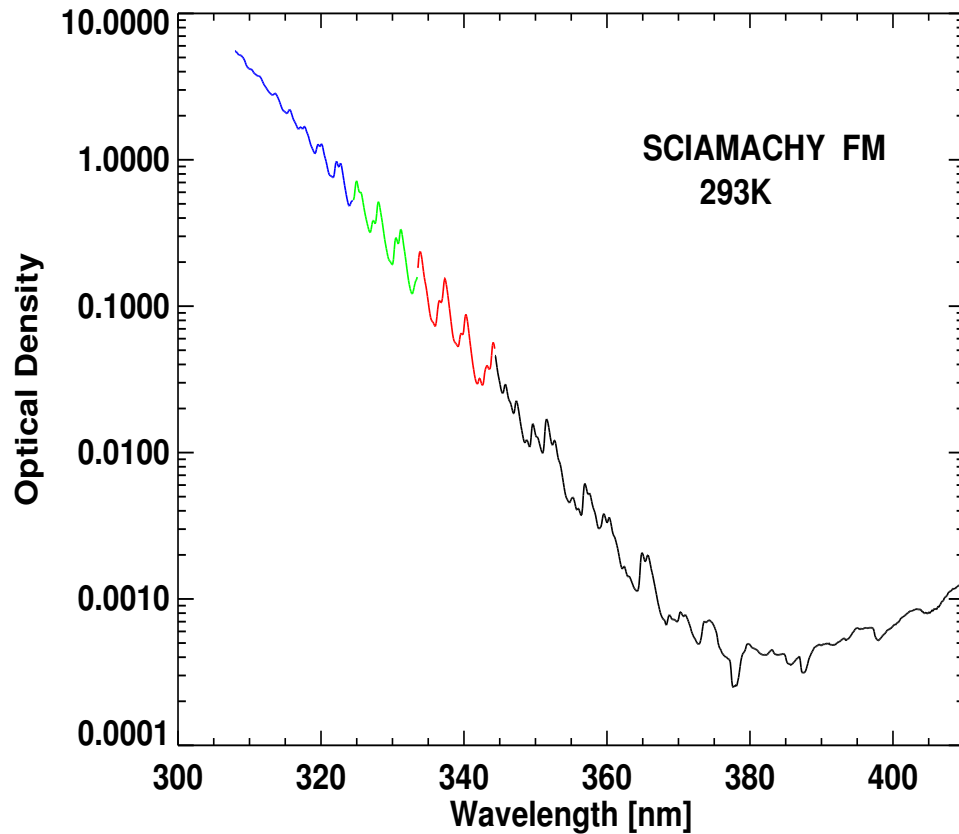


*Figure 4.6: Full spectra of ozone optical density (channel 2) obtained by concatenating the useful parts of each absorption measurement as indicated by different colors.*

#### GOME-2

A single smooth and continuous optical density spectrum covering the wavelength range of 230 – 790 nm (GOME-2 spectral range) can be obtained by scaling the various spectra from different mixtures to a selected starting OD spectrum. The scaling is derived in the overlapping regions where both spectra are within the OD limits and is then applied to the spectrum before gluing both spectra. The spectrum of "mixture 3" was chosen as a starting point which contains both parts of the Huggins (UV) and Chappuis (visible) bands within the chosen optimal optical density range. A least square fit of the data in the overlapping region between the neighbouring mixtures was used to define the scale of the optical densities of the neighbouring mixtures. The standard deviations were used as weights in the fits. The manual concatenation is illustrated in Figs. 4.7 and 4.8.

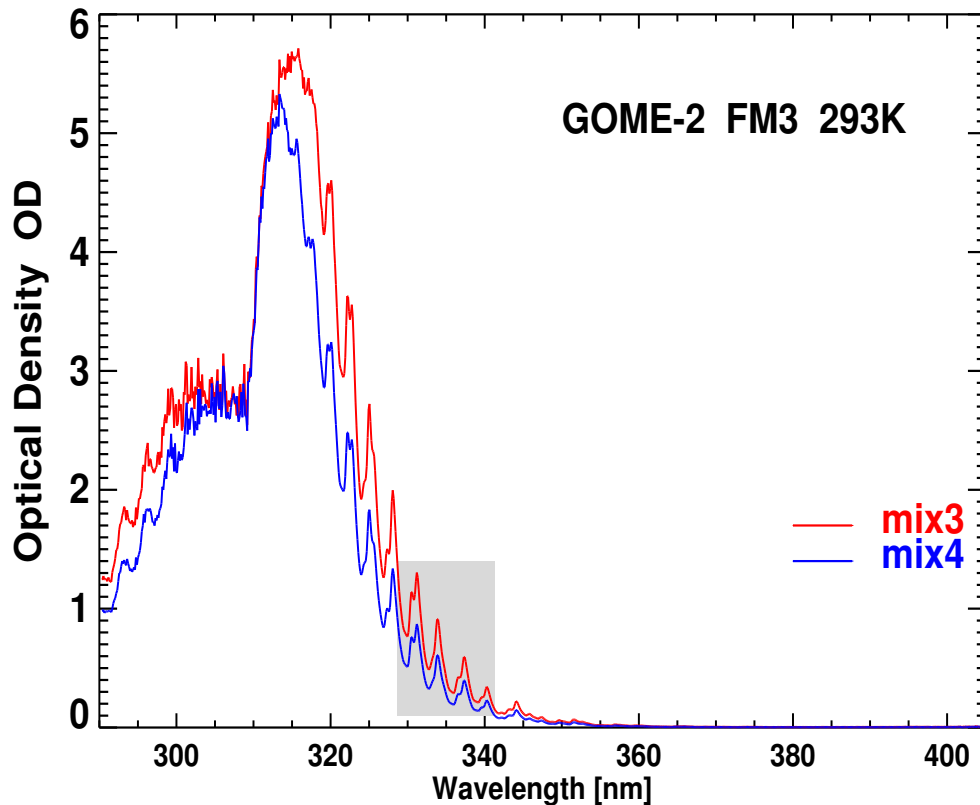


*Figure 4.7: GOME-2 spectra of optical density obtained from the absorption measurements "mixture 3" (red) and "mixture 4" (blue) in the Huggins band (channel 2) at 293 K using different ozone concentrations and optical lengths. Only the partial spectra in the shaded area ( $0.1 \leq OD \leq 1.5$ ) are usable for scaling.*

Figure 4.7 shows the complete original OD spectra of mixtures 3 (red) and 4 (blue) in the Huggins band (channel 2) at 293 K. Only very limited regions of each spectrum are useful, as in most parts saturation is present below 320 nm, in the region around 350 nm the signal is close to or below the detection limit. The part of the spectra that fall within the optical density range  $0.1 \leq OD \leq 1.5$  (shaded area) where the pixel exposure is expected to be linear, and the mixture's data lying within 1-2% of statistical dispersion of repeated measurements are chosen for manual concatenation. In some cases OD values up to 2.5 were permitted if no other mixtures are available. The useful sections of both spectra are termed as partial spectra and shown in the shaded area.

Figure 4.8 shows the partial spectra that are used in concatenation, the red spectrum is held fixed and the blue is scaled relative to it. An

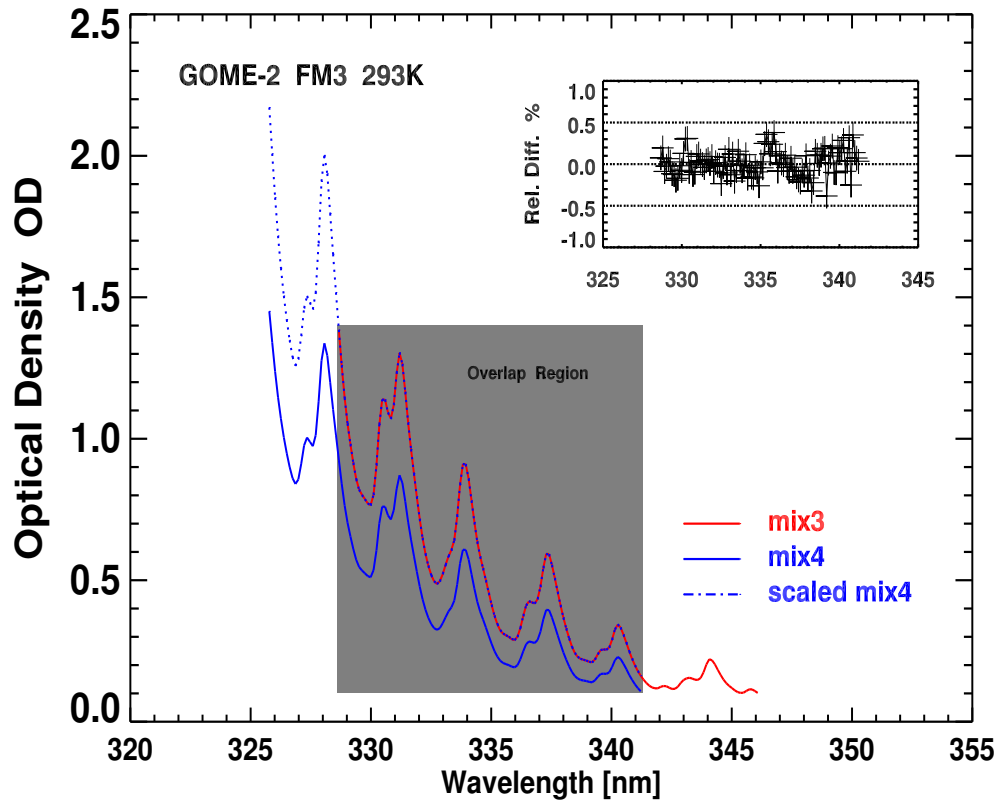


**Figure 4.8:** Concatenated partial spectrum after the spectrum of "mixture 4" was scaled to "mixture 3". The overlap region, indicated by the grey area, is used to determine the scaling factor. The fit residuals from linear fitting between the scaled spectrum of "mixture 4" (blue dotted) and "mixture 3" in the overlap region are shown in the inset.

overlapping region between the partial spectra is first defined, the wavelength range 328 and 342 nm (grey area) is found to be the optimal overlapping region. A least square fit is then applied to data of the adjacent partial spectra in the overlapping region to determine a scaling factor. Therefore the scaling of the partial spectrum of "mixture 4" to "mixture 3" is performed by applying the scaling factor, the scaled spectrum is displayed as blue dotted line. The agreement between the optical densities of the two measurements after scaling is verified with the relative difference (in percent) between the measurements in the overlap region, the inset shows that the typical values obtained are within  $\pm 1\%$ .

In the same fashion the other mixtures are successively concatenated to obtain at the end the full, but arbitrarily scaled, optical density spectrum (Fig. 4.9).

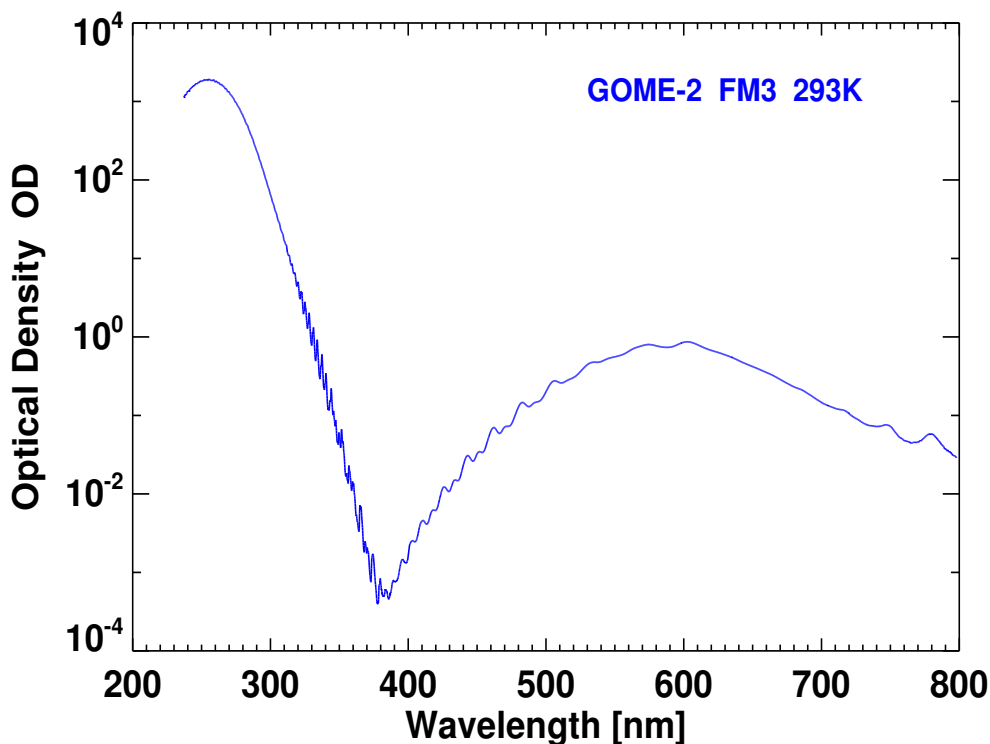


*Figure 4.9: Final concatenated optical density spectrum at 293 K.*

### 4.4.3 Absolute Scaling

The OD spectra are relative cross sections. The  $O_3$  concentrations and optical path lengths ( $n \cdot l$  in Eq. 4.1) cannot be determined in the gas flow setup used here, thus the OD spectra have to be scaled to absolute cross section using published literature data: BMD [Brion et al., 1993, 1998; Malicet et al., 1995; Daumont et al., 1992] and Bass and Paur [Bass and Paur, 1985; Paur and Bass, 1985].

These literature cross sections are convenient for scaling since they are measurements of absolute  $O_3$  cross sections, cover the temperature range at which our absorption measurements were conducted and they are available at high spectral resolution that were smoothed to each spectrometer's resolution by convolving them with the wavelength dependent slit function of each spectrometer.

### SCIAMACHY

The concatenated absorption cross section spectra for each temperature were scaled to absolute absorption cross section using Bass and Paur cross section data [Bass and Paur, 1985; Paur and Bass, 1985]. The Bass Paur data were convolved with the wavelength dependent SCIAMACHY slit function varying from about 0.2 nm to 0.4 nm. The instrument slit function varies in channel 2 and was determined by matching a high resolution solar spectrum, measured with the Fourier transform spectrometer at the McMath solar telescope at Kitt Peak, Arizona [Kurucz, 1995], to the SCIAMACHY measured solar spectrum in a non-linear least squares fit. This is particularly important in the Huggins band with strong differential features which smooth out at lower spectral resolution. The OD spectra are scaled directly in the 312 – 335 nm range to the convolved Bass Paur data for each temperature.

Figure 4.10 shows SCIAMACHY's temperature dependent cross section spectra in absolute units displaying the Hartley, Huggins, Chappuis and Wulf bands.

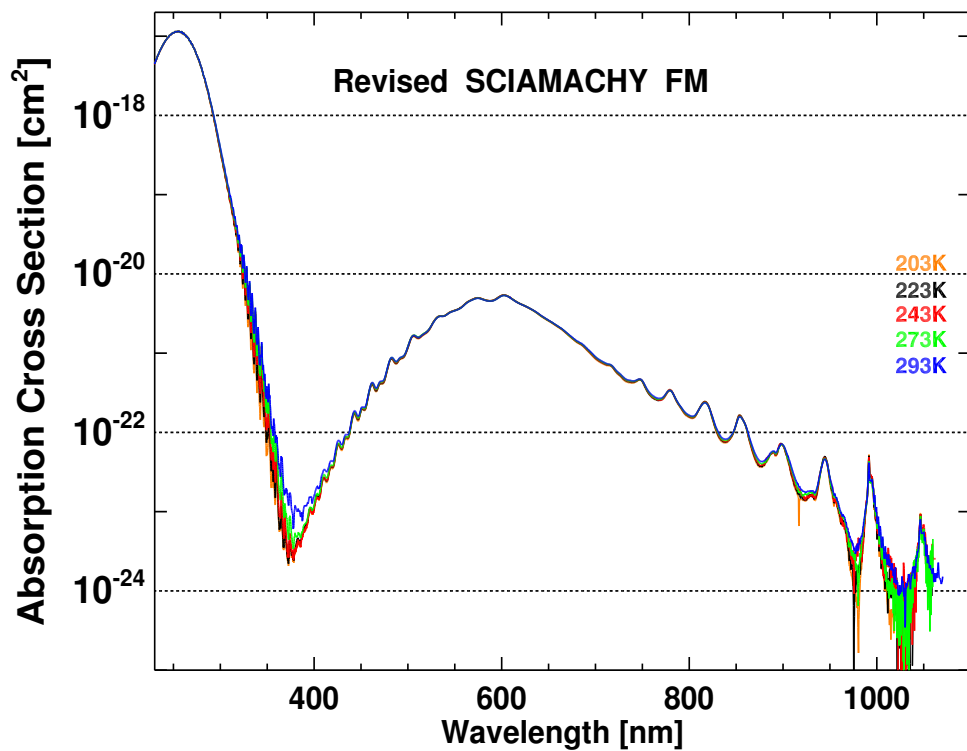


**Figure 4.10:** Revised temperature dependent ozone absorption cross section spectra measured with SCIAMACHY spectrometer (230 – 1070 nm). The cross section data cover the Hartley, Huggins, Chappuis and the Wulf bands and were recorded at 203 K, 223 K, 243 K, 273 K and 293 K.

## GOME-2

The optical density spectra at a given temperature need to be scaled to absolute absorption cross section values according to BMD and Bass-Paur datasets. The O<sub>3</sub> cross sections at high spectral resolution are smoothed to GOME-2 spectral resolution by convolving them with the wavelength dependent GOME-2 instrumental slit function. The slit function shape was characterized at a sub-pixel resolution independently for each spectrometer using a slit function stimulus during the on-ground calibration and characterization campaign [TPD, 2005b; Siddans et al., 2006].

The absolute scaling of the OD spectra was performed according to the following procedure:

- The OD spectra were first placed on the correct relative temperature dependence by normalizing them to unit integrated optical density of the electronic band.
- A scaling factor was determined between the five optical densities of GOME-2 spectra and the absolute cross section of the literature data at selected wavelengths from the Hartley, Huggins and the Chappuis bands.
- A single scaling factor was calculated as the weighted average of the scaling factors obtained from selected individual wavelengths.

All OD spectra were scaled at once preserving the correct temperature dependence, Fig. 4.11 shows the temperature profiles spectra of GOME-2 displaying the Hartley, Huggins, and Chappuis bands in absolute units.

## 4.5 Evaluation of the Re-analysis

### SCIAMACHY

Direct comparison in the Huggins band (DOAS spectral window) between the cross section obtained in this work at 223 K (blue spectrum) and Bogumil et al. [2003] (black dotted spectrum) SCIAMACHY FM (version 3) as well as literature data is displayed in Fig. 4.12.

The comparison show a clear difference, the amplitudes between absorption maxima and minima (absorption structures) in the DOAS window of the revised data in the 315 - 340 nm region are larger than that

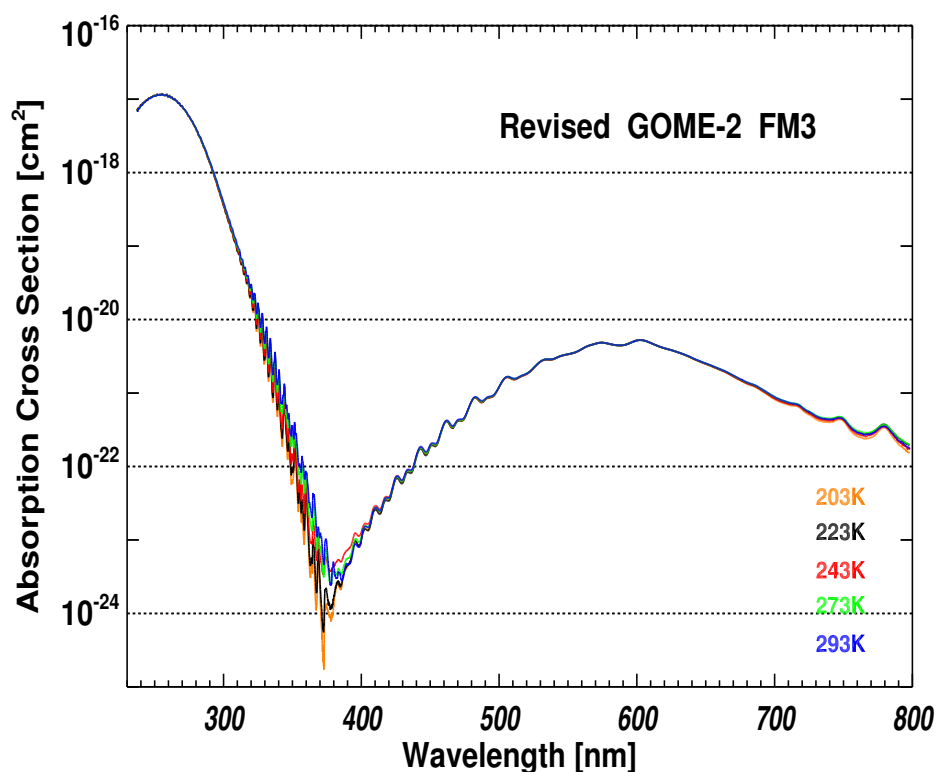


**Figure 4.11:** Revised temperature dependent ozone absorption cross section spectra measured with GOME-2 spectrometer (230 – 790 nm). The cross section data cover the Hartley, Huggins and the Chappuis bands and were recorded at 203 K, 223 K, 243 K, 273 K and 293 K.

in the Bogumil et al. [2003] data (smaller cross section values of the absorption minima) and agree better with literature data convolved with the appropriate SCIAMACHY slit function.

On the other hand, the revised FM data shows the correct temperature dependence in the Chappuis band (Fig. 4.13).

The improvements are due to the procedures followed to correct the ozone cross sections. The major improvements in this study were that different raw measurements were used to derive the relative cross section (OD) spectra, the concatenation uses different segments of the useful parts as compared to earlier analysis and finally, the literature data were properly convolved to SCIAMACHY spectral resolution before scaling the unit-less concatenated cross section spectra. This modification corrects the discrepancies seen in the SCIAMACHY total ozone retrieval (see Section 5.4).

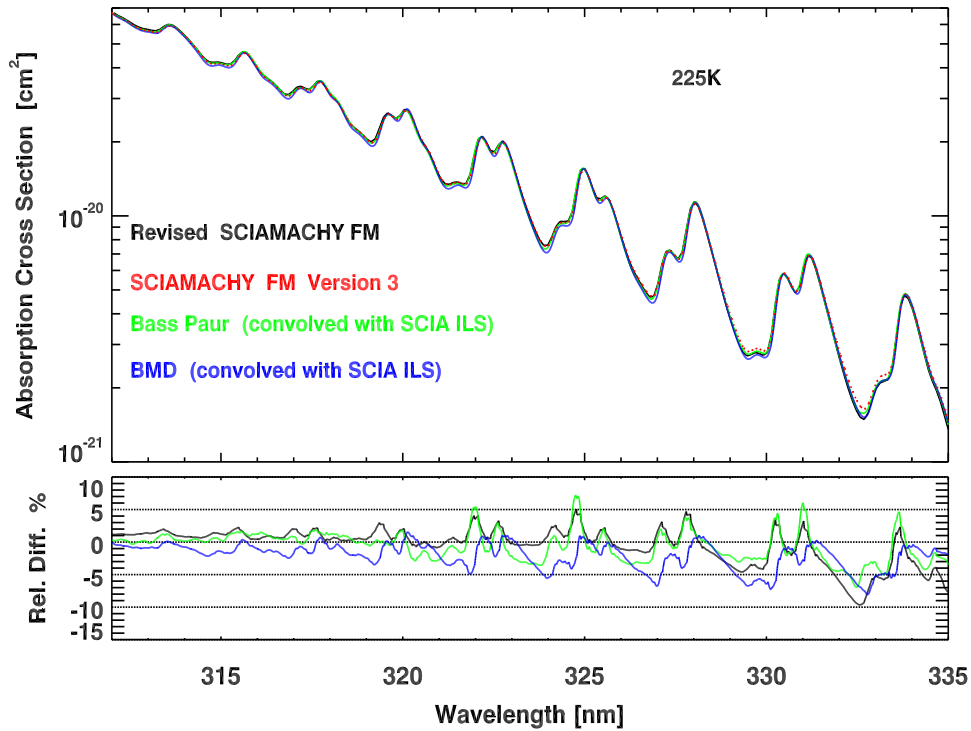


**Figure 4.12:** Comparison between Bogumil et al. [2003] version 3 (black dotted spectrum), revised data in red, Bass Paur in green and BMD in blue in the Huggins band (DOAS region). The amplitudes of the Bogumil et al. [2003] data are smaller compared to Bass Paur, BMD and revised data. The lower sub-panels show the difference relative to Bogumil et al. [2003] data.

## GOME-2

A new procedure is used in the manual concatenation in which the neighbouring measurements are scaled to each other in the overlap region according to:

$$OD_2 = a \cdot OD_1 + b \quad (4.3)$$

Equation 4.3 represents the best approach for scaling between two independent measurements and allows the corrections for some background intensity ("baseline or zero absorption level"). In the GOME-2 FM3 Version 3 data [Gür et al., 2005; Gür, 2006] mean spectral ratios were used which corresponds to a fit to Eq. 4.3 with  $b = 0$ .

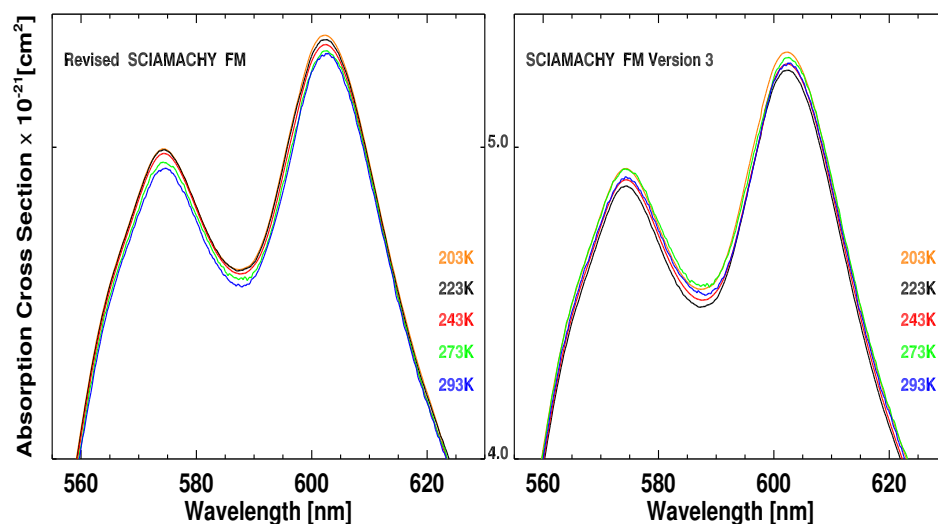


**Figure 4.13:** Left: Revised temperature dependent SCIAMACHY FM ozone absorption cross section spectra in the Chappuis band. Right: SCIAMACHY FM version 3. The revised spectra preserve the correct temperature dependence.

The concatenated optical density spectrum normalized to unit integrated optical density of the electronic band obtained from this approach, is larger as compared to the spectrum reported in Gür et al. [2005] and Gür [2006]. Figure 4.14 shows the OD spectra in the Hartley and Huggins band obtained from both approaches at 273 K.

The lower inlet shows the comparisons in the Hartley band, the revised FM3 (red spectrum) is clearly larger than that of version 3 data (blue) and the relative difference is within 2%. In the Huggins band (upper inlet) the relative difference between the normalised spectra reach 4 – 6%.

Gür et al. [2005] and Gür [2006] reported that the scaling factor calculated at 334 nm (Huggins band) deviates 8% from the mean factor used to absolutely scale the relative OD spectra. This value like other wavelengths in the Huggins band was not used in the analysis of FM3 version 3 data. This resulted in absorption cross section values that are smaller in the Huggins band ultimately leading to an overestimation of the retrieved ozone, this can be clearly seen in the upper inlet of Fig. 4.14 .

In the re-analysis, more wavelengths in the Huggins band are used and the scaling factors at each of the selected wavelength now agree

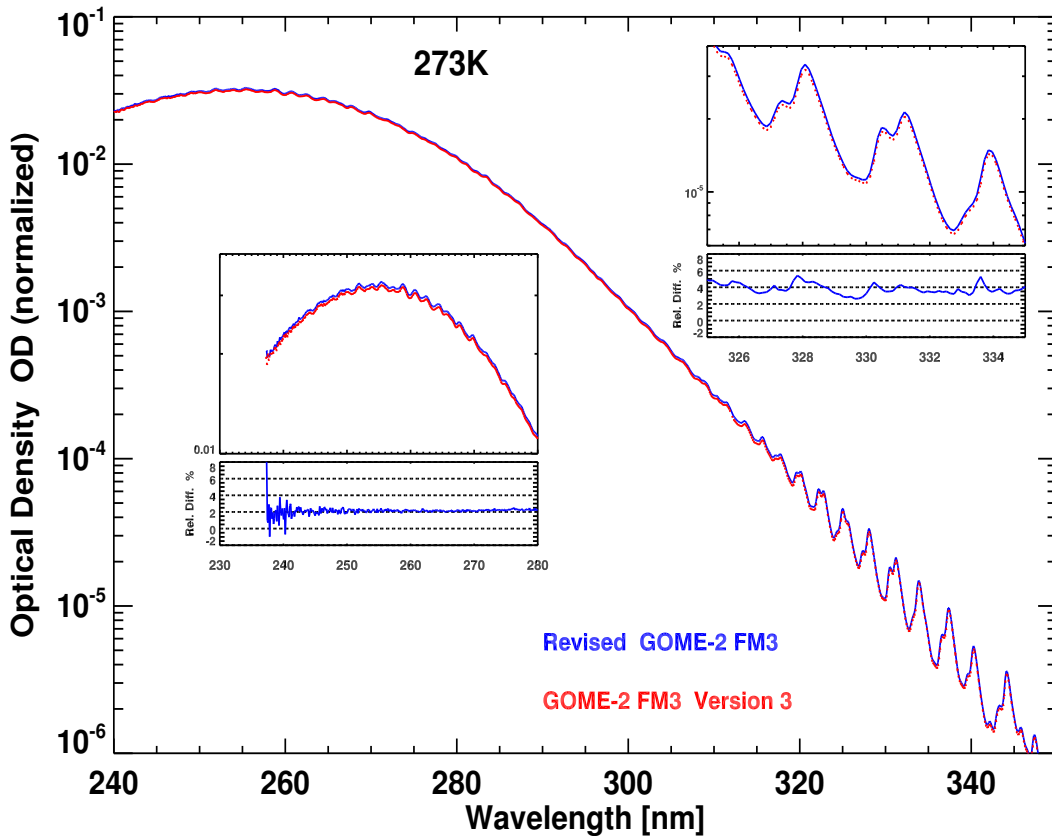


**Figure 4.14:** Comparison between the 273 K OD spectrum reported in Gür *et al.* [2005] and Gür [2006] (red) and the newly concatenated (blue). The insets are zooming-in into the 230 – 280 nm and 320 – 340 nm spectral regions of the Hartley and Huggins bands respectively with lower sub-panels showing the relative difference between the spectra.

within 0.5%. Figure 4.15 shows that revised data in the DOAS retrieval window in the Huggins band at 225 K is higher compared to version 3 and close to the literature data. Our new approach reduced the deviations in the Huggins and, therefore, improved the total ozone retrieval (see Section 5.4).

Another important change from prior analysis of the GOME-2 FM was that the overlapping regions for scaling the various mixtures were made wider, if possible within the OD limit, to further improve the concatenation.

The new analysis also improved the temperature dependence of the absorption spectra for both satellites, these improvements together with other quality assessment of the revised data are introduced in the next

chapter.

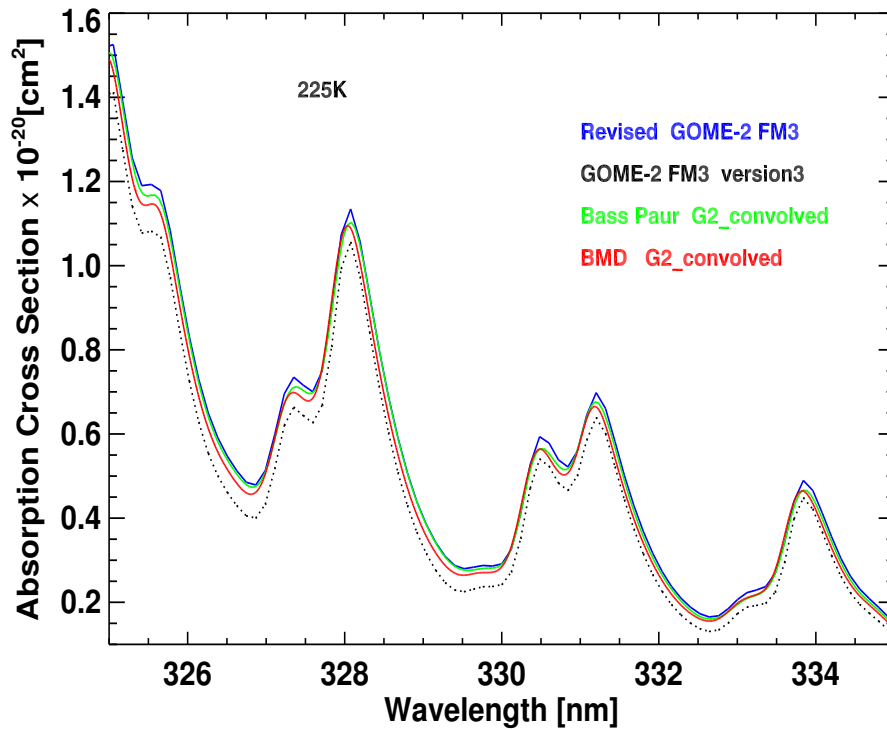


*Figure 4.15: Comparison between the GOME-2 FM3 version 3 data (black dotted spectrum), revised data (blue) and the literature data convolved to GOME-2 slit function in the Huggins band (DOAS region) at 225 K. The amplitudes of the version 3 data from Gür et al. [2005] and Gür [2006] are smaller compared to the literature and revised data.*



## Validation of the Revised Cross Section Spectra and Application in Satellite Retrievals

This chapter presents the revised ozone temperature dependent absorption measurements performed with the SCIAMACHY and GOME-2 satellite spectrometers and conducted at five temperatures 203 K, 223 K, 243 K, 273 K, and 293 K. An extensive analysis of the data is performed by comparing them to high spectral resolution measurements available in the literature data base, as well as the last versions of the FM measurements in order to assess their quality and to validate whether the revised data are appropriate for atmospheric remote sensing. The comparisons were carried out at single wavelengths and over broad spectral regions with

---

<sup>1</sup>Part of this chapter is published in:

Cehade, W., Gür, B., Spietz, P., Gorshelev, V., Serdyuchenko, A., Burrows, J. P., and Weber, M., Temperature dependent ozone absorption cross section spectra measured with the GOME-2 FM3 spectrometer and first application in satellite retrievals, *Atmos. Meas. Tech.*, 6, 7, 1623–1632, doi:10.5194/amt-6-1623-2013, <http://www.atmos-meas-tech.net/6/1623/2013/>, 2013.

Cehade, W., Gorshelev, V. Serdyuchenko, A. Burrows, J. P. and Weber, M., Revised temperature dependent ozone absorption cross section spectra (Bogumil et al.) measured with the SCIAMACHY satellite spectrometer, *Atmos. Meas. Tech.*, 6, 11, 3055–3065, doi:10.5194/amt-6-3055-2013, <http://www.atmos-meas-tech.net/6/3055/2013/>, 2013.

an emphasis on the total ozone retrieval spectral window (325 – 335 nm) in the Huggins band taking into account the influence of spectral resolution and wavelength accuracy on the cross sections. Finally, the revised spectra are tested in the total ozone retrieval. The next section presents the absorption cross sections in the different spectral regions: Hartley, Huggins, Chappuis and Wulf bands and discusses the temperature dependence of each band. Section 2 shows the different comparisons performed: at ten selected single wavelengths corresponding to Hg lamp and He–Ne laser lines located in the Hartley and Chappuis band at room temperature, integrated absorption cross sections at different temperatures and the different bands and comparisons between modelled and measured cross sections in the Huggins band. Section 3 presents the non-linear square fit and the results obtained in the DOAS retrieval window. The last section presents total ozone column algorithm and retrievals from SCIAMACHY and GOME-2 observations using the revised SCIAMACHY FM and GOME-2 FM3 ozone cross section data compared to the reference retrieval.

## 5.1 Absorption Cross Sections

The accuracy of the cross sections and their correct temperature dependence in the different absorption bands must be considered in the ozone retrieval from atmospheric observations (e.g. Weber et al. [2005]). The total ozone is retrieved from nadir viewing instruments in the Huggins band (325 – 335 nm) as well as the larger spectral range 275 – 340 nm for profile retrieval. The visible range of the Chappuis band 450 – 600 nm is used in DOAS and SAOZ (Système d'Analyse par Observation Zénithale) measurements from the ground [Hendrick et al., 2011]. The temperature dependence in the Huggins ozone band is particularly valuable to improve the determination of tropospheric ozone from profile retrieval [Chance et al., 1997]. Ozone temperature dependent absorption cross sections are also required in determination of other trace gases by differential technique after subtracting the ozone contribution [Burrows et al., 1995]. On the other hand, the ozone profiles derived from SCIAMACHY limb measurements use a mixture of information from the Hartley, Huggins, and Chappuis bands, good consistency among the bands is needed.

This section presents the final GOME-2 FM3 and SCIAMACHY FM ozone absorption cross section spectra and investigates the temperature dependence of the cross section spectra in the different bands by comparison to literature data.

### Hartley Band

Hartley band is the strong broad continuum extending from 200 to 310 nm and peaks at 255 nm. The smooth shape of the band is due to the fast photo-dissociation of ozone in the upper electronic band. Weak vibrational structures lay on top of the broad band.

In this study, the cross sections (Figs 5.1 and 5.2) show a weak temperature effect. A slight decrease in the cross section values in the 240 – 260 nm range is observed when temperature rises. Above 260 nm (inversion point) the cross sections increase. The temperature variations and the inversion point were observed to be in good agreement with other laboratory measurements.

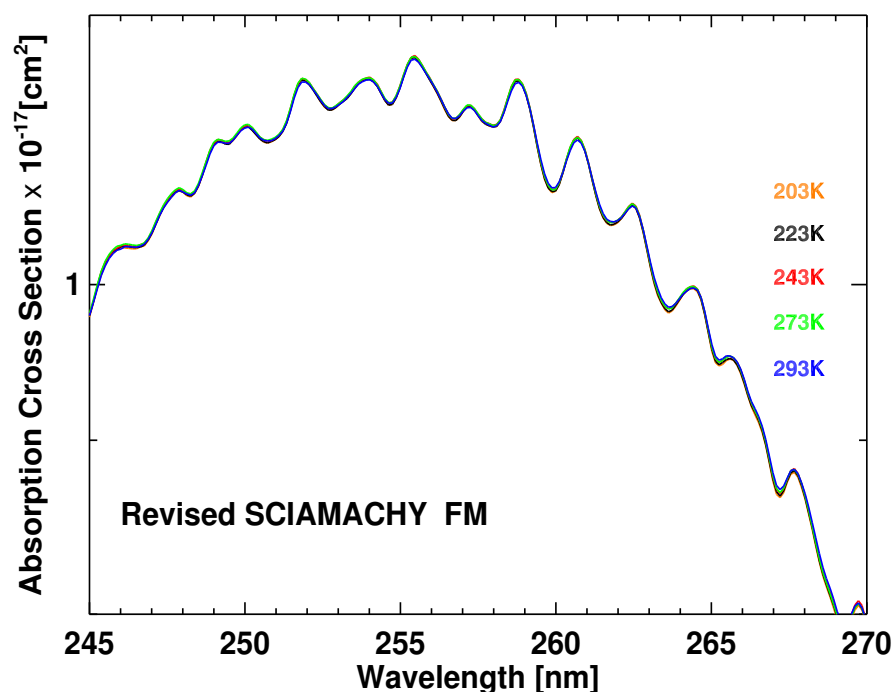


*Figure 5.1: Revised SCIAMACHY FM temperature dependent absorption cross section spectra in the Hartley band.*

At the the mercury line wavelength (253.65 nm), the GOME-2 cross sections decrease 1.5% for a temperature rise from 203 K to 293 K while SCIAMACHY's spectra show even weaker temperature dependence (0.1%). This variation in GOME-2 data is in good agreement with the value (1.6%) found by Burrows et al. [1999a] and comparable to the values of about 1% reported by Molina and Molina [1986], Bass Paur and BMD for

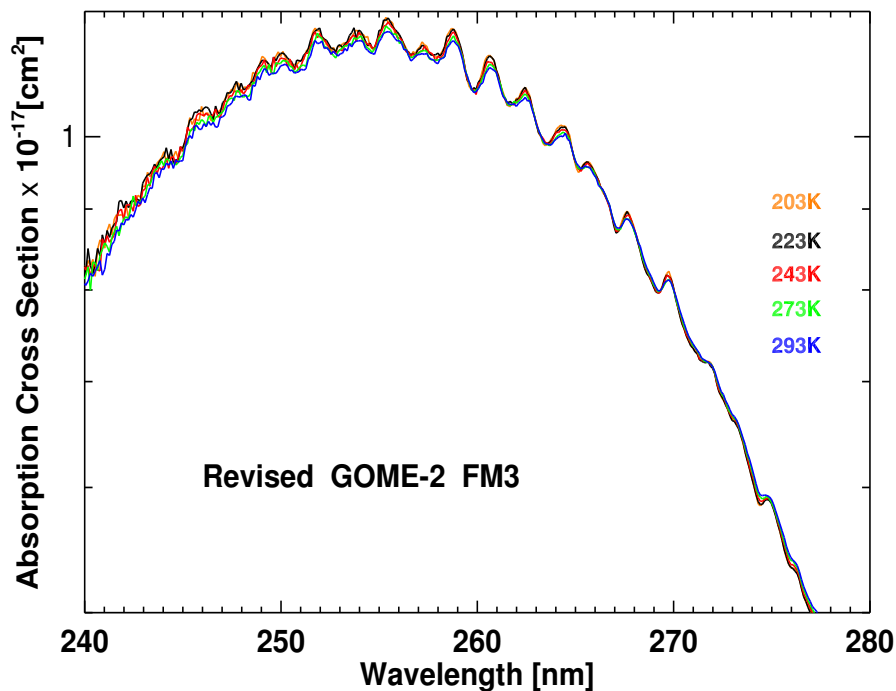


*Figure 5.2: Revised GOME-2 FM3 temperature dependent absorption cross section spectra in the Hartley band.*

temperature change from low temperatures (218 – 226 K) to room temperature.

### Huggins Band

The Huggins band (310 – 380 nm) is characterized by discrete absorption structures. The temperature effect is very strong and the cross section increases as the temperature increases. The ozone retrieval in the Huggins band from nadir viewing instruments like GOME-2 and SCIAMACHY requires accurate temperature dependence of the ozone cross sections.

Figures 5.3 and 5.4 show the total ozone retrieval window between 325 and 335 nm (DOAS window), where strong variations in the cross sections are observed specially in the region between the absorption peaks with a shift towards higher wavelengths as the temperature increase, in good agreement with previous measurements. The magnitude of the variations depends on the spectral resolution of the instrument. The temperature dependence in the Huggins band is explained by changes in the rotational and vibrational distributions in the electronic ground state.

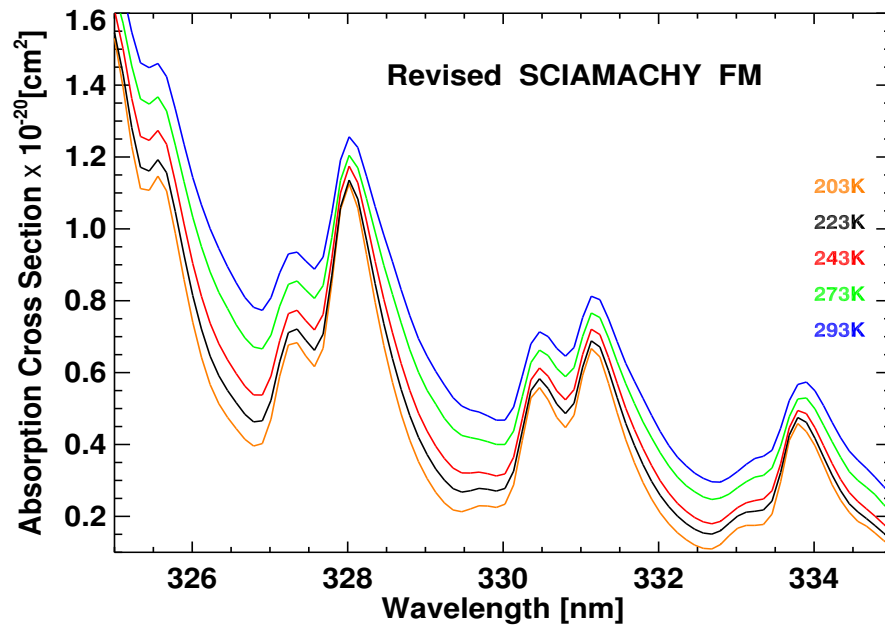


Figure 5.3: Revised SCIAMACHY FM temperature dependent absorption cross section spectra in the Huggins band.

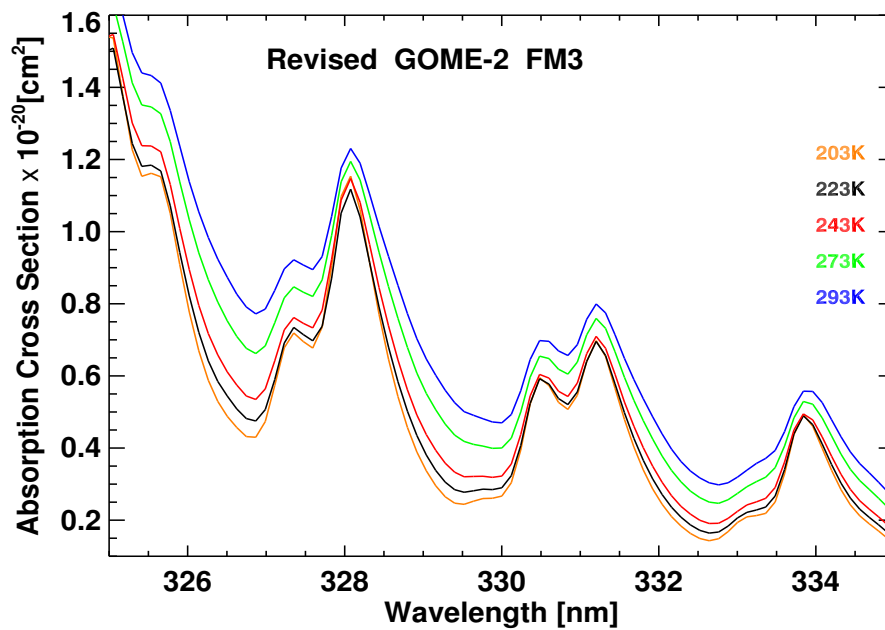
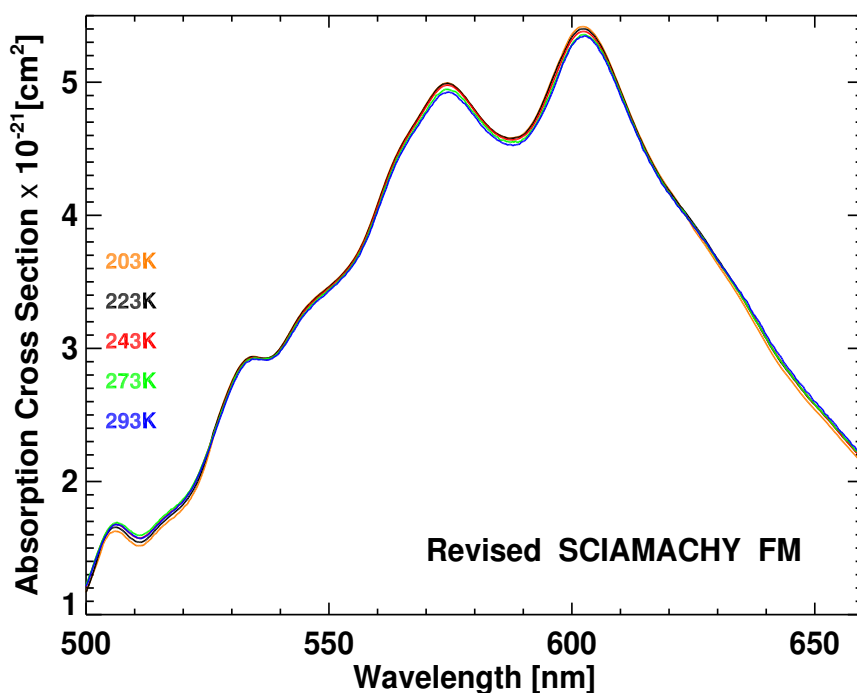


Figure 5.4: Revised GOME-2 FM3 temperature dependent absorption cross section spectra in the Huggins band.

### Chappuis band

The Chappuis band is a broad continuum extending from 380 to 680 nm with vibrational structures due to the interactions of two excited electronic states. The GOME-2 FM3 and SCIAMACHY FM data are generally in good agreement with literature data.

The cross sections (Figs. 5.7 and 5.6) increase with increasing temperature below 560 – 565 nm and above 610 – 620 nm (inversions points), between the inversion points the temperature effect is the opposite. At the maximum absorption peak (602.4 nm), an increase of 0.7% and 0.5% in the cross section values is observed when the temperature drops from 293 to 203 K in SCIAMACHY FM and GOME-2 FM3 data, respectively. This variation is in good agreement with values reported in Burkholder and Talukdar [1994] as well as Brion et al. [1998].



*Figure 5.5: Revised SCIAMACHY FM temperature dependent absorption cross section spectra in the Chappuis band.*

### Wulf band

The Wulf absorption band is beyond 700 nm in the near-infrared spectral region and consists of a continuum extended from the visible region

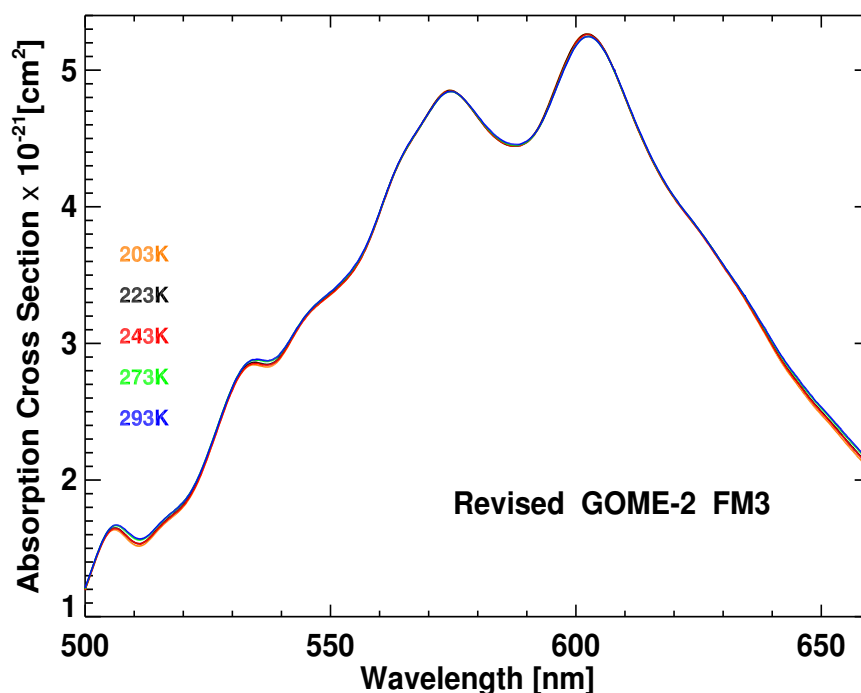


*Figure 5.6: Revised GOME-2 FM3 temperature dependent absorption cross section spectra in the Chappuis band.*

with a series of peaks superimposed on it. The band shows weak structured absorptions as the visible and near-IR contributions to ozone electronic spectrum are weak compared to the Hartley band (five orders of magnitude), but remain significant in the atmospheric window region, beyond 1050 nm ozone absorption decreases drastically. This region contains an absorption band of oxygen around 762 nm, which is visible since the measurements were conducted in an oxygen/ozone mixture.

A precise knowledge of the ozone absorption spectrum in this region is required for the ozone retrieval in limb and occultation experiments. Moreover, ozone is an interfering species and its pronounced structures should be taken into account with the atmospheric trace gas absorption structures and aerosol measurements. The oxygen A-band is used for cloud detection and determination of cloud properties [Kuze and Chance, 1994; Kurosu et al., 2001], while water vapour is retrieved in the 930 – 950 nm spectral window [Chu and McCormick, 1979; Chu et al., 1989].

In this region the absorption cross section decreases as the temperature drops due to the shift of the population distributions into the first rotational levels and just above the dissociation limit of the ground

state of the  $O_3$  molecules. The peaks of the absorption cross section increase as the temperature drops since the population concentrates to the first rotational levels around its ground state resulting in narrowing line shape of absorption. The temperature dependence of the Wulf band is in good agreement with the new high spectral resolution cross section data measured in our laboratory [Serdyuchenko et al., 2011, 2013; Gorshelev et al., 2013].

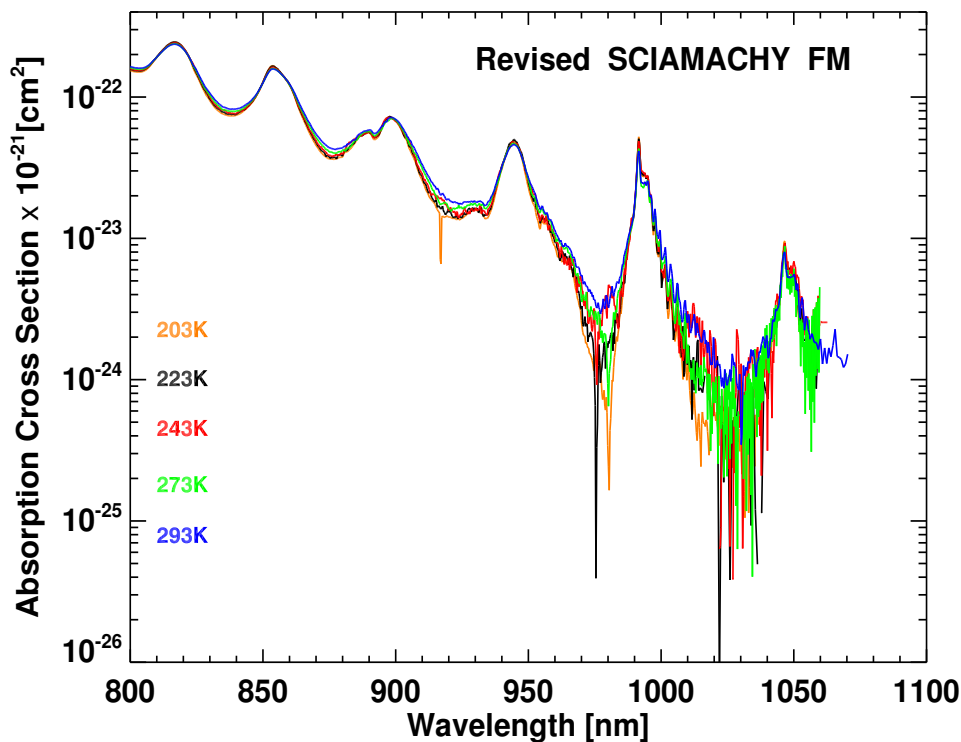


Figure 5.7: Revised SCIAMACHY FM temperature dependent absorption cross section spectra in the Wulf band.

## 5.2 Comparisons with Literature Data

To investigate the quality of the revised cross section data, they are compared with published literature data: BMD [Brion et al., 1993, 1998; Malicet et al., 1995; Daumont et al., 1992], Bass Paur (BP) [Bass and Paur, 1985; Paur and Bass, 1985], GOME FM [Burrows et al., 1999a] and Burkholder and Talukdar [Burkholder and Talukdar, 1994] data as well as SCIAMACHY FM version 3 data [Bogumil et al., 2003] and GOME-2 FM3 version 3

data [Gür et al., 2005; Gür, 2006]. The comparisons are performed at single wavelengths and over broad wavelength intervals highlighting the Hartley, Huggins and Chappuis bands where ozone is most commonly retrieved from nadir and limb viewing instruments and cross sections changes rapidly with temperature and wavelength. The comparisons follow the procedures performed in the ESA study by Orphal [2002] and also summarised in Orphal [2003].

### 5.2.1 Comparisons at Hg Lamp and He-Ne Laser Lines at Room Temperature

The revised GOME-2 FM3 and SCIAMACHY FM data were directly compared to available literature data of absolute absorption cross sections at room temperature and at ten single wavelengths. The selected wavelengths correspond to the Hg lamp and He-Ne laser lines and are located in the Hartley and Chappuis bands where the effects of temperature, wavelength calibration and spectral resolution are weak. The results are summarized in Table 5.1.

As shown in the table, the FM3 data at the selected wavelengths agree well with the high resolution absolute measurement data BMD and Bass-Paur as well as Burrows data. At the Hg line (253.65 nm), the mean value is  $1141 \times 10^{-20} \text{ cm}^2 \cdot \text{molecule}$  and the literature values agree with each other within 2.3%. The mean value is in excellent agreement with the revised GOME-2 FM3 value which is now 2.2% higher compared to the value reported in Gür et al. [2005] and Gür [2006]. The FM3 cross section values in the Chappuis band show high degree of consistency when compared to BMD and GOME FM. The agreement between FM3 and Burkholder and Talukdar [1994] data is slightly worse.

The cross section values of the revised SCIAMACHY FM data did not show any change in the Hartley band since the re-analysis did not include scaling the Delta2-PI-Period data since it was already corrected. The values of the revised SCIAMACHY FM cross-section data in the Chappuis band agree very well with the mean values as well as BMD.

**Table 5.1:** Comparison of revised SCIAMACHY FM and GOME-2 FM3 ozone cross sections with literature data at ten selected wavelengths at room temperature. The absorption cross sections are given in units of  $10^{-20} \text{ cm}^2$ , the second column indicates the mean from all available literature data at  $298 \pm 5 \text{ K}$  provided by the ESA study [Orphal, 2002].

$\lambda$ [nm]	Mean value	Bass Paur	BMD	Molina	Burk. Tal.	GOME FM	SCIAMACHY FM V3	Revised FM	GOME-2 FM3 V3	Revised FM3
253.65	$1141 \pm 0.9\%$	1145	1130.5	1157	–	1150	1145	<b>1145</b>	1117	<b>1141.1</b>
289.36	$149 \pm 2.0\%$	150	151	154	–	151	151	<b>151</b>	150	<b>152.9</b>
296.73	$60.3 \pm 1.6\%$	60.7	61.5	62.3	–	61	61.4	<b>61.4</b>	60	<b>61.4</b>
302.15	$29.2 \pm 1.8\%$	29.4	29.80	30.1	–	29.9	29.8	<b>29.8</b>	29.5	<b>29.8</b>
543.52	$0.0314 \pm 1.3\%$	–	0.0312	–	0.0308	0.0317	0.0315	<b>0.0321</b>	0.0311	<b>0.0313</b>
576.96	$0.0477 \pm 0.8\%$	–	0.0477	–	0.0469	0.0483	0.0484	<b>0.0488</b>	0.0478	<b>0.0479</b>
594.10	$0.0470 \pm 1.2\%$	–	0.0468	–	0.0464	0.0476	0.0473	<b>0.0476</b>	0.0468	<b>0.0470</b>
604.61	$0.0522 \pm 1.0\%$	–	0.0518	–	0.0509	0.0524	0.0526	<b>0.0529</b>	0.0518	<b>0.0520</b>
611.97	$0.0466 \pm 0.7\%$	–	0.0463	–	0.0453	0.0469	0.0469	<b>0.0473</b>	0.0468	<b>0.0464</b>
632.82	$0.0346 \pm 1.2\%$	–	0.0339	–	0.0335	0.0350	0.0349	<b>0.0352</b>	0.0342	<b>0.0343</b>

### 5.2.2 Integrated Cross Sections at Different Temperatures

The integrated absorption cross section is insensitive to differences in wavelength calibrations and spectral resolution and therefore can be used as a tool to evaluate the quality of the new data in the different bands. The integrated absorption cross sections over an electronic band unity depend on the number of molecules in the lower state and the transition probability [Burrows et al., 1999a]. Cross sections are integrated over the regions:

- Hartley and Huggins bands between 245 and 340 nm.
- Huggins band between 325 and 340 nm.
- Chappuis band between 410 and 690 nm.

and compared with literature data as presented in Tables 5.2, 5.3 and 5.4.

The proposed regions are defined hereby the spectral limits and quality of considered datasets rather than the real band boundaries. Moreover, bands are overlapped (e.g. the high-energy tail of the Huggins band continuously goes over into the Hartley band system). Separation of the Wulf-Chappuis and Huggins-Hartley bands probably can be achieved by subtracting a bell-shaped functions from the spectrum. However, correct computation of the shape function is a very challenging task whereas any numerical assumption affects the accuracy.

Because of the large dynamic range of the cross section, main contribution in integration is due to the strongest part of the spectrum. Therefore, the comparison of integrated cross sections reflects mainly uncertainty of the cross sections on the top of the bands. However, the method can be used for rough analysis of agreement between broadband data with different spectral resolutions.

The values of the revised GOME-2 FM3 and SCIAMACHY FM integrated cross-section data in the different bands agree very well with the mean values as well as BMD and Bass Paur. Integrated cross-sections in Hartley band agree within 1% or better for all considered datasets.

**Table 5.2:** Comparison of integrated cross sections in the Hartley and Huggins bands (245 – 340 nm) in units of  $10^{-16} \text{ cm}^2\text{nm}/\text{molecule}$ , the second column indicates the mean from all available literature [Orphal, 2002].

Temperature [K]	Mean value	Bass Paur	BMD	GOME FM	SCIAMACHY FM V3	Revised FM	GOME-2 FM3 V3	Revised FM3
203	3.53± 1.2%	3.52	–	3.56	3.56	<b>3.53</b>	3.52	<b>3.55</b>
223	3.53± 1.1%	3.53	3.50	3.56	3.56	<b>3.53</b>	3.52	<b>3.55</b>
243	3.54± 1.1%	3.54	3.50	3.58	3.56	<b>3.55</b>	3.52	<b>3.55</b>
273	3.55± 1.0%	3.54	–	3.58	3.56	<b>3.55</b>	3.52	<b>3.55</b>
293	3.55± 0.6%	3.55	3.52	3.57	3.55	<b>3.56</b>	3.52	<b>3.55</b>

**Table 5.3:** Comparison of integrated cross sections in the Huggins band (325 – 340 nm) in units of  $10^{-20} \text{ cm}^2\text{nm}/\text{molecule}$ , the second column indicates the mean from all available literature [Orphal, 2002].

Temperature [K]	Mean value	Bass Paur	BMD	GOME FM	SCIAMACHY FM V3	Revised FM	GOME-2 FM3 V3	Revised FM3
203	5.64± 1.6%	5.44	–	5.93	5.44	<b>5.19</b>	5.70	<b>5.72</b>
223	5.89± 3.3%	5.70	5.65	6.16	5.96	<b>5.69</b>	5.77	<b>5.95</b>
243	6.30± 1.8%	6.21	6.23	6.41	6.46	<b>6.28</b>	6.29	<b>6.39</b>
273	7.42± 2.9%	7.27	7.16	7.73	7.51	<b>7.23</b>	7.19	<b>7.36</b>
293	8.30± 0.7%	8.20	8.32	8.36	8.33	<b>8.13</b>	8.20	<b>8.18</b>

**Table 5.4:** Comparison of integrated cross sections in the Chappuis band (410 – 690 nm) in units of  $10^{-19} \text{ cm}^2\text{nm}/\text{molecule}$ , the second column indicates the mean from all available literature [Orphal, 2002].

Temperature [K]	Mean value	BMD	GOME FM	Burk. and Taluk.	SCIAMACHY FM V3	Revised FM	GOME-2 FM3 V3	Revised FM3
203	6.48± 1.6%	–	6.62	–	6.42	<b>6.40</b>	6.64	<b>6.28</b>
223	6.354± 2.4%	–	6.55	6.15	6.33	<b>6.43</b>	6.33	<b>6.30</b>
243	6.35± 1.7%	–	6.44	6.17	6.36	<b>6.44</b>	6.54	<b>6.29</b>
273	6.44± 2.3%	–	6.58	6.20	6.43	<b>6.45</b>	6.55	<b>6.33</b>
293	6.38± 1.6%	–	6.45	6.21	6.41	<b>6.48</b>	6.36	<b>6.34</b>

In the Huggins band, the agreement between datasets is within 3%, the revised data deviate from the mean values by about 1 – 3% but within the reported standard deviations. The revised SCIAMACHY integrated Huggins band are smaller than the values presented in Bogumil et al. [2003] version 3 data as the new concatenation produced bigger absorption structures (deeper minimas) as seen in Fig. 4.12. On the other hand, integrated revised GOME-2 FM3 are bigger than the values determined from Gür et al. [2005] and Gür [2006] version 3 data due to the modified concatenation that resulted in larger OD spectra in the Huggins band as displayed in Fig. 4.14. In the Chappuis band, the datasets agree within 3%.

The results show a clear systematic temperature dependency in the Huggins band and none in the other bands.

### 5.2.3 Temperature Parametrizations and Smoothness Comparisons

The quadratic temperature parametrization of the cross section data approximates the cross-section at any temperatures as follows:

$$\sigma(\lambda, T) = a_o(\lambda)[1 + a_1(\lambda) \cdot T + a_2(\lambda) \cdot T^2] \quad (5.1)$$

This parametrization empirically describes the dependence of the cross sections on the temperature as a second order polynomial and this can be used to interpolate between temperatures. The parametrization, also termed as Bass-Paur, is used in the radiation transfer model as part of the total ozone retrieval (see Section 5.4).

Figures 5.8 and 5.9 show the fitted quadratic temperature coefficients ( $a_1(\lambda)$  and  $a_2(\lambda)$ ) of the revised data together with that of other literature data smoothed to each spectrometer's spectral resolution. The comparison between the temperature coefficients of the different data is a good tool to examine the difference between them.

The first quadratic temperature coefficients ( $a_1(\lambda)$ ) of the different data are presented in the upper panel. For GOME-2, the coefficient displayed in black, agree very well Bass Paur and GOME FM data especially in the DOAS retrieval window indicated by the shaded area, BMD coefficient values are slightly higher. Larger differences are observed for Gür et al. [2005] and Gür [2006] version 3 data. The coefficient of revised SCIAMACHY agrees with the other data better than version 3 data.

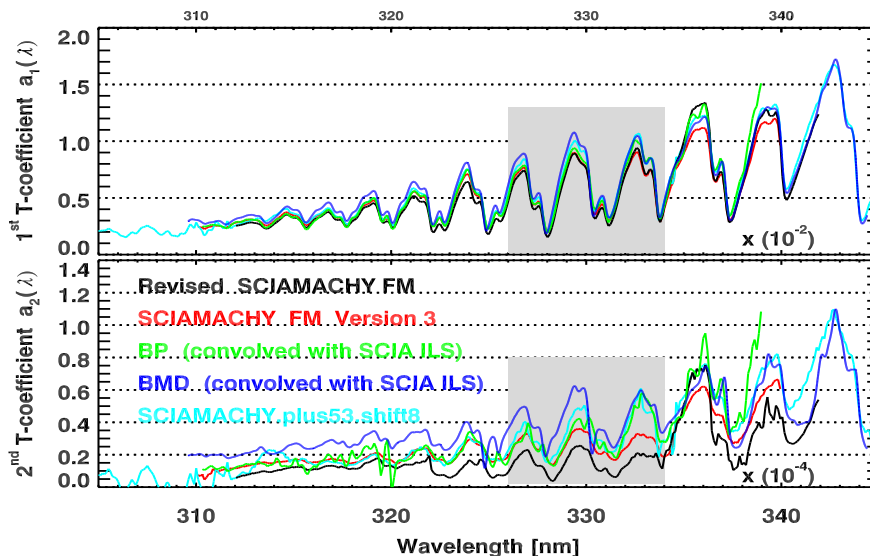


*Figure 5.8: Quadratic temperature coefficients in Eq. 5.1 of revised SCIAMACHY FM (black), version 3 (red) and literature data (BP in green and BMD in blue) convolved to the spectrometer slit function, Scia.plus53.shift8 is Bogumil et al. [2003] data with a differential scaling of +5.3% and shift of 0.08 nm used in the current standard retrieval. Upper panel  $a_1(\lambda)$ , lower panel  $a_2(\lambda)$ . The grey shaded area is the classical DOAS window.*

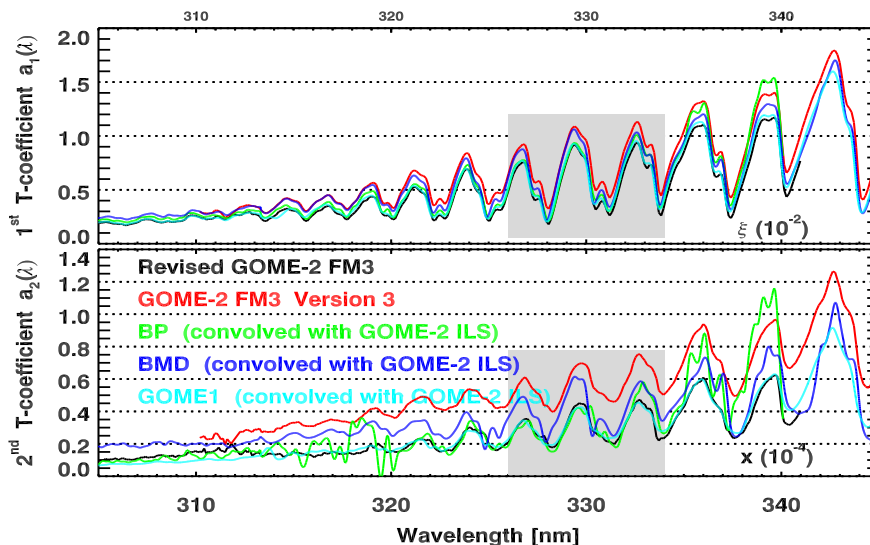


*Figure 5.9: Quadratic temperature coefficients for GOME-2 FM3 ozone absorption spectra and literature data analogous to Fig. 5.8, GOME FM convolved with GOME-2 slit function is used in the current standard retrieval.*

The second temperature coefficients ( $a_2(\lambda)$ ) generally do not match well except the excellent agreement between GOME-2 and GOME FM as well Bass Paur.

The smoothness of the temperature behaviour of the absorption cross sections is another mean to study the quality of the data, the revised data are tested regarding the deviations from the quadratic parametrization (Eq. 5.1). Figures 5.10 and 5.11 show the temperature dependence of the revised SCIAMACHY and GOME-2 (in solid and dotted lines) in comparison with the measured absorption (solid and unfilled circles) cross sections at an absorption maximum (328 nm) and minimum (330 nm) in the DOAS retrieval window. The revised data (in black) are closer to the literature data. The amplitudes of the absorption structures of SCIAMACHY data are now bigger for temperatures 203 K, 223 K, 243 K and 273 K, while GOME-2 data at both maxima and minima are scaled up. This has a direct influence on the total ozone retrieval.

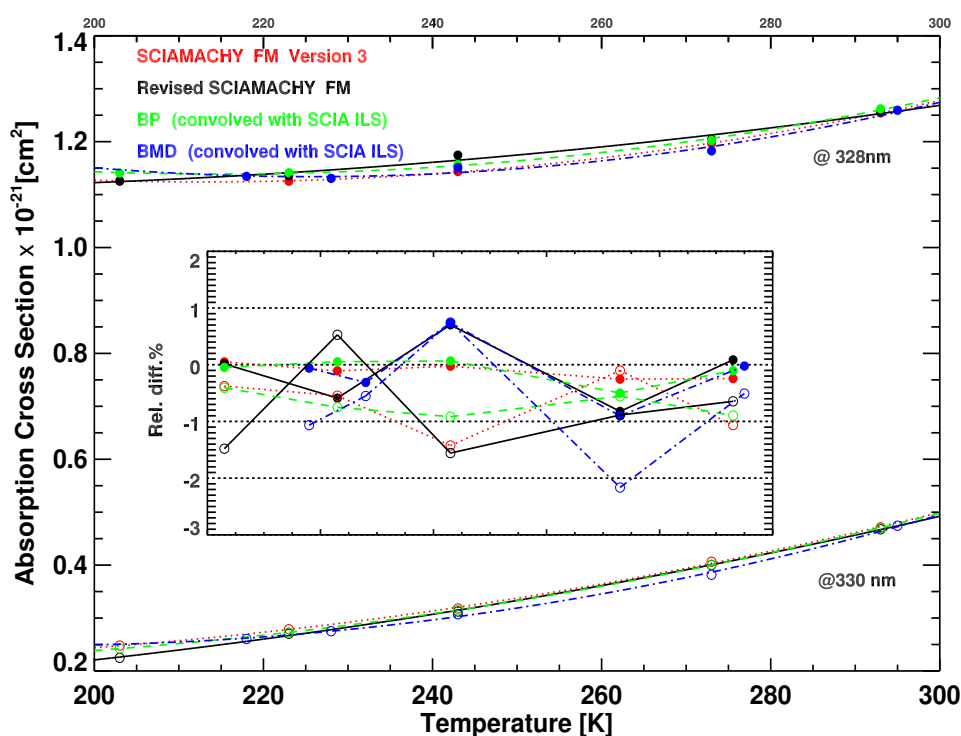


**Figure 5.10:** Measured and modelled (according to Eq. 5.1) absorption cross sections for SCIAMACHY FM ozone absorption spectra (revised in black and the latest version available in red) and literature data (BP in green and BMD in blue) convolved to the spectrometer slit function (lines) at 328 and 330 nm in the upper sub-panels. The relative differences between both measured and modelled cross sections are shown in the inset.

The differences between the measured and modelled cross sections

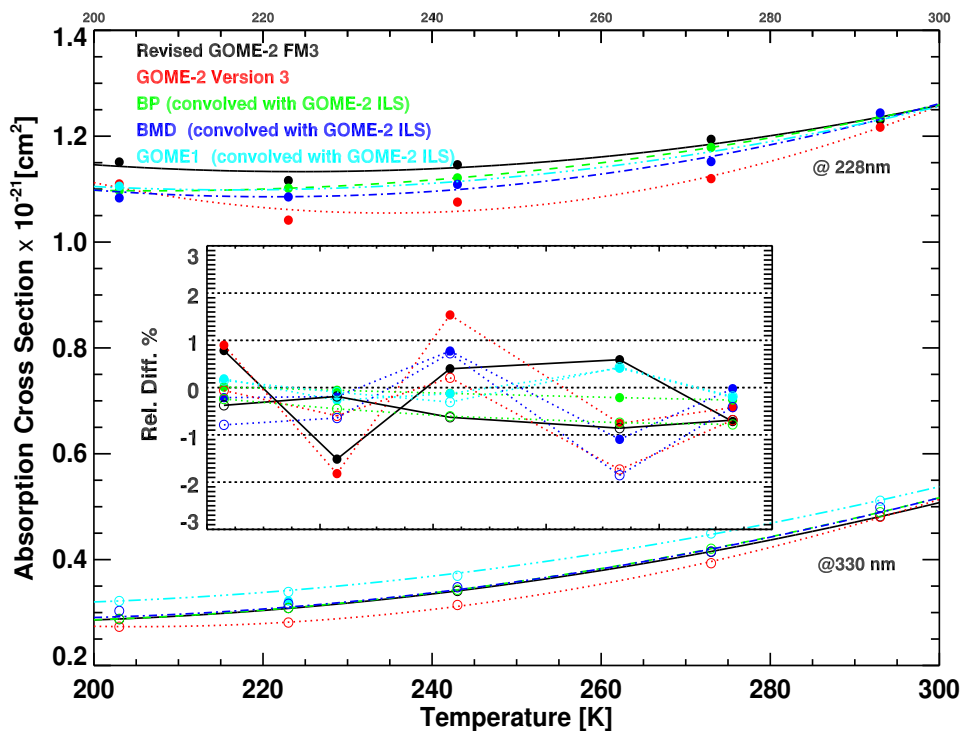


Figure 5.11: Measured and modelled ozone absorption spectra for GOME-2 analogous to Fig. 5.10.

are displayed in the insets, typical values are within 2%, the deviations from the Bass-Paur temperature dependence of the revised SCIAMACHY data is similar to Bogumil et al. [2003] data while for GOME-2, the deviations get smaller.

### 5.3 Comparisons in DOAS Retrieval Window

The absolute accuracy of the ozone cross section and wavelength calibration are crucial in improving the quality of the retrieved ozone amounts and reducing the ozone fit residuals<sup>2</sup>. A more quantitative and direct comparison between the revised FM data and the high spectral resolution data (BMD and Bass Paur) cannot be performed in the Huggins band, due the strong sensitivity of the Huggins band to differences in spectral resolution and wavelength calibration of the data. To minimize the

<sup>2</sup>Ozone fit residuals are the root mean square of the difference between the measured and modelled nadir radiance used in the ozone retrieval algorithm.

effects of differences in wavelength calibrations, baseline drifts and spectral resolutions, a non-linear least square fit is applied to match the high resolution cross sections, like Bass Paur and BMD, to SCIAMACHY and GOME-2 data. From this DOAS type fit a (differential) scaling factor and wavelength shift can be determined that can be directly translated into expected changes in retrieved total ozone. The fitting program is well explained in Weber et al. [2011] and retrieves six parameters:

- a scaling factor to adjust the amplitude of the differential absorption structures of the cross sections (one parameter:  $c_0$ ).
- a wavelength shift to correct for differences in the wavelength calibrations (one parameter:  $c_1$ ).
- a cubic polynomial to account for baseline drifts (four parameters :  $c_2$  to  $c_5$ , differential fit).

For this fitting, a Marquardt-Levenberg non-linear least squares estimation is applied to match the reference spectra  $f_{ref}(\lambda)$  to the lower spectral resolution cross section spectrum  $f(\lambda)$  as follows:

$$f(\lambda) = c_0 \cdot f_{ref}(\lambda - c_1) + \sum_{i=0}^3 c_{2+i} \cdot \lambda^i \quad (5.2)$$

where  $\lambda$  is the wavelength and  $c_i$  are fitting coefficients.

Before comparing, the literature data were smoothed to each spectrometer spectral resolution by convolving them with the wavelength dependent slit function. The comparisons were made in the DOAS retrieval window (326.6 – 334.5 nm) at 225 and 240 K. The cross sections at the selected temperatures are calculated using the Bass-Paur temperature parametrization (Eq. 5.1).

SCIAMACHY revised data is compared to BMD, Bass Paur and SCIAMACHY FM version 3 data [Bogumil et al., 2003]. For GOME-2, the data compared are BMD, Bass Paur, GOME FM and FM3 version 3 data [Gür et al., 2005; Gür, 2006]. GOME FM is first deconvolved with GOME slit function and the de-convolved spectra are convolved with the GOME-2 slit function. Sample fits are shown in Figs. 5.12, 5.13, 5.14 and 5.15, the top graph shows the revised FM and the reference data to be compared, in the bottom graph the fitted revised FM data (scaled and shifted) is plotted with the reference spectra together with the residuals between them and the retrieved baseline polynomial. The results are summarized

in Tables 5.5 and 5.6.

In order to match the literature data, the calculated wavelength shifts and scaling factors, both defined with respect to the reference data, should be applied to the revised FM cross sections. There is a high degree of consistency between the high spectral resolution data and the revised SCIAMACHY FM data, the differential scaling factors are below 0.5%, The differential scaling factors between the Bogumil et al. [2003] data and the revised data are 3 to 4%. Changing the absorption cross section by a differential scaling factor of +1% results in a 1% decrease in the total retrieved column. The scaling factors (ratios) determined here are consistent with the differences in the retrieved total ozone amounts reported in Eskes et al. [2005].

The wavelength shifts and scaling coefficients listed in Table 5.6 are such that they need to be applied to the GOME FM3 cross sections in order to match the other data. The scaling factors for GOME-2 FM3 are better than 3%. To match Burrows et al. [1999a] data, the FM3 data should be scaled by about +1%, while a 2 – 3% scaling factor (depending on temperature) is required to match BMD and Bass Paur data. On the other hand, the comparison of revised FM3 data with the version 3 data shows an increase in the scaling of 7 to 8% comparison, the increase obtained for the revised GOME-2 FM3 is consistent to the values presented in Fig. 4.14 and consistent with the overestimation in the retrieved total ozone column [Weber et al., 2011].

**Table 5.5:** Direct comparison of SCIAMACHY FM revised data to literature data using a non-linear least square fitting program in the DOAS fitting window (325 - 335). The scaling factor and wavelength shifts indicated in bold are the one that should be applied to the revised SCIAMACHY data in order to match the reference data.

	Bass Paur		BMD		SCIAMACHY FM V3	
	shift	<b>ratio</b>	shift	<b>ratio</b>	shift	<b>ratio</b>
225K	-0.014	<b>1.00</b>	0.009	<b>1.00</b>	–	<b>1.033</b>
240K	-0.012	<b>1.002</b>	0.008	<b>1.005</b>	–	<b>1.035</b>

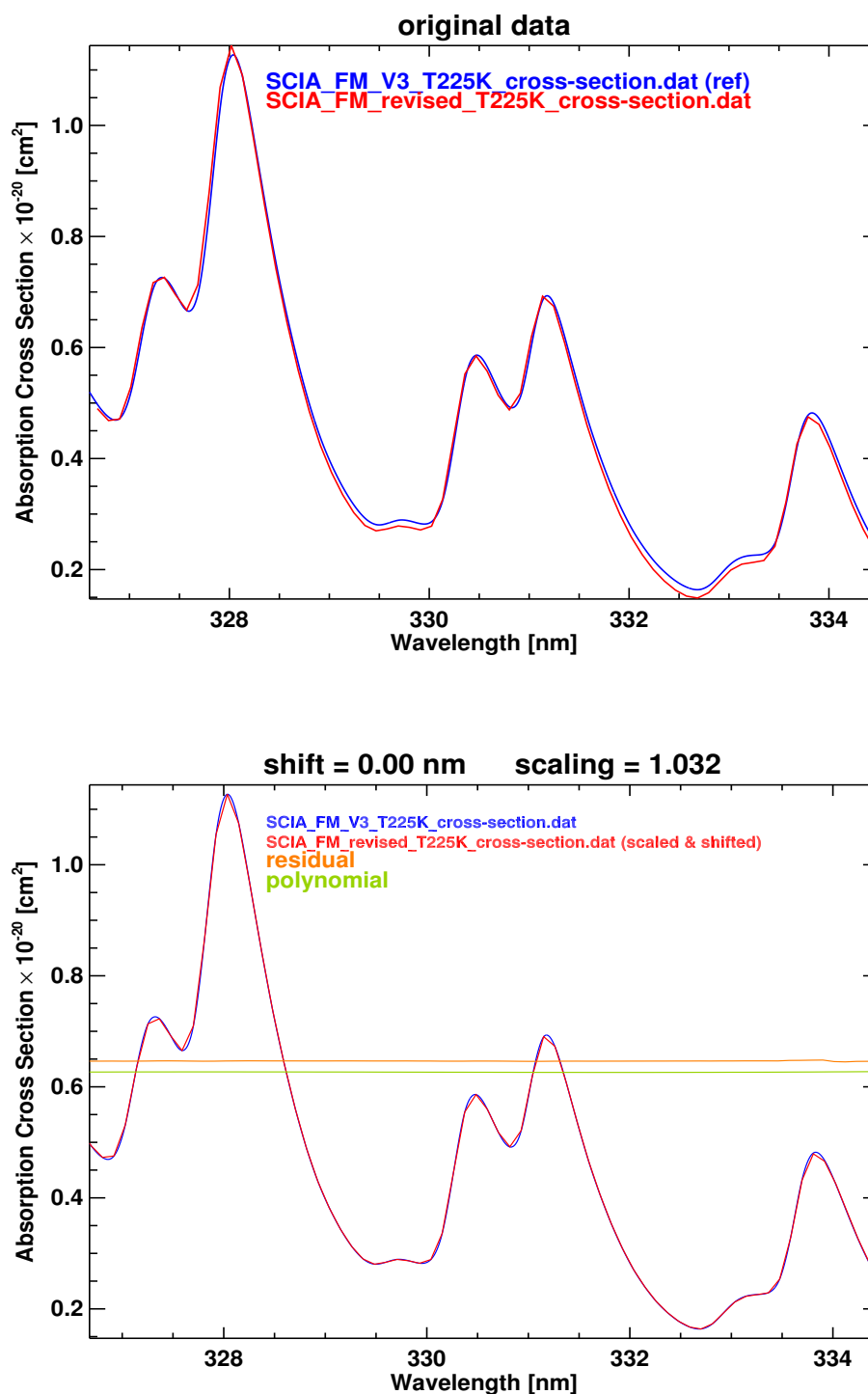


*Figure 5.12: Non-linear square fit comparison for SCIAMACHY revised FM data with Bogumil et al. [2003] version 3 data in the DOAS fitting window (326.6 – 334.5 nm). Top: SCIAMACHY FM revised data in red with Bogumil et al. [2003] version 3 data in blue (reference) at 225 K. Bottom: The fitted revised SCIAMACHY FM data (scaled and shifted) and Bogumil et al. [2003] data together with the residuals (orange) and the retrieved baseline polynomial (green) both shifted vertically for clarity.*

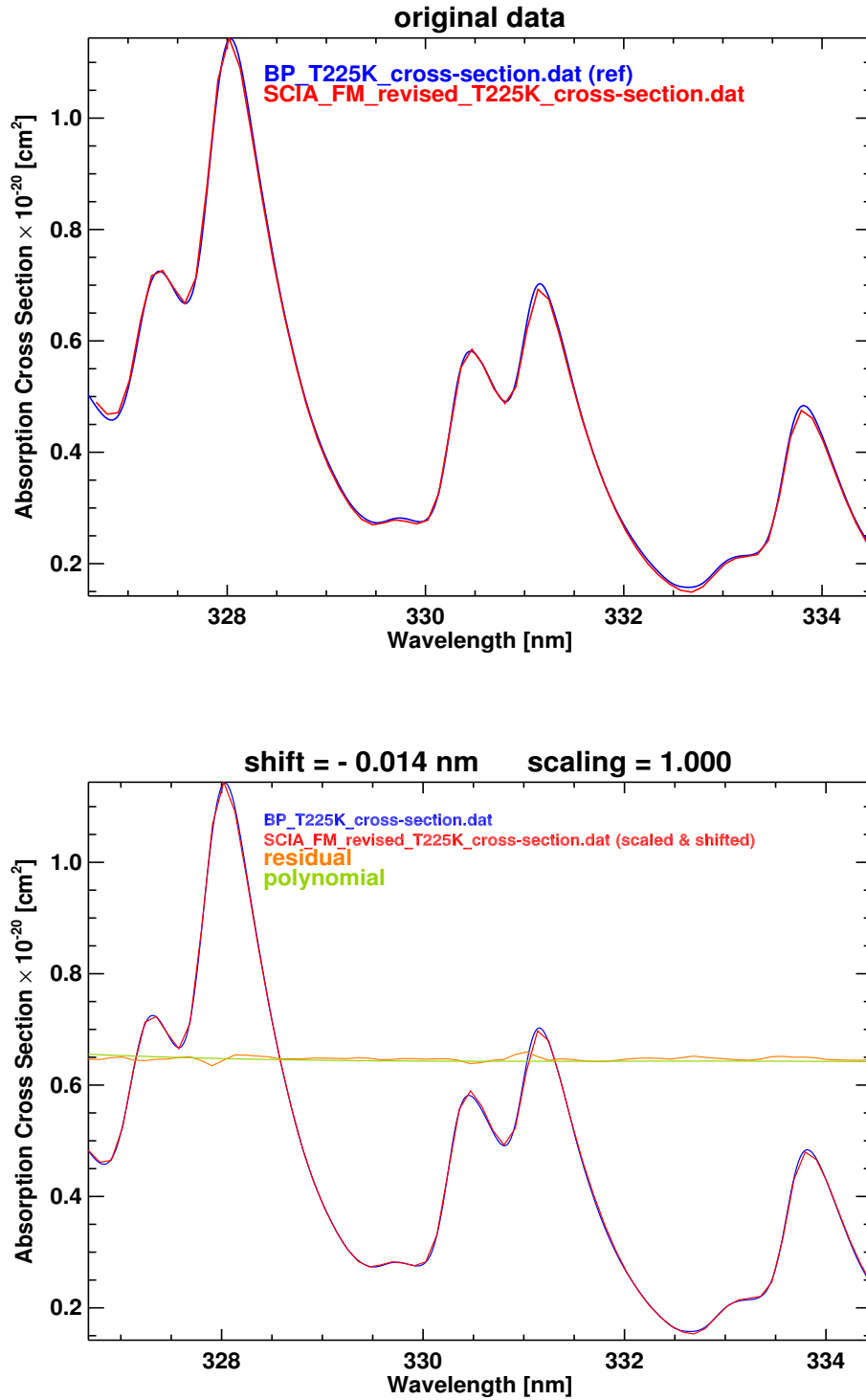
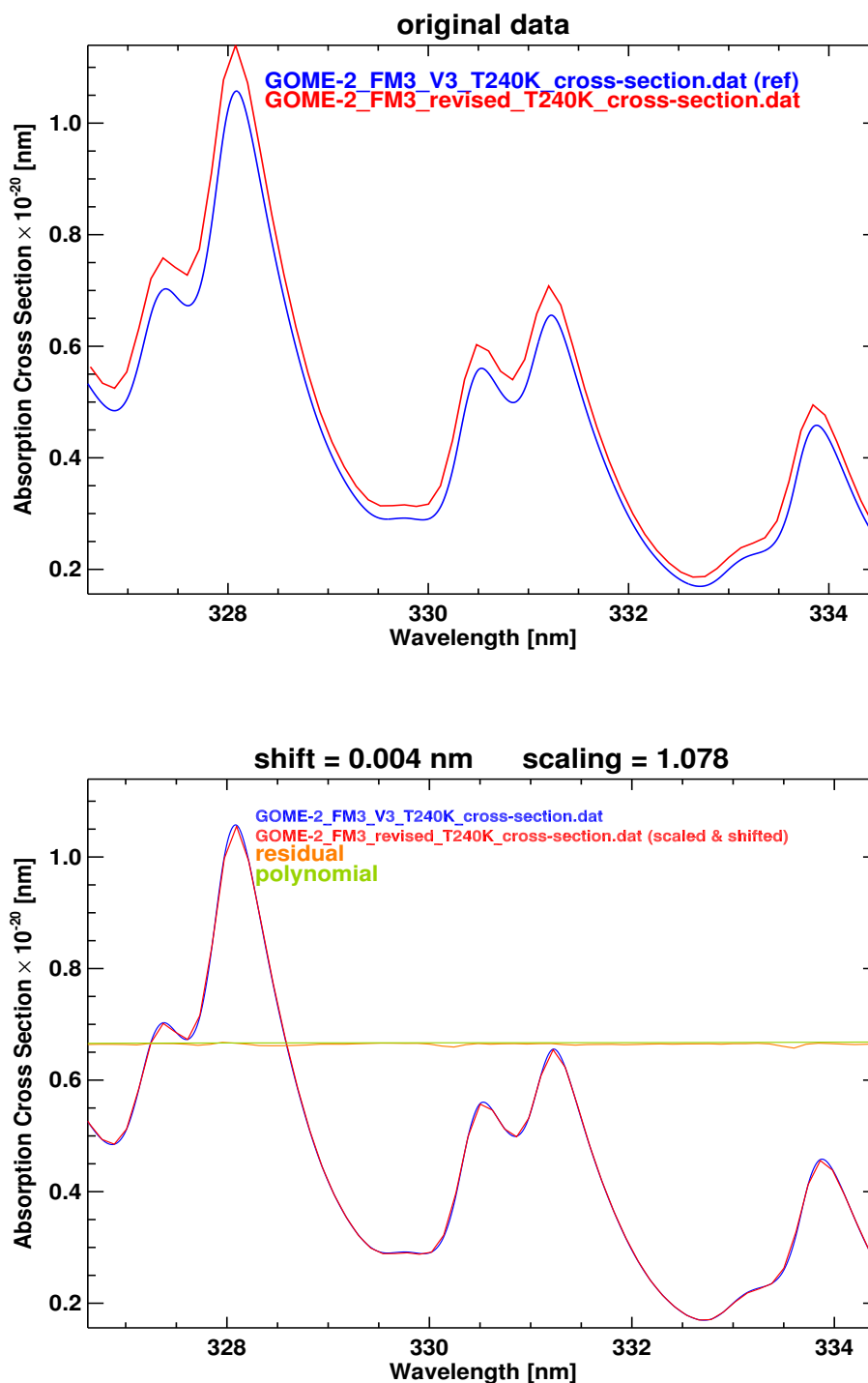


Figure 5.13: Non-linear square fit comparison for SCIAMACHY revised FM data with BP data in the DOAS fitting window (326.6 – 334.5 nm) at 225 K analogous to Figs. 5.12.



**Figure 5.14:** Non-linear square fit comparison for for GOME-2 revised data with GOME-2 FM3 version 3 data in the DOAS fitting window (326.6 – 334.5 nm) at 240 K. Top: GOME-2 FM3 revised data in red with Gür et al. [2005] and Gür [2006] version 3 data in blue (reference) at 240 K. Bottom: The fitted revised GOME-2 FM3 data (scaled and shifted) and Gür et al. [2005] and Gür [2006] version 3 data together with the residuals (orange) and the retrieved baseline polynomial (green) both shifted vertically for clarity.

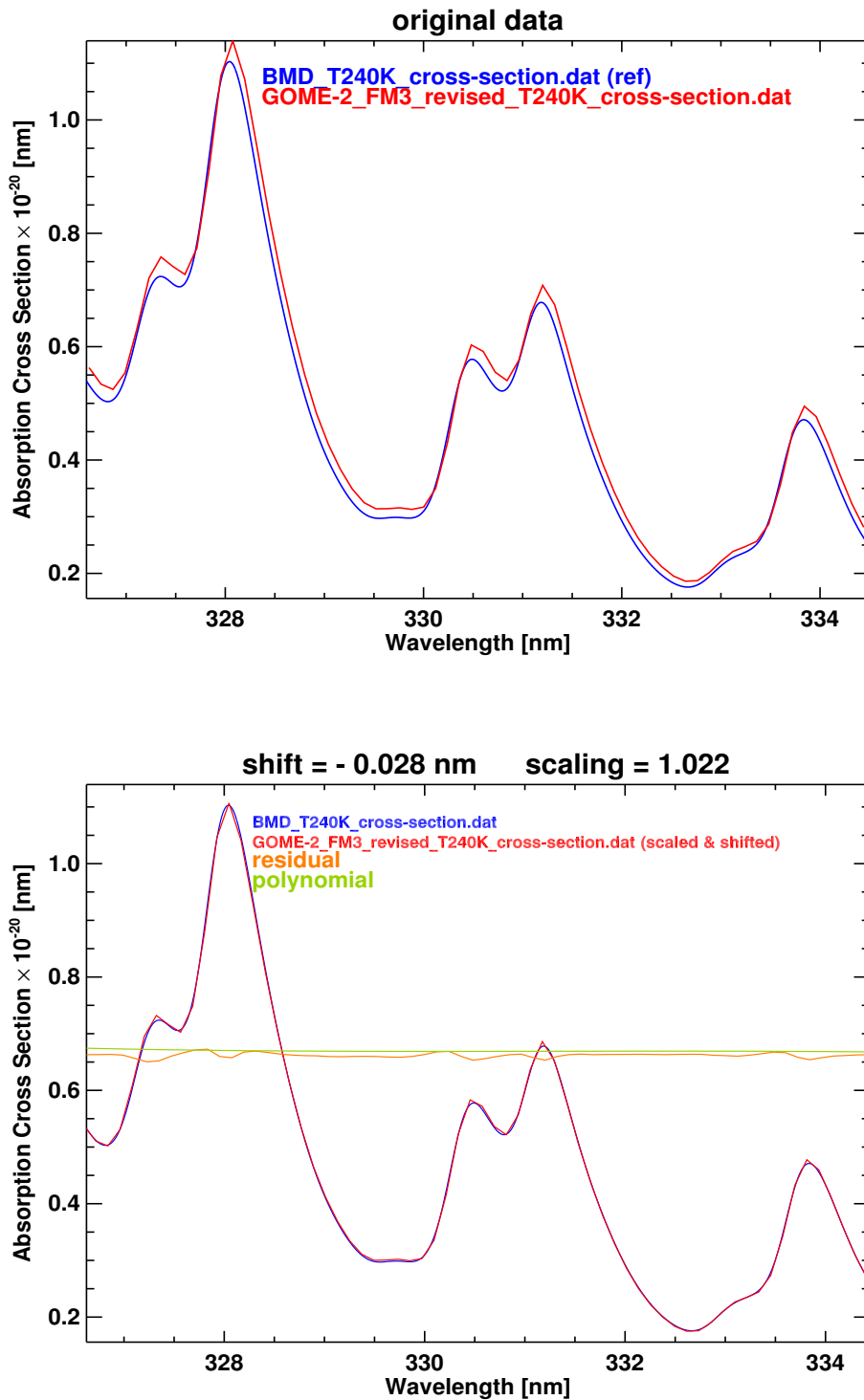


Figure 5.15: Non-linear square fit comparison for for GOME-2 revised data with BMD data in the DOAS fitting window (326.6 – 334.5 nm) at 240 K analogous to Fig. 5.14.

**Table 5.6:** Direct comparison of GOME-2 FM3 revised data to literature data using a non-linear least square fitting program in the DOAS fitting window (325 - 335). The scaling factor and wavelength shifts indicated in bold are the one that should be applied to the revised GOME-2 data in order to match the reference data.

	Bass Paur		BMD		GOME FM		GOME-2 FM3 V3	
	shift	ratio	shift	ratio	shift	ratio		
225K	–	<b>1.026</b>	-0.028	<b>1.025</b>	-0.044	<b>1.00</b>	–	<b>1.069</b>
240K	0.003	<b>1.020</b>	-0.028	<b>1.022</b>	-0.045	<b>1.00</b>	0.004	<b>1.078</b>

## 5.4 Retrieval Tests Using the Revised Ozone Cross Section Data

The total ozone retrieval is carried out using the Weighting Function Differential Optical Absorption Spectroscopy (WFDOS) algorithm in the 326.6 – 334.5 nm spectral window. The WFDOS algorithm uses a wavelength dependent weighting function of ozone and temperature that describes the relative radiance change due to a vertical profile change, the measured atmospheric optical depth is approximated around a reference intensity employing a Taylor series expansion (with weighting functions as derivatives) plus a cubic polynomial.

$$\begin{aligned}
 \ln I_i^{mea}(V^t, b^t) &= \ln I_i^{mod}(\bar{V}, \bar{b}) \\
 &+ \frac{\partial I_i^{mod}}{\partial V} \Big|_{\bar{V}} \otimes (\hat{V}, \bar{V}) \\
 &+ \frac{\partial I_i^{mod}}{\partial T} \Big|_{\bar{T}} \otimes (\hat{T}, \bar{T}) \\
 &+ SCD_{NO_2} \cdot \sigma_{i,NO_2} \\
 &+ SCD_{BrO} \cdot \sigma_{i,BrO} \\
 &+ SCD_{Ring} \cdot \sigma_{i, Ring} \\
 &+ SCD_{unsamp} \cdot \sigma_{i, unsamp} \\
 &+ P_i
 \end{aligned} \tag{5.3}$$

The weighting function for the ozone column change is obtained by integrating vertically the altitude dependent weighting function. A large set of reference spectra constructed for different atmospheric conditions. The total column information is obtained from differential trace gas structures.

The cubic polynomial is added to the algorithm to account for all broadband contributions from surface albedo and aerosols. Similar to the DOAS approach, additional parameters as Ring effect, under sampling correction (treated as effective absorbers) and temperature shifts are used as fit parameters. The minor absorbers present in the same wavelength window as  $\text{NO}_2$  and  $\text{BrO}$  to which the slant column filling is applied. A linear least squares minimization is used for deriving all of the above mentioned fitting parameters. The radiance spectra and weighting functions were computed using the multiple scattering SCIATRAN radiative transfer model. Ozone and temperature profiles are taken from TOMS (Total Ozone Mapping Spectrometer) V7 climatology. The ghost vertical column that is hidden below the (partial) cloud is determined from an ozone climatology and then added to the retrieved column to obtain the final total ozone amount.

Bass-Paur parametrization (Eq. 5.1) is used to interpolate between different temperatures. This parametrization is used in the radiation transfer code together with temperature climatology to express the change of ozone absorption with altitude.

The WFDOAS algorithm as presented by Coldewey-Egbers et al. [2005], was successfully applied and validated for GOME ozone retrieval [Weber et al., 2005]. The precision of the total ozone retrieval is better than 3% for solar zenith angles below  $80^\circ$ . Weber et al. [2005] presented an elaborate global validation study of GOME WFDOAS with ground based data from the WOUDC (World Ozone and UV Radiation Data Centre), an agreement within 1% was observed, at high latitudes and high solar zenith angles the differences can reach few percents.

The algorithm was also used in SCIAMACHY data processing to retrieve total ozone columns [Bracher et al., 2005] and a relative differences to within 1% between SCIAMACHY WFDOAS and collocated GOME WFDOAS data was obtained at low and mid latitudes. Convolved GOME FM absorption cross section data [Burrows et al., 1999a] were used in GOME retrieval. SCIAMACHY FM ozone cross sections [Bogumil et al., 2003] differentially scaled by 5.3% and shifted by 0.008 nm, is the cross

section data used currently in the standard SCIAMACHY WFDOAS retrieval [Weber et al., 2007]. The total ozone amounts are within 0.5% to that retrieved using GOME FM data [Weber et al., 2011].

The WFDOAS algorithm was also successfully tested in GOME-2 data processing [Weber et al., 2007]. GOME FM, convolved with the wavelength dependent GOME-2 slit function, is the reference data used currently in the GOME-2 retrieval, which shows a bias of about -1% with respect to GOME, while using BMD and Bass Paur data lead to an over-estimation of about 2 – 3% compared to the current amounts [Weber et al., 2011].

For a detailed investigation of the revised FM cross section data, the optimum wavelength shift applied to the cross section data in the ozone retrieval has to be found. The optimum shift minimises the ozone fit residuals (RMS) as shown in Fig. 5.16 as the fit residuals in ozone retrieval are determined with the application of various systematic wavelength shifts for a given SCIAMACHY and GOME-2 ground pixel. Ozone fit residuals are the root mean square of the difference between the measured and modelled nadir radiance used in the WFDOAS algorithm. Minimum RMS are found at shifts of -0.038 nm and +0.018 nm indicated in solid circles in the blue and red curves of GOME-2 and SCIAMACHY, respectively. These values are consistent with the values determined in previous tests using version 3 datasets [Weber et al., 2005, 2007, 2011]. It should be noted here that the total ozone columns decrease by 2% with a 0.01 nm shift in the absorption cross sections.

The top panels of Fig. 5.17 show the total ozone columns (TOZ) retrieved using the revised cross sections (displayed in blue) with the optimum wavelength shift applied for selected arbitrary SCIAMACHY orbits in September 24, 2008 (orbit 34339) and March 20, 2009 (orbit 36873), together with columns retrieved using the SCIAMACHY FM version 3 data (red) and the columns currently retrieved (black). The total ozone values retrieved are roughly 1% higher compared to the total ozone currently retrieved as seen in the sub-panels. The relative difference is calculated as the difference between both ozone columns divided by the amounts currently retrieved (in percent). The re-analysis of the FM data corrected total ozone amounts by 3 – 4%, which is in agreement with results obtained from the direct comparisons (Section 5.3). The higher differences obtained at higher latitudes could be due to differences in the temperature dependence between the cross section data. The fit residuals in 10° latitude bin for the same orbits, remain unchanged using Bogumil et al.

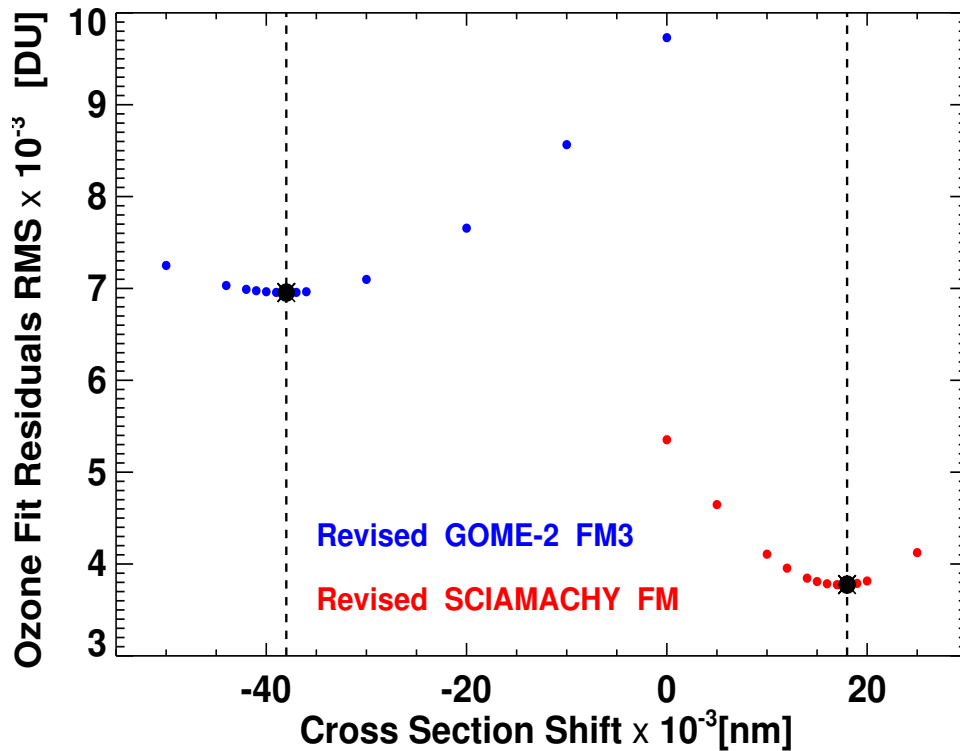


*Figure 5.16: Spectral fit residuals RMS for GOME-2 (blue) and SCIAMACHY (red) as a function of the applied wavelength shifts to the FM data. Minimum RMS are found at shifts of  $-0.038$  nm and  $+0.018$  nm indicated in solid circles for GOME-2 and SCIAMACHY, respectively.*

[2003] and the revised cross section data as shown in Fig. 5.19.

Similarly, the total ozone column is retrieved for two selected GOME-2 orbit using different cross section data. The top panels of Fig. 5.18 display ozone columns retrieved on April 15 (orbit 018090) and September 24 2010 (orbit 020392) using the revised GOME-2 FM3 data shifted by  $-0.038$  nm (blue), GOME-2 version 3 data (red) and GOME FM data (blue), the latter with the proper spectral resolution adjustments. The sub-panels show the relative difference between them. The total ozone values retrieved using the GOME-2 FM3 cross sections are roughly 0.5% higher compared to the total ozone currently retrieved, at higher latitudes the differences reach +1.5%, this could be probably due to differences in the temperature dependence between GOME FM and GOME-2 FM3 data. Figure 5.20 demonstrates that the fit residuals (RMS) are about the same.

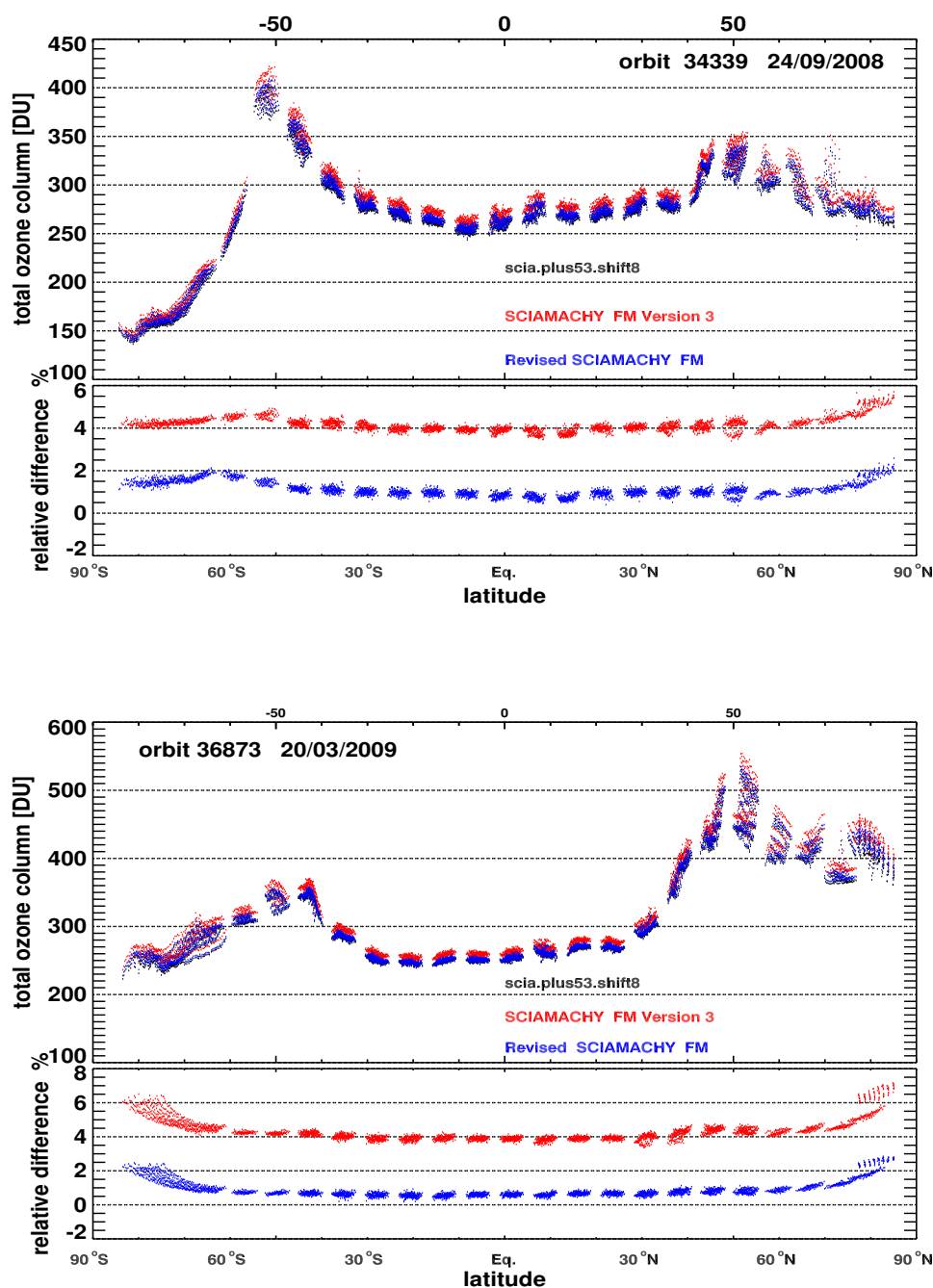


*Figure 5.17: SCIAMACHY total ozone columns with different cross sections. The upper subpanels display SCIAMACHY's total ozone column retrieved using different cross section data for orbits 34339 (24/09/2008) and 36873 (20/03/2009). Scia.plus53.shift8 (black) is the SCIAMACHY FM data [Bogumil et al., 2003] with a differential scaling of +5.3% and shift of 0.08 nm from a direct comparison to GOME FM cross sections [Weber et al., 2011] as used in the current standard retrieval. The lower subpanels display the relative difference of total ozone columns compared to the values retrieved currently using scia.plus53.shift8 cross section.*

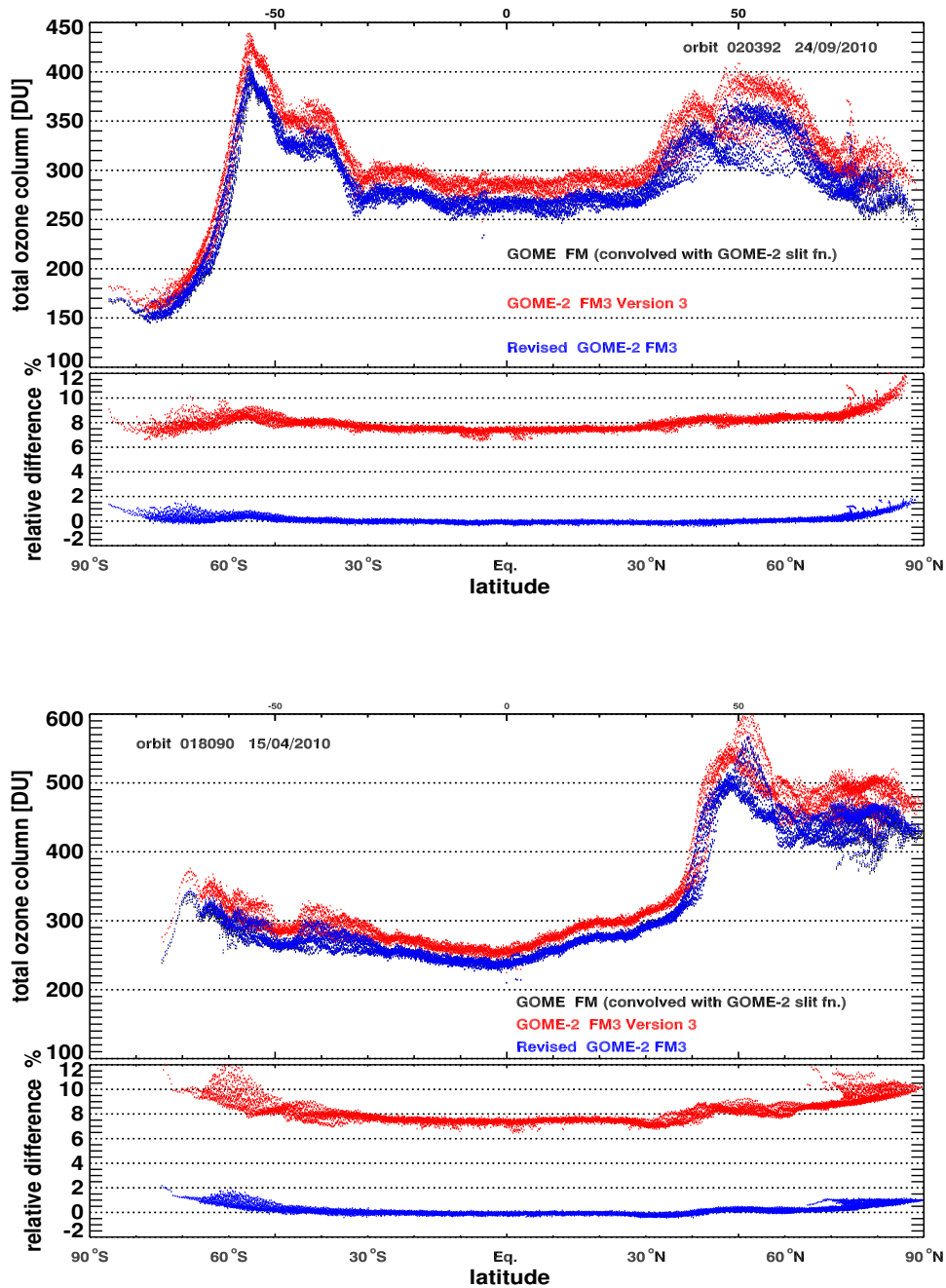


*Figure 5.18: GOME-2 total ozone columns with different cross sections. The upper subpanels display GOME-2 total ozone column retrieved using different cross section data for orbits 020392 (24/09/2010) and 36873 (20/03/2009). GOME FM convolved with GOME-2 slit function (black) is used in the current standard retrieval. The lower subpanels display the relative difference of total ozone columns compared to the values retrieved currently using GOME FM cross section.*

## 5.4. Retrieval Tests Using the Revised Ozone Cross Section Data

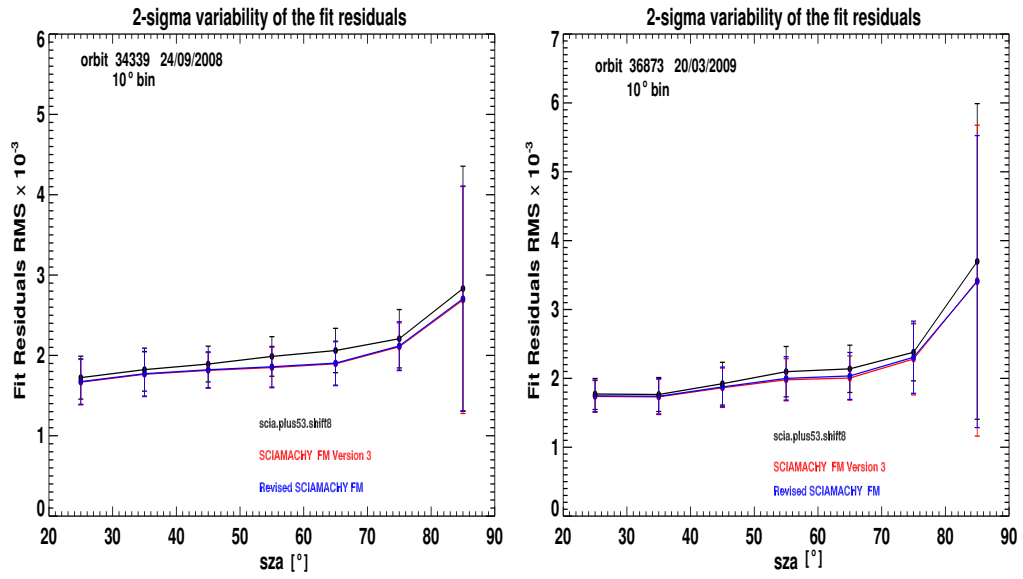


Figure 5.19: SCIAMACHY's fit residuals (RMS) with different cross section data for the same orbits 34339 (24/09/2008) and 36873 (20/03/2009) as in Fig. 5.17.

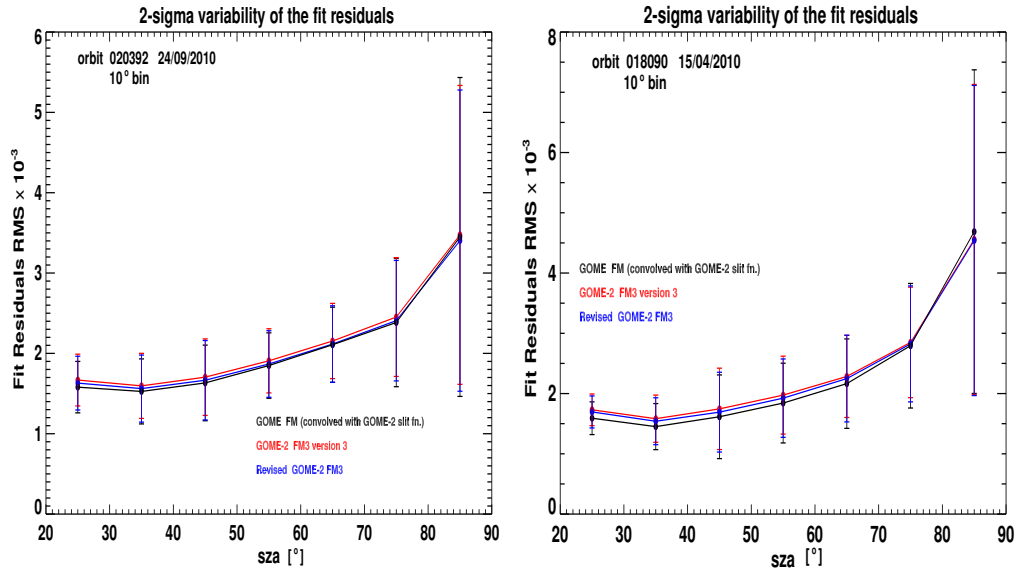


Figure 5.20: GOME-2 fit residuals (RMS) with different cross section data for the same orbits 020392 (24/09/2010) 36873 (20/03/2009) as in Fig. 5.18.



## Part III

# Ozone Trend Analysis



# Chapter 6

## Total Ozone Trends and Variability during 1979 – 2012 from Merged Datasets of Various Satellites

Total ozone changes reflect changes in lower stratospheric ozone that are governed by chemical and dynamical short-term as well as long-term variability. Global ozone amounts decreased severely between the eighties and the mid-nineties where they reached minimum values. This decline was mainly due to the impact of the uncontrolled anthropogenic emissions containing the halogens, chlorine and bromine (chlorofluorocarbons CFCs, halons), which depleted the stratospheric ozone through catalytic chemistry. The chemical processes involving the ozone depleting substances (ODS), in particular the heterogeneous reactions in the polar region (ozone hole), are well known and documented in previous studies (e.g. Solomon [1999]; Staehelin et al. [2001]) and ozone assessments (e.g. WMO [1999, 2003, 2007, 2011], Stratospheric Processes

---

<sup>1</sup>Sections 6.1 – 6.5 of this chapter are an extended version of the following publication: Chehade W., Burrows J. P., and Weber M.: Total ozone trends and variability during 1979 – 2012 from merged datasets of various satellites, *Atmospheric Chemistry and Physics Discussions*, 13, 2013, 11, 30407 – 30452, <http://www.atmos-chem-phys-discuss.net/13/30407/2013/>, 10.5194/acpd-13-30407-2013

Section 6.6 has contributed to WMO – UNEP Ozone Assessment, 2014: CHAPTER 2, “Update on Global Ozone: Past, Present and Future”.

And their Role in Climate SPARC [1998]). The ODS emissions were controlled by the implementation of the Montreal Protocol (1987) and its Amendments and Adjustments and global ozone levels showed a slowing in the decline and started to increase since mid-nineties in response to the phase out of ODS in the stratosphere (WMO, 2003, 2007, 2011 and references therein). Some studies on the other hand demonstrated a significant evidence of a decadal time scale influence of atmospheric dynamics on ozone variability during the decline till the mid-nineties (e.g. Hood and Soukharev [2005]; Wohltmann et al. [2007]; Mäder et al. [2007]; Harris et al. [2008]) as well as the increase over northern latitudes afterwards (e.g. Reinsel et al. [2005]; Dhomse et al. [2006]; Wohltmann et al. [2007]; Harris et al. [2008]). Long-term variability of stratospheric ozone is also seen to be influenced by variations in solar radiation [Chandra and McPeters, 1994; Bojkov and Fioletov, 1995; Miller et al., 1996; Zerefos et al., 1997; McCormack et al., 1997; Hood, 1997; Ziemke et al., 1997; Lee and Smith, 2003; Soukharev and Hood, 2006; Fioletov, 2009] and aerosols injected in the stratosphere after volcanic eruptions [Hofmann and Solomon, 1989; Peter, 1997; Solomon, 1999].

Analysis of long-term changes in ozone in order to detect a statistically significant trend after the levelling off the ODS in the stratosphere requires the full understanding and proper accounting of all the processes contributing to decadal ozone variability, which induces considerable uncertainty in trend determination, and to quantify and separate the relative influence of chemical and dynamical contributors. Global and long-term total ozone measurements acquired from various satellite borne atmospheric chemistry sensors (multi-decadal datasets) are very useful to monitor and study the interannual and decadal ozone variability and to determine long term global trends.

Previous trend assessments modelled the response of ODS related signal in terms of linear trends based on the expected linear increase and phasing out of ODS. This statistical approximation of the ODS is well known as the piecewise linear trend (PWLT or hockey stick) model with a turnaround in the late 1990s, when the stratospheric halogens (released from ODS) reached maximum. In this study we used multiple linear regression which is a standard trend analysis tool to quantitatively assess the observed total ozone variations due to different natural and anthropogenic influences (WMO, 2003, 2007, 2011 and references therein), with the long-term trend in ozone related to ODS described by the equivalent effective stratospheric chlorine function (EESC).

The aim of this study is first to assess and update the global trends of ozone recovery and its statistical significance as expected from the turnaround and slow decrease in stratospheric halogen after measures

introduced by the Montreal Protocol and amendments to phase out ODS. The trends are determined from a statistical analysis of thirty four year of total ozone data. The estimated EESC-based trends are compared with the trends obtained from PWLT analysis to assess the differences between the models as the latter is sensitive to adding more data after the turnaround point. Moreover, the same statistical analysis is applied to different consolidated ozone datasets to investigate the uncertainty in the long-term trends due to the use of different ozone satellite datasets.

In Section 6.1, the major chemical and dynamical processes contributing to ozone variability are briefly summarized. The zonal mean total ozone data sets of the merged TOMS/SBUV/OMI (1979 – 2012) MOD 8.0 are briefly described in Section 6.2, and the multiple linear regression model applied to the zonal total ozone data is presented in the following section. Section 6.4 discusses the results in details and the estimates of the trends are introduced in Sect. Sect. 6.5. The sensitivity of using different ozone datasets in the regression are presented in Section 6.6.

## 6.1 Main Contributors to Ozone Variability

The various natural and anthropogenic processes representing the state of the atmosphere (dynamical and chemical), modify the global ozone distributions and consequently contributing to its variability in a changing climate employed in the multiple linear regression, are displayed in Fig. 6.1.

### 6.1.1 Brewer-Dobson Circulation

The ozone abundances in different regions of the atmosphere are determined by a balance between photochemical processes (production and loss), catalytic destruction and, transport. Ozone is produced in the tropical stratosphere but most of ozone is found at higher latitudes away from its production source. Ozone is transported through a slow atmospheric circulation in the lower to middle stratosphere that moves the upwelling air parcels from the tropics poleward, and then subsides in extratropics and high latitudes where it builds up. The circulation is a broad hemispheric-scale meridional overturning which is limited to the winter season and historically known as the Brewer-Dobson circulation (BDC). The main features of the poleward drift of air masses in stratosphere were

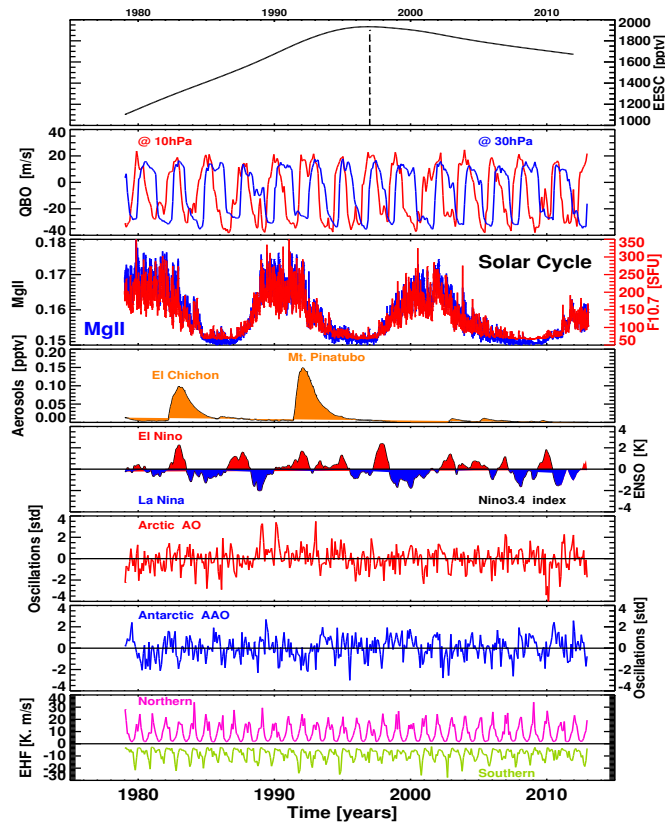


**Figure 6.1:** Time series of the different explanatory variables used in this study are displayed in the panels: Stratospheric loading of ODS (first panel) in terms of Equivalent Effective Stratospheric Chlorine (EESC) in pptv. The EESC concentration (black curve) peaked in 1997 and started a slow decline afterwards. Quasi-Biennial Oscillation (QBO) index at 10 hPa (red) and at 30 hPa (blue) are shown in the second panel. The equatorial zonal winds at both levels are out of phase by about  $\pi/2$ . The third panel displays the 11-year solar cycle as expressed by the solar flux at 10.7 cm (red) and core-to-wing ratio of the MgII line at 280 nm (blue). Time series of mean optical thickness at 550 nm (orange) to account for volcanic aerosol enhancements are presented in the fourth panel; the dominant features are the 1982 eruption of EL Chicohón and the 1991 eruption of Mt. Pinatubo. Nino 3.4 index describing the state of the El Niño/Southern Oscillation (ENSO) is shown in panel five: El Niño (red) and La Niña (blue). The next two panels show the teleconnection patterns: Arctic Oscillation (AO) index in red and Antarctic Oscillation (AAO) index in blue. In the last panel, extra-tropical eddy heat flux at 100h Pa averaged over midlatitudes (area weight averaged between  $45^{\circ}\text{N}$  and  $75^{\circ}\text{N}$ ) and averaged from October to March in the NH (magenta) and from April to September in the SH (green).

inferred from Brewer [1949] and Dobson [1956] water vapour and ozone measurements, respectively.

This meridional circulation is driven by the planetary scale atmospheric waves (Rossby and gravity waves) which are generated in the troposphere and propagated upwards to the stratosphere [Haynes et al., 1991; Rosenlof and Holton, 1993; Newman et al., 2001; Plumb, 2002]. The waves break and dissipate at a critical level and deposit their momentum, this decelerate the mean zonal air flow [Andrews et al., 1987]. As a result, a poleward motion is established to balance the Coriolis force and pressure gradient (geostrophic balance) and due to mass conservation large-scale vertical motions in the tropics and extratropics set in, this induces meridional overturning from equator to pole. In the tropics, the rising air cools down due to adiabatic expansion while in the polar region the subsiding air is heated by adiabatic compression. This leads to reducing (enhancing) of stratospheric temperatures below (above) the local radiative equilibrium temperature in the tropics (extratropical) region and as a result diabatic heating warms the tropical upwelling air and diabatic cooling cools the extratropical downwelling branch [Haynes et al., 1991; Newman et al., 2001]. The diabatic circulation of air (also considered as residual circulation) from the tropical tropopause to the lower polar stratosphere has a mean transport time of five to six years [Waugh and Hall, 2005] and confined in the winter hemisphere [Rosenlof and Holton, 1993; Chipperfield and Jones, 1999] during which the upward propagating waves deposit their easterly momentum (by wave breaking) in the stratospheric mean westerly flow.

The influence of the meridional circulation in a given winter impacts the ozone variability well into spring and summer [Fioletov and Shepherd, 2003; Weber et al., 2011]. In the polar region, the accumulation of the lower stratospheric ozone is strongly governed by the intensity of diabatic circulation; the stronger the intensity in the wintertime, the stronger is the meridional mixing and the diabatic descent. This increases the stratospheric temperatures which weakens the polar vortex and less ozone is destructed by heterogeneous reactions [Chipperfield and Jones, 1999; Fusco and Salby, 1999; Randel and Stolarski, 2002].

The magnitude of the easterly momentum deposited in the stratosphere by wave breaking is approximated by the divergence of the Eliassen Palm (EP) flux  $F$ , i.e. [Newman et al., 2001]. The net upward flux of wave activity is measured by the vertical component of the EP flux ( $F_z$ ) which is proportional to the zonal mean poleward eddy heat flux  $\mathbf{vT}$  [Andrews et al., 1987]. The winter accumulated lower stratosphere eddy heat flux is considered a good measure (proxy) of the inter-annual variability of ozone due to the BDC variations [Fusco and Salby, 1999; Newman et al.,

2001; Randel and Stolarski, 2002; Dhomse et al., 2006; Weber et al., 2011].

The contribution of the large scale stratospheric circulation to ozone fluctuations can also be determined by other dynamical explanatory variables such as the dominant recurrent non-seasonal (with no particular periodicity) sea level pressure variation pattern north/south of 20°S/N latitude known as the Arctic Oscillation (AO) (or North Annular Mode (NAM)) and Antarctic Oscillation (AAO) (or Southern Annular Mode (SAM)) indices [Fusco and Salby, 1999; Hartmann et al., 2000; Appenzeller et al., 2000; Randel and Stolarski, 2002; Kieseewetter et al., 2010; Steinbrecht et al., 2011]. The QBO phase (see later section) also influences the wave propagation and relates to variability in the BDC [Baldwin et al., 2001].

### 6.1.2 Quasi-biennial Oscillation

The equatorial stratosphere is characterized by a slow recurring variability in its zonal winds which influences the interannual variability of total ozone columns [Baldwin et al., 2001]. The winds propagate downwards and alternatively changing (oscillating) in the strength and direction, i.e. reverse from easterly to westerly in the lower and middle stratosphere (~16 – 50 km) with an average period of about 28 months [Reed et al., 1961]. The fluctuating winds are termed the quasi-biennial oscillation (QBO) [Angell and Korshover, 1964] and are the result from the upward propagating equatorial waves and mean-flow interaction in the stratosphere [Lindzen and Holton, 1968; Plumb, 1977].

The QBO is a longitudinally symmetric tropical phenomenon [Belmont and Dartt, 1968] extending in latitude around 15°S/N with no seasonal dependence and maximum amplitude centered over the equator. This oscillation has a clear influence on the global stratosphere [Holton and Tan, 1980]. The oscillation of the tropical zonal winds modulates the stratospheric temperature structure and the Brewer-Dobson circulation [Baldwin et al., 2001]. The changes in wind direction produce temperature anomalies; the descending westerly wind shear (positive) is associated with the warmest temperatures at the equator while the propagating easterlies (increasing easterly winds with height) are associated with the coldest temperatures according to the thermal wind relationship. The temperature anomalies influence ozone by modulating the photochemical reaction rates in the tropical stratosphere as well as modifying the stronger global residual circulation [Reed et al., 1961]. Therefore a secondary meridional circulation by the QBO is induced and superimposed on the normal Brewer-Dobson circulation which either enhances

or weakens the BDC depending on the phase of QBO. During the westerly phase, maximum diabatic cooling to space occurs and the air parcels sink leading to an increase in total ozone. This downward descent is balanced by air parcels rising in the extratropics (decrease in total ozone) and an equator-ward drift that slows the BDC. During the easterly phase of the QBO, the induced circulation reverses. The QBO signal also affects the ozone variability at high latitudes [Bowman, 1989; Lait et al., 1989; Chandra and Stolarski, 1991] and even effects the distortion of wintertime stratospheric polar vortex by modulating the propagating extratropical wave flux or Eliassen Palm flux [Dunkerton and Baldwin, 1991]. This modulation is called the Holton-Tan effect [Holton and Tan, 1980] with largest signal in winter and spring [Tung and Yang, 1994; Randel and Cobb, 1994; Baldwin et al., 2001].

### 6.1.3 El Niño-Southern Oscillation

El Niño Southern Oscillation (ENSO) is a coupled atmospheric and tropical Pacific Ocean interaction phenomenon (zonal) of warming or cooling fluctuations in sea surface temperatures (SST) and alternating air surface pressure (SP) between the central/eastern and western tropical Pacific. El Niño events, the warmer phase, occur when the sea surface temperatures in the eastern tropical Pacific (South American coast) are warmer than average due to drift of warm waters from the western Pacific (Indonesia) resulting from the weakened easterly trade winds and occur about every 3 to 7 years. The atmospheric component of the phenomenon (coincided with El Niño and termed "Southern Oscillation") represents the occurrence of lower sea-level pressure near Tahiti and higher sea-level pressure in Australia. During the La Niña the opposite occurs.

ENSO is the dominant source of interannual variability of tropical climate. Beside SST and SP oscillations, it induces interannual global scale changes in ocean currents, surface pressure, convections, atmospheric temperature and winds, clouds and precipitation, and impacts the chemistry of trace gases in the troposphere.

During the 1997/8 El Niño event, highest amounts of tropospheric column ozone (up to 25 DU increase) were registered in the tropics [Chandra et al., 1998; Fujiwara et al., 1999; Thompson et al., 2001], half of the increase were attributed to biomass burning over Indonesia during September-November 1997 and the remaining amounts resulted from El Niño driven large scale changes in the ocean-atmosphere dynamics that transported ozone rich air from the stratosphere to the troposphere as reported by some modelling studies e.g. Sudo and Takahashi [2001]; Chandra et al.

[2002]; Zeng and Pyle [2005]. Ziemke et al. [2010] even proposed a new El Niño index derived from column ozone.

ENSO phases have a global impact, affecting the circulation in the extratropics by modulating the generation and propagation of Rossby wave which is strongly evident in the northern winter months [Trenberth et al., 2002]. The warm phase is associated with stratospheric warming [van Loon and Labitzke, 1987; Labitzke and van Loon, 1999], and a strengthened BDC in the middle atmosphere yielding an enhanced upwelling of ozone-rich air from the tropics and a weaker polar vortex [Newman et al., 2001; Randel and Stolarski, 2002; Bronnimann et al., 2004; Manzini et al., 2006; Taguchi and Hartmann, 2006; Camp and Tung, 2007]. ENSO results in temperature and ozone anomalies in the stratosphere that are opposite to the tropospheric anomalies.

#### 6.1.4 Chlorine and Bromine containing ODS

Anthropogenic halogenated substances (chlorofluorocarbons CFCs, halons) have been the principal source of stratospheric ozone depletion through catalytic chemistry over the past few decades [Stolarski and Cicerone, 1974; Molina and Rowland, 1974]. Their very long atmospheric residence times allow them to be transported to the upper stratosphere where they photo-dissociate producing Cl and Br atoms which destroy ozone. Solomon [1999] presents a review of the key processes involved in ozone depletion.

The evolution of the long-lived ODS is a key parameter to describe long term ozone changes. Equivalent Effective Stratospheric Chlorine (EESC) index is used as a measure of the inorganic chlorine and bromine amounts accumulated in the stratosphere weighted by their ozone destructive potential and fractional release rate [WMO, 1999, 2003, 2007, 2011]. This is proportional to changes in total column ozone [Daniel et al., 1995]. Stratospheric EESC is calculated from the surface measurements of tropospheric ODS abundances taking into account the greater per-atom potency of stratospheric Br compared to Cl in its ozone destruction with a constant factor,  $\alpha$  ( $EESC = Cl + \alpha \cdot Br$ ), conversion of  $Cl_y$  and  $Br_y$ , and for the transit times (or ages) the air takes to be transported from surface to different regions in the stratosphere. The implementation of Montreal Protocol and its Amendments and Adjustments, enacted in 1987, succeeded in reducing the abundances of the dominant ODS. EESC has levelled off through the late mid-nineties and afterwards started a slow decline. The EESC index has already been used in several ozone trends statistical models e.g., Newman et al. [2004]; Fioletov and Shepherd [2005]; Dhomse et al. [2006]; Stolarski and Frith [2006]; Randel [2007]; Harris

et al. [2008]; Kieseewetter et al. [2010].

### 6.1.5 Solar Cycle

Sun is the primary source of energy for Earth, any variation in the emitted energy output has a significant impact on climate and atmosphere [Lean and Rind, 2001; Rind, 2002; Haigh, 2003]. Global total ozone amounts vary by 2 to 3% during a solar cycle [WMO, 2003, 2007, 2011]. Solar variability is considered as a dominant form of long-term ozone changes and has been included in all ozone trend assessments [WMO, 1999, 2003, 2007, 2011].

The variations of the solar ultraviolet spectral irradiance largely modify ozone photochemistry in the upper stratosphere [Brasseur, 1993]. More ozone is produced during the maximum phase of the cycle during which more oxygen photo-dissociate since the amplitude of solar cycle variability is greater in the far ultraviolet. An increase of 4 – 6% in upper stratospheric ozone is reported in the statistical studies between the solar minima and maxima (e.g. McCormack and Hood [1996]; Hood [1997]). These amounts are compatible with the 4 – 8% variability in ultraviolet energy output ( $\lambda \leq 240$  nm) over a typical cycle [Dessler et al., 1998]. Solar cycle also modulates ozone chemistry.  $\text{NO}_y$  are generated in the upper mesosphere through ionization of nitrogen and oxygen molecules by enhanced precipitating energetic electrons and solar protons during solar minima which are transported into the stratosphere causing ozone catalytic destruction [Callis et al., 1998; Sinnhuber et al., 2003; Rozanov et al., 2005; Langematz et al., 2005]. This effect can reach the lower stratosphere propagating equatorwards [Jackman et al., 2006]. In the lowermost stratosphere, the solar cycle couples with QBO and modulates stratospheric circulation which indirectly effects ozone transport [Labitzke and van Loon, 1993; Kodera and Kuroda, 2002; Hood and Soukharev, 2003]. In relation to the 11-year solar cycle, a clear decadal response is detected in long-term ozone records and is in phase with it [Chandra and McPeters, 1994; Bojkov and Fioletov, 1995; Miller et al., 1996; Zerefos et al., 1997; McCormack et al., 1997; Hood, 1997; Ziemke et al., 1997; Lee and Smith, 2003; Soukharev and Hood, 2006; Fioletov, 2009].

### 6.1.6 Aerosols

Major volcanic eruptions inject large amounts of sulfate aerosols into the stratosphere that perturb stratospheric temperature and circulation and enhance catalytic ozone depletion through heterogeneous chemistry [Hofmann and Solomon, 1989; Peter, 1997; Solomon, 1999] releasing chlorine and bromine from ODS. The eruptions of the tropical volcanoes of El Chichón (Mexico, 1982) and Mt. Pinatubo (Philippines, 1991) were the major volcanic activities since the late 1970s and huge enhancements of sulfur dioxide (SO<sub>2</sub>) that oxidized to form sulfuric acid (H<sub>2</sub>SO<sub>4</sub>) and condensed to create aerosols. Heterogeneous reactions take place mostly on the surface area of liquid sulfuric acid aerosols in the lower stratosphere and enhance ozone depletion. The volcanic aerosols were mixed relatively rapidly throughout the stratosphere in both hemispheres and sedimented out within couple of years. Stratospheric ozone reduced significantly following the eruptions in the Northern Hemisphere [Randel et al., 1995; Solomon et al., 1996; SPARC, 1998; WMO, 1999, 2003, 2007, 2011] which persisted for two to three years, while Southern Hemisphere ozone records did not show any pronounced ozone deficit [Fioletov et al., 2002; WMO, 2003, 2007, 2011]. The high aerosol load also impacts the atmospheric radiative balance by absorbing and scattering terrestrial (infrared) and solar radiations that warm the lower stratosphere and cool the troposphere respectively, these changes modulate the atmospheric circulation as well as the stratosphere-troposphere interaction [WMO, 2007, 2011]. Several studies [Schnadt Poberaj et al., 2011; Aquila et al., 2013] showed that enhanced ozone transport through changes in dynamical processes counteracted the chemical losses.

## 6.2 Satellite Total Ozone Time Series

Zonal mean total ozone columns from the TOMS/SBUV/OMI Merged Ozone Dataset (MOD) Version 8.0 [Stolarski and Frith, 2006] were used in this study. This dataset combines data from eight independent backscatter ultraviolet technique (BUV-type) satellite instruments (Total Ozone Mapping Spectrometer TOMS, Solar Backscatter Ultraviolet SBUV/SBUV-2, and Ozone Monitoring Instrument OMI) with measurements from 1979 – 2012. Drifts and biases in overlapping periods among instruments were removed [Stolarski and Frith, 2006]. V8.0 dataset can be obtained from [http://acd-ext.gsfc.nasa.gov/Data\\_services/merged/](http://acd-ext.gsfc.nasa.gov/Data_services/merged/).

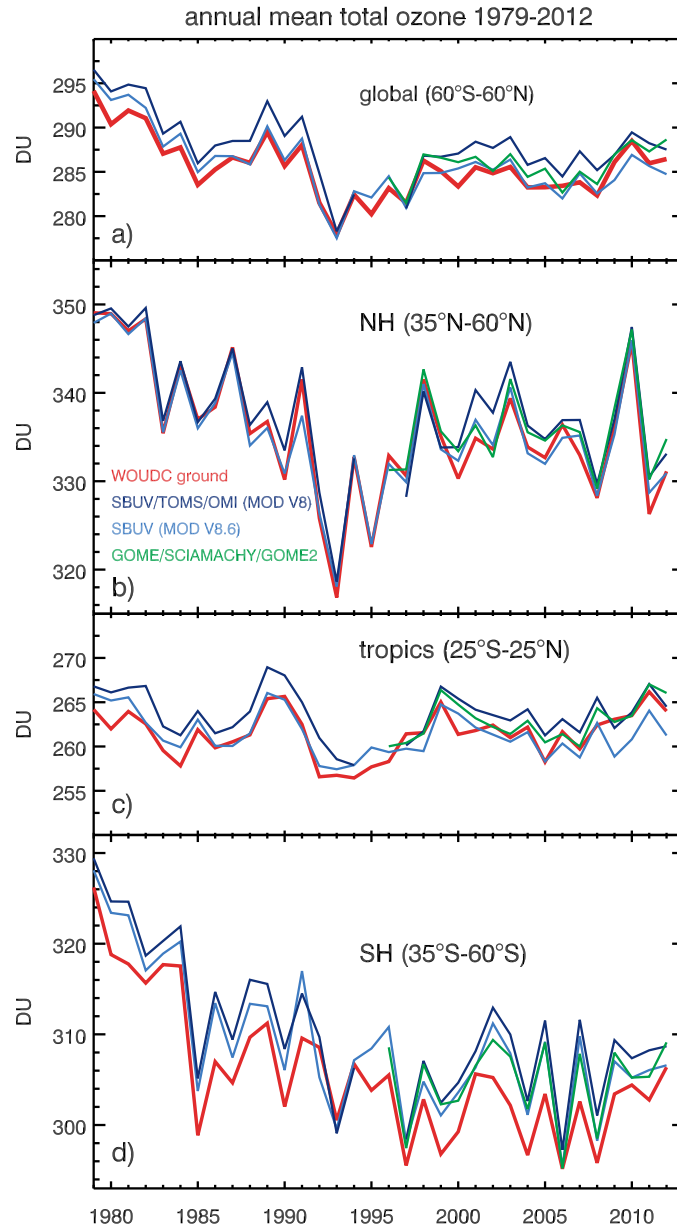


**Figure 6.2:** Annual mean area-weighted total ozone time series of ground-based measurements combining Brewer, Dobson, and filter spectrometer data (red, [Fioletov et al., 2002, 2008; Hendrick et al., 2011]), the merged SBUV/TOMS/OMI MOD V8.0 (dark blue: [Stolarski and Frith, 2006]), the merged SBUV/SBUV-2 MOD V8.6 (blue: Frith et al. [2012]; DeLand et al. [2012]; Bhartia et al. [2013]; McPeters et al. [2013]), and GOME/SCIAMACHY/GOME-2 “GSG” (green, [Kiesewetter et al., 2010; Weber et al., 2011, 2012, 2013]), in the zonal bands: a)  $60^{\circ}\text{N} - 60^{\circ}\text{N}$  (global), b)  $30^{\circ}\text{N} - 60^{\circ}\text{N}$  (NH), c)  $25^{\circ}\text{S} - 25^{\circ}\text{N}$  (tropics), and d)  $35^{\circ}\text{S} - 60^{\circ}\text{S}$  (SH) zonal bands.

Figure 6.2 shows annual means of the area-weighted total ozone columns over the period 1979 – 2012 of the different global datasets used in this study including the ground-based measurements which combines Brewer, Dobson, and filter spectrometer data and merged satellite data for various zonal bands: global (60°S – 60°N), middle latitudes in both hemispheres (35° – 60°) and the tropics (25°S – 25°N), respectively.

### 6.3 Multivariate Linear Regression

Trends in global total ozone are investigated through a multivariate linear regression model consisting of various explanatory parameters (as discussed above) which account for chemical and dynamical processes in the atmosphere. This statistical method has been frequently used in ozone assessments (Bojkov et al. [1990]; SPARC [1998]; CCMVal [2010]; WMO [1999, 2003, 2007, 2011] and references therein) in order to assess the contributions of various natural and anthropogenic changes to long-term and short-term variability of ozone. The annual mean total ozone column (TOZ) time series is constructed as a simple linear sum of explanatory variables time series as follows:

$$\begin{aligned}
 \text{TOZ}(\mathbf{n}) &= \text{TOZ}(\mathbf{n})^\circ + \alpha^{EESC} \cdot \text{EESC}(\mathbf{n}) \\
 &+ \alpha^{qbo} \cdot \mathbf{qbo}(\mathbf{n}) \\
 &+ \alpha^{solar} \cdot \mathbf{solar}(\mathbf{n}) \\
 &+ \alpha^{aer} \cdot \mathbf{aer}(\mathbf{n}) \\
 &+ \alpha^{ENSO} \cdot \mathbf{ENSO}(\mathbf{n}) \\
 &+ \alpha^{AO/AAO} \cdot \mathbf{AO/AAO}(\mathbf{n}) \\
 &+ \alpha^{EHF} \cdot \mathbf{EHF}(\mathbf{n}) \\
 &+ \varepsilon(\mathbf{n})
 \end{aligned} \tag{6.1}$$

where  $\mathbf{n}$  is a running index (from zero to 34) corresponding to all years during the period 1979 – 2012 while  $\alpha^X$  represents the time dependent regression coefficients of each proxy ( $X$ ) and  $\varepsilon$  is the residual or noise time series. The EESC concentrations were obtained from NASA Goddard Space Flight Center web site ([http://acdb-ext.gsfc.nasa.gov/Data\\_services/automailer/index.html](http://acdb-ext.gsfc.nasa.gov/Data_services/automailer/index.html)) and were calculated for a mean age of air of three years and width of age-of-air distribution of one and half years [Newman et al., 2006, 2007] and bromine efficiency of  $\alpha=60$  was used [Sinnhuber et al., 2009]. Equatorial zonal winds at 10 and 30 hPa pressure

levels (from FU Berlin, <http://www.geo.fu-berlin.de/en/met/ag/strat/-produkte/qbo/index.html>) were used to provide the QBO index in the regression analysis. QBO at 10 and 30hPa are out of phase ( $\sim \pi/2$ , Bojkov and Fioletov [1995]; Steinbrecht et al. [2003]) and account for the effect of QBO strength and phase on ozone at different latitudes. This obviates the need to find the optimal time lag since the effect on ozone in the extratropics is represented by an optimal lag relation [Bojkov et al., 1990].

To account for the effect of volcanic aerosols after El Chichón and Mount Pinatubo eruptions, time dependent stratospheric aerosol optical depth at 550 nm [Sato et al., 1993] is used. The optical depth (<http://data.giss.nasa.gov/modelforce/strataer/>) is multiplied by the stratospheric chlorine content (EESC) [Wohltmann et al., 2007]. To investigate the impact of UV solar irradiance modulation related to the 11-year solar cycle, core-to-wing ratio of the MgII line at 280 nm (<http://www.iup.uni-bremen.de/gome/>) as well as solar radio flux at 10.7 cm wavelength ([ftp://ftp.ngdc.noaa.gov/STP/space-weather/solar-data/solar-features/solar-radio/noontime-flux/pentiction/pentiction\\_adjusted/listings/listing\\_drao\\_noontime-flux-adjusted\\_daily](ftp://ftp.ngdc.noaa.gov/STP/space-weather/solar-data/solar-features/solar-radio/noontime-flux/pentiction/pentiction_adjusted/listings/listing_drao_noontime-flux-adjusted_daily)) are used as proxies. For the El Niño-Southern Oscillation phenomenon, the Nino 3.4 index (<http://www.cpc.ncep.noaa.gov/data/indices/ersst3b.nino.mth.81-10.ascii>) is included in the regression. The AO/AAO index is obtained from NOAA National Weather Service Climate Prediction Center website ([http://www.cpc.ncep.noaa.gov/products/precip/CWlink/daily\\_ao\\_index/teleconnections.html](http://www.cpc.ncep.noaa.gov/products/precip/CWlink/daily_ao_index/teleconnections.html)) and the extratropical 100 hPa eddy heat flux (EHF) averaged over midlatitudes between  $45^\circ$  and  $75^\circ$  in each hemisphere is obtained from ECMWF ERA-Interim as described by Weber et al. [2011].

The explanatory variables time series used in a multivariate linear trend analysis must be fully independent (uncorrelated); in this study the correlations between predictors are small (between 0.1 and 0.2) except for the aerosol and ENSO term (0.34). In order to account for auto-regression, a Cochrane-Orcutt transformation [Cochrane and Orcutt, 1949] is applied to the regression using the residual ( $\varepsilon(n)$ ) auto-correlation estimate with a time lag of one year in order to ensure their normal distribution. The transformation does not change the estimates of the fitting coefficients, however, the fitting errors increase due to the reduction in degree of freedom.

## 6.4 Results

The regression analysis (Eq. 6.1) is applied to TOMS/SBUV/OMI annual mean zonal mean total ozone data from 65°S to 65°N in steps of 5°. An example of the model and the contributions (in Dobson Units, DU) of the different natural as well as anthropogenic explanatory variables are illustrated in Fig. 6.3 for the 60 – 65°N latitude band. The regressed ozone time series (blue, first panel) fits well to the ozone measurements (red) and follows the general features capturing the decline of ozone to the mid-1990s, the pronounced ozone losses after the Mt. Pinatubo eruption and the slow increase after that. The black curve (EESC) describes long-term variations attributed to anthropogenic emissions of ODS. After 1997, a small increase ( $3.5 \pm 0.8$  DU/decade) is attributed to the EESC decline. The regression fit shows a correlation ( $r$ ) of 0.78 between modelled and measured total ozone, while the coefficient of determination, i.e.  $R^2$  (the ratio of the variance of all terms in Eq. 6.1 to the total variance), is 0.63. This implies that about 63% of the observed variance of total ozone column can be explained by the regression.

The green line in the second panel displays the regression residuals between measured and regressed data (in percent). The fitted signal of each explanatory parameter  $\alpha^X \cdot X$  is shown in the third to seventh panel of Fig. 6.3. The overall combined QBO related component (black,  $\alpha^{qbo10} \cdot qbo10 + \alpha^{qbo30} \cdot qbo30$ ) comprises the highest contribution to interannual ozone variability, the fluctuation from easterly to westerly QBO phase at 10 hPa (red) and 30 hPa (blue) attributes around 14 DU. The 11-year solar cycle contribution (blue, MgII index) reaches about 13 DU from solar minimum to solar maximum. The aerosol response associated with El Chichón and Mount Pinatubo eruptions (orange) accounts for about 11 DU and 15 DU loss in total ozone in 1983 and 1992, respectively. The influence of ENSO (turquoise) is typically about  $\pm 8$  DU, whereas the 1997/8 El Niño event contributed +4 DU. Eddy heat flux related ozone contribution (magenta) amounts  $\pm 4$  DU while the negative and positive phases of AO/AAO oscillation (lime-green) contribute  $\pm 5$  DU. Both dynamical proxies were included in the analysis as the regression model worked better and improved the correlation and the coefficient of determination (not shown here). The regression coefficients of the various proxies along with the standard deviation (in brackets) are noted as well in the plot.

The residual circulation transports more stratospheric ozone in winter and the wintertime ozone anomalies remain evident till autumn. Weber et al. [2011] reported positive correlation between spring-to-fall ozone

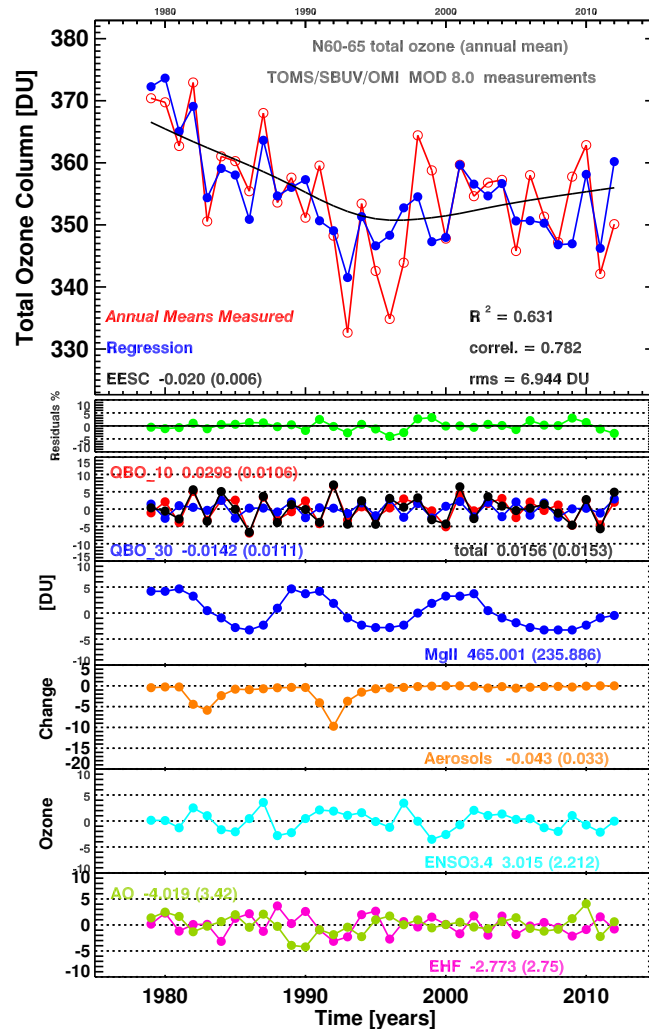


**Figure 6.3:** Annual mean total ozone variations for  $60^\circ\text{N} - 65^\circ\text{N}$  in DU (TOMS/SBUV/OMI V8.0 dataset from 1979 – 2012) and magnitude of contributing factors obtained by multiple linear regressions. Top panel: Observed total annual mean data (red), corresponding fit (blue) and the EESC curve (black). Green line marks the residuals between the observed ozone and regressed time series (second panel). Bottom panels show the contributions from: QBO at 10 hPa, (red), at 30 hPa (blue) and total effect (black), blue: 11-year solar cycle (MgII index); orange: enhanced stratospheric aerosols; turquoise: ENSO (3.4 index), eddy heat flux in magenta and AO/AAO oscillation in lime-green, respectively. The correlation between the observed and regressed ozone ( $R$ ), coefficient of determination ( $R^2$ ) and residual mean square (rms) are indicated in the first panel. The regression coefficients of various proxies along with the standard deviation (in brackets) are also indicated in each panel.

ratio and the winter mean eddy heat flux above and below 50°S/N, while in the tropics (till 40°S/N) the relation is anti-correlated (Fig. 6.4).

To account for ozone wintertime build up and its persistence through the summer, winter mean of eddy heat flux (from October of the previous year until March (NH) and April to September (SH)) are used in the regression equation (Eq. 6.1) instead of the annual mean used in Fig. 6.3. Figure 6.5 displays the regression results for the same latitude band as in Fig. 6.3 but using the winter mean eddy heat flux. The ozone reconstructions and contributions of EESC, QBO, solar cycle, aerosols and ENSO show the same features and patterns as in Fig. 6.3, respectively. The  $R^2$  has now improved to 0.76, correlation is about 0.87 and the residual mean square (rms, the sample estimate of the variance of the regression residuals) is 5.6 DU.

Moreover, the choice of wintertime dynamical term EHF has a significant impact on the effect of the solar cycle, aerosols, ENSO and EHF processes since the contributions of aerosols, ENSO and EHF are statistically significant at  $2\sigma$  level and explain most of the observed ozone variations. The corresponding amplitudes of total ozone variation increased by almost 70% for aerosol and ENSO terms, and by 75% for solar cycle and EHF terms, with highest contribution to total ozone variability arising from EHF reaching about 20 DU. The AO terms are now not statistically significant (as they are most likely represented in the eddy heat flux term). The linear trend after 1997 due to the ODS declines remained unchanged.

### 6.4.1 Contribution of Proxies to Ozone Variability

The statistical trend model was applied to twenty six 5° wide latitude mean ozone data bands from 65°S to 65°N and the contributions of the different explanatory variables in each latitude band are illustrated in Appendix A.

Figure 6.6 is a summary plot displaying the measured and modelled ozone for each latitude band. The reconstructed ozone generally captures the temporal ozone variations and follows the general features of the slow decline till the mid-nineties and the increase after that. The residuals (violet, right scale of the panels) are typically within 3%. The correlation,  $R^2$  and rms are also displayed for each latitude band.

The effect of each proxy on the interannual variability of total ozone measurements is also estimated. Figure 6.7 shows the estimates of fitting coefficients of the different explanatory variables (using the same

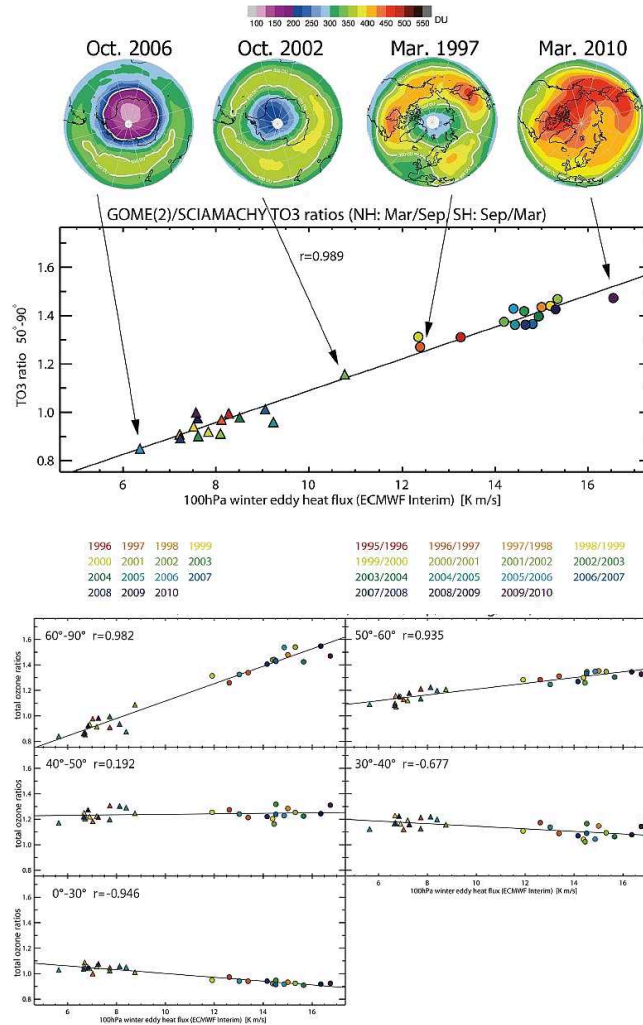


**Figure 6.4:** (top panel) Spring-to-fall ratio of observed polar cap total ozone ( $>50^\circ$ ) as a function of the extratropical winter mean eddy heat flux (September to March and March to September in the respective hemispheres) derived from ECMWF ERA-Interim data separately in the respective hemisphere. Data from the Southern Hemisphere are shown as triangles (September over March ozone ratios) and from the Northern Hemisphere as solid circles (March over September ratios). (bottom panel) Winter-to-fall ratio of observed total ozone for various zonal bands from the polar region to the tropics as a function of the mean absolute extratropical cumulative eddy heat flux between September and February in the NH and between March and August in the SH from ERA-Interim. Data from the Southern Hemisphere are shown as triangles (August over March ozone ratios) and from the Northern Hemisphere as solid circles (February over September ratios) [Weber et al., 2011].

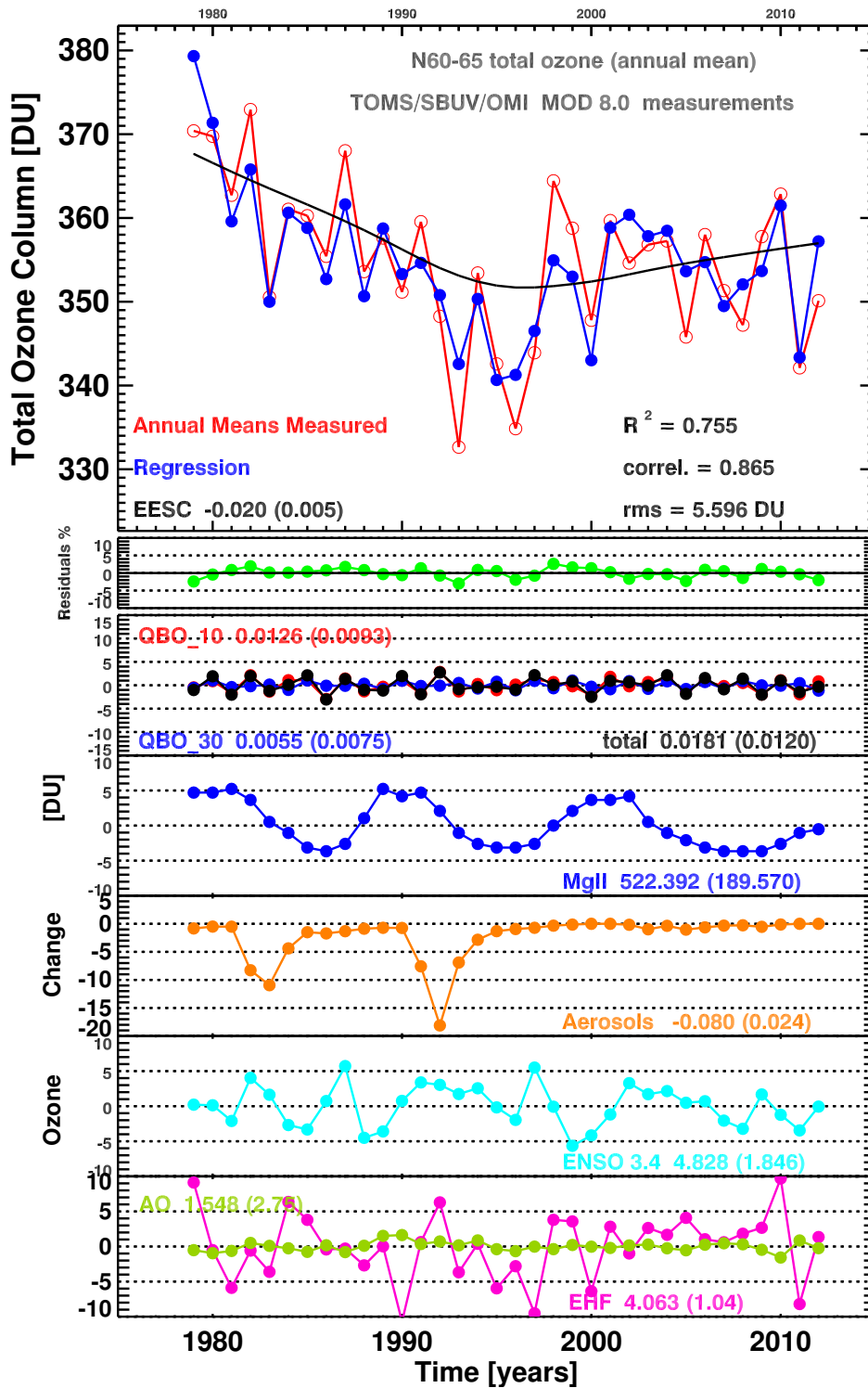
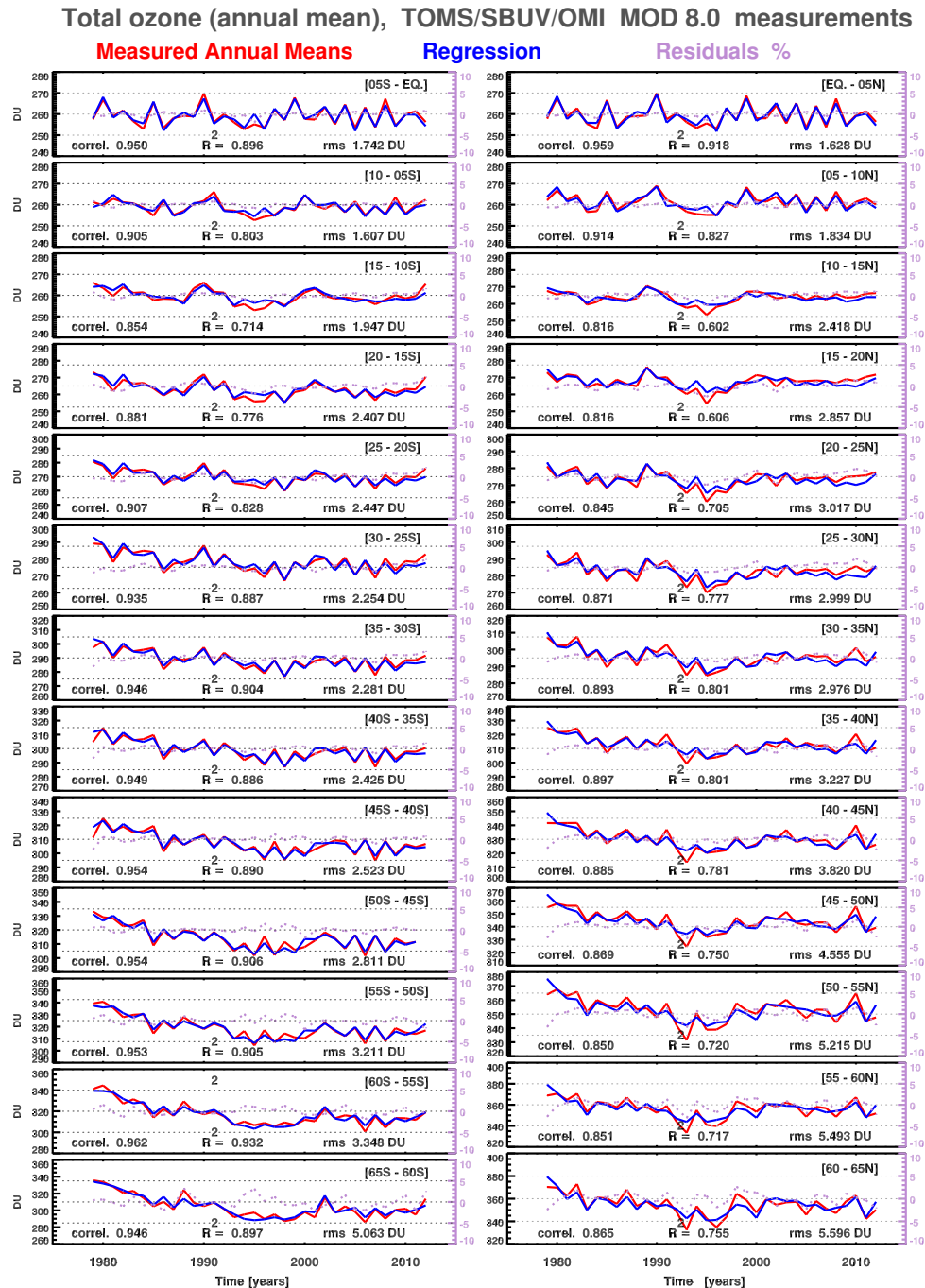


Figure 6.5: Same as Fig. 6.3, except for the winter mean eddy heat flux replacing the ozone variability weighted annual mean EHF).



*Figure 6.6: Observed TOMS/SBUV/OMI V8.0 (red) annual zonal mean total ozone columns for 5° wide latitude bands from 65°S to 65°N and regressed (blue) ozone obtained from regression models (with winter mean EHF dynamical proxy). The right hand scale in each panel gives the residuals in percent (violet). The correlation,  $R^2$  and rms are also noted for each latitude band.*

color notation as in Figs. 6.3 and 6.5) for each latitude band as obtained from the regression analysis. The top panel displays the correlation between measured annual ozone and regression results. Typical values are higher than 0.80 across all latitude bands. The model works well with the choice of the terms included in the regression since the values of  $R^2$  are larger than 0.6. This indicates that the statistical model explains the major part of the total ozone variance, in the tropics (within  $5^\circ\text{S}/\text{N}$ ) and southern subtropics the regression describes the total ozone variations almost completely.

The second panel shows the total ozone response related to ODS abundance in the selected latitude bands as represented by the EESC term. The EESC coefficient increases in magnitude with increasing latitude. In the inner tropics the EESC trends are zero. The EESC response is larger in the Southern Hemisphere as compared to the same latitudes in the Northern Hemisphere latitudes. The largest ozone loss attributed to the chemical ozone depletion by the accumulated anthropogenic ODS, is found south of  $50^\circ\text{S}$  in the “ozone hole” region. This indicates that the Antarctic ozone loss has a higher impact on the long-term decline at Southern Hemisphere midlatitudes [Chipperfield, 2003; Fioletov and Shepherd, 2005; Kieseewetter et al., 2010]. The error bars indicate the statistical significance at two sigma level (95% significance level). The EESC term is statistically significant in all latitude bands except the tropics (north of  $20^\circ\text{S}$  and south  $15^\circ\text{N}$ ).

The total QBO coefficient is symmetric about the equator (shown in black in the third panel) and dominates ozone variability in the tropical and southern sub-tropical regions with highest and clear influence between  $5^\circ\text{S}$  and  $5^\circ\text{N}$  latitude bands while it is insignificant in the northern subtropics. Not unexpected, the 30 hPa QBO term is dominating over the 10 hPa QBO term. The QBO phase change from the equator to the subtropics are due to a secondary circulation with the downward branch in the tropic and the upwelling branch in the subtropics (positive ozone anomalies in the tropics and negative in the  $20 - 40^\circ\text{S}/\text{N}$  subtropical regions).

The solar coefficients are statistically significant. When the core-to-wing ratio of the MgII line is replaced by the solar radio flux at 10.7 cm as a solar proxy in the regression model (Eq. 6.1), the same ozone signal between solar maximum and solar minimum was found and did not alter the influence of other processes (see Appendix B) as well as the correlation, determination coefficient and rms.

The coefficients of stratospheric aerosols (orange) in the fifth panel, are mostly negative and increases with increasing latitude. El Chichón and Mt. Pinatubo eruptions significantly influence total ozone over the

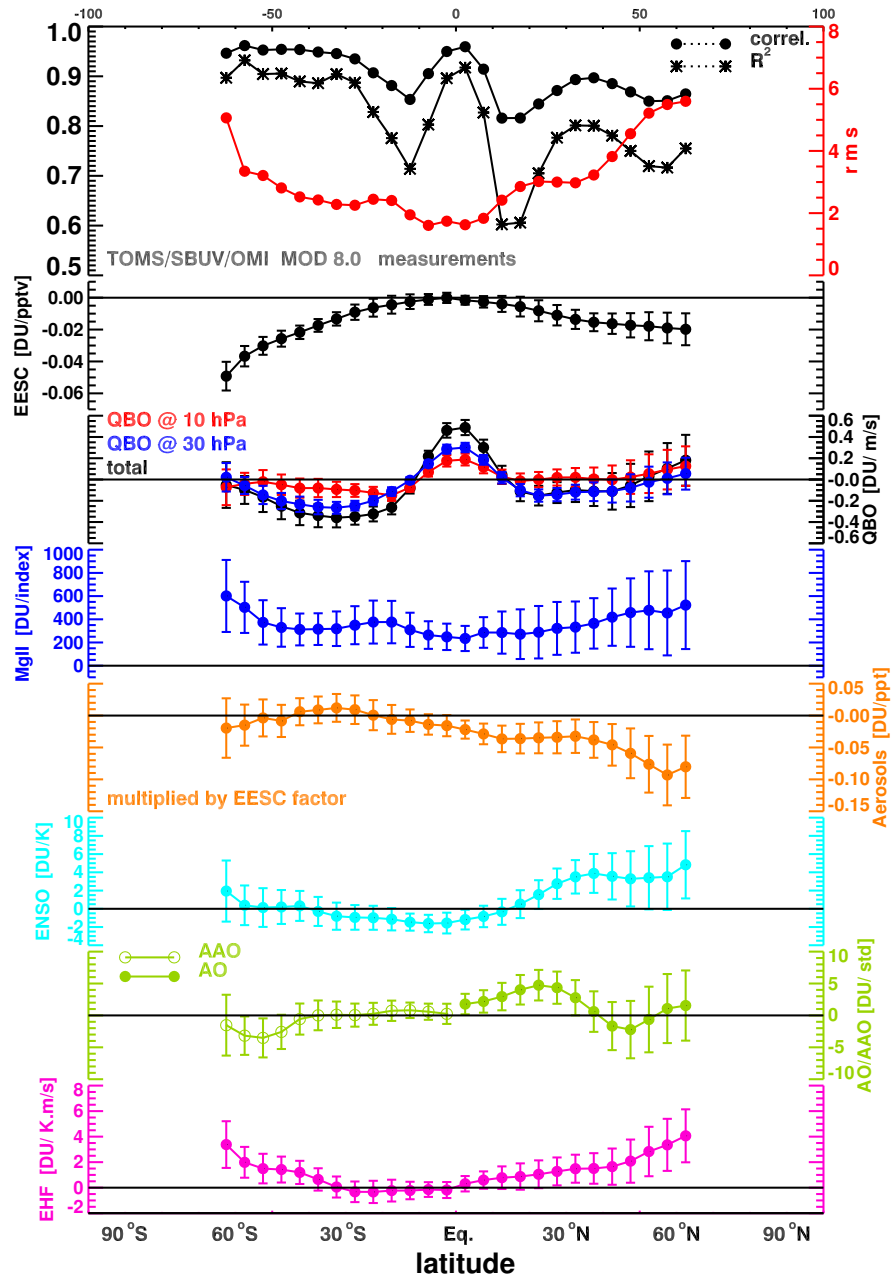


**Figure 6.7:** (top panel) The correlation,  $R^2$  and rms calculated from multiple linear regression of 1979 – 2012 merged TOMS/SBUV/OMI 5° latitude zonal annual total ozone from 65°S to 65°N (results based on regression Eq. 6.1 with wintertime EHF dynamical proxy). (The second to eighth panel) The fitting coefficients of the different explanatory variables used in this study for each latitude band are displayed in respective colors as in Figs. 6.3 and 6.5. Error bars indicate the statistical significance at two sigma level.

northern latitudes and the negative ozone signal is in good agreement with results reported in previous studies [Staehelin et al., 1998; Fioletov et al., 2002; Mäder et al., 2007; Wohltmann et al., 2007; Harris et al., 2008; Rieder et al., 2010a,b, 2011; WMO, 2007, 2011]. At southern mid-latitudes the signal is unexpectedly positive. Similar results were noted by [Fioletov et al., 2002] and were also documented in the WMO reports [WMO, 2003, 2007, 2011]. This spatial pattern emanates from the dynamical processes in which enhanced ozone transport to southern mid-latitudes driven by strong warm ENSO phase and negative AAO accompanied by the shifting and stretching of the vortex towards the Antarctic Peninsula suppressed the ozone signal [Schnadt Poberaj et al., 2011; Aquila et al., 2013; Rieder et al., 2013].

The sixth panel shows the distribution of the ENSO coefficient over the studied latitude range. A significant moderate negative influence on total ozone is centered over the tropical region ( $15^{\circ}\text{S} - 5^{\circ}\text{N}$ ). The positive patterns in the northern high latitudes are interpreted as consequences of enhanced transport from the tropics during warm ENSO events while the coefficient are statistically insignificant towards southern high latitudes.

The AO estimates are found to be significant over the northern latitudes with large positive coefficients in the sub-tropics decreasing the total ozone column ozone during the positive phase of AO and large negative coefficients enhancing ozone during the negative phases of AO in the extra-tropics. The extremely negative AO index in 2010 resulted in very high ozone throughout the northern extratropics [Steinbrecht et al., 2011]. Similar to the NH, the negative AAO phases enhances SH ozone transport, however, the AAO contribution at high southern latitudes in the regression is statically not significant.

The winter mean eddy heat coefficients are statistically significant and dominates ozone variability in the higher latitudes of both hemispheres above  $50^{\circ}$ .

## 6.5 ODS Related Trends in Ozone Total Column

Ozone trends related to ODS are calculated for all latitude bands according to the full regression model (Eq. 6.1). Based on the EESC curves, two clear linear trends can be estimated. A decline in ozone amounts starting at the beginning of the measurements due to the increases in stratospheric ODS loading ( $0.447 \text{ ppbv/decade}$ ) till the turnaround of the

ODS levels in 1997 (EESC maximum), and a negative trend following the levelling-off and phase out of ODS in the stratosphere (- 0.179 ppbv / decade) accompanied with an increase in total column levels. Both phases of the ODS related ozone trends can be approximated as the slopes of the declining and increasing phases of EESC multiplied by the EESC coefficient [DU/decades].

The negative until 1997 and positive turnaround after 1997 EESC-based trends (red solid circles) as a function of latitude are displayed in the bottom panel of Fig. 6.8. The positive trends after 1997 increase in magnitude with latitude and are statistically significant across nearly all latitude bands except the tropics (south of 20°N and north 20°S). In the northern sub-tropics and extra-tropics, the positive trends are smaller than those in southern counterparts. This can be explained by the large dynamically driven variations dominating the ozone variability in northern latitudes [Reinsel et al., 2005; Dhomse et al., 2006; Wohltmann et al., 2007; Harris et al., 2008]. The statistically significant trends can be attributed to the onset of anthropogenic (or ODS related) ozone recovery after 1997.

The ozone trends before and after the ODS turnaround can also be described by calculating piecewise linear trends (PWLT or hockey stick) [Reinsel et al., 2002, 2005; Newchurch et al., 2003; Miller et al., 2006; Vyushin et al., 2007, 2010; Yang et al., 2009]. The PWLT model replaces the EESC term ( $\alpha^{EESC} \cdot \mathbf{EESC}(\mathbf{n})$ ) in Eq. 6.1 by two separate linear trend terms:

$$\alpha^{EESC} \cdot \mathbf{EESC}(\mathbf{n}) = \alpha^{t1} \cdot \delta(\leq 1997) + \alpha^{t2} \cdot \delta(> 1997) \quad (6.2)$$

As for the EESC regression, the results obtained from the PWLT model (see Appendix C) showed the same patterns as in Fig. 6.7 with the correlation and coefficient of determination better than 0.82 and 0.73, respectively, the contributions of the other explanatory variables slightly altered. The MgII coefficient increased in the sub-tropics of both hemispheres (10 – 15%), the eddy heat flux coefficient increased by 5 – 10% in southern latitudes while in the northern latitudes it decreased largely and is statistically significant only north of 55°N. The AO coefficient is smaller (15 – 30%) in 10 – 35°N bands and higher (35%) in 40 – 50°N bands when PWLT is used.

Both of the above mentioned approaches equally well describe the total ozone changes during the last thirty years. Both EESC and PWLT related trends before and after 1979 are shown in Fig. 6.8.

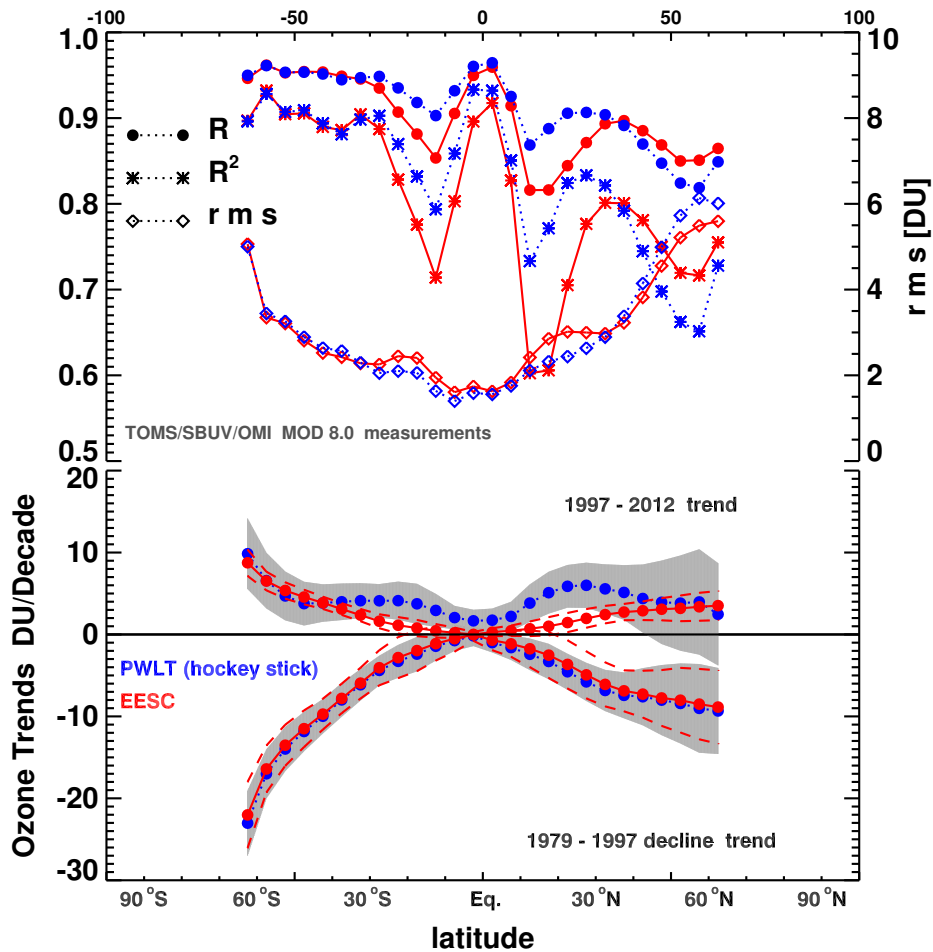


**Figure 6.8:** (top panel) Zonal distribution of the correlation,  $R^2$  and rms estimated for the 1979 – 2012 TOMS/SBUV/OMI V8.0 merged dataset from regression model based on Eq. 6.1 in red and the piecewise linear trend (PWLT or hockey stick) model in blue. (bottom panel) Zonal distribution of the linear trend of ozone in DU/decade units calculated for the EESC-based declining part of EESC during 1979 – 1997 and for the increasing part of EESC during 1997 – 2012 (red) as well as the trends before and after the ODS turnaround (1997) calculated by the PWLT model (blue). The statistical significance at two sigma level is indicated as grey shades for PWLT and dashed lines for EESC.

Both EESC and PWLT trends before 1979 are close to each other and agree within the 2-sigma error bars (grey shades for PWLT and dashed lines for EESC). The positive trends after 1997 are almost identical south of 40°S and north of 50°N (statistically insignificant) while elsewhere, larger differences are observed. The post-1997 PWLT trend in the low to middle latitudes are up to four times larger than the EESC based trend

but agree within the 95% error bars (15 – 30°N). The PWLT trend after 1997 are larger than expected and cannot be accounted as a full true response to the ODS decline after 1997 since PWLT regression analysis is very sensitive to the length of the data record after 1997 [Vyushin et al., 2010]. As the ODS related upward trend is fairly small, the PWLT is more strongly affected by uncertainties in the short-term variability.

## 6.6 Sensitivity of the Trends Acquired from Different Satellite Ozone Data Records

In this study, the merged WFDOAS GOME/SCIAMACHY/GOME-2 (GSG, 1995 – 2012) zonal total ozone dataset [Kiesewetter et al., 2010; Weber et al., 2011, 2012, 2013], SBUV/SBUV-2 MOD 8.6 (version 8.6), NASA ozone data product (1979 – 2012) [Frith et al., 2012; DeLand et al., 2012; Bhartia et al., 2013; McPeters et al., 2013] and NOAA SBUV/SBUV-2 V8.6 (1979 – 2012) [Wild et al., 2012; McPeters et al., 2013], the ground based measurements (1979 – 2012) [Fioletov et al., 2002, 2008; Hendrick et al., 2011], the GOME-Type total ozone record (GTO, 1996 – 2011) [Van Roozendael et al., 2006; Loyola and Coldewey-Egbers, 2012; Lerot et al., 2013] as well as the Multi Sensor Reanalysis (MSR) of total ozone [van der A et al., 2010] were also analysed in the regression model (Eq. 6.1, with winter-time eddy heat flux) to investigate the uncertainty in the long-term trends due to the use of different ozone datasets. The statistical analysis was applied for the same latitude range (65°S – 65°N). These ozone records had been used in the previous ozone assessments for trend analysis WMO [2011].

### 6.6.1 Quality of Satellite Ozone Data Records

The total ozone column datasets (1979 – 2012) used in the sensitivity study are summarized in Tables 6.1. The Table also provide the spectrometers from which the merged datasets are established with the published references for these datasets and URL sources.

The ground-based total ozone data record based on Dobson and Brewer spectrometer and filter ozonometer observations. Total ozone column measurements from Dobson and Brewer are precise (better than 1%) while ozone measurement from filter instruments are accurate within 3%. The

*Table 6.1: The total ozone column datasets used in the sensitivity study.*

Dataset	Spectrometers	Publication	URL source
Ground Measurements	Dobson Brewer SAOZ	Fioletov et al. [2002] Fioletov et al. [2008] Hendrick et al. [2011]	<a href="http://www.woudc.org">http://www.woudc.org</a>
SBUV V8.6 (NASA)	BUV Nimbus-4 SBUV Nimbus-7 SBUV/2 NOAA 9 to 19	Frith et al. [2012] DeLand et al. [2012] Bhartia et al. [2013] McPeters et al. [2013]	<a href="http://acd-ext.gsfc.nasa.gov/Data_services/merged/">http://acd-ext.gsfc.nasa.gov/Data_services/merged/</a>
SBUV V8.6 (NOAA)	SBUV Nimbus-7, SBUV/2 NOAA 9 to 19	Wild et al. [2012] McPeters et al. [2013]	<a href="ftp://ftp.cpc.ncep.noaa.gov/SBUV_CDR/">ftp://ftp.cpc.ncep.noaa.gov/SBUV_CDR/</a>
GSG (IUP - Bremen)	GOME SCIAMACHY GOME-2	Kiesewetter et al. [2010] Weber et al. [2011] Weber et al. [2012] Weber et al. [2013]	<a href="http://www.iup.uni-bremen.de/gome/wfdoas/merged/">http://www.iup.uni-bremen.de/gome/wfdoas/merged/</a>
GOME-Type (GTO)	GOME SCIAMACHY GOME-2	Van Roozendael et al. [2006] Loyola and Coldewey-Egbers [2012] Lerot et al. [2013]	<a href="http://www.esa-ozone-cci.org/">http://www.esa-ozone-cci.org/</a>
Multiple Satellite Reanalysis (MSR)	TOMS SBUV GOME SCIAMACHY GOME-2 OMI (assimilated)	van der A et al. [2010]	<a href="http://www.temis.nl/protocols/O3global.html">http://www.temis.nl/protocols/O3global.html</a>

ground-based dataset can provide a stable reference for validation of inter-instrument biases and drifts in satellite total-ozone measurements.

The construction of NASA SBUV/SBUV-2 Version 8.6 (MOD 8.6) ozone data product (1979 – 2012) is based on the calibration and analysis processes presented in Frith et al. [2012], DeLand et al. [2012], Bhartia et al. [2013] and McPeters et al. [2013]. On the other hand, the construction of NOAA SBUV/SBUV-2 V8.6 data [Wild et al., 2012; McPeters et al., 2013] is similar to the NASA dataset (satellites and time intervals) and included the removal of the drifts and biases in overlapping periods among instruments. The SBUV ozone columns show an agreement to within 1% when compared to ground based data from Brewer and Dobson spectrophotometers over the past 40 years.

The European satellite-borne sensors GOME/ERS-2, SCIAMACHY/ENVISAT and GOME-2/METOP-A perform UV spectral measurements and merged total ozone columns record is established by using different retrieval algorithms.

The merged WFDOAS GOME/SCIAMACHY/GOME-2 (GSG) total ozone dataset extends from 1995 to 2012 and combines data from GOME (1995 – 2003) [Coldewey-Egbers et al., 2005; Weber et al., 2005], SCIAMACHY (2002 – 2006) [Bracher et al., 2005] and GOME-2 (2007 – present) [Weber et al., 2007]. GOME was very stable over the operational period (1995 – 2012) and selected as a reference for bias adjusting SCIAMACHY and GOME-2 data [Kiesewetter et al., 2010; Weber et al., 2011, 2012, 2013]. Adjustments were made by determining a mean scaling factor for GOME-2 and SCIAMACHY from the monthly mean zonal mean ozone ratio with respect to GOME. The GSG data (March 1996 – December 2012) was combined with TOMS/SBUV data (January 1979 – February 1996) without adjustments of the GSG data.

The GOME-Type total ozone record (GTO) combines the measurements from the three European satellite-borne sensors. The GTO data is based on the DOAS approach using products obtained with the GOME Data Processor (GDP5/GODFIT) [Van Roozendaal et al., 2006; Loyola and Coldewey-Egbers, 2012; Lerot et al., 2013]. Similar to GSG data, the GTO data (July 1995 – December 2012) was combined with TOMS/SBUV data (January 1979 – June 1995) without adjustments.

The European datasets obtained from both algorithms show very good agreement (within 1%) with ground-based data and with other satellite data [Weber et al., 2005; Fioletov et al., 2008; Koukouli et al., 2012; Lerot et al., 2013].

The sensitivity study also included the Multi Sensor Reanalysis (MSR) of total ozone [van der A et al., 2010] which is a single coherent total

ozone dataset created from all available ozone column data (14 datasets) measured by polar orbiting satellites (see Table 6.1) in the near-ultraviolet Huggins band in the last thirty five years. A bias correction scheme based on independent ground-based total ozone data (WOUDC) was applied to all satellite observations, then data assimilation based on a chemical transport model driven by ECMWF meteorological fields was applied to create a global dataset of total ozone analyses. The bias of the MSR analyses is less than 1% compared to the corrected satellite observations.

## 6.6.2 EESC/Linear Trends for all Data Records

The statistical model (Eq. 6.1, with wintertime eddy heat flux) was applied for the same latitude range ( $65^{\circ}\text{S} - 65^{\circ}\text{N}$ ) of the different datasets, the results are generally in good agreement with the MOD 8.0 results, the fit coefficients of the different datasets follow the same pattern as that for the MOD 8.0 merged dataset and are agree within 2-sigma.

The piecewise linear trend is also applied to the above mentioned datasets and the quality of the PWLT trends in comparison with the EESC trends are shown in Figs. 6.9 and 6.10. The PWLT trends for the different datasets are shown in colored bars with 2-sigma error variability while the grey shadow depicts the spread of the EESC-trend ( $\pm 2$ -sigma).

The pre-turnaround trends before 1979 for both EESC and PWLT approaches are very close to each other, the negative ODS trend dominates as expected from the ODS increase. On the other hand, the positive trends after 1997 are greatly influenced by the short-term variability (and indirectly through the low-frequency components of the corresponding proxy) and therefore significantly differs from the EESC trends in some latitudes (subtropics) and between datasets. It is noticeable that the PWLT linear trends in NASA V8.6 data at low latitudes (tropics) are much smaller than the other records, however, they fit very well to the EESC trends. There are also some negative trends in the northern mid-latitudes for WOUDC dataset, but not significantly different from zero. The linear trends are close to 3–5 DU/decade for most datasets and latitudes, at southern high latitudes the trends get higher and in the extratropics they agree to within  $2\sigma$  with EESC trends. In the sub-tropics (below  $25^{\circ}\text{S/N}$ ), the datasets show linear trends that are significantly different from the post 1997 EESC trend, nevertheless, within 2-sigma fit parameters for all datasets agree. Between  $40^{\circ}\text{S}$  and  $40^{\circ}\text{N}$ , most datasets now show more or less statistically significant total ozone column increases since 1997. The EESC trends are almost identical and indicates that all the data sets are highly consistent.

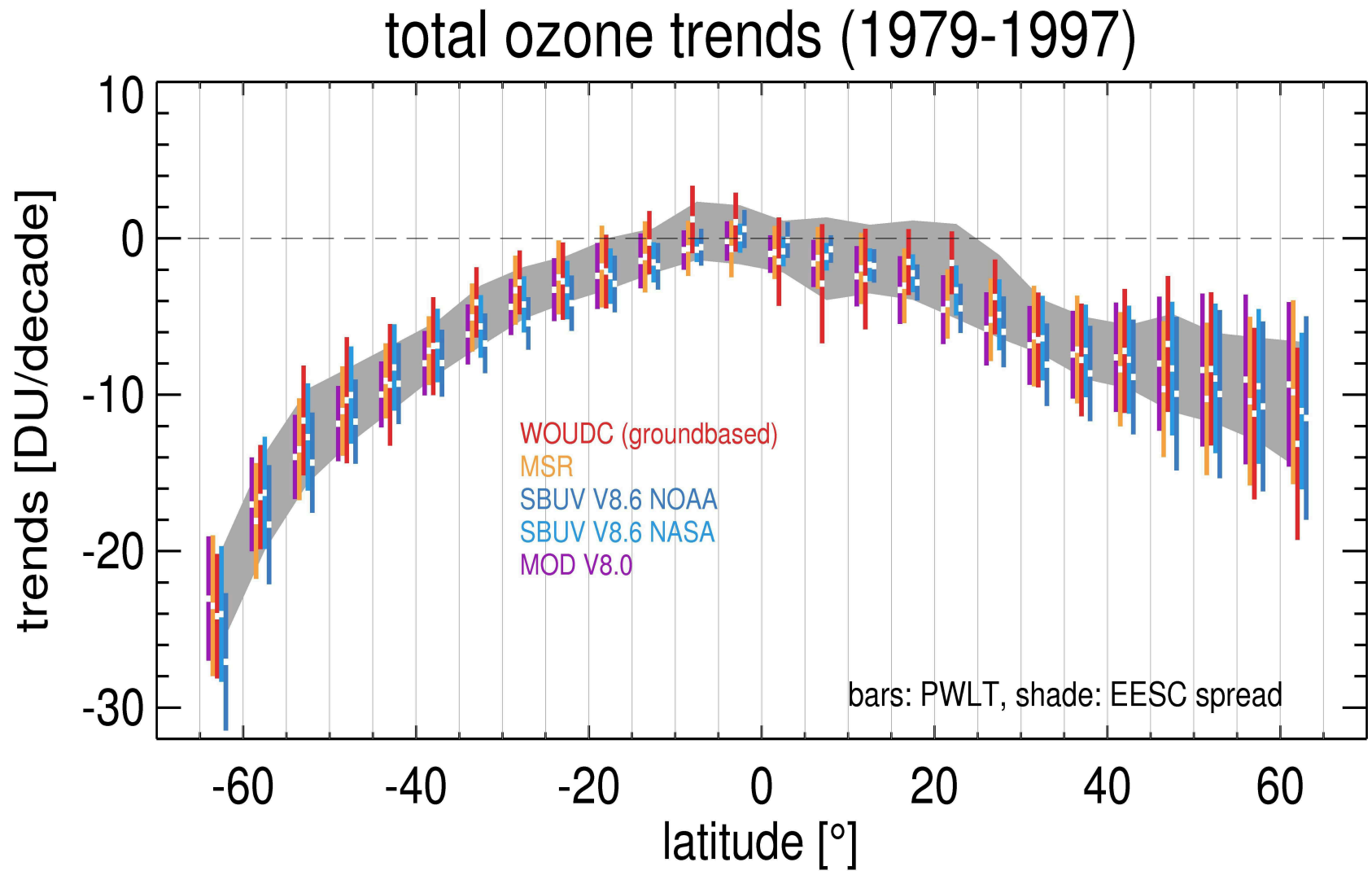


*Figure 6.9: Comparisons between the spread of the EESC (grey shadow) and PWLT trends (in colored bars with 2-sigma error) before 1997 for the different ozone datasets.*

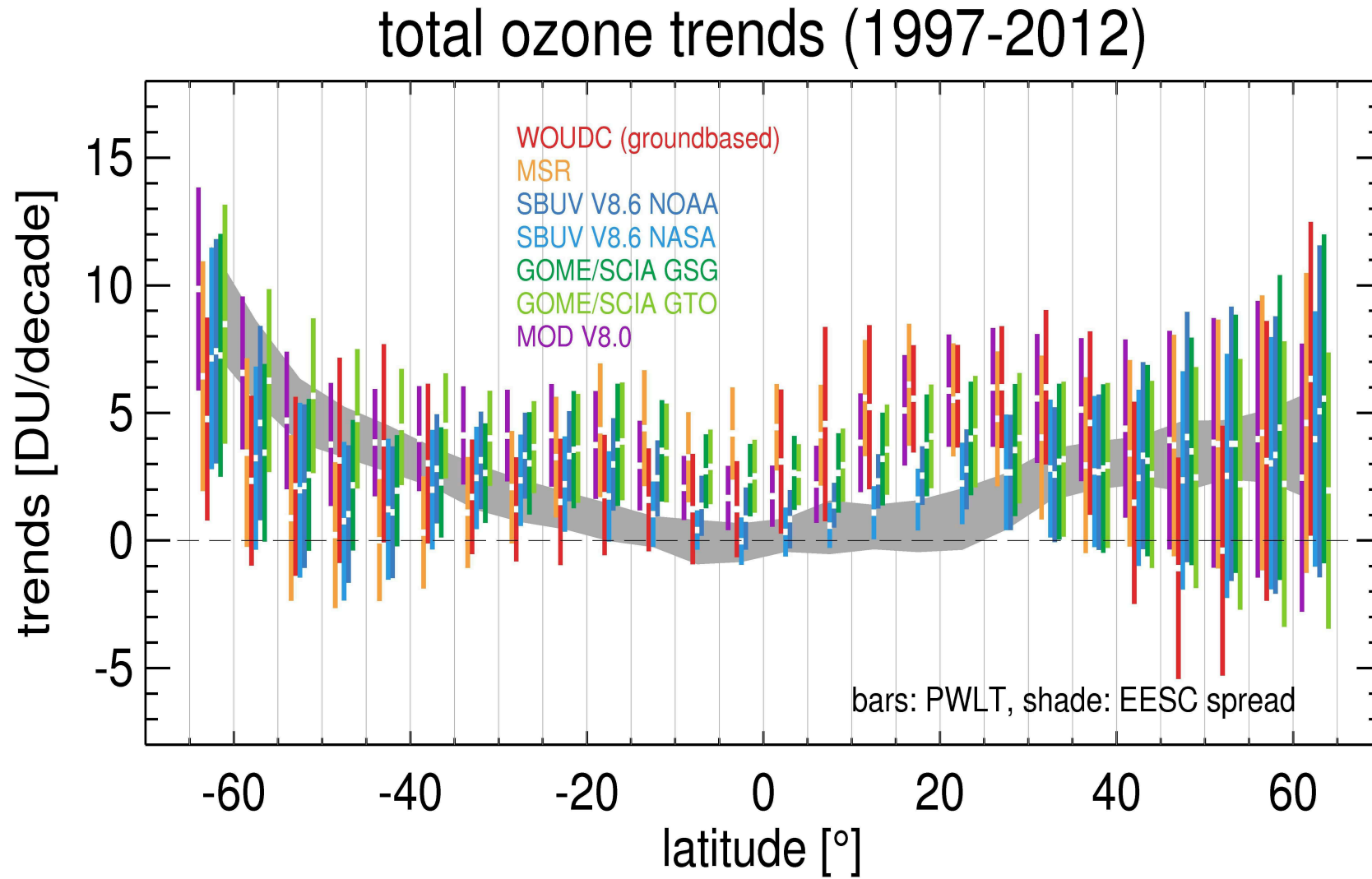


*Figure 6.10: Comparisons between the spread of the EESC (grey shadow) and PWLT trends (in colored bars with 2-sigma error) after 1997 for the different ozone datasets.*

Figures. 6.9 and 6.10 display a change in the total ozone column trends from a steady decline until 1997 to a slightly increasing trend afterwards. The recent increase in total ozone can not be attributed solely to the declining ODS since the rate of decline is slow and the year-to-year variability of the various factors dominates the ozone variability. This is demonstrated in the larger variability in the linear trend among the different datasets with the error bars frequently crossing the zero-trend line. Nevertheless, this increase confirms that the Montreal Protocol is succeeding in hindering total ozone decline.



## Summary and Perspectives

### 7.1 Summary

The harmonisation of ozone temperature dependent absorption cross section spectra of SCIAMACHY and GOME-2 was carried out by the re-evaluation of the available FM cross section data. This comprises the understanding of the physical problems associated with the measured  $O_3$  absorption cross section spectra, understanding the data selection to judge which results should be taken as a starting point for re-analysis and understanding the previous analysis procedures used to enable improving the algorithm to be used in future measurements. The re-analysis re-evaluated the concatenation of ozone optical density measurements obtained from CATGAS measurements and applied new ways to absolutely calibrate the cross sections using absolute reference cross section data at reference wavelengths and broad spectral windows.

The new concatenation of the partial spectra of the eight absorption measurements for each temperature from the GOME-2 FM3 campaign produced relative cross section spectra covering the GOME-2 spectral

range and correctly preserved the temperature dependence in each band. The absolute scaling of the optical density spectra using the literature data convolved to GOME-2 slit function showed an increase of around 1% compared to the absolute scaling done in the first analysis. Moreover the absolute scaling at wavelengths in the Huggins band are in an excellent agreement compared to the absolute scaling at wavelengths in the Hartley and Chappuis bands, the discrepancy of 8% between the scaling at 334 nm and the other selected wavelengths in the Gür version does not exist in the new concatenation and absolute scaling.

The revised data show good agreement with high resolution absolute measurement data (BMD and Bass Paur) in the different bands when the integrated absorption cross sections are compared. The integrated cross sections are insensitive to spectral resolution and wavelength calibration. A non-linear least square fit is used to further compare the data in the DOAS region (retrieval window), the fit includes parameters that account for the spectral resolution, wavelength calibration and baseline drifts. The fit confirmed the good quality of the new data and showed an increase 2–7% in the differential scaling compared to the Gür data.

The retrieval of total ozone column (WFDOAS) using the revised reference data corrects the 8% overestimation when the FM3 version 3 data is used and is now 1% within the values currently retrieved based upon convolved GOME FM cross section data [Burrows et al., 1999a]. Moreover, the fit residuals are slightly improved with the new data.

The re-analysis of the SCIAMACHY FM data is performed with a new concatenation that produced a bigger absorption structures in the Huggins band and preserved the correct temperature dependence in the Chappuis and Wulf bands. The new data agrees well when compared to the literature data in the Hartley and the Chappuis band and a slight decrease in the Huggins band is found. On the other hand, the non-linear least square fit in the DOAS region shows a high degree of consistency with the data of BMD and Bass Paur and an increase of around 3.5% to Bogumil data, the consistency persists. The revised data obtained in this study was successfully tested in the SCIAMACHY data processing, the retrieved total ozone amounts are found 3.5% smaller when compared to the amounts measured using Bogumil data and are within +0.5% compared to the amounts routinely retrieved with SCIAMACHY which use Bogumil et al. data but with a differential scaling of 5.3% and a shift of 0.08 nm applied to match the GOME WFDOAS total ozone retrieval.

The ozone cross section data of both spectrometers are also in good agreement with new high spectral resolution cross section data measured in our laboratory [Serdyuchenko et al., 2011, 2013; Gorshelev et al., 2013]. The revised ozone cross section spectra are available on the homepage of the UV satellite data and science group of the Institute of the Environmental Physics, University of Bremen ([http://www.iup.uni-bremen.de/UVSAT\\_material/data/xsections/SCIA\\_O3\\_Temp\\_cross-section\\_V4.1.DAT](http://www.iup.uni-bremen.de/UVSAT_material/data/xsections/SCIA_O3_Temp_cross-section_V4.1.DAT) and [http://www.iup.uni-bremen.de/UVSAT\\_material/data/xsections/GOME-2\\_FM3\\_O3\\_Temp\\_cross-section\\_V5\\_0.txt](http://www.iup.uni-bremen.de/UVSAT_material/data/xsections/GOME-2_FM3_O3_Temp_cross-section_V5_0.txt)).

In this study, long-term evolution of zonal mean annual mean total ozone measurements TOMS/SBUV/OMI Merged Ozone Data set (MOD) Version 8.0 [Stolarski and Frith, 2006] from merged datasets of various satellites over the period 1979 – 2012 in 5° zonal bands between 65°S and 65°N, were analysed by multiple linear regression. The regression analysis included different explanatory variables representing dynamical and chemical processes that modify global ozone distributions such as QBO, solar cycle, aerosols, ENSO, eddy heat flux, AO/AAO and the EESC terms. The TOMS/SBUV/OMI merged data were analysed first. The regression model explained about 60 – 95% of the ozone variability across the considered latitude range. The QBO signal dominates the tropical region and contributes up to  $\pm 7$  DU depending on its phase while at higher latitudes the eddy heat flux signal ( $\pm 10$  DU) and to lesser extent the ENSO and AO/AAO signals represent the major attribution to ozone variations. The effects of El Chichón (1982) and Mt. Pinatubo (1991) are limited to the periods of volcanic eruptions and are responsible for a large fraction of ozone loss (up to -14 DU and -22 DU, respectively), the signal is more prominent and statistically significant in the Northern Hemisphere. The signature of the 11 year solar cycle is evident over all latitude bands and the contribution to ozone variability can reach about 13 DU from solar maximum to solar minimum. Replacing the MgII index by the F10.7 cm proxy, does not change the ozone signal of the other explanatory variables or the statistical significance of the model although the Mg II index is believed to correlate better with solar UV irradiance changes than the F10.7 cm solar flux [Viereck et al., 2001, 2004].

Figure 6.6 shows that the EESC function is the dominant cause of long-term ozone decline in the stratosphere before 1997 and an increase afterwards. The trend is statistically significant and indicates the onset of ozone recovery as expected from the slow decrease in the stratospheric halogens after measures introduced by the Montreal Protocol and amendments to phase out the ODS. The comparison with the trends ob-

tained from PWLT model yields similar results for the long-term decline before 1997. On the other hand, the positive PWLT turnaround trends are larger than the EESC trend at northern middle latitudes. The observed ozone changes are as expected from the turnaround in the ODS since 1997, however, the large year-to-year variability still masks the exact magnitude of the recent (and weak) ODS related trend.

A sensitivity study was carried out by comparing the results obtained from the regression model (Eq. 6.1) for MOD 8.0 dataset and the results obtained from the merged GOME/SCIAMACHY/GOME-2 WFDOAS dataset [Kiesewetter et al., 2010; Weber et al., 2011, 2012, 2013], NASA SBUV/SBUV-2 MOD 8.6 ozone data from 1979 till 2012 [Frith et al., 2012; DeLand et al., 2012; Bhartia et al., 2013; McPeters et al., 2013] and NOAA data product [Wild et al., 2012; McPeters et al., 2013], the ground based measurements (1979 – 2012) [Fioletov et al., 2002, 2008; Hendrick et al., 2011] and the GOME-Type total ozone record (GTO, 1995 – 2011) [Van Roozendaal et al., 2006; Loyola and Coldewey-Egbers, 2012; Lerot et al., 2013] as well as the Multi Sensor Reanalysis (MSR) of total ozone [van der A et al., 2010]. This allows us to assess the uncertainty which may arise from the observational data record. Although, some changes in the individual fit parameters were found, within the 2-sigma error bars the results were identical.

The fits of the different datasets are generally in good agreement with the TOMS/SBUV/OMI MOD8.6 results, the fit coefficients follow the same pattern as that for the MOD 8.0 merged dataset and are agreed within 2-sigma.

The piecewise linear trend is applied to the above mentioned datasets and the quality of the PWLT trends are assessed by the comparison with the EESC trends.

In particular, the EESC related ozone trend is almost identical for the different total ozone datasets, so that the data quality of total ozone data appears to be not an issue here. The PWLT after 1997 is generally higher than the linear part of the EESC trend but except for the northern subtropics they agree within 2-sigma.

In summary, the updated trends up to end of 2012 consolidate the re-

sults from other studies (e.g. Mäder et al. [2010]) that the observed trend change since 1997 proves the effectiveness of the Montreal Protocol phasing out ODS depleting substances. Since the ODS decline is now fairly slow (Fig. 6.1), the recent extratropical annual mean total ozone trends are strongly influenced by large year-to-year variability in atmospheric dynamics.

## 7.2 Perspectives

The revised GOME-2 FM3 and SCIAMACHY FM ozone absorption cross section data obtained in this study are ready and suitable for SCIAMACHY and GOME-2 data processing (retrieval) since they show a high degree of inter-consistency and consistency with other cross section data. The new data generally slightly improved the fit residuals. It is recommended to use the quadratic parameterisation of the spectra to reduce the impact from a cross section spectrum at one temperature.

The comparisons and validations conducted in Chapter 5 can be applied to the temperature dependent absorption cross section spectra of ozone for MetOP-B GOME-2 spectrometer (FM21) to assess the quality of the data and investigate whether a re-analysis is needed. The procedure performed to correct the FM3 data can be used to carry out the re-analysis.

The detecting of ozone recovery corresponding to the implementation of the Montreal Protocol is essential, separation of the signatures of ODS-related ozone trends from those of low-frequency variability in atmospheric dynamics remains challenging, additional work can be performed for better assessment. The regression analysis could be improved to evaluate an accurate ODS related trend after 1997 over the different latitudes by using additional explanatory variables (e.g., equivalent latitude EESC). Moreover, the evaluated trends can be compared with the trends estimated from the simulations by Chemistry Climate Models (CCM) to examine recent ozone changes by climate change (greenhouse gases).

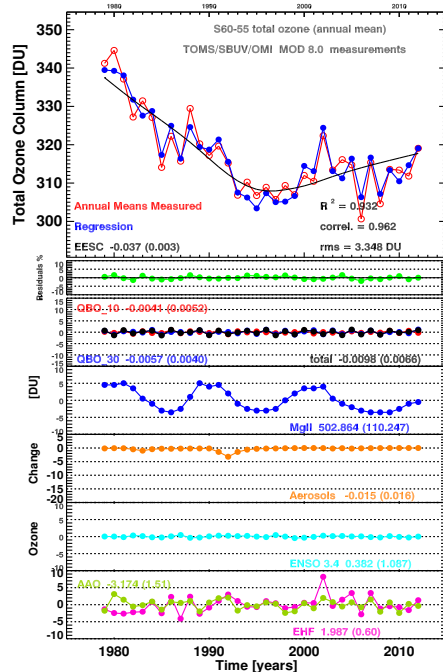
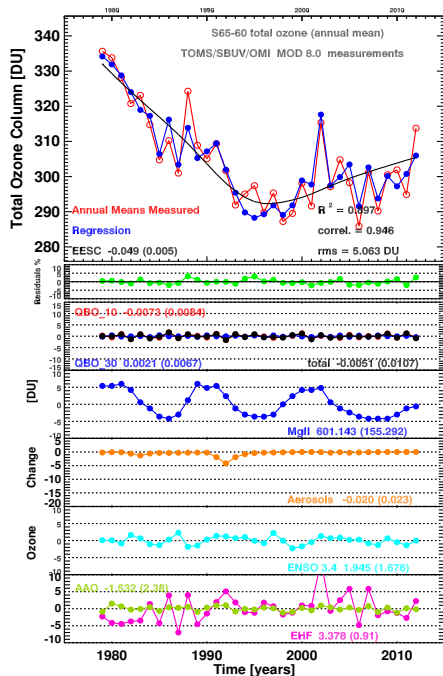


# Appendix

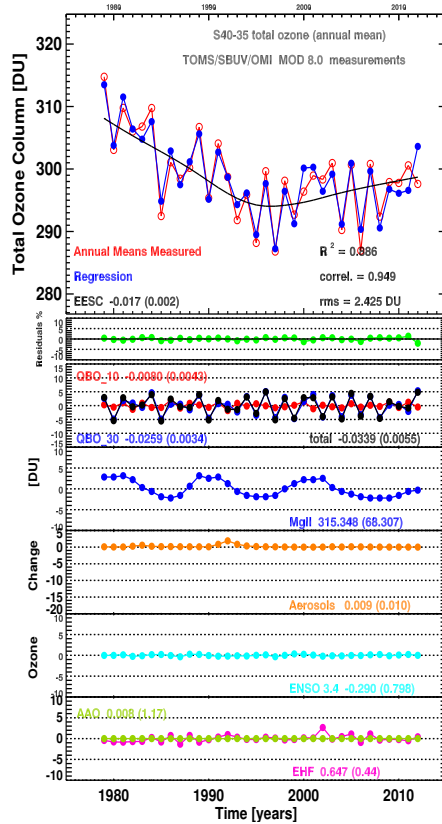
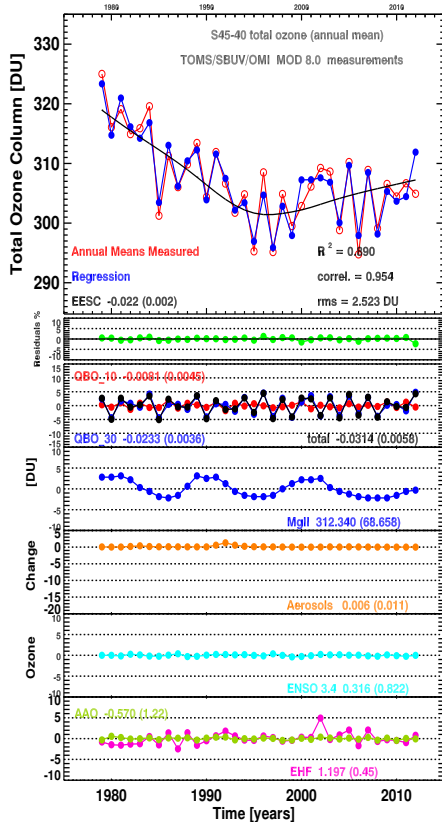
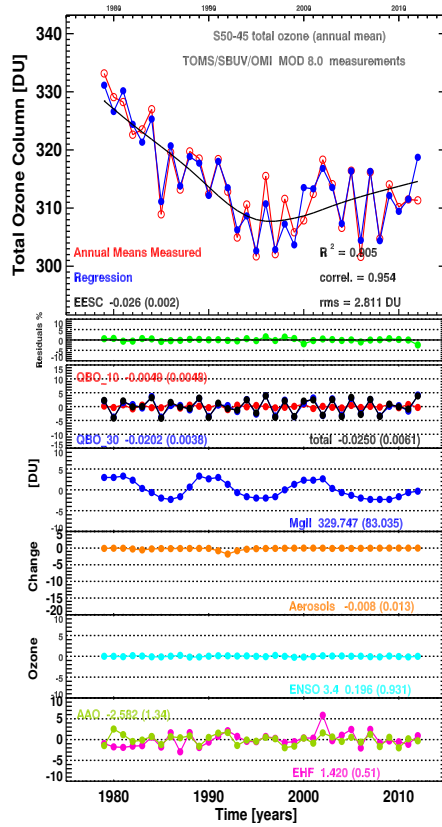
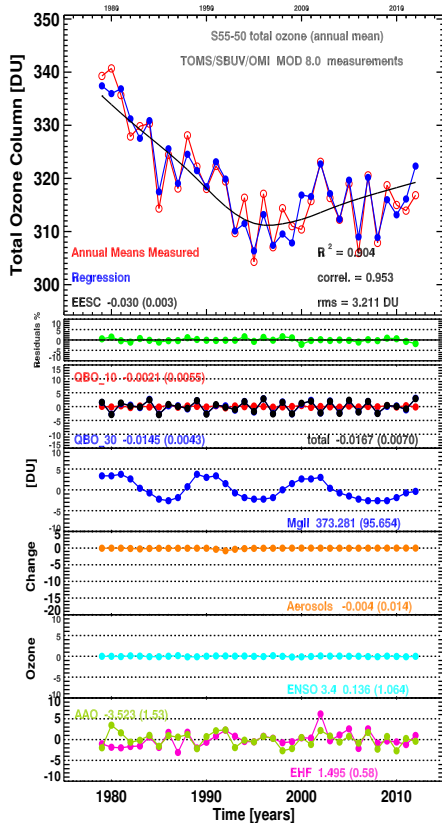


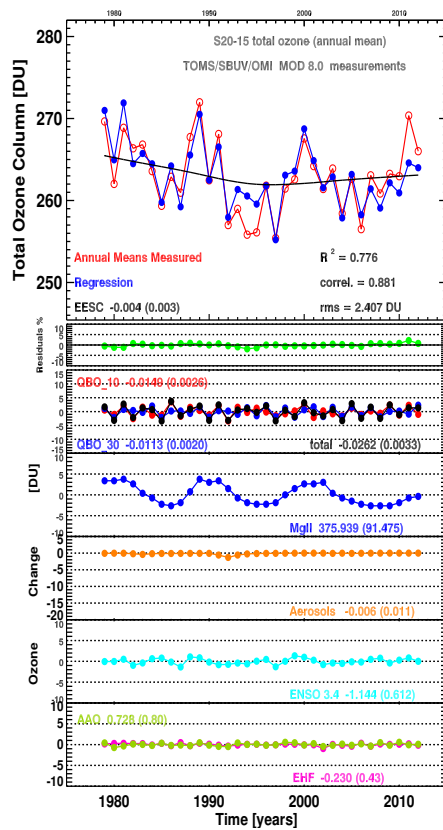
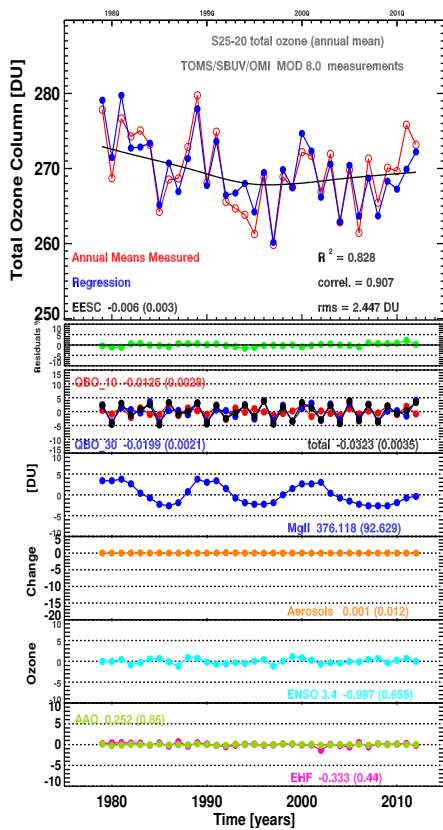
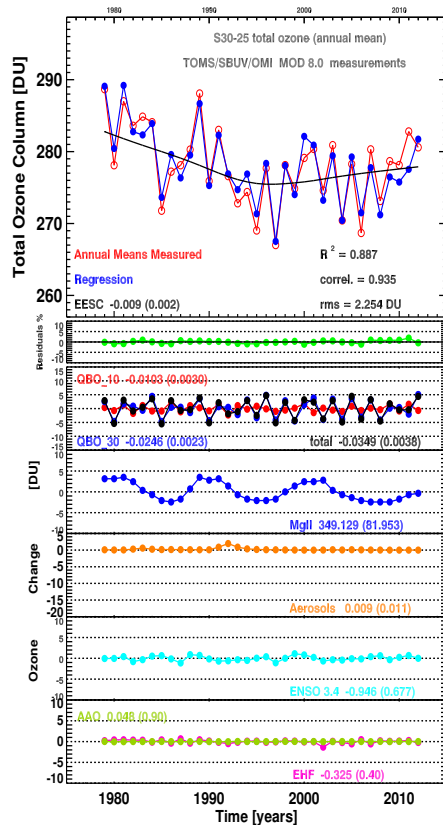
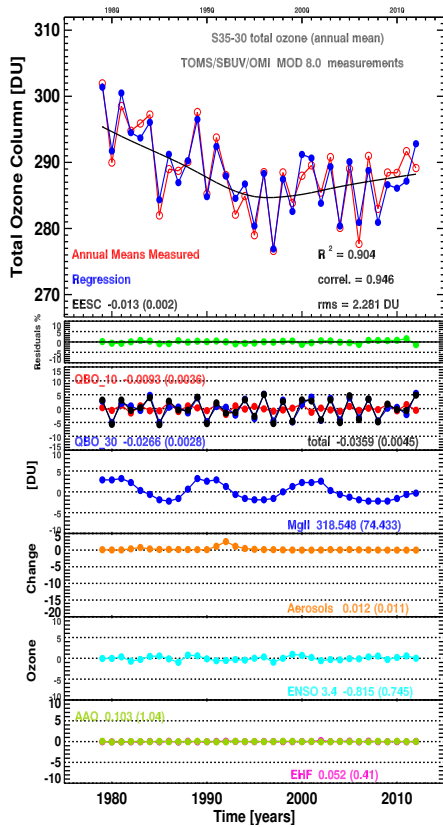
# Total Ozone Trends (EESC) TOMS/SBUV/OMI MOD V8.0 (1979 – 2012)

Ozone variations attributed to the different explanatory variables estimated from the statistical multiple linear regression model applied to TOMS/SBUV/OMI MOD 8.0 (1979 – 2012) of the twenty six 5° wide latitude mean ozone data bands from 65°S to 65°N.

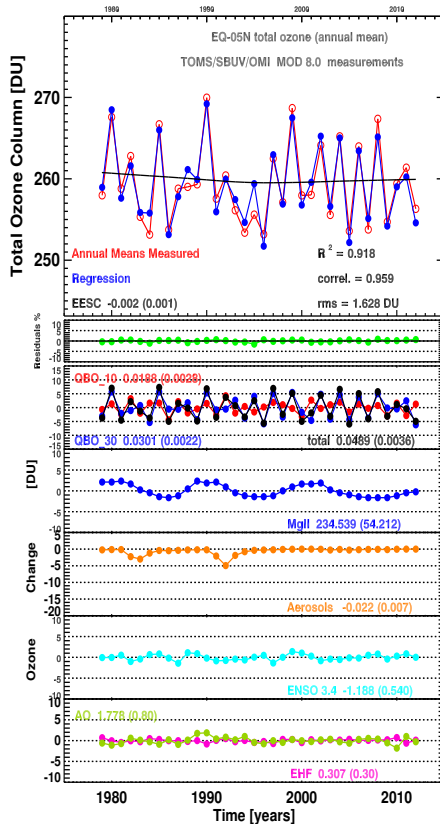
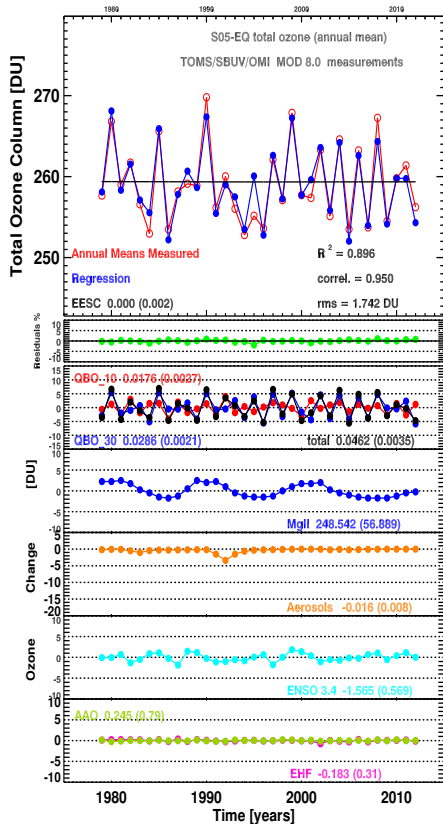
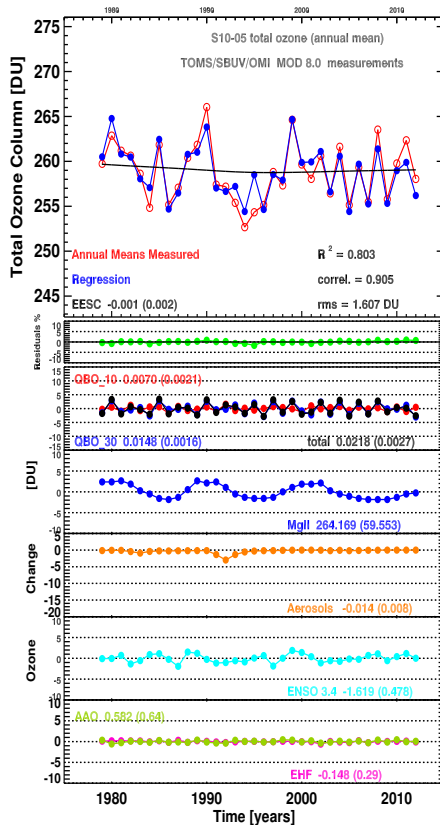
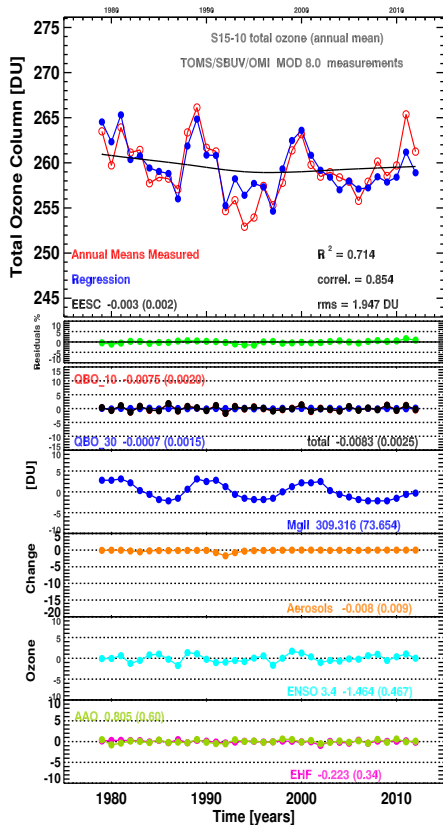


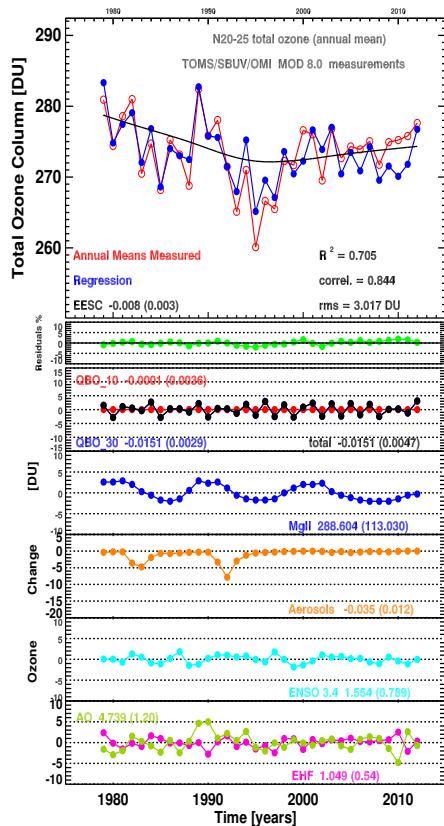
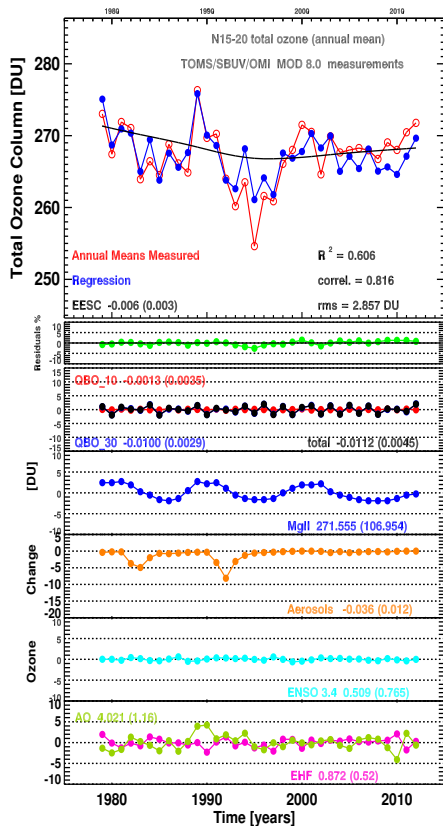
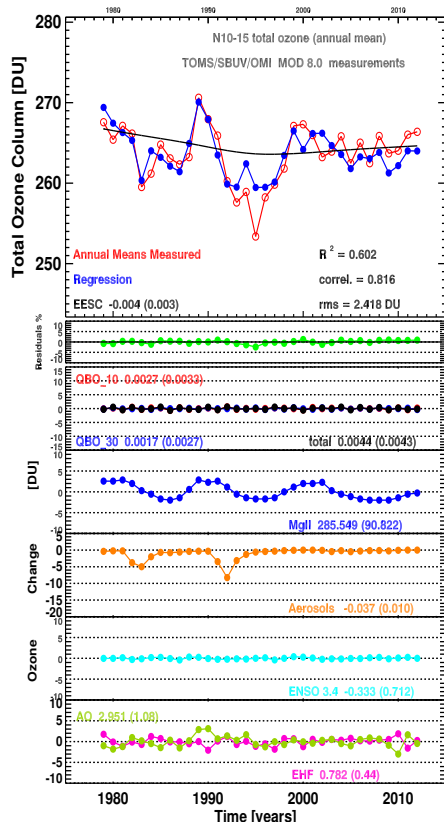
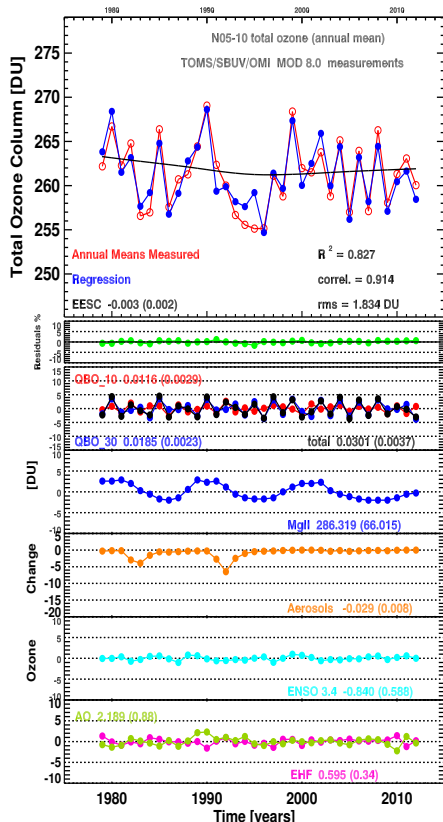
APPENDIX A. TOTAL OZONE TRENDS (EESC)  
TOMS/SBUV/OMI MOD V8.0 (1979 – 2012)



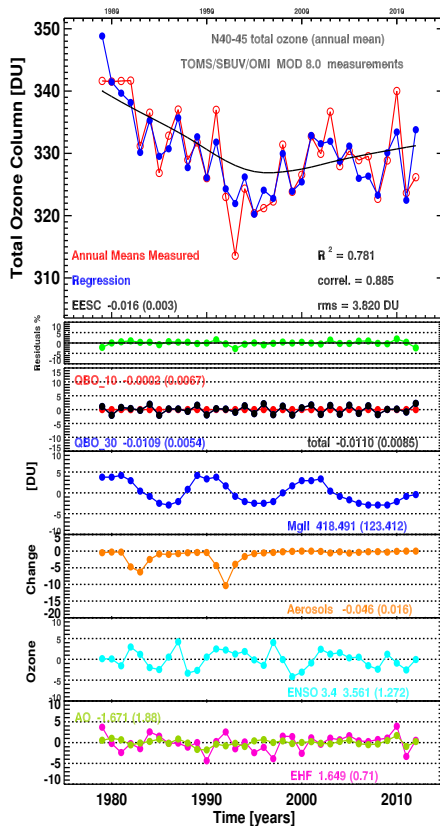
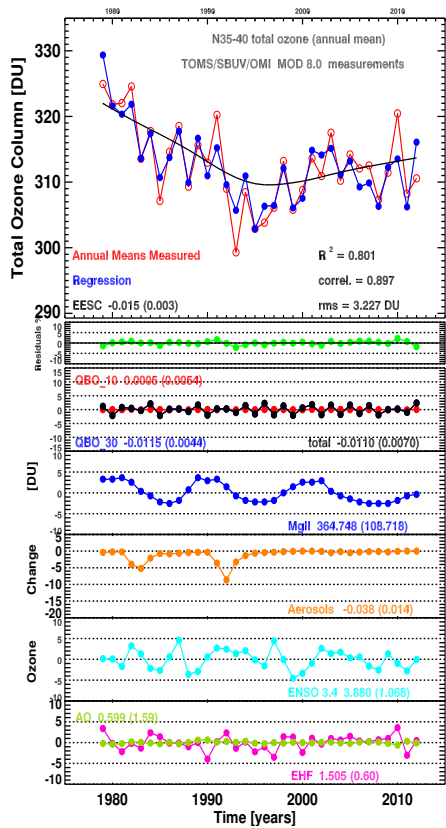
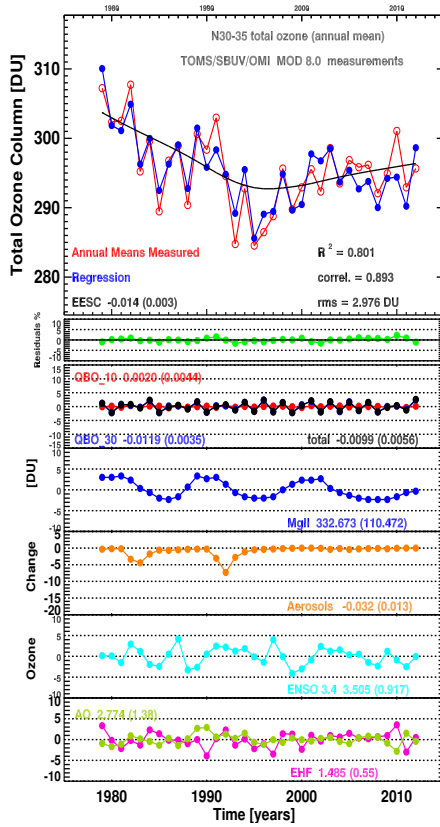
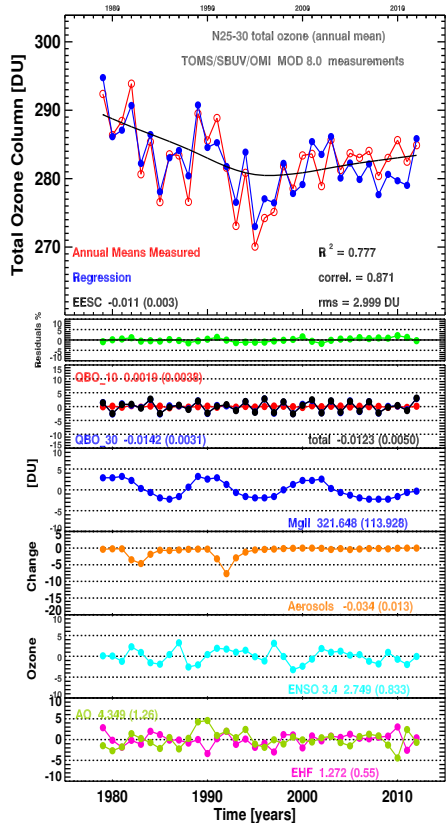


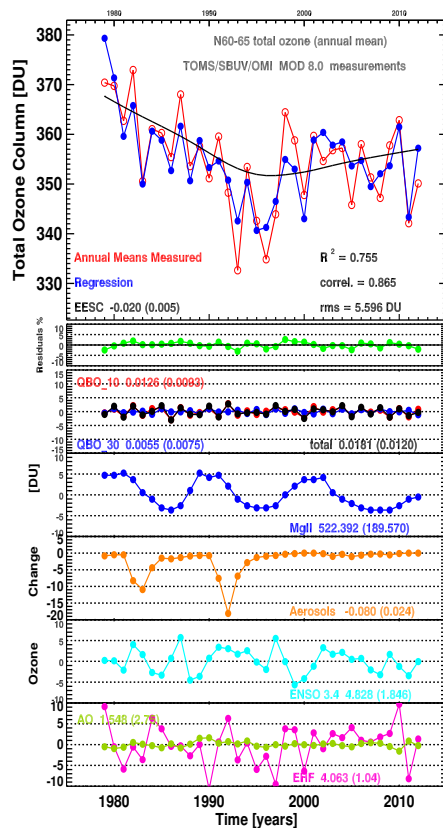
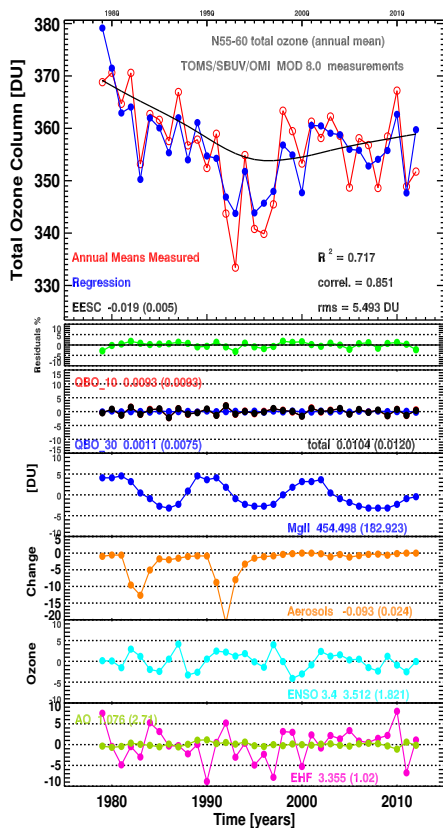
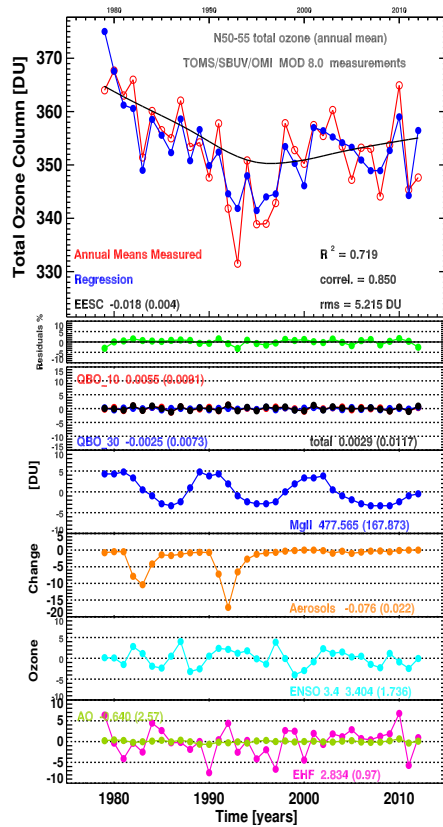
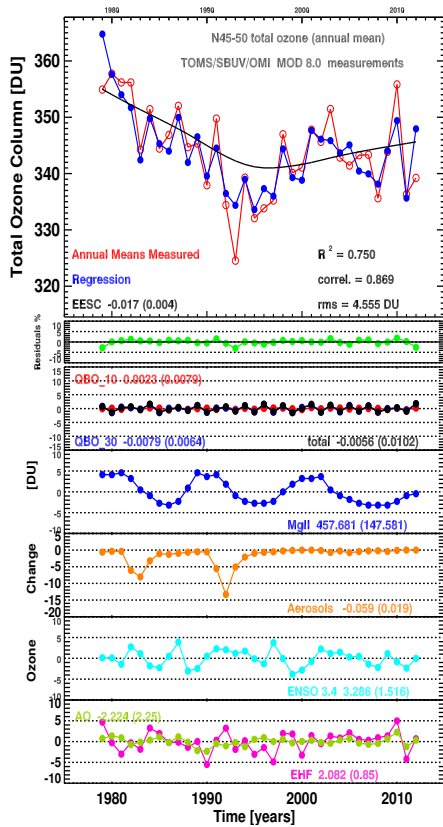
APPENDIX A. TOTAL OZONE TRENDS (EESC)  
TOMS/SBUV/OMI MOD V8.0 (1979 – 2012)





APPENDIX A. TOTAL OZONE TRENDS (EESC)  
TOMS/SBUV/OMI MOD V8.0 (1979 – 2012)





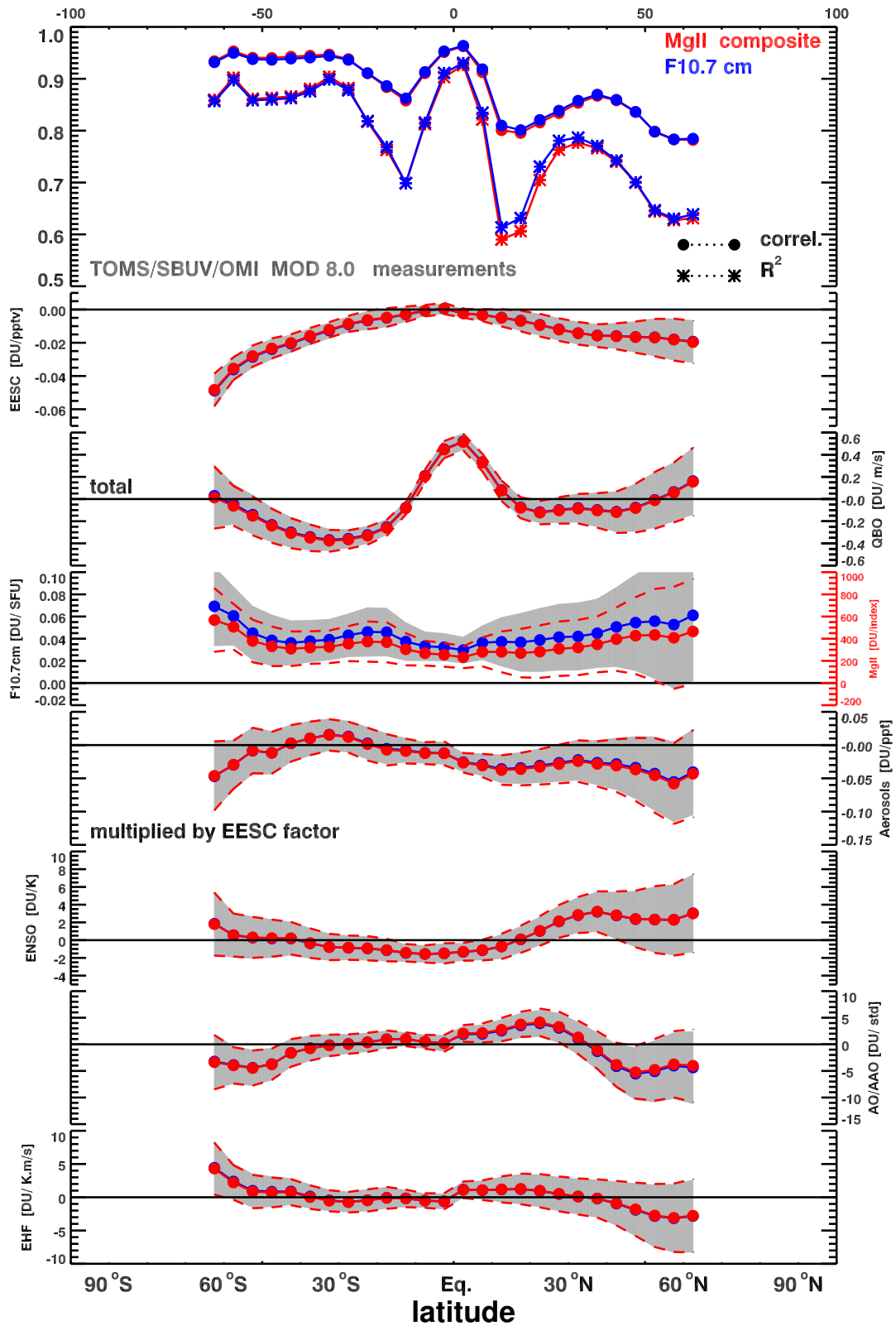


# Appendix **B**

## Total Ozone Trends F10.7 cm vs. MgII Index

Ozone variations attributed to the different explanatory variables estimated from the statistical multiple linear regression model applied to TOMS/SBUV/OMI MOD 8.0 (1979 – 2012) of the twenty six 5° wide latitude mean ozone data bands from 65°S to 65°N using the solar flux at 10.7 cm (blue) and core-to-wing ratio of the MgII line at 280 nm (red). The statistical significance at two sigma level for proxy contributions is indicated as grey shades for 10.7 cm analysis and red dashed lines for MgII analysis.

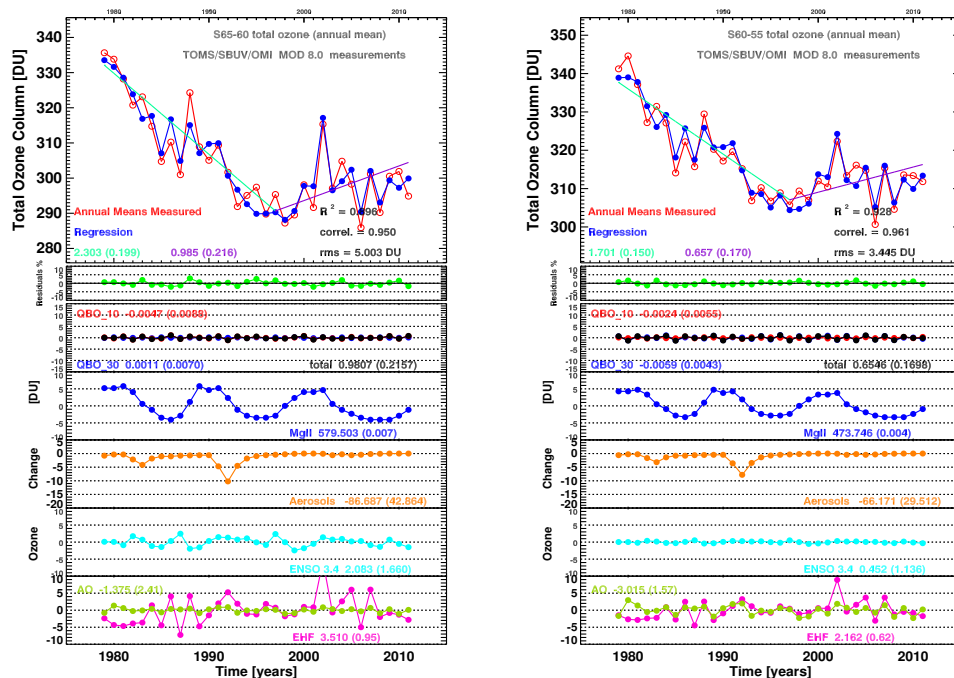
APPENDIX B. TOTAL OZONE TRENDS  
 F10.7 CM VS. MGII INDEX



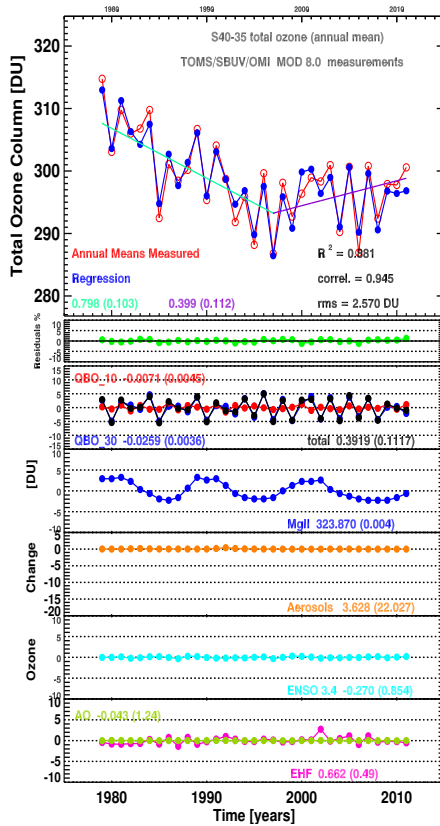
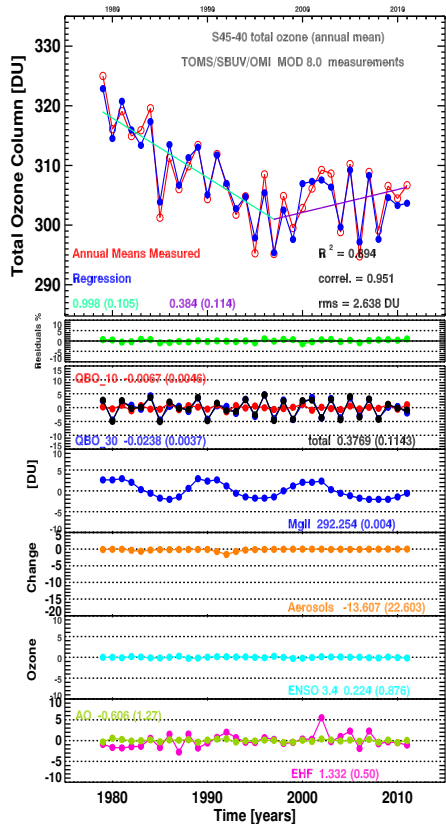
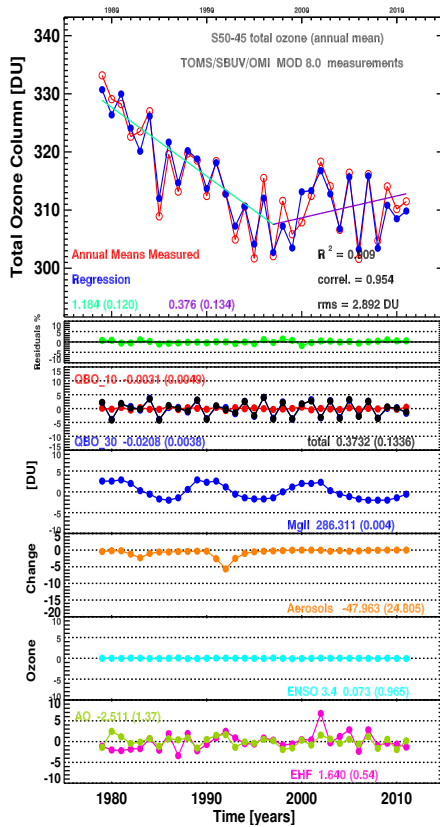
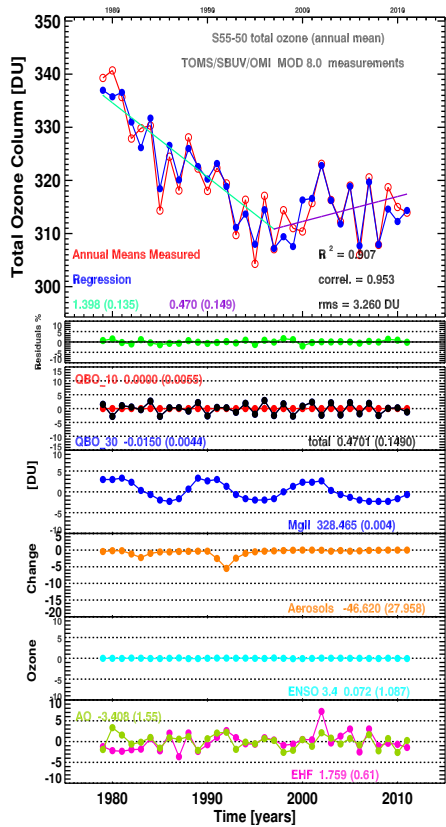
# Appendix C

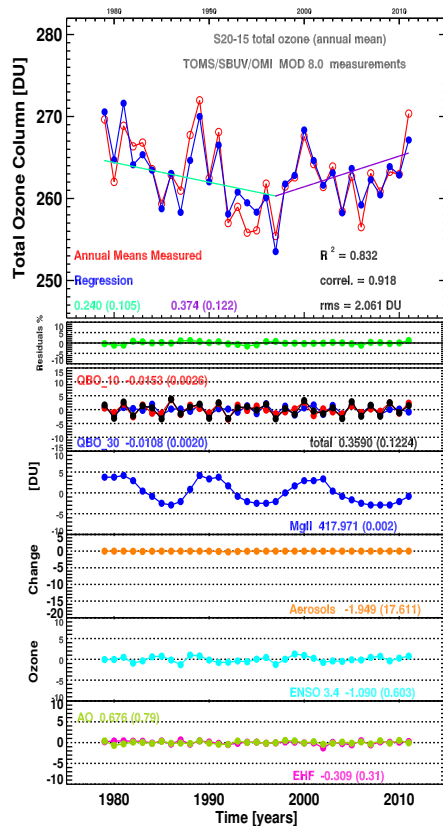
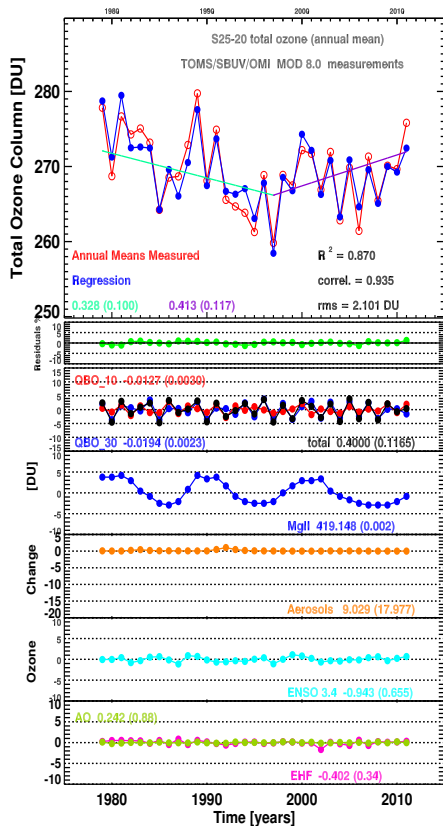
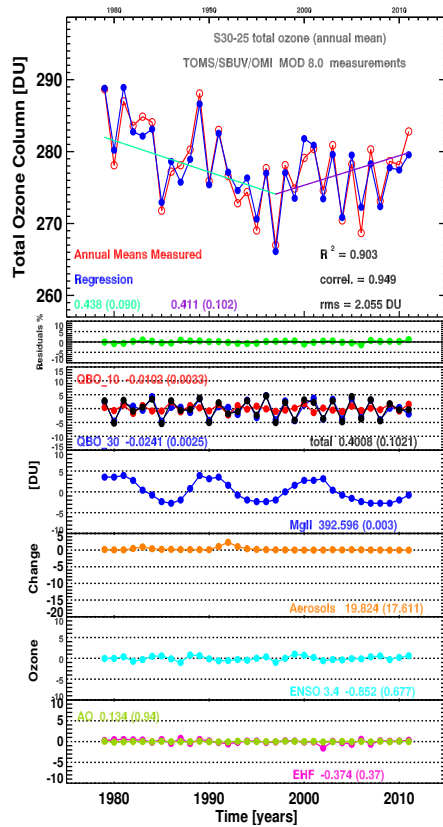
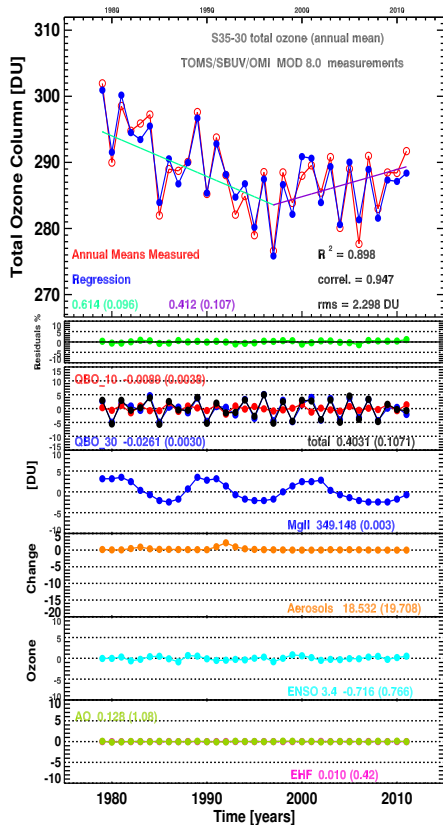
## Total Ozone Trends (PWLT) TOMS/SBUV/OMI MOD V8.0 (1979 – 2012)

Ozone variations attributed to the different explanatory variables estimated from the statistical multiple piecewise linear trend (PWLT) regression model applied to TOMS/SBUV/OMI MOD 8.0 (1979 – 2012) of the twenty six 5° wide latitude mean ozone data bands from 65°S to 65°N.

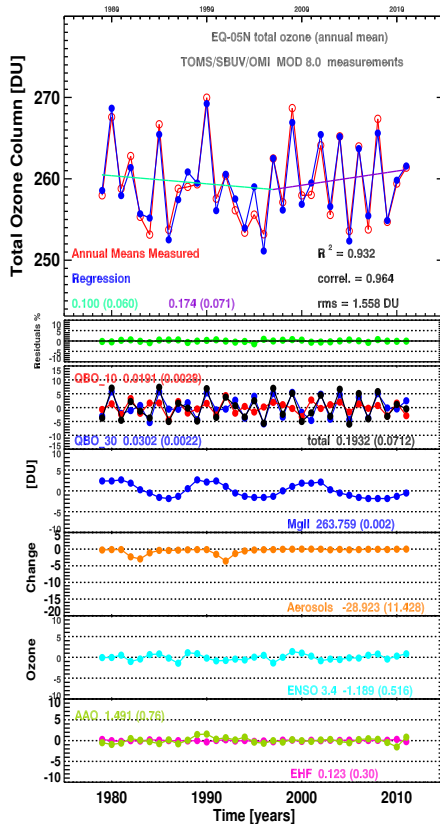
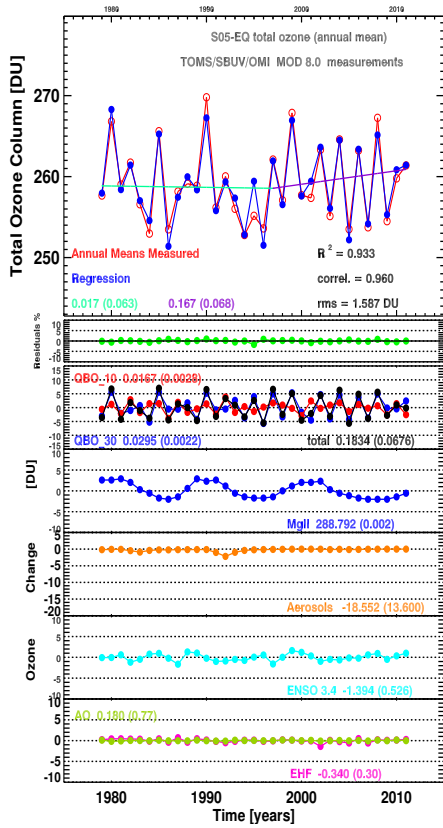
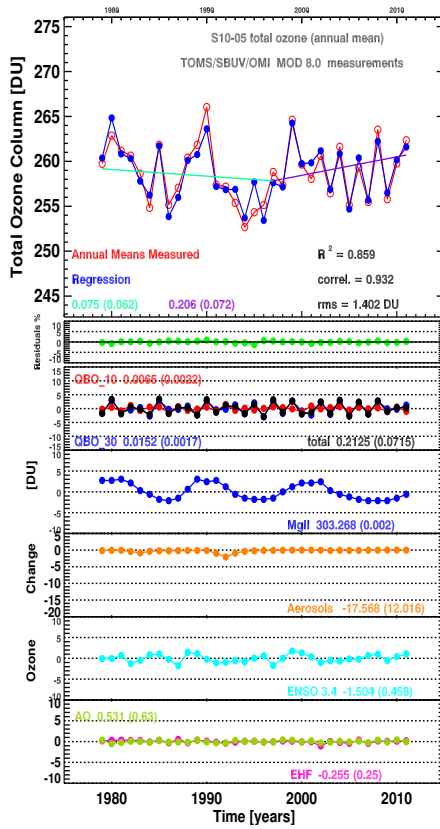
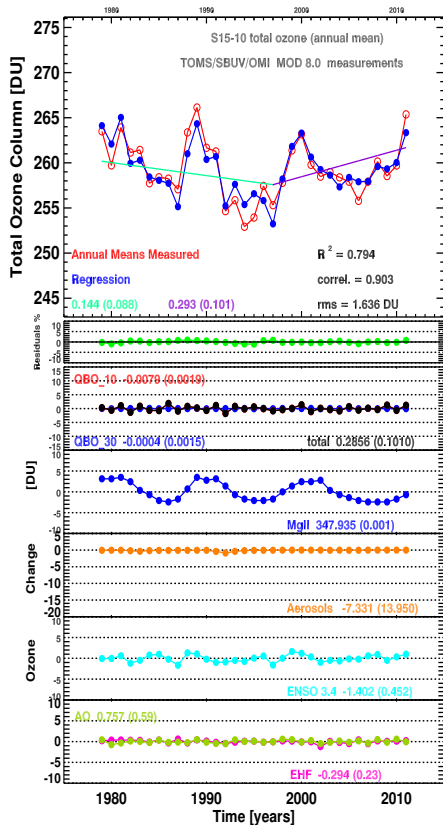


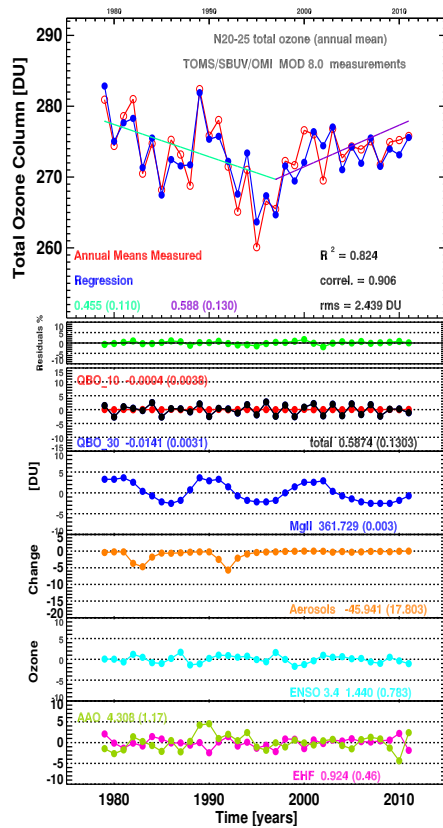
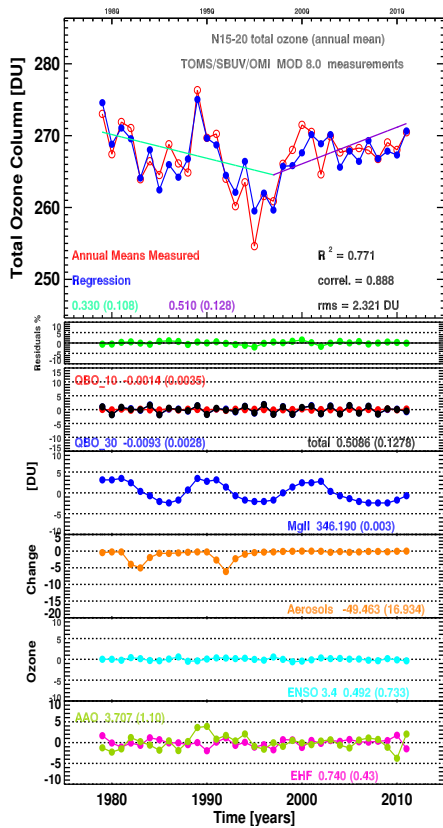
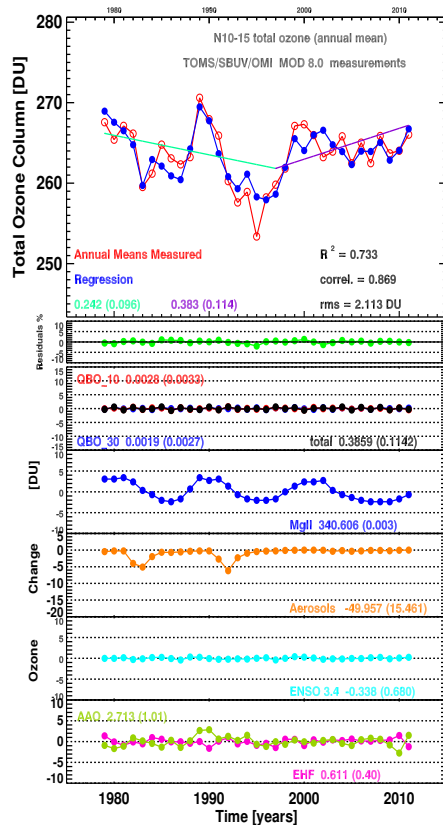
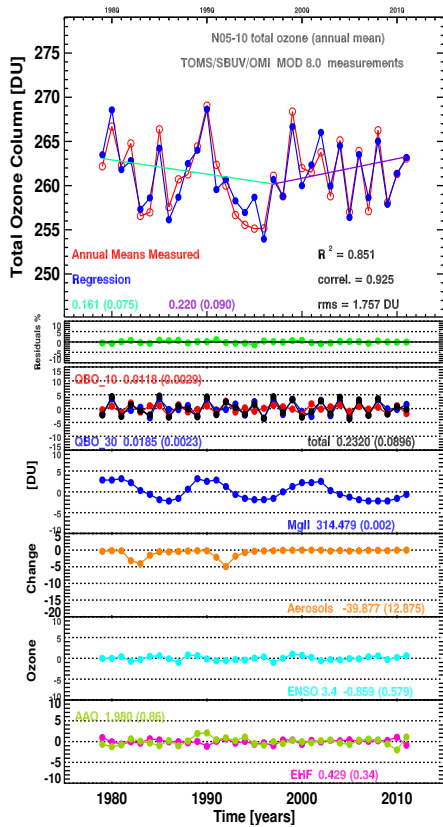
APPENDIX C. TOTAL OZONE TRENDS (PWLT)  
TOMS/SBUV/OMI MOD V8.0 (1979 – 2012)



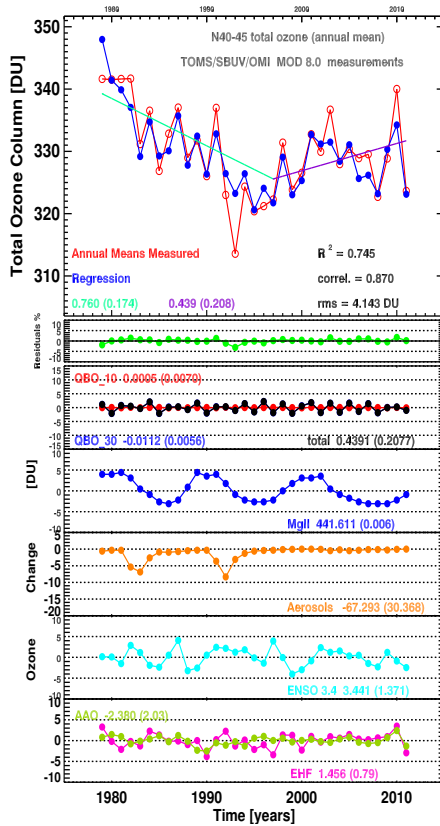
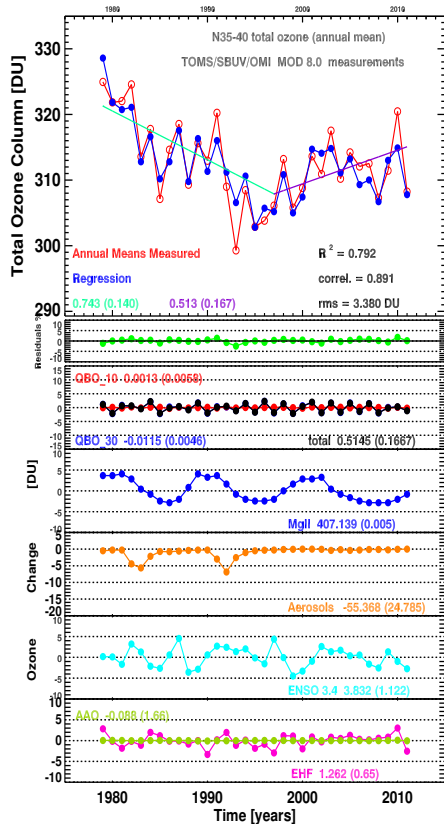
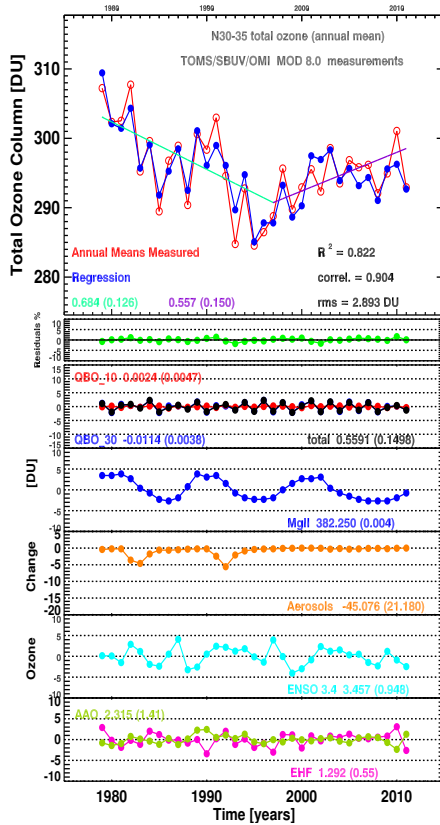
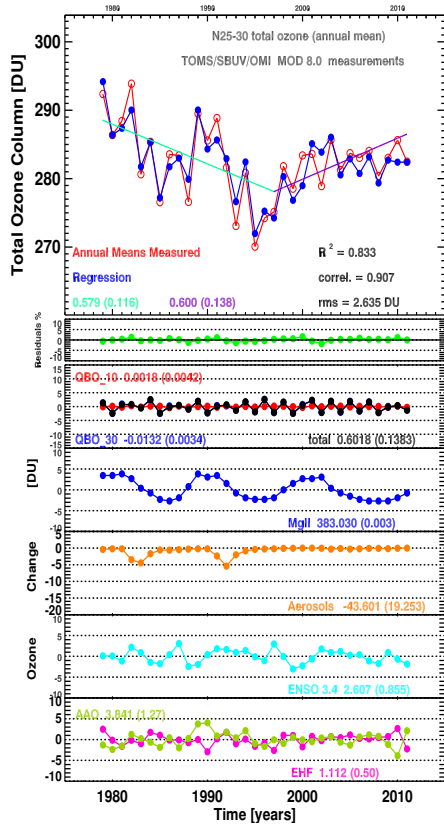


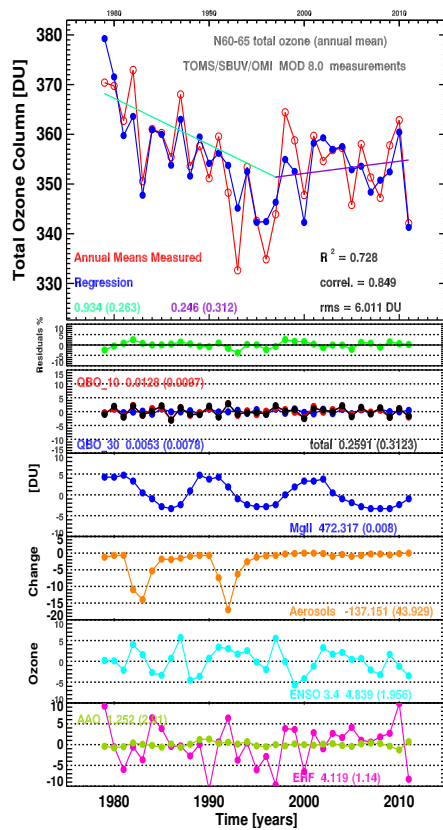
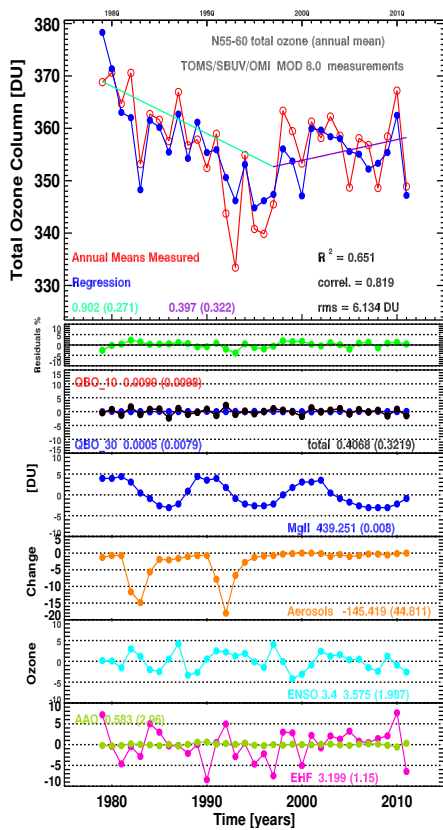
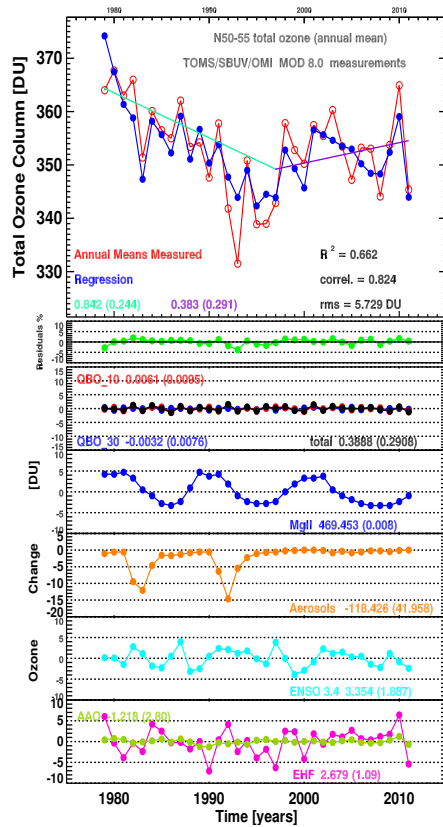
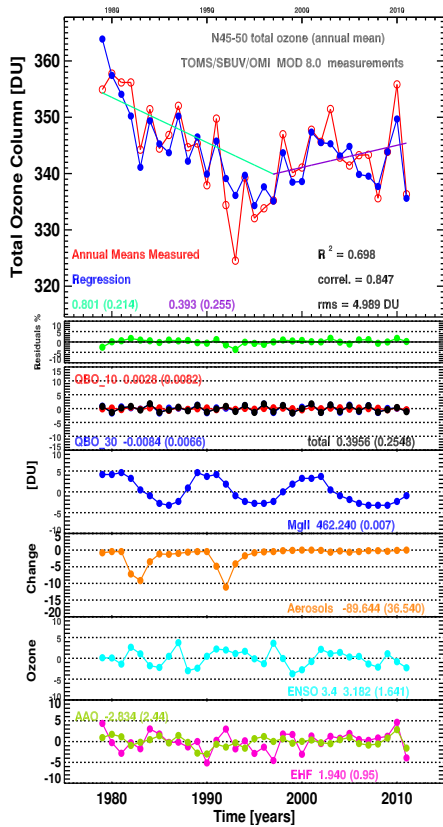
APPENDIX C. TOTAL OZONE TRENDS (PWLT)  
TOMS/SBUV/OMI MOD V8.0 (1979 – 2012)



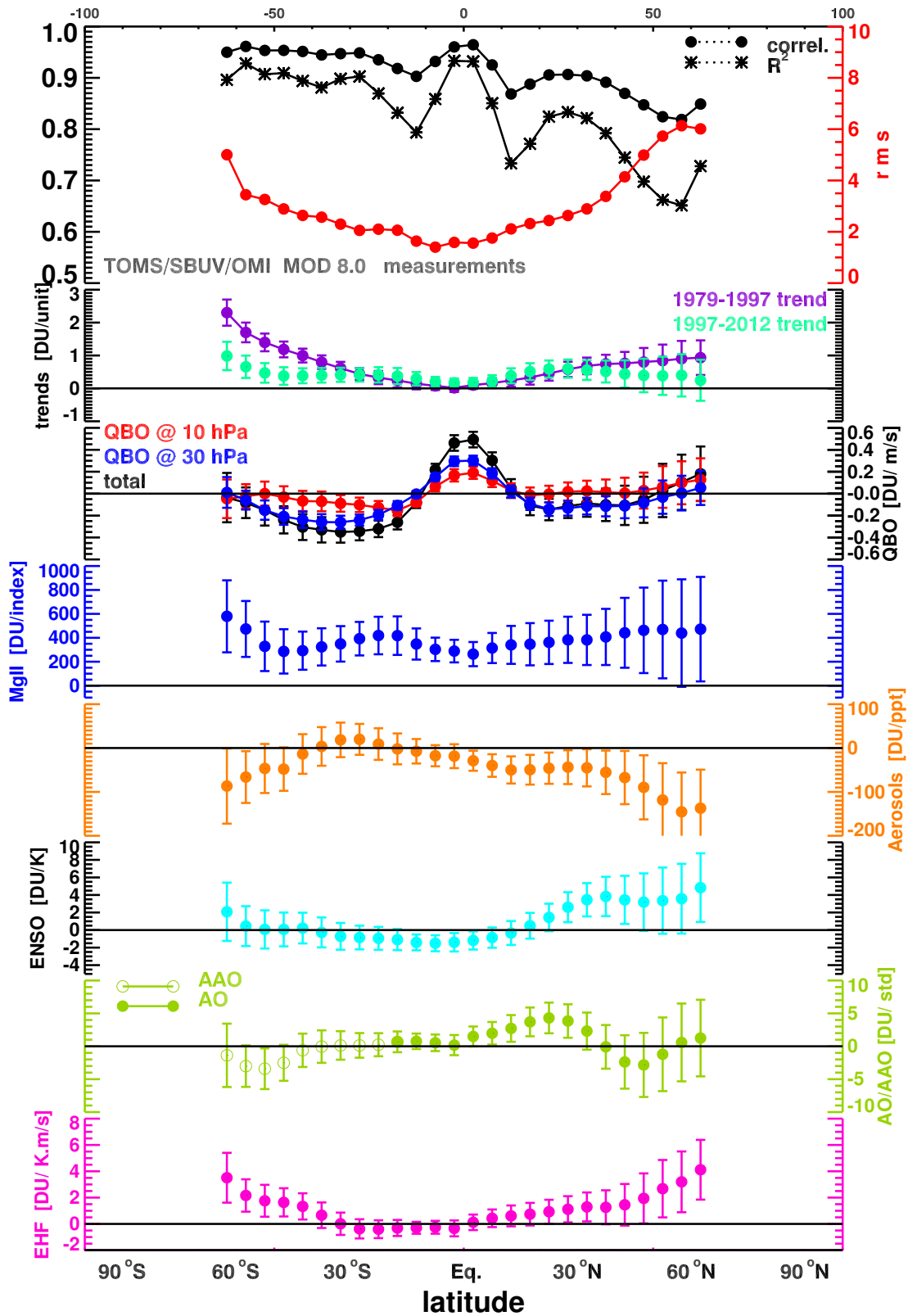


APPENDIX C. TOTAL OZONE TRENDS (PWLT)  
TOMS/SBUV/OMI MOD V8.0 (1979 – 2012)





APPENDIX C. TOTAL OZONE TRENDS (PWLT)  
 TOMS/SBUV/OMI MOD V8.0 (1979 – 2012)



# List of Figures

2.1	Vertical structure of the atmosphere . . . . .	16
2.2	Ozone layer . . . . .	21
2.3	Fraction of odd-oxygen loss rate. . . . .	24
2.4	Brewer-Dobson circulation . . . . .	32
2.5	Ozone measurement techniques. . . . .	33
3.1	Ozone molecule . . . . .	38
3.2	Resonance structure of ozone molecule . . . . .	39
3.3	Symmetry elements of ozone molecule in the $C_{2v}$ point group	39
3.4	Electronic excited states of the ozone molecule . . . . .	41
3.5	Potential energy surfaces of ozone lowest states . . . . .	42
3.6	Temperature dependent ozone absorption cross section spectra . . . . .	43
4.1	Comparison between Bogumil et al. [2003] version 3, Bass Paur and BMD data in the Huggins band . . . . .	50
4.2	Temperature variation of Bogumil et al. [2003] version 3 data in the Chappuis and Wulf bands . . . . .	51
4.3	Spectra of Gür et al. [2005] and Gür [2006] GOME-2 FM3 version 3 data and literature data in the DOAS retrieval window at 225 K. . . . .	51
4.4	Temperature variation of Gür et al. [2005] and Gür [2006] GOME-2 FM3 version 3 data. . . . .	52
4.5	SCIAMACHY's absorption measurements in the Huggins band . . . . .	60
4.6	SCIAMACHY's manual concatenation . . . . .	61
4.7	GOME-2 absorption measurements in the Huggins band . . . . .	62
4.8	GOME-2 manual concatenation . . . . .	63
4.9	GOME-2 OD spectrum at 293 K . . . . .	64
4.10	SCIAMACHY temperature dependent ozone absorption cross section spectra . . . . .	65

---

4.11	GOME-2 temperature dependent ozone absorption cross section spectra . . . . .	67
4.12	Evaluation of SCIAMACHY revised spectra in the Huggins band . . . . .	68
4.13	Evaluation of SCIAMACHY revised spectra in the Chappuis band . . . . .	69
4.14	Evaluation of GOME-2 FM3 revised spectra in the Hartley and Huggins bands . . . . .	70
4.15	Spectra of GOME-2 FM3 revised data and literature data in the DOAS retrieval window at 225 K. . . . .	71
5.1	Revised SCIAMACHY FM temperature dependent absorption cross section spectra in the Hartley band. . . . .	75
5.2	Revised GOME-2 FM3 temperature dependent absorption cross section spectra in the Hartley band. . . . .	76
5.3	Revised SCIAMACHY FM temperature dependent absorption cross section spectra in the Huggins band. . . . .	77
5.4	Revised GOME-2 FM3 temperature dependent absorption cross section spectra in the Huggins band. . . . .	77
5.5	Revised SCIAMACHY FM temperature dependent absorption cross section spectra in the Chappuis band. . . . .	78
5.6	Revised GOME-2 FM3 temperature dependent absorption cross section spectra in the Chappuis band. . . . .	79
5.7	Revised SCIAMACHY FM temperature dependent absorption cross section spectra in the Wulf band. . . . .	80
5.8	Comparison between quadratic temperature coefficients of SCIAMACHY FM and literature data. . . . .	86
5.9	Comparison between quadratic temperature coefficients of GOME-2 FM3 and literature data. . . . .	86
5.10	Comparison between measured and modelled SCIAMACHY FM and literature data. . . . .	87
5.11	Comparison between measured and modelled GOME-2 FM3 and literature data. . . . .	88
5.12	Non-linear square fit for SCIAMACHY revised with Bogumil et al. [2003] version 3 in the DOAS fitting window (326.6 – 334.5 nm) at 225 K . . . . .	91
5.13	Non-linear square fit for SCIAMACHY revised with BP data in the DOAS fitting window (326.6 – 334.5 nm) at 225 K . . . . .	92
5.14	Non-linear square fit for GOME-2 revised data and GOME-2 FM3 version 3 data in the DOAS fitting window (326.6 – 334.5 nm) at 240 K . . . . .	93
5.15	Non-linear square fit for GOME-2 revised data with BMD data in the DOAS fitting window (326.6 – 334.5 nm) at 240 K . . . . .	94
5.16	Optimal wavelength shift for SCIAMACHY and GOME-2. . . . .	98

---

5.17	SCIAMACY total ozone columns with different cross sections . . . . .	99
5.18	GOME-2 total ozone columns with different cross sections	100
5.19	SCIAMACY fit residuals (RMS) with different cross sections	101
5.20	GOME-2 fit residuals (RMS) with different cross sections .	101
6.1	Main Contributors to Ozone Variability . . . . .	108
6.2	Annual mean area-weighted total ozone time series . . . . .	115
6.3	Ozone variations attributed to the explanatory variables for the 60°N – 65°N latitude band . . . . .	118
6.4	Spring-to-fall ratio of total ozone as a function of the winter mean eddy heat flux . . . . .	119
6.5	Ozone variations attributed to the explanatory variables for the 60°N – 65°N latitude band with winter mean eddy heat flux . . . . .	119
6.6	Measured and modelled ozone for 5° wide latitude bands from 65°S to 65°N . . . . .	120
6.7	Fitting coefficients of the different explanatory variables from 65°S to 65°N with winter mean eddy heat flux . . . . .	121
6.8	Zonal distribution of ozone linear trends: EESC-based and PWLT . . . . .	124
6.9	Comparisons between the different trend before 1997 using different datasets . . . . .	129
6.10	Comparisons between the different trend after 1997 using different datasets . . . . .	130



# List of Tables

2.1	Atmospheric constituents. . . . .	15
4.1	Spectral ranges and resolutions of SCIAMACHY channels. . . . .	54
4.2	Spectral ranges and resolutions of GOME-2 channels. . . . .	55
5.1	Comparisons at Hg lamp and He-Ne laser lines at room temperature. . . . .	82
5.2	Integrated cross sections in the Hartley and Huggins bands. . . . .	84
5.3	Integrated cross sections in the Huggins band. . . . .	84
5.4	Integrated cross sections in the Chappuis band. . . . .	84
5.5	Non linear square fit of revised SCIAMACHY FM and literature data. . . . .	90
5.6	Non linear square fit of revised GOME-2 FM3 and literature data. . . . .	95
6.1	Total ozone column datasets. . . . .	126



# References

- SCIAMACHY PFM calibration results review data package, TPD-TNO, Delft, The Netherlands, 1999.
- GOME-2 FM3 CALIBRATION, TPD Document number: MO-TN-TPD-GO-0060i1, Tech. Report, 2005a.
- GOME-2 FM3 CALIBRATION, TPD Document number: MO-TR-TPD-GO-0097i3 (2005) Tech. Report: Wavelength Calibration and Slit Function, 2005b.
- Anderson, J. G., Brune, W. H., Lloyd, S. A., Toohey, D. W., Sander, S. P., Starr, W. L., Loewenstein, M., and Podolske, J. R.: Kinetics of O<sub>3</sub>, destruction by ClO and BrO within the Antarctic vortex: An analysis based on in situ ER-2 data, *J. of Geophys. Res.*, 94, 11 480–11 520, doi: 10.1029/89JD00932, 1989.
- Andrews, D., Holton, J., and Leovy, C.: *Middle Atmosphere Dynamics*, Academic Press, San Diego, CA, 1987.
- Angell, J. K. and Korshover, J.: Quasi-biennial variations in temperature, total ozone, and tropopause height, *J. Atmos. Sci.*, 21, 479–492, 1964.
- Appenzeller, C., Weiss, A. K., and Staehelin, J.: North Atlantic Oscillation modulates total ozone winter trends, *Geophys. Res. Lett.*, 27(8), 1131–1134, 2000.
- Aquila, V., Oman, L. D., Stolarski, R., Douglass, A. R., and Newman, P. A.: The Response of Ozone and Nitrogen Dioxide to the Eruption of Mt. Pinatubo at Southern and Northern Midlatitudes, *J. Atmos. Sc.*, 70:3, 894–900, 2013.
- Baldwin, M. P., Gray, L. J., Dunkerton, T. J., Hamilton, K., Haynes, P. H., Randel, W. J., Holton, J. R., Alexander, M. J., Hirota, I., Horinouchi, T., Jones, D. B. A., Kinnerson, J. S., Marquardt, C., Sato, K., and Takahashi,

- M.: The Quasi-Biennial Oscillation, *Reviews of Geophysics*, 39, 179–229, 2001.
- Balis, D., Lambert, J. C., Van Roozendaal, M., Spurr, R., Loyola, D., Livschitz, Y., Valks, P., Amiridis, V., Gerard, P., Granville, J., and Zehner, C.: Ten years of GOME/ERS2 total ozone data—The new GOME data processor (GDP) version 4: 2. Ground-based validation and comparisons with TOMS V7/V8, doi:10.1029/2005JD006376, 2007.
- Banichevich, A. and Peyerimhoff, S. D.: Theoretical study of the ground and excited states of ozone in its symmetric nuclear arrangement, *J. Chem. Phys.*, 174, 93 – 109, doi:10.1016/0301-0104(93)80054-D, 1993.
- Banichevich, A., Peyerimhoff, S. D., and Grein, F.: Ab initio potential surfaces for ozone dissociation in its ground and various electronically excited states, *Chem. Phys. Lett.*, 178, 1 – 6, 1990.
- Banichevich, A., Peyerimhoff, S. D., and Grein, F.: Potential energy surfaces of ozone in its ground state and in the lowest-lying eight excited states, *J. Chem. Phys.*, 178, 155 – 188, doi:10.1016/0301-0104(93)85059-H, 1993.
- Bass, A. M. and Paur, R. J.: The Ultraviolet Cross-Sections of Ozone: Part I. The Measurements, edited by Zerefos S., Ghazi A., Reidel D.(Eds.), Halkidiki Greece, Proceedings of the Quadrennial Ozone Symposium on Atmospheric Ozone, Norwell., pp. 606–610, 1985.
- Bates, D. R. and Nicolet, M.: The photochemistry of atmospheric water vapor, *J. Geophys. Res.*, 55, 301–327, 1950.
- Belmont, A. D. and Dartt, D. G.: Variation with longitude of the quasi-biennial oscillation, *Mon. Weather Rev.*, 96, 767 – 777, 1968.
- Bhartia, P. K., McPeters, R. D., Flynn, L. E., Taylor, S., Kramarova, N. A., Frith, S., Fisher, B., and DeLand, M.: Solar Backscatter UV (SBUV) total ozone and profile algorithm, *Atmos. Meas. Tech.*, 6, 2533–2548, doi: 10.5194/amt-6-2533-2013, 2013.
- Bogumil, K., Orphal, J., Homann, T., Voigt, S., Spietz, P., Fleischmann, O. C., Vogel, A., Hartmann, M., Bovensmann, H., Frerick, J., and Burrows, J. P.: Measurements of molecular absorption spectra with the SCIAMACHY pre-flight model: instrument characterisation and reference data for atmospheric remote-sensing in the 230–2380 nm region, *J. Photochem. Photobiol.*, A157, 157–167, 2003.
- Bojkov, R. D. and Fioletov, V. E.: Estimating the global ozone characteristics during the last 30 years, *J. Geophys. Res.*, 100, 16 537–16 552, 1995.
- Bojkov, R. D., Bishop, L., Hill, W. J., Reinsel, G. C., and Tiao, G. C.: A

- statistical trend analysis of revised Dobson Total Ozone data over the Northern hemisphere, *J. Geophys. Res.*, 95, 9785–9807, 1990.
- Bovensmann, H., Burrows, J. P., Buchwitz, M., Frerick, J., Noel, S., Rozanov, V. V., Chance, K. V., and Goede, A. P. H.: SCIAMACHY: Mission Objectives and Measurement Modes, *J. Atmos. Sci.*, 56, 127–150, 1999.
- Bowman, K. P.: Global patterns of the quasi-biennial oscillation in total ozone, *J. Atmos. Sci.*, 46, 3328–3343, 1989.
- Bracher, A., Lamsal, L. N., Weber, M., Bramstedt, K., Coldewey-Egbers, M., and Burrows, J. P.: Global satellite validation of SCIAMACHY O<sub>3</sub> columns with GOME WFDOAS, *Atmos. Chem. Phys.*, 5, 2357–2368, 2005.
- Brasseur, G.: The response of the middle atmosphere to long-term and short-term solar variability: A two-dimensional model, *J. Geophys. Res.*, 98, 23 079–23 090, 1993.
- Brewer, A. W.: Evidence for a world circulation provided by the measurements of helium and water vapour distribution in the stratosphere, *Q. J. R. Meteorol. Soc.*, 75, 351–363, 1949.
- Brion, J., Chakir, A., Daumont, D., Malicet, J., and Parisse, C.: High-resolution laboratory absorption cross section of O<sub>3</sub>. Temperature effect, *Chem. Phys. Lett*, 213, 610–612, 1993.
- Brion, J., Chakir, A., Charbonnier, J., Daumont, D., Parisse, C., and Malicet, J.: Absorption spectra measurements for the ozone molecule in the 350 – 830 nm region, *J. Atmos. Chem.*, 30, 291–299, 1998.
- Bronnimann, S., Luterbacher, J., Staehelin, J., Svendby, T., Hansen, G., and Svenoe, T.: Extreme climate of the global troposphere and stratosphere in 1940–42 related to El Niño, *Nature*, 431, 971–974, doi:10.1038/nature02982, 2004.
- Burkholder, J. B. and Talukdar, R. K.: Temperature Dependence of the Ozone Absorption Spectrum over the Wavelength Range 410 to 760 nm, *Geophys. Res. Lett*, 21, No. 7, 581–584, 1994.
- Burrows, J. P., Holzle, E., Goede, A. P. H., Visser, H., and Fricke, W.: SCIAMACHY - Scanning Imaging Absorption Spectrometer for Atmospheric Chartography, *Acta Astronaut*, 35, 445–451, 1995.
- Burrows, J. P., Dehn, A., Deters, B., Himmelmann, S., Richter, A., Voigt, S., and Orphal, J.: Atmospheric remote-sensing reference data from GOME: 1. Temperature-dependent absorption cross-sections of NO<sub>2</sub>

- in the 231–794 nm range, *J. Quant. Spectrosc. and Radiat. Transfer*, 60, 1025–1031, 1998.
- Burrows, J. P., Dehn, A., Deters, B., Himmelmann, S., Richter, A., Voigt, S., and Orphal, J.: Atmospheric remote-sensing reference data from GOME: 1. Temperature-dependent absorption cross-sections of O<sub>3</sub> in the 231–794 nm range, *J. Quant. Spectrosc. and Radiat. Transfer*, 60, 509–517, 1999a.
- Burrows, J. P., Weber, M., Buchwitz, M., Rozanov, V. V., Ladstädter-Weissenmayer, A., Richter, A., de Beek, R., Hoogen, R., Bramstedt, K., Eichmann, K. U., Eisinger, E., and Perner, D.: The Global Ozone Monitoring Experiment (GOME): Mission Concept and First Scientific Results, *J. Atmos. Sci.*, 56, 151–157, 1999b.
- Callies, J., Corpaccioli, E., Eisinger, M., Hahne, A., and Lefebvre, A.: GOME-2 Metop's Second-Generation Sensor for Operational Ozone Monitoring, *ESA Bulletin* 102, 28 – 36, 2000.
- Callis, L. B., Natarajan, M., Lambeth, J., and Baker, D. N.: Solar-atmospheric coupling by electrons (SOLACE): 2. Calculated stratospheric effects of precipitating electrons, 1979–1988, *J. Geophys. Res.*, 103, 28 421–28 438, 1998.
- Camp, C. D. and Tung, K. K.: Stratospheric polar warming by ENSO in winter: A statistical study, *Geophys. Res. Lett.*, 34, L04 809, doi:10.1029/2006GL028521, 2007.
- CCMVal, S.: SPARC CCMVal (Stratospheric Processes And their Role in Climate), SPARC Report on the Evaluation of Chemistry-Climate Models, edited by V. Eyring, T.G. Shepherd, and D.W. Waugh, SPARC Report No. 5, WCRP-132, WMO/TD-No. 1526, 478 pp., available: [http://www.atmos.physics.utoronto.ca/SPARC/ccmval\\_final/index.php](http://www.atmos.physics.utoronto.ca/SPARC/ccmval_final/index.php), (last access: Nov. 2013), 2010.
- Chance, K. V., Burrows, J. P., Perner, D., and Schneider, W.: Satellite measurements of atmospheric ozone profiles, including tropospheric ozone, from ultraviolet/visible measurements in the nadir geometry: a potential method to retrieve tropospheric ozone, *J. Quant. Spectrosc. and Radiat. Transfer*, 57(4), 467–476., 1997.
- Chandra, S. and McPeters, R. D.: The solar cycle variation of ozone in the stratosphere inferred from NIMBUS7 and NOAA11 satellites, *J. Geophys. Res.*, 99, 20 665–20 671, 1994.
- Chandra, S. and Stolarski, R. S.: Recent trends in stratospheric total ozone: Implications of dynamical and El Chichón perturbations, *Geophys. Res. Lett.*, 18, 2277–2280, 1991.

- Chandra, S., Ziemke, J. R., Min, W., and Read, W. G.: Effects of 1997–1998 El Niño on tropospheric ozone and water vapour, *Geophys. Res. Lett.*, 25, 3867–3870, 1998.
- Chandra, S., Ziemke, J. R., Bhartia, P. K., and Martin, R. V.: Tropical tropospheric ozone: Implications for dynamics and biomass burning, *J. Geophys. Res.*, 107(D14), 4188, doi:10.1029/2001JD000447, 2002.
- Chapman, S.: A theory of upper-atmospheric ozone, *Memoirs of the R. Meteor. Soc.*, 3, 103, 1930.
- Chipperfield, M. P.: A three-dimensional model study of long-term mid-high latitude lower stratosphere ozone changes, *Atmos. Chem. Phys.*, 3, 1253–1265, 2003.
- Chipperfield, M. P. and Jones, R. L.: Relative influences of atmospheric chemistry and transport on arctic ozone trends, *Nature*, 400, 551–554, 1999.
- Chu, W. and McCormick, M. P.: Inversion of stratospheric aerosol and gaseous constituents from spacecraft solar extinction data in the 0.38 – 1.0  $\mu\text{m}$  wavelength region, *Applied Optics*, 18, 1404 – 1413, 1979.
- Chu, W., McCormick, M. P., Lenoble, J., Brogniez, C., and Pruvost, P.: SAGE II inversion algorithm, *J. Geophys. Res.*, 94, 8339 – 8351, 1989.
- Cochrane, D. and Orcutt, G. H.: Application of least squares regression to relationships containing autocorrelated error terms, *J. Amer. Stat. Assoc.*, 44, 32 – 61, 1949.
- Coldewey-Egbers, M., Weber, M., Lamsal, L. N., de Beek, R., Buchwitz, M., and Burrows, J. P.: Total ozone retrieval from GOME UV spectral data using the weighting function DOAS approach, *Atmos. Chem. Phys.*, 3, 5015–5025, 2005.
- Crutzen, P. J.: The influence of nitrogen oxide on the atmospheric ozone content, *Q. J. R. Meteorol. Soc.*, 96, 320 – 325, 1970.
- Crutzen, P. J.: A discussion of the chemistry of some minor constituents in the stratosphere and troposphere, *Pure and Appl. Geophys.*, 106–108, 1385–1399, 1973.
- Crutzen, P. J.: Photochemical reaction initiated by and influencing ozone in unpolluted tropospheric air, *Tellus*, 26, 45–55, 1974.
- Crutzen, P. J. and Arnold, F.: Nitric Acid Cloud Formation in the Cold Antarctic Stratosphere: A Major Cause for the Springtime 'Ozone hole', *Nature*, 324, 651–655, doi:10.1038/324651a0, 1986.

- Daniel, J. S., Solomon, S., and Albritton, D. L.: On the evaluation of halocarbon radiative forcing and global warming potentials, *J. Geophys. Res.*, 100 (D1), 1271–1285, 1995.
- Daumont, D., Brion, J., Charbonnier, J., and Malicet, J.: Ozone UV spectroscopy I: Absorption cross-sections at room temperature, *J. Atmos. Chem.*, 15, 145–155, 1992.
- DeLand, M. T., Taylor, S. L., Huang, L. K., and Fisher, B. L.: Calibration of the SBUV version 8.6 ozone data product, *Atmos. Meas. Tech. Discuss.*, 2, 5151–5203, 2012.
- Dessler, A. E., Burrage, M. D., Grooss, J. U., Holton, J. R., Lean, J. L., Massie, S. T., Schoeberl, M. R., Douglass, A. R., and Jackman, C. H.: Selected science highlights from the first five years of the Upper Atmosphere Research Satellite (UARS) program, *Rev. Geophys.*, 36, 183–210, 1998.
- Dhomse, S., Weber, M., Wohltmann, I., Rex, M., and Burrows, J. P.: On the possible causes of recent increases in Northern Hemispheric total ozone from a statistical analysis of satellite data from 1979 to 2003, *Atmos. Chem. Phys.*, 6, 1165–1180, 2006.
- Dobson, G. M.: Origin and distribution of the polyatomic molecules in the atmosphere, *Proc. Roy. Soc. Ldn.*, A236, 187–193, 1956.
- Dunkerton, T. J. and Baldwin, M. P.: Quasi-biennial modulation of planetary-wave fluxes in the Northern Hemisphere winter, *J. Atmos. Sci.*, 48, 1043–1061, 1991.
- El Helou, Z., Churassy, S., Wannous, G., Bacis, R., and Boursey, E.: Absolute cross sections of ozone at atmospheric temperatures for the Wulf and the Chappuis bands, *J. Chem. Phys.*, 122, 244311, doi:10.1063/1.1937369, 2005.
- Eskes, H. J., van der A, R. J., Brinksma, E. J., Veefkind, J. P., de Haan, J. F., and Valks, P. M. J.: Retrieval and validation of ozone columns derived from measurements of SCIAMACHY on Envisat, *Atmos. Chem. Phys. Disc.*, 5, 4429–4475, 2005.
- Eyring, V., Harris, N. R. P., Rex, M., Shepherd, T. G., Fahey, D. W., Amannatidis, G. T., Austin, J., Chipperfield, M. P., Dameris, M., Forster, P. D. F., Gettelman, A., Graf, H. F., Nagashima, T., Newman, P. A., Pawson, S., Prather, M. J., Pyle, J. A., Salawitch, R. J., Santer, B. D., and Waugh, D. W.: A strategy for process-oriented validation of coupled chemistry climate models, *Bull. Amer. Met. Soc.*, 86, 1117 – 1133, doi: 10.1175/BAMS-86-8-1117, 2005.

- Fahey, D. W., Kawa, S. R., Woodbridge, E. L., Tin, P., Wilson, J. C., Jonsson, H. H., Dye, J. E., Baumgardner, D., and Borrmann, S.: In situ measurements constraining the role of sulfate aerosols in mid-latitude ozone depletion, *Nature*, 363, 509–514, 1993.
- Farman, J. C., Gardner, B. G., and Franklin, J. D.: Large losses of total ozone in Antarctica reveal seasonal  $\text{ClO}_x$  and  $\text{NO}_x$  interaction, *Nature*, 315, 207–210, 1985.
- Farmer, C. B., Toon, G. C., Schaper, P. W., Blavier, J. F., and Lowes, L. L.: Stratospheric trace gases in the spring 1986 Antarctic atmosphere, *Nature*, 329, 126–130, 1987.
- Fioletov, V. E.: Estimating the 27-day and 11-year solar cycle variations in tropical upper stratospheric ozone, *J. Geophys. Res.*, 114, D02 302, doi:10.1029/2008JD010499, 2009.
- Fioletov, V. E. and Shepherd, T. G.: Seasonal persistence of midlatitude total ozone anomalies, *Geophys. Res. Lett.*, 20, 1417, doi:10.1029/2002GL016739, 2003.
- Fioletov, V. E. and Shepherd, T. G.: Summertime total ozone variations over middle and polar latitudes, *Geophys. Res. Lett.*, 32, L04 807, doi:10.1029/2004GL022080, 2005.
- Fioletov, V. E., Bodeker, G. E., Miller, A. J., McPeters, R. D., and Stolarski, R.: Global and zonal total ozone variations estimated from ground-based and satellite measurements: 1964–2000, *J. Geophys. Res.-Atmos.*, 107, 4647, doi:10.1029/2001jd001350, 2002.
- Fioletov, V. E., Labow, G., G. Evans, R., Hare, E. W., Köhler, U. McElroy, C. T., Miyagawa, K., Redondas, A., Savastiouk, V., Shalamyansky, A. M., Staehelin, J., Vanicek, K., and Weber, M.: The performance of the ground-based total ozone network assessed using satellite data, *J. Geophys. Res.*, 113, D14 313, doi:10.1029/2008JD009809, 2008.
- Frith, S., McPeters, R., Kramarova, N., Bhartia, P. K., Labow, G., Stolarski, R., Taylor, S., Fisher, B., and DeLand, M.: A 40-year Record of Profile Ozone from the SBUV(/2) Instrument Series, p. 6043, 2012.
- Fujiwara, M., Kita, K., Kawakami, S., Ogawa, T., Komala, N., Saraspriya, S., and Suropto, A.: Tropospheric ozone enhancements during the Indonesian forest fire events in 1994 and in 1997 as revealed by ground-based observations, *Geophys. Res. Lett.*, 26(16), 2417–2420, doi:10.1029/1999GL900117, 1999.
- Fusco, A. C. and Salby, M. L.: Interannual variations of total ozone and their relationship to variations of planetary wave activity, *J. Climate*, 12, 1619–1629, 1999.

- Gorshchev, V., Serdyuchenko, A., Weber, M., Chehade, W., and Burrows, J. P.: High spectral resolution ozone absorption cross-sections; Part 1: Measurements, data analysis and comparison with previous measurements around 293 K, *Atmospheric Measurement Techniques Discussions*, 6, 6567–6611, doi:10.5194/amtd-6-6567-2013, URL <http://www.atmos-meas-tech-discuss.net/6/6567/2013/>, 2013.
- Gottwald, M. and Bovensmann, H., eds.: *SCIAMACHY – Exploring the Changing Earth’s Atmosphere*, ISBN 978-90-481-9895-5, Springer, Dordrecht, doi:10.1007/978-90-481-9896-2, 2011.
- Gür, B.: Temperature Dependent Absorption Cross-Sections of O<sub>3</sub> and NO<sub>2</sub> in the 240 – 790 nm range determined by using the GOME-2 Satellite Spectrometers for use in Remote Sensing Applications, Ph.D. thesis, Universität Bremen, 2006.
- Gür, B., Spietz, P., Orphal, J., and Burrows, J. P.: Absorption Spectra Measurements with the GOME-2 FMs using the IUP/IFE-UB’s Calibration Apparatus for Trace Gas Absorption Spectroscopy CATGAS, Final Report, ESA / EUMETSAT, 2005.
- Haigh, J. D.: The effects of solar variability on the Earth’s climate, *Phil. Trans. Roy. Soc.*, A361, 95–111, 2003.
- Harris, N. R. P., Kyrö, E., Staehelin, J., Brunner, D., Andersen, S. B., Godin-Beekmann, S., Dhomse, S., Hadjinicolaou, P., Hansen, G., Isaksen, I., Jrrar, A., Karpetchko, A., Kivi, R., Knudsen, B., Krizan, P., Lastovicka, J., Mäder, J., Orsolini, Y., Pyle, J. A., Rex, M., Vanicek, K., Weber, M., Wohltmann, I., Zanis, P., and Zerefos, C.: Ozone trends at northern mid- and high latitudes - a European perspective, *Ann. Geophys.*, 26, 1207–1220, doi:10.5194/angeo-26-1207-2008, 2008.
- Hartmann, D. L., M.Wallace, J., Limpasuvan, V., Thompson, D., and Holton, J. R.: Can ozone depletion and global warming interact to produce rapid climate change?, *Proc. Nat. Acad. Sci.*, 97, 1412–1417, 2000.
- Hay, P. J. and Dunning, T. H.: Geometries and Energies of the Excited States of O<sub>3</sub> from ab initio Potential Energy Surfaces, *J. Chem. Phys.*, 67, 2290 – 2303, doi:doi:10.1063/1.435064, 1977.
- Haynes, P. H., Marks, C. J., McIntyre, M. E., Shepherd, T. G., and Shine, K. P.: On the "downward control" of extratropical diabatic circulations by eddy-induced mean zonal forces, *J. Atmos. Sci.*, 48, 651–678, 1991.
- Hendrick, F., Pommereau, J. P., Goutail, F., Evans, R. D., Ionov, D., Pazmino, A., Kyrö, E., Held, G., Eriksen, P., Dorokhov, V., Gil, M., and Van Roozendaal, M.: NDACC/SAOZ UV-visible total ozone measurements: improved retrieval and comparison with correlative ground-

- based and satellite observations, *Atmos. Chem. Phys.*, 11, 5975 – 5995, doi:10.5194/acp-11-5975-2011, 2011.
- Hofmann, D. J. and Solomon, S.: Ozone destruction through heterogeneous chemistry following the eruption of El Chichón, *J. Geophys. Res.*, 94, 5029–5041, 1989.
- Holloway, A. M. and Wayne, R. P.: *Atmospheric Chemistry*, ISBN:978-1-84755-807-7, Royal Society of Chemistry, Cambridge CB4 0WF, UK, 2010.
- Holton, J. R. and Tan, H. C.: The influence of the equatorial quasi-biennial oscillation on the global circulation at 50 mb, *J. Atmos. Sci.*, 37, 2200–2208, 1980.
- Holton, J. R., Haynes, P. H., Douglass, A. R., Rood, R. B., and Pfister, L.: Stratosphere – troposphere exchange, *Rev. Geophys.*, 33, 403 – 439, 1995.
- Hood, L. L.: The solar cycle variation of total ozone: Dynamical forcing in the lower stratosphere, *J. Geophys. Res.*, 102(D1), 1355–1370, 1997.
- Hood, L. L. and Soukharev, B. E.: Quasi-decadal variability of the tropical lower stratosphere: The role of extratropical wave forcing, *J. Atmos. Sci.*, 60, 2389–2403, 2003.
- Hood, L. L. and Soukharev, B. E.: Interannual variations of total ozone at northern midlatitudes correlated with EP flux and potential vorticity, *J. Atmos. Sci.*, 62, 3724–3740, 2005.
- IPCC: Intergovernmental Panel on Climate Change, *Climate Change 1994: Radiative Forcing of Climate Change and an Evaluation of the IPCC IS92 Emission Scenarios*, edited by J. T. Houghton et al., Cambridge Univ. Press, New York, 1995.
- Jackman, C. H., DeLand, M. T., Labow, G. J., Fleming, E. L., and Lòpes-Puertas, M.: "Satellite Measurements of Middle Atmospheric Impacts by Solar Proton Events in Solar Cycle 23", *Space Sci. Rev.*, 125, 381–391, 2006.
- Joens, J. A.: An assignment of the structured features in the Hartley band absorption spectrum of ozone, *J. Chem. Phys.*, 100 (5), 3407 – 3414, 1994a.
- Joens, J. A.: Reassignment of the vibrational structure of the Huggins absorption band of ozone, *J. Chem. Phys.*, 101, 5431–5437, 1994b.
- Katayama: The UV Huggins bands of ozone, *J. of Chem. Phys.*, 85 (11), 6809 – 6810, 1986.

- Katayama, D. H.: New vibrational quantum number assignments for the UV absorption bands of ozone based on the isotope effect, *J. of Chem. Phys.*, 71 (2), 815 – 820, 1979.
- Kiesewetter, G., Sinnhuber, B. M., Weber, M., and Burrows, J. P.: Attribution of stratospheric ozone trends to chemistry and transport: a modelling study, *Atmos. Chem. Phys.*, 10, 12 073–12 089, doi:10.5194/acp-10-12073-2010, 2010.
- Kodera, K. and Kuroda, Y.: Dynamical response to the solar cycle: Winter stratopause and lower stratosphere, *J. Geophys. Res.*, 1007, 4749, doi: 310.1029/2002JD002224, 2002.
- Komhyr, W. D., Grass, R. D., and Leonard, R. K.: Total ozone decrease at South Pole Antarctica 1964–1985, *Geophys Res. Lett.*, 13, 1248–1251, 1986.
- Koukouli, M. E., Balis, D. S., Loyola, D., Valks, P., Zimmer, W., Hao, N., Lambert, J.-C., Van Roozendaal, M., Lerot, C., and Spurr, R. J. D.: Geophysical validation and long-term consistency between GOME-2/MetOp-A total ozone column and measurements from the sensors GOME/ERS-2, SCIAMACHY/ENVISAT and OMI/Aura, *Atmos. Meas. Tech.*, 5, 2169–2181, doi:doi:10.5194/amt-5-2169-2012,, 2012.
- Kurosu, T. P., Chance, K. V., Yokota, T., and Sasano, Y.: Polar stratospheric cloud detection from the ILAS instrument, in: Y. Sasano, J. Wang, T. Hayasaka (Eds.), *Proceedings of SPIE on Optical Remote Sensing of the Atmosphere and Clouds*, vol. II, pp. 68 – 75, 2001.
- Kurucz, H. L.: *The Solar Spectrum: Atlases and Line Identifications*, Workshop on Laboratory and Astronomical High Resolution Spectra., Astronomical Society of the Pacific Conference Series; Proceedings of ASP Conference No. 81 held in Brussels; Belgium 29 August – 2 September 1994, San Francisco: Astronomical Society of the Pacific (ASP); edited by A.J. Sauval, R. Blomme, and N. Grevesse, 1995.
- Kuze, A. and Chance, K. V.: Analysis of cloud top height and cloud coverage from satellites using the O<sub>2</sub> A and B bands, *J. Geophys. Res.*, 99, 14 481 – 14 491, 1994.
- Labitzke, K. and van Loon, H.: Some recent studies of probable connections between solar and atmospheric variability, *Ann. Geophys.*, 11, 1084–1094, 1993.
- Labitzke, K. and van Loon, H.: *The Stratosphere*, Springer-Verlag, New York, p. 179 pp, 1999.
- Lait, L. R., Schoeberl, M. R., and Newman, P. A.: Quasibiennial modula-

- tion of the Antarctic ozone depletion, *J. Geophys. Res.*, 94, 1559–11 571, 1989.
- Langematz, U., Grenfell, J. L., Matthes, K., Mieth, P., Kunze, M., Steil, B., and Brhl, C.: Chemical effects in 11-year solar cycle simulations with the Freie Universitt Berlin Climate Middle Atmosphere Model with on-line chemistry (FUB-CMAM-CHEM), *Geophys. Res. Lett.*, 32, L13 803, doi:10.1029/2005GL022686, 2005.
- Le Quèrè, F. and Leforestier, C.: Theoretical calculation of the Huggins band of ozone, *Chem. Phys. Lett.*, 189 (6), 537 – 541, 1992.
- Lean, J. and Rind, D.: SUN-CLIMATE CONNECTIONS: Earth’s Response to a Variable Sun, *Science*, 292, 234–236, 2001.
- Lee, H. and Smith, A. K.: Simulation of the combined effects of solar cycle, quasi-biennial oscillation, and volcanic forcing on stratospheric ozone changes in recent decades, *J. Geophys. Res.*, 108 (D2), 4049, doi: 10.1029/2001JD001503, 2003.
- Lerot, C., Van Roozendaal, M., Spurr, R., Loyola, D., Coldewey-Egbers, M., Kochenova, S., van Gent, J., Koukouli, M., Balis, D., Lambert, J.-C., Granville, J., and Zehner, C.: Homogenized total ozone data records from the European sensors GOME/ERS-2, SCIAMACHY/Envisat and GOME-2/MetOp-A, *J. Geophys. Res.*, doi:10.1002/2013JD020831, 2013.
- Lillesand, T. M. and Kiefer, R. W.: *Remote Sensing and Image Interpretation*, vol. Sec. Ed., John Wiley and Sons, Inc.: Toronto, ISBN 0471845175, 1987.
- Lindzen, R. S. and Holton, J. R.: A theory of the quasi-biennial oscillation, *J. Atmos. Sci.*, 25, 1095–1107, 1968.
- Loyola, D. and Coldewey-Egbers, M.: Multi-sensor data merging with stacked neural networks for the creation of satellite long-term climate data records, *EURASIP Journal on Advances in Signal Processing*, 2012:991, 1–10, doi:10.1186/1687-6180-2012-91, 2012.
- Mäder, J. A., Staehelin, J., Brunner, D., Stahel, W. A., Wohltmann, I., and Peter, T.: Statistical modeling of total ozone: selection of appropriate explanatory variables, *J. Geophys. Res. Atmos*, 112, D11 108, doi:10.1029/2006jd007694, 2007.
- Mäder, J. A., Staehelin, J., Peter, T., Brunner, D., Rieder, H. E., and Stahel, W. A.: Evidence for the effectiveness of the Montreal Protocol to protect the ozone layer, *Atmos. Chem. Phys.*, 10, 12 161–12 171, doi:10.5194/acp-10-12161-2010, 2010.

- Malicet, J., Daumont, D., Charbonnier, J., Chakir, C., Parisse, A., and Brion, J.: Ozone UV Spectroscopy II: Absorption cross sections and temperature dependence, *J. Atmos. Chem.*, 21, 263–173, 1995.
- Manzini, E., Giorgetta, M. A., Esch, M., Kornblueh, L., and Roeckner, E.: The influence of sea surface temperatures on the northern winter stratosphere: Ensemble simulations with the MAECHAM5 model, *J. Clim.*, 19, 3863–3881, doi:10.1175/JCLI3826.1, 2006.
- Mason, N. J. and Pathak, S. K.: Spectroscopic studies of ozone- the Earth's UV filter, *Contemporary Physics*, 38:4, 289 – 299, doi:10.1080/001075197182360, 1997.
- McCormack, J. P. and Hood, L. L.: Apparent solar cycle variations of upper stratospheric ozone and temperature: Latitude and seasonal dependences, *J. Geophys. Res.*, 101(D15), 20 933–20 944, 1996.
- McCormack, J. P., Hood, L. L., Nagatani, R., Miller, A. J., Planet, W. G., and McPeters, R. D.: Approximate separation of volcanic and 11-year signals in the SBUV-SBUV/2 total ozone record over the 1979–1995 period, *Geophys. Res. Lett.*, 24, 2729–2732, 1997.
- McCormick, M. P., Steele, H. M., Hamill, P., Chu, W. P., and Swisler, T. J.: Polar Stratospheric Cloud Sightings by SAM, *J. Atmo. Sci.*, 39, 1387–1397, doi:10.1175/1520-0469, 1982.
- McElroy, M. B., Salawitch, R. J., Wofsy, S. C., and Logan, J. A.: Reduction of antarctic ozone due to synergistic interactions of chlorine and bromine, *Nature*, 321, 759–762, 1986.
- McPeters, R. D., Bhartia, P. K., Haffner, D., Labow, G. J., and Flynn, L.: The version 8.6 SBUV ozone data record: An overview, *J. Geophys. Res. Atmos.*, 118, 8032–8039, doi:10.1002/jgrd.50597, 2013.
- Miller, A. J., Hollandsworth, S. M., Flynn, L. E., Tiao, G. C., Reinsel, G. C., Bishop, L., McPeters, R. D., Planet, W. G., DeLuisi, J. J., Mateer, C. L., Wuebbles, D., Kerr, J., and Nagatani, R. M.: Comparisons of observed ozone trends and solar effects in the stratosphere through examination of ground-based Umkehr and combined solar backscattered ultraviolet (SBUV) and SBUV 2 satellite data, *J. Geophys. Res.*, 101, 9017–9021, 1996.
- Miller, A. J., Cai, A., Taio, G., Wuebbles, D. J., Flynn, L. E., Yang, S. K., Weatherhead, E. C., Fioletov, V., Petropavlovskikh, I., Meng, X. L., Guillas, S., Nagatani, R. M., and Reinsel, G. C.: Examination of ozonesonde data for trends and trend changes incorporating solar and Arctic oscillation signals, *J. Geophys. Res.*, 111, D13 305, doi: 10.1029/2005JD006684, 2006.

- Molina, L. T. and Molina, M. J.: Absolute Absorption Cross-Sections of Ozone in the 185-350 nm Wavelength Range, *J. Geophys. Res.*, 91, 14 501–8, doi:10.1029/JD091iD13p14501, 1986.
- Molina, L. T. and Molina, M. J.: Production of  $\text{Cl}_2\text{O}_2$  from the selfreaction of the ClO radical, *J. Phys. Chem.*, 91, 433–436, 1987.
- Molina, M. J. and Rowland, F. S.: Stratospheric sink for chlorofluoromethanes: Chlorine atom catalyzed destruction of ozone, *Nature*, 249, 820–812, 1974.
- Mount, G. H., Sanders, R. W., Schmeltekopf, A. L., and Solomon, S.: Visible spectroscopy at McMurdo Station Antarctica. 1. Overview and daily variations of  $\text{NO}_2$  and  $\text{O}_3$  during austral spring, 1986, *J. Geophys Res.*, 92, 8320–8328, 1987.
- Munro, R., Eisinger, M., Anderson, C., Callies, J., Corpaccioli, E., Lang, R., Lefebvre, A., Livschitz, Y., and Perez Albinana, A.: GOME-2 on MetOp: From in-orbit verification to routine operations, in: Proceedings of EU-METSAT Meteorological Satellite Conference, Helsinki, Finland 12–16 June 2006, 2006.
- Newchurch, M. J., Yang, E. S., Cunnold, D. M., Reinsel, G. C. and Zawodny, J. M., and Russell, J. M.: Evidence for slowdown in stratospheric ozone loss: First stage of ozone recovery, *J. Geophys. Res.*, 108(D16), 4507, doi:10.1029/2003JD003471, 2003.
- Newman, P. A., Nash, E. R., and Rosenfield, J.: What controls the temperature of the arctic stratosphere during the spring?, *J. Geophys. Res.*, 106, 19 999–20 010, 2001.
- Newman, P. A., Kawa, S. R., and Nash, E. R.: On the size of the Antarctic ozone hole, *Geophys. Res. Lett.*, 31, L21 104, doi:10.1029/2004GL020596, 2004.
- Newman, P. A., Nash, E. R., Kawa, S. R., Montzka, S. A., and Schaufli, S. M.: When will the Antarctic ozone hole recover?, *Geophys. Res. Lett.*, 33, L12 814, doi:10.1029/2005GL025232, 2006.
- Newman, P. A., Daniel, J. S., Waugh, D. W., and Nash, E. R.: A new formulation of equivalent effective stratospheric chlorine (EESC), *Atmos. Chem. Phys.*, 7, 4537–4552, doi:10.5194/acp-7-4537-2007, 2007.
- O’Keeffe, P., Ridley, T., Lawley, K. P., and Donovan, R. J.: Re-analysis of the ultraviolet absorption spectrum of ozone, *J. Chem. Phys.*, 115, 9311 – 9319, 2001.
- Orphal, J.: A Critical Review of the Absorption Cross-Sections of  $\text{O}_3$  and

- NO<sub>2</sub> in the 240 – 790 nm Region, Part I. Ozone, ESA Technical Note MO-TN-ESA-GO-0302, 2002.
- Orphal, J.: A Critical Review of the Absorption Cross-Sections of O<sub>3</sub> and NO<sub>2</sub> in the ultraviolet and visible., *J. Photochem. Photobiol.*, A157, 185–209, 2003.
- Orphal, J., Bogumil, K., Dehn, A., Deters, B., Dreher, S., Fleischmann, O. C., Hartmann, M., Himmelmann, S., Homann, T., Kromminga, H., Spietz, P., Türk, A., Vogel, A., Voigt, S., and Burrows, J. P.: Laboratory Spectroscopy in Support of UV-Visible Remote-Sensing of the Atmosphere, In *Recent Research Developments in Physical Chemistry*, 2002.
- Paur, R. J. and Bass, A. M.: The Ultraviolet Cross-Sections of Ozone: Part II. Results and temperature dependence, edited by Zerefos S., Ghazi A., Reidel D.(Eds.), Halkidiki Greece, *Proceedings of the Quadrennial Ozone Symposium on Atmospheric Ozone*, Norwell., pp. 611–615, 1985.
- Peter, T.: Microphysics and heterogeneous chemistry of polar stratospheric clouds, *Annu. Rev. Phys. Chem.*, 48, 785–822, 1997.
- Plumb, R. A.: The interaction of two internal waves with the mean flow: Implications for the theory of the quasi-biennial oscillation, *J. Atmos. Sci.*, 34, 1847–1858, 1977.
- Plumb, R. A.: Stratospheric transport, *J. Meteor. Soc. Jpn.*, 80, 793–809, 2002.
- Qu, Z. W., Zhu, H., Grebenshchikov, S. Y., Schinke, R., and Farantos, S. C.: The Huggins band of ozone: A theoretical analysis, *J. Chem. Phys.*, 121(23), 11 731 – 11 745, doi:10.1063/1.1814098, 2004a.
- Qu, Z. W., Zhu, H., Tashiro, M., Schinke, R., and Farantos, S. C.: The Huggins band of ozone: Unambiguous electronic and vibrational assignment, *J. Chem. Phys.*, 120(15), 6811 – 6814, doi:10.1063/1.1711589, 2004b.
- Randel, W. J. and Wu, F.: A stratospheric ozone profile data set for 1979 – 2005: Variability, trends, and comparisons with column ozone data, *J. Geophys. Res.*, 112, D06 313, doi:10.1029/2006JD007339, 2007.
- Randel, W. J. and Wu, F. and Stolarski, R.: Changes in column ozone correlated with the stratospheric EP flux, *J. Meteorol. Soc. Jpn.*, 80, 849–862, 2002.
- Randel, W. J. and Cobb, J. B.: Coherent variations of monthly mean column ozone and lower stratospheric temperature, *J. Geophys. Res.*, 99, 5433–5447, 1994.

- Randel, W. J., Wu, F., Russell III, J. M., Waters, J. W., and Froidevaux, L.: Ozone and temperature changes in the stratosphere following the eruption of Mt. Pinatubo, *J. Geophys. Res.*, 100, 16 753–16 764, 1995.
- Reed, R., Campbell, W. J., Rasmussen, L. A., and Rogers, D. G.: Evidence of downward-propagating annual wind reversal in the equatorial stratosphere, *J. Geophys. Res.*, 66, 813–818, 1961.
- Reinsel, G. C., Weatherhead, E. C., Tiao, G. C., Miller, A. J., Nagatani, R. M., Wuebbles, D. J., and Flynn, L. E.: On detection of turnaround and recovery in trend for ozone, *J. Geophys. Res.*, 107(D10), 4078, doi:10.1029/2001JD000500, 2002.
- Reinsel, G. C., Miller, A. J., Weatherhead, E. C., Flynn, L. E., Nagatani, R. M., Tiao, G. C., and Wuebbles, D. J.: Trend analysis of total ozone data for turnaround and dynamical contributions, *J. Geophys. Res.*, 110, D16 306, doi:10.1029/2004JD004662, 2005.
- Rieder, H. E., Staehelin, J., Mäder, J. A., Peter, T., Ribatet, M., Davison, A. C., Stübi, R., Weihs, P., and Holawe, F.: Extreme events in total ozone over Arosa – Part 1: Application of extreme value theory, *Atmos. Chem. Phys.*, 10, 10 021–10 031, doi:10.5194/acp-10-10021-2010, 2010a.
- Rieder, H. E., Staehelin, J., Mäder, J. A., Peter, T., Ribatet, M., Davison, A. C., Stübi, R., Weihs, P., and Holawe, F.: Extreme events in total ozone over Arosa – Part 2: Fingerprints of atmospheric dynamics and chemistry and effects on mean values and long-term changes, *Atmos. Chem. Phys.*, 10, 10 033–10 045, doi:10.5194/acp-10-10033-2010, 2010b.
- Rieder, H. E., Jancso, L. M., Di Rocco, S., Staehelin, J., Mäder, J. A., Peter, T., Ribatet, M., Davison, A. C., De Backer, H., Koehler, U., Krzyżcin, J., and Vaniček, K.: Extreme events in total ozone over the northern mid-latitudes: an analysis based on long-term data sets from five European ground-based stations, *Tellus B, North America*, 63, 860 –874, doi:10.1111/j.1600-0889.2011.00575.x, 2011.
- Rieder, H. E., Frossard, L., Ribatet, M., Staehelin, J., Maeder, J. A., Di Rocco, S., Davison, A. C., Peter, T., Weihs, P., and Holawe, F.: On the relationship between total ozone and atmospheric dynamics and chemistry at mid-latitudes – Part 2: The effects of the El Niño/Southern Oscillation, volcanic eruptions and contributions of atmospheric dynamics and chemistry to long-term total ozone changes, *Atmos. Chem. Phys.*, 13, 165–179, doi:10.5194/acp-13-165-2013, 2013.
- Rind, D.: The sun's role in climate variations, *Science*, 296, 673–677, 2002.
- Rosenlof, K. and Holton, J. R.: Estimates of the stratospheric residual

- circulation using the downward control principle, *J. Geophys. Res.*, 98, 10 465–10 479, 1993.
- Rozanov, E., Callis, L., Schlesinger, M., Yang, F., Andronova, N., and Zubov, V.: Atmospheric response to  $\text{NO}_y$  source due to energetic electron precipitation, *Geophys. Res. Lett.*, 32, L14 811, doi:10.1029/2005GL023041, 2005.
- Sato, M., Hansen, J. E., McCormack, M. P., and Pollack, J. B.: Stratospheric aerosol optical depth, *J. Geophys. Res.*, 98, 1850–1990, 1993.
- Schnadt Poberaj, C., Staehelin, J., and Brunner, D.: Missing stratospheric ozone decrease at Southern Hemisphere middle latitudes after Mt. Pinatubo: a dynamical perspective, *J. Atmos. Sci.*, 68, 1922–1945, 2011.
- Serdyuchenko, A., Gorshchev, V., Weber, M., and Burrows, J. P.: New broadband high-resolution ozone absorption cross-sections, *Spectroscopy Europe*, 23, 14–17, 2011.
- Serdyuchenko, A., Gorshchev, V., Weber, M., Chehade, W., and Burrows, J. P.: High spectral resolution ozone absorption cross-sections; Part 2: Temperature dependence, *Atmospheric Measurement Techniques Discussions*, 6, 6613–6643, doi:10.5194/amtd-6-6613-2013, URL <http://www.atmos-meas-tech-discuss.net/6/6613/2013/>, 2013.
- Siddans, R., Kerridge, B. J., Latter, B. G., Smeets, J., and Otter, G.: Analysis of GOME-2 Slit function measurements, Algorithm Theoretical Basis Document, EUM/CO/04/1298/RM., 2006.
- Sinha, A., Imre, D., Goble, J. J. H., and Kinsey, J. L.: Excitation spectroscopy of jet-cooled ozone: The Huggins system, *J. of Chem. Phys.*, 84 (11), 6108 – 6114, 1986.
- Sinnhuber, B. M., Sheode, N., Sinnhuber, M., Chipperfield, M. P., and Feng, W.: The contribution of anthropogenic bromine emissions to past stratospheric ozone trends: a modelling study, *Atmos. Chem. Phys*, 9, 2863–2871, 2009.
- Sinnhuber, M., Burrows, J. P., Chipperfield, M. P., Jackman, C. H., Kallenrode, M.-B., Künzi, K. F., and Quack, M.: A model study of the impact of magnetic field structure on atmospheric composition during solar proton events, *Geophys. Res. Lett.*, 30, 1818, doi:10.1029/2003GL017625, 2003.
- Solomon, S.: Stratospheric ozone depletion: a review of concepts and history, *Rev. Geophys.*, 37, 275–316, 1999.
- Solomon, S., Portman, R. W., Garcia, R. R., Thomason, L. W., Poole, L. R., and McCormack, M. P.: The role of aerosol variations in anthropogenic

- ozone depletion at northern midlatitudes, *J. Geophys. Res.*, 101, 6713–6727, 1996.
- Soukharev, B. E. and Hood, L. L.: Solar cycle variation of stratospheric ozone: Multiple regression analysis of long-term satellite data sets and comparisons with models, *J. Geophys. Res.*, 111, D20 314, doi:10.1029/2006JD007107, 2006.
- SPARC: Stratospheric Processes And their Role in Climate: Assessment of trends in the vertical distribution of ozone, SPARC Report 1, edited by: Harris, N., Hudson, R., and Phillips, C., SPARC Report No. 1, 1998.
- Staehelin, J., Kegel, R., and Harris, N. R. P.: trend analysis of the homogenized total ozone series of Arosa (Switzerland), 1926–1996, *J. Geophys. Res.-Atmos.*, 103, 8389–8399, 1998.
- Staehelin, J., Harris, N. R. P., Appenzeller, C., and Eberhard, J.: Ozone trends: A review, *Rev. Geophys.*, 39, 231–290, 2001.
- Steinbrecht, W., Hassler, B., Claude, H., Winkler, P., and Stolarski, R. S.: Global distribution of total ozone and lower stratospheric temperature variations, *Atmos. Chem. Phys.*, 3, 3411–3449, 2003.
- Steinbrecht, W., Köhler, U., Claude, H., Weber, M., Burrows, J. P., and van der A, R. J.: Very high ozone columns at northern mid-latitudes in 2010, *Geophys. Res. Lett.*, 38, L06 803, doi:10.1029/2010GL046634, 2011.
- Steinfeld, J. I., Adler-Golden, S. M., and Gallagher, J. W.: Critical Survey of Data on the Spectroscopy and Kinetics of Ozone in the Mesosphere and Thermosphere, *J. Phys. Chem. Ref. Data.*, 16, 911 – 951, 1987.
- Stolarski, R. S. and Cicerone, R. J.: Stratospheric chlorine: A possible sink for ozone, *Can. J. Chem.*, 52, 1610–1615, 1974.
- Stolarski, R. S. and Frith, S. M.: Search for evidence of trend slowdown in the long-term TOMS/SBUV total ozone data record: the importance of instrument drift uncertainty, *Atmos. Chem. Phys.*, 6, 4057–4065, doi: 10.5194/acp-6-4057-2006, 2006.
- Stolarski, R. S., Krueger, A. J., Schoeberl, M. R., McPeters, R. D., Newman, P. A., and Alpert, J. C.: Nimbus-7 satellite measurements of the springtime antarctic ozone decrease, *Nature*, 322, 808–811, 1986.
- Sudo, K. and Takahashi, M.: Simulation of tropospheric ozone changes during 1997–1998 El Niño: Meteorological impact on tropospheric photochemistry, *Geophys. Res. Lett.*, 23, 4091–4094, 2001.
- Taguchi, M. and Hartmann, D. L.: Increased occurrence of stratospheric

- sudden warming during El Niño as simulated by WACCM, *J. Climate*, 19, 324–332, 2006.
- Tang, X., Madronich, S., Wallington, T., and Calamari, D.: Changes in tropospheric composition and air quality, *Photochem. Photobiol. B*, 46, 83 – 95, 1998.
- Thompson, A. M., Witte, J. C., Hudson, R. D., Guo, H., Herman, J. R., and Fujiwara, M.: Tropical tropospheric ozone and biomass burning, *Science*, 291, 2128–2132, 2001.
- Thunemann, K. H., Peyerimhoff, S. D., and Buenker, R. J.: Configuration Interaction Calculations for the Ground and Excited States of Ozone and Its Positive Ion: Energy Locations and Transition Probabilities, *J. Mol. Spectrosc.*, 70, 432–448, doi:10.1016/0022-2852(78)90181-9, 1978.
- Trenberth, K. E., Caron, J. M., Stepaniak, D. P., and Worley, S.: Evolution of El Niño–Southern Oscillation and global atmospheric surface temperatures, *J. Geophys. Res.*, 107(D8), 4065, doi:10.1029/2000JD000298, 2002.
- Tung, K. and Yang, H.: Global QBO in circulation and ozone, part I, Re-examination of observational evidence, *J. Atmos. Sci.*, 51, 2699–2707, 1994.
- van der A, R. J., Allaart, M. A. F., and Eskes, H. J.: Multi sensor re-analysis of total ozone, *Atmos.Chem. Phys.*, 10, 11 277–11 294, doi: 10.5194/acp-10-11277-2010, 2010.
- van Loon, H. and Labitzke, K.: The Southern Oscillation. Part V: The anomalies in the lower stratosphere of the Northern Hemisphere in winter and a comparison with the Quasi–Biennial Oscillation, *Mon. Weather Rev.*, 115, 357–369, 1987.
- Van Roozendaal, M., Loyola, D., Spurr, R., Balis, D., Lambert, J. C., Livschitz, Y., Valks, P., Ruppert, T., Kenter, P., Fayt, C., and Zehner, C.: Ten years of GOME/ERS-2 total ozone data: the new GOME Data Processor (GDP) version 4: Algorithm Description, *J. Geophys. Res.*, 111, D14 311, doi:doi:10.1029/2005JD006375, 2006.
- Viereck, R. A., Puga, L., McMullin, D., Judge, D., Weber, M., and Tobiska, W. K.: The Mg II index: A proxy for solar EUV, *Geophys. Res. Lett.*, 28(7), 1343–1346, 2001.
- Viereck, R. A., Floyd, L. E., Crane, P. C., Woods, T. N., Knapp, B. G., Rottman, G., Weber, M., Puga, L. C., and DeLand, M. T.: A composite Mg II index spanning from 1978 to 2003, *Space Weather*, 2, S10 005, doi: 10.1029/2004SW000084, 2004.

- Vyushin, D., Fioletov, V. E., and Shepherd, T. G.: Impact of long-range correlations on trend detection in total ozone, *J. Geophys. Res.*, 112, D14 307, doi:10.1029/2006JD008168, 2007.
- Vyushin, D., Shepherd, T. G., and Fioletov, V. E.: On the statistical modeling of persistence in total ozone anomalies, *J. Geophys. Res.*, 115, D16 306, doi:10.1029/2009JD013105, 2010.
- Waugh, D. and Hall, T.: Age of stratospheric air: Theory, observations, and models, *Rev. Geophys.*, 40(4), 1010, doi:10.1029/2000RG000101, 2005.
- Weber, M., Lamsal, L. N., Coldewey-Egbers, M., K., B., and Burrows, J. P.: Pole-to-pole validation of GOME WFDOAS total ozone with ground-based data, *Atmos. Chem. Phys.*, 5, 1341–1355, 2005.
- Weber, M., Lamsal L, N., and Burrows, J. P.: Improved SCIAMACHY WFDOAS total ozone retrieval: steps towards homogenising long-term total ozone datasets from GOME, SCIAMACHY, and GOME2, Proc. 'Envisat Symposium 2007', Montreux, Switzerland, 23-27 April 2007, ESA SP-636, July 2007 [Available online at <http://envisat.esa.int/envisatsymposium/proceedings/posters/3P4/463281we.pdf>.] (last access: Nov. 2013), 2007.
- Weber, M., Dikty, S., Burrows, J. P., Garny, H., Dameris, M., Kubin, A., Abalichin, J., and Langematz, U.: The Brewer–Dobson circulation and total ozone from seasonal to decadal time scales, *Atmos. Chem. Phys.*, 11, 11 221–11 235, doi:10.5194/acp-11-11221-2011, 2011.
- Weber, M., Steinbrecht, W., Long, C. S., Fioletov, V. E., Frith, S. H., Stolarski, R. S., and Newman, P. A.: Global Climate] Stratospheric Ozone in State of the Climate in 2011, *Bull. Amer. Meteor. Soc.*, 93, S46–S48, 2012.
- Weber, M., Chehade, W., Fioletov, V. E., Frith, S. M., Long, C. S., Steinbrecht, W., and Wild, J. D.: Stratospheric Ozone in [Blunden, J., and D.S. Arndt, State of the Climate in 2012]., *Bull. Amer. Meteor. Soc.*, 94, S36–S37, doi:10.1175/2013BAMSSStateoftheClimate.1,, 2013.
- White, J. U.: Long Optical Paths of Large Aperture, *J. of the Opt. Soc. Amer.*, 32, 285—288, 1942.
- Wild, J., Long, C., Barthia, P., and McPeters, R.: Constructing a Long-Term Ozone Climate Data Set (1979 – 2010) from V8.6 SBUV/2 Profiles, 2012.
- WMO: World Meteorological Organization: Global Ozone Research and Monitoring Project. Scientific Assessment of Ozone Depletion: 1994 ,Report No. 37, World Meteorological Organization, Geneva, 1995.

- WMO: World Meteorological Organization: Global Ozone Research and Monitoring Project. Scientific Assessment of Ozone Depletion: 1998, Report No. 44, World Meteorological Organization, Geneva, 1999.
- WMO: World Meteorological Organization: Global Ozone Research and Monitoring Project. Scientific Assessment of Ozone Depletion: 2002, Report No. 47, World Meteorological Organization, Geneva, 2003.
- WMO: World Meteorological Organization: Global Ozone Research and Monitoring Project. Scientific Assessment of Ozone Depletion: 2006, Report No. 50, World Meteorological Organization, Geneva, 2007.
- WMO: World Meteorological Organization: Global Ozone Research and Monitoring Project. Scientific Assessment of Ozone Depletion: 2010, Report No. 52, World Meteorological Organization, Geneva, 2011.
- Wofsy, S. C., McElroy, M. B., and Yung, Y. L.: The chemistry of the atmospheric bromine, *Geophys Res. Lett.*, 2, 215–218, 1975.
- Wohlmann, I., Lehmann, R., Rex, M., Brunner, D., and Mäder, J. A.: A process-oriented regression model for column ozone, *J. Geophys. Res. Atmos.*, 112, D12 304, doi:10.1029/2006jd007573, 2007.
- Yamashita, K., Morokuma, K., Le Quèrè, F., and Leforestier, C.: New ab initio potential surfaces and three dimensional quantum dynamics for transition state spectroscopy in the ozone photodissociation, *Chem. Phys. Lett.*, 191 (6), 515 – 520, 1992.
- Yang, S. K., Long, C. S., Miller, A. J., He, X., Yang, Y., Wuebbles, D. J., and Tiao, G.: Modulation of natural variability on a trend analysis of updated cohesive SBUV(/2) total ozone, *Int. J. Remote Sens.*, 30, 3975–3986, doi:10.1080/01431160902821924, 2009.
- Yung, Y. L., Pinto, J. P., Watson, R. T., and P., S. S.: Atmospheric bromine and ozone perturbations in the lower stratosphere, *J. Atmos. Sci.*, 37, 339–353, 1980.
- Zeng, G. and Pyle, J. A.: Influence of El Niño Southern Oscillation on stratosphere/troposphere exchange and the global tropospheric ozone budget, *Geophys. Res. Lett.*, 32, L0814,, doi:10.1020/2004GL021353, 2005.
- Zerefos, C. S., Tourpali, K., Bojkov, R., Balis, D., Rognerund, B., and Isaksen, I.: Solar activity – total ozone relationships: observations and model studies with heterogeneous chemistry, *J. Geophys. Res.*, 102, 1561–1569, 1997.
- Ziemke, J. R., Chandra, S., McPeters, R. D., and Newman, P. A.: Dynam-

ical proxies of column ozone with applications to global trend models, *J. Geophys. Res.*, 102, 6117–6129, 1997.

Ziemke, J. R., Chandra, S., Oman, L. D., and Bhartia, P. K.: A new ENSO index derived from satellite measurements of column ozone, *Atmos. Chem. Phys.*, 10, 711–3721, doi:10.5194/acp-10-3711-2010, 2010.



# Acknowledgements

I would like to thank all the people who contributed to my scientific career at IUP. My deep gratitude to Prof. John Burrows for the motivational encouragement, guidance and support at all stages of my PhD. I feel privileged to be your student, your lectures provided the solid grounds for my endeavors in PhD. I am indebted to Dr. Heinrich Bovenmann for selecting me as a PhD student at the institute.

My earnest thanks and appreciation to Dr. Mark Weber for a marvelous and friendly supervision, for stimulating and fruitful discussions and the useful critiques. Your expertise in my topic of research has been inspirational and guiding light. You always gave me very generous time whenever I needed your guidance or had some questions. Thanks for always encouraging me to publish my results and giving me ample time to work on my publications.

Its my pleasure that Prof. Otto Schrems accepted to be my second Gutachter, many thanks to you. I am also very thankful to Dr. Helmut Fisher and PD. Dr. Volker Perlick for being my Examiners.

I am very grateful to PD. Dr. Annette Ladstätter for the incredible support starting from the time I joined the institute. Thanks for all invaluable advices and directions. My sincere thanks to Anja Getzka and Petra Horn for the great administrative assistance and care, I sincerely appreciate that.

I would like to extend my thanks to the colleagues at UV-Sat, Limb, GHG, Terrestrial Physics and the Molecular Physics groups and the senior scientists around for a friendly and cooperative atmosphere around and for the exchange of knowledge.

I am thankful to the PIP administration for providing me travel support as a PhD student to travel to conferences, summer schools and workshops.

## Acknowledgements

---

I am thankful to Claus, who did not only share the office with me but also fruitful discussions. Thanks to my colleagues Luca and Ali for refreshing little breaks. I am grateful to my friends with whom I had a wonderful time, who were always there for me.

My great appreciation for Faiza, nothing can replace this enormous 24/7 support.

The unconditional love and care from my father, mother, sister and brothers has always been there, thanks for your trust in my pursuits. It's a great pleasure for me to dedicate my thesis to you.

# Erklärung

Hiermit erkläre ich, dass ich die Arbeit ohne unerlaubte fremde Hilfe angefertigt habe, dass ich weiterhin keine anderen als die angegebenen Quellen und Hilfsmittel benutzt und die den benutzten Werken wörtlich oder inhaltlich entnommenen Stellen als solche kenntlich gemacht habe.

*Wissam Chegade*